



國立臺灣大學天文物理研究所

博士論文

Graduate Institute of Astrophysics

National Taiwan University

Doctorial Dissertation

運用 SMA 與 ALMA 研究原恆星盤的形成與演化

An Observational Scenario of Keplerian Disk Formation around
Protostars Revealed with the SMA and ALMA

顏士韋

Hsi-Wei Yen

指導教授：賀曾樸博士、高桑繁久博士與大橋永芳博士

Advisor: Dr. Paul T.P. Ho, Dr. Shigehisa Takakuwa,
and Dr. Nagayoshi Ohashi

中華民國 102 年 8 月

Aug, 2013



An Observational Scenario of Keplerian Disk Formation around Protostars Revealed with the SMA and ALMA

Hsi-Wei Yen

August 15, 2013



誌謝

首先誠摯的感謝我的指導教授高桑繁久博士、大橋永芳博士、以及賀曾樸博士，謝謝他們這幾年來無私的教誨與指導，使我得以順利完成這篇博士論文。本論文的完成亦得感謝林仁良博士、李景輝博士、平野尚美博士、呂聖元博士、蘇裕農博士以及卡兒博士不厭其煩的指出我研究中的缺失，且總能在我迷惘時為我解惑，使得本論文能夠更完整而嚴謹。謝謝譚遠培博士和湯雅雯博士當初引領我一窺天文領域的奧妙，且鼓勵我致力於天文的研究。也要感謝劉君帆、謝佩穎、呂浩宇、林蓮宣、張世昕、何宜庭、楊淳惠等學長姐，還有王亮堯、茅耀元等好友於學術上的協助與討論。最後，謹以此文獻給我摯愛的雙親與親愛的太太賴虹君，他們的默默支持是我前進的動力。特別的感謝我的兒子運辰有效的提升了我的工作效率。



Acknowledgment

I would like to express the deepest appreciation to my supervisors Dr. Takakuwa Shigehisa, Dr. Nagayoshi Ohashi, and Dr. Paul T.P. Ho. Without their guidance, persistent help, and support, this thesis project would not have been possible. I would like to thank Dr. Jeremy Lim, Dr. Chin-Fei Lee, Dr. Naomi Hirano, Dr. Sheng-Yuan Liu, Dr. Yu-Nung Su, and Dr. Jennifer Karr for their insightful comments and suggestions on this thesis project. I am deeply grateful to Dr. Ronald Taam and Dr. Ya-Wen Tang for introducing me to this field and giving me encouragement. I thank my friends Liang-Yao Wang, I-Ting Ho, Chun-Hui Yang, Yao-Yuan Mao, Pei-Ying Hsieh, Chun-Fan Liu, and Shi-Shin Chang for their enormous help, encouragement, and stimulating discussions. I would like to show my greatest appreciation to my parents and my wife Hung-Chun Lai for supporting me spiritually throughout my life. Special thanks to my baby who helps me to improve my working efficiency.



摘要

行星系統誕生於環繞著原恆星的盤狀結構。為了瞭解行星系統的形成機制，就必須研究此類盤狀結構是如何形成的。目前天文學家認為，此類盤狀結構是隨著原恆星的誕生一起形成的，而且其形成的機制與演化和角動量如何從周圍的氣體傳遞到盤狀結構上息息相關。因此，為了研究盤狀結構的形成與演化，我運用了 SMT, ASTE, SMA 和 ALMA 觀測了數個不同演化程度的原恆星，測量其周圍氣體的旋轉速度，研究了（1）從半徑 10,000 到 100 天文單位的角動量分佈，（2）角動量分佈如何演化，（3）周圍氣體如何傳遞角動量給中央的盤狀結構。我的觀測結果顯示：（1）原恆星的周圍氣體有較小的角動量，而離原恆星較遠的氣體帶有比較大的角動量。（2）在比較老的原恆星周圍的氣體旋轉的速度比較快，並且遵循克卜勒運動；而在比較年輕的原恆星周圍的氣體，旋轉速度較慢，並且位於不同半徑的氣體都帶有相同的角動量。（3）原恆星演化到後期，周圍氣體塌縮的速率已經下降，並且周圍氣體只沿著數條氣流吸積到中央的盤狀結構上，與演化初期氣體會均向的流向中央有所不同。運用理論學家所提出的氣體塌縮理論，我建立了一套解析解的模型，計算了角動量分佈的演化，並利用這套模型解釋了上述的觀測結果。

關鍵詞： 恆星形成；原恆星；原恆星盤；星際介質的動力學



Abstract

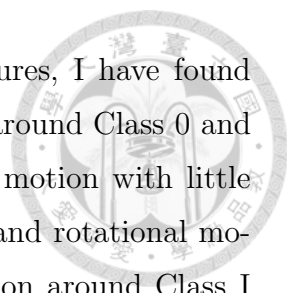
Circumstellar disks around young stellar objects are sites of planet formation. It is intriguing to understand the formation process of such circumstellar disks. In the formation process of a low-mass star, a circumstellar disk is expected to form in the innermost (<100 AU) region of a protostellar envelope around a protostar at an early evolutionary stage, and envelope material infalls and feeds the central protostar and circumstellar disk. Formation and evolution of circumstellar disks are closely related to the mechanism of angular momentum transportation in protostellar envelopes from the envelope scale (thousands of AU) down to the disk scale (~ 100 AU). To study this mechanism, it is essential to reveal the kinematics of protostellar envelopes around representative protostellar sources and to compare the kinematics among sources at different evolutionary stages. Therefore, I have conducted SMT, ASTE, SMA and ALMA observations toward a sample of protostellar sources, and studied (1) the rotational motion on the scales from 10,000 AU to 100 AU around a Class 0 protostar B335, (2) evolution of the rotational motions on the scales of 1000–100 AU of a sample of Class 0 and I protostars, and (3) the connection between the disk and the protostellar envelope around a Class I protostar L1489 IRS.

To study rotational motion from large to small scales in protostellar sources, I have conducted observations in the millimeter C^{18}O (2–1) and submillimeter CS (7–6) lines with the SMT, ASTE and SMA toward a prototypical Class 0 protostar, B335. In B335, the C^{18}O (2–1) emission traces the protostellar envelope on the scales from $\sim 10,000$ AU to a few hundred AU, while the CS (7–6) emission shows a compact envelope component with a size of ~ 800 AU surrounded by an east-west elongated outflow component with a size of ~ 3000 AU. On the scale of 10,000 AU, the C^{18}O envelope exhibits rotational motion with a specific angular momentum of $\sim 2 \times 10^{-3} \text{ km s}^{-1} \text{ pc}$ ($V_{\text{rot}} \sim 0.04 \text{ km s}^{-1}$ at a radius of 9000 AU), comparable to those of other NH_3 dense cores. On the scale of a few hundred AU, the C^{18}O

envelope exhibits infalling motion but no signature of rotational motion ($V_{\text{rot}} < 0.04$ km s⁻¹ at a radius of 370 AU). The CS (7–6) line, having a higher upper energy level and a higher critical density than the C¹⁸O (2–1) line, can trace an inner dense and warm region around protostars, where rotational velocity is likely higher than that in an outer region. On the scale of ~ 100 AU, the CS envelope shows rotational motion ($V_{\text{rot}} = 0.11$ km s⁻¹ at a radius of 110 AU) but no signature of infalling motion. These results show that the specific angular momenta of the rotational motion in B335 decrease from radii of 10,000 AU to a few hundred AU, and the specific angular momenta on the scale of a few hundred AU are one to two orders of magnitude lower than those in other Class I and II sources.

To study evolution of rotational motions of protostellar sources, I have conducted observations in the C¹⁸O (2–1) line with the SMA toward three Class 0, one Class 0/I, and two Class I protostars. My observational results show that two Class 0 sources, B335 and NGC 1333 IRAS 4B, do not exhibit detectable rotational motion on hundreds of AU scale, while L1527 IRS (Class 0/I) and L1448-mm (Class 0) exhibit rotational motions with radial profiles of $V_{\text{rot}} \propto r^{-1.0 \pm 0.2}$ and $\propto r^{-1.0 \pm 0.1}$, respectively. The other Class I sources, TMC-1A and L1489 IRS, exhibit the fastest rotational motions among the sample, and their rotational motions have flatter radial profiles of $V_{\text{rot}} \propto r^{-0.6 \pm 0.1}$ and $\propto r^{-0.5 \pm 0.1}$, respectively. The rotational motions with the radial dependence of $\sim r^{-1}$ can be interpreted as rotation with a conserved angular momentum in a dynamically infalling envelope, while those with the radial dependence of $\sim r^{-0.5}$ can be interpreted as Keplerian rotation.

To study the connection between circumstellar disks and their surrounding protostellar envelopes, I have conducted observations in the 1.3 mm continuum and the ¹²CO (2–1), C¹⁸O (2–1), and SO (5₆–4₅) lines with the ALMA toward a Class I protostar L1489 IRS. A circumstellar disk in Keplerian rotation around L1489 IRS is clearly identified in the ¹²CO and C¹⁸O emission, and the central protostellar mass is estimated to be $2.0 M_{\odot}$. In addition, there are arm-like structures attached to the circumstellar disk, and their kinematics cannot be explained by the Keplerian rotation. These non-Keplerian structures could trace accretion flow following parabolic trajectories toward the disk. The SO emission primarily traces the transitional regions between the accretion flow and the disk, which could be due to the enhancement in the SO abundance in the regions of accretion shocks.



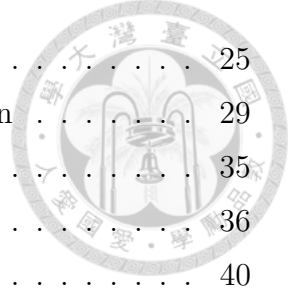
From my observational results as well as those from literatures, I have found the kinematics of protostellar envelopes on 100–1000 AU scales around Class 0 and I protostars can be categorized into three groups, (1) infalling motion with little rotational motion around Class 0 protostars, (2) both infalling and rotational motions around Class 0 and I protostars, and (3) Keplerian rotation around Class I protostars. I propose that the three categories reflect the evolution sequence from infalling envelopes to formation of Keplerian disks. In an early stage of collapse of a dense core, the envelope material with a small angular momentum in the vicinity of the protostar collapses first, and the protostellar envelope on 100–1000 AU scales shows infalling motion but little rotational motion. As the expansion wave propagates outwardly, the envelope material with a larger angular momentum in an outer region start to collapse. As more angular momenta travel toward the center with the infalling motion, rotational velocities of the protostellar envelope on 100–1000 AU scales and the size of the central disk increase. With time, the protostellar envelope dissipates due to the mass ejection from outflows and the mass accretion onto the central protostar and disk. At a later evolutionary stage, the envelope material is infalling along few parabolic flows (not isotropically) due to the protostellar envelope is partially dissipated, and a Keplerian disk with an outer radius of hundreds of AU appears. Based on the inside-out collapse theory of protostellar envelopes, I have constructed an analytical model and computed evolution of radial profiles of rotational velocities, to interpret the observed results in the context of formation of large-scale (>100 AU) disk.

Keywords: star formation; protostar; circumstellar disk; ISM kinematics

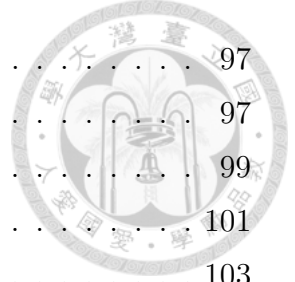


Contents

誌謝	i
Acknowledgment	ii
摘要	iii
Abstract	vi
List of Figures	x
List of Tables	xiv
1 Introduction	1
1.1 Star Formation	1
1.2 Evolutionary Scenario of Low-Mass Star Formation	1
1.3 Classification of Protostellar Sources and Young Stellar Objects	3
1.4 Recent Observational and Theoretical Studies of Keplerian Disks around Protostars and YSOs	5
1.5 Motivation of this Thesis	6
1.6 Outline of this Thesis	8
2 High-Velocity Jets and Slowly Rotating Envelope in B335	10
2.1 Abstract	10
2.2 Introduction	11
2.3 Observation	13
2.4 Results	14
2.4.1 1.3 mm Continuum Emission	14
2.4.2 ^{12}CO (2–1) Emission	16
2.4.3 ^{13}CO (2–1) Emission	19
2.4.4 C^{18}O (2–1) Emission	22
2.5 Discussion	25



2.5.1	High-velocity ^{12}CO Component	25
2.5.2	The Origin and Kinematics of the C^{18}O Emission	29
2.5.3	Infalling Motion in the Envelope	35
2.5.4	Non-Conserved Angular Momentum in B335	36
2.6	Summary	40
3	Physical Conditions and Kinematics Traced by Millimeter and Sub- millimeter Lines on a Few Hundreds of AU Scale in B335	43
3.1	Abstract	43
3.2	Introduction	44
3.3	Observation	46
3.4	Results	47
3.4.1	Single-dish, SMA, and the Combined Images in Millimeter C^{18}O and Submillimeter CS Emissions	49
3.4.2	Velocity Structures	52
3.5	LVG Analyses	60
3.6	Discussion	67
3.6.1	Physical Conditions of the Outflow and Envelope	67
3.6.2	Rotation, Infall, and the Evolution of Protostellar Envelopes Traced by the Millimeter and Submillimeter Line Emissions	69
3.7	Summary	75
3.8	Appendix Combining SMA and Single-dish Data and Imaging Simulation of the Combing Process	77
4	Unveiling the Evolutionary Sequence from Infalling Envelopes to Keplerian Disks around Low-Mass Protostars	82
4.1	Abstract	82
4.2	Introduction	83
4.3	Sample	86
4.3.1	Overview	86
4.3.2	Individual Sources	88
4.4	Observations	91
4.5	Spatial and Kinematics Structures of the C^{18}O (2–1) Emission	94



4.5.1	B335	97
4.5.2	IRAS 4B	97
4.5.3	L1527 IRS	99
4.5.4	L1448-mm	101
4.5.5	TMC-1A	103
4.5.6	L1489 IRS	104
4.6	Analysis	105
4.6.1	Method to Derive Rotational Profiles	105
4.6.2	Uncertainties of the Measured Rotational Profiles	110
4.7	Discussion	114
4.7.1	Variations of the Rotational Motions around the Protostellar Sources	114
4.7.2	Observations and MHD Simulations of Disk Formation	121
4.7.3	Keplerian Disks around Class I Protostars	124
4.8	Summary	125
4.9	Appendix	127
4.9.1	1.3 mm Continuum Images	127
4.9.2	Measuring Rotational Profiles from Position–Velocity Diagrams	129

5 ALMA Observation of Accretion Flows onto the Keplerian Disk

around a Class I protostar L1489 IRS		134
5.1	Abstract	134
5.2	Introduction	135
5.3	Observations	138
5.4	Results	139
5.4.1	1.3 mm Continuum Emission	139
5.4.2	^{12}CO (2–1) Emission	140
5.4.3	C^{18}O (2–1) Emission	142
5.4.4	SO (5_6-4_5) Emission	147
5.5	Analysis	150
5.5.1	Keplerian Disk Surrounded by a Torus in L1489 IRS	150
5.5.2	Infalling Gas Flows onto the Keplerian Disk	160
5.6	Discussion	166
5.7	Summary	169

6 Summary of this Thesis

7 Future Work





List of Figures

1.1	Four Stages of Low-mass Star Formation of a Single Star	3
2.1	1.3 mm Continuum Map of B335	15
2.2	Moment 0 Maps of the ^{12}CO (2–1) Emission in B335	17
2.3	P – V Diagrams of the ^{12}CO (2–1) Emission	18
2.4	Moment 0 Maps of the ^{13}CO (2–1) Emission in B335	20
2.5	P – V Diagrams of the ^{13}CO (2–1) Emission	21
2.6	Moment 0 Map of the C^{18}O (2–1) Emission in B335	22
2.7	Velocity Channel Maps of the C^{18}O (2–1) Emission in B335	23
2.8	P – V Diagrams of the C^{18}O (2–1) Emission	24
2.9	Moment 0 Maps of the C^{18}O and ^{13}CO Emissions	30
2.10	The Configuration of the Outflow and the Infalling Flattened Envelope in B335	31
2.11	Simple Model P – V s of an Infalling and Rotating Gaussian Disk . . .	34
3.1	Moment 0 Maps of the SMT, SMA, and Combined Data of the C^{18}O (2–1) Emission in B335	50
3.2	Moment 0 Maps of the ASTE, SMA, and Combined Data of the CS (7–6) Emission in B335	51
3.3	Moment 0 Maps of the Combined Data, SMT + SMA in the C^{18}O (2–1) Emission and ASTE + SMA in the CS (7–6) Emission	51
3.4	Line Profiles of the C^{18}O (2–1) Emission in the SMT, SMA, and Combined Data and the CS (7–6) Emission in the ASTE, SMA, and Combined Data	53
3.5	Velocity Channel Maps of the Combined C^{18}O (2–1) Data	54
3.6	Velocity Channel Maps of the Combined CS (7–6) Data	55

3.7	Moment 0 Maps of the C ¹⁸ O (2–1) and CS (7–6) Emissions Integrated in Different Velocity Ranges	57
3.8	Velocity Channel Maps of the Combined CS (7–6) Data	58
3.9	SMT and SMT + SMA <i>P</i> – <i>V</i> Diagrams of the C ¹⁸ O (2–1) Emission	59
3.10	ASTE + SMA <i>P</i> – <i>V</i> Diagrams of the CS (7–6) Emission	60
3.11	Results of the LVG Calculations	64
3.12	Temperature and Density Maps of the CS Emitting Region	65
3.13	Specific Angular Momentum of Rotation Plotted as a Function of Radius	71
3.14	Amplitude and Amplitude Ratio as a Function of <i>u</i> – <i>v</i> Distance	79
3.15	Images of the Model After the Combining Process and the Original Model	80
3.16	Intensity Profiles of the Model Combined Map and the Original Model Image	81
4.1	C ¹⁸ O (2–1) Moment 0 and 1 Maps of B335, IRAS 4B, L1527 IRS, L1448-mm, TMC-1A, and L1489 IRS	95
4.2	Velocity Channel Maps of the C ¹⁸ O (2–1) Emission in IRAS 4B	98
4.3	Velocity Channel Maps of the C ¹⁸ O (2–1) Emission in L1527 IRS	100
4.4	Velocity Channel Maps of the C ¹⁸ O (2–1) Emission in L1448-mm	102
4.5	Velocity Channel Maps of the C ¹⁸ O (2–1) Emission in TMC-1A	103
4.6	Velocity Channel Maps of the C ¹⁸ O (2–1) Emission in L1489 IRS	104
4.7	C ¹⁸ O (2–1) <i>P</i> – <i>V</i> Diagrams of B335, IRAS 4B, L1527 IRS, L1448-mm, TMC-1A, and L1489 IRS	106
4.8	Schematic Representation of the Method to Derive Rotational Profiles	109
4.9	Derived Rotational Profiles in L1527 IRS, L1448-mm, TMC-1A, and L1489 IRS	110
4.10	Comparison of the Rotational Profiles in L1527 IRS, L1448-mm, TMC- 1A, L1489 IRS, and Other Class 0 and I Protostars	116
4.11	Rotational Profiles Calculated from the Analytical Model	120
4.12	1.3 mm Continuum Images of B335, IRAS 4B, L1527 IRS, L1448-mm, TMC-1A, and L1489 IRS	128
4.13	Imaging Simulations of Infalling and Rotating Envelopes	132
4.14	Rotational Profiles Measured from the Simulated <i>P</i> – <i>V</i> diagrams	133

5.1	1.3 mm Continuum Image of L1489 IRS	140
5.2	^{12}CO (2–1) Moment 0 and 1 Maps of L1489 IRS	141
5.3	C^{18}O (2–1) Moment 0 and 1 Maps of L1489 IRS	142
5.4	C^{18}O (2–1) Velocity Channel Maps of L1489 IRS	145
5.5	Moment 0 Map of the High-velocity, Medium-velocity, and Low-velocity C^{18}O (2–1) Emission in L1489 IRS	146
5.6	SO (5_6-4_5) Moment 0 and 1 Maps of L1489 IRS	148
5.7	SO (5_6-4_5) Velocity Channel Maps of L1489 IRS	149
5.8	Moment 0 Map of the High-velocity, Medium-velocity, and Low-velocity SO (5_6-4_5) Emission in L1489 IRS	151
5.9	Best-fit Results of Fitting Disk Models to ALMA C^{18}O (2–1) Data . .	155
5.10	Comparison between the 1.3 mm Continuum Emission and the Best- fit Disk Model	157
5.11	P–V diagrams in the ^{12}CO , C^{18}O , and SO Emission	159
5.12	P–V Diagrams of Disk, Torus, and Ring Models	161
5.13	Trajectories of the Infalling Flows	163
5.14	Edge-on and Face-on View of the Model	164
5.15	Comparison between the Model Images and Observational Data . . .	165
6.1	Schematic Figure of the Evolution of Protostellar envelopes into For- mation of Keplerian Disks	173



List of Tables

2.1	Summary of the Observational Parameters	14
2.2	Comparison of Collimated High-velocity ^{12}CO Emissions Among Dif- ferent Sources	26
2.3	Comparison of ^{12}CO Jet Activities Among Different Sources.	27
2.4	Comparison of the Protostellar Properties Between B335 and the Other Sources Associated with SiO Jets	28
2.5	Keplerian Radius of the Protostellar Sources	38
3.1	Summary of the Observational Parameters	48
3.2	Physical Conditions of the Outflow and the Inner Envelope	66
4.1	Sample of Sources	87
4.2	Summary of Observations	92
4.3	Resolutions and Noise Levels of the C^{18}O (2–1) Images	93
4.4	Power-law Indices of the Rotational Profiles and the Estimated Pro- tostellar Mass	111
4.5	Summary of the 1.3 mm Continuum Observations	128
5.1	Best-Fit Physical Parameters of the Keplerian disk	154



Chapter 1

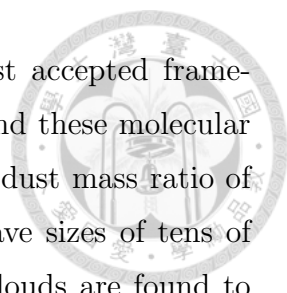
Introduction

1.1 Star Formation

Star formation is a fundamental phenomenon in the universe. Stars are one of the basic components of galaxies. In the early universe, there are only hydrogen and helium. All the heavy elements are produced through the nuclear synthesis in stars. Different heavy elements are produced via nuclear fusion inside stars with different masses, and the elements heavier than iron are formed during the death of massive stars. After stars die, they spread the heavy elements into interstellar medium, and those heavy elements become the material of the next generation stars. Therefore, the formation of stars controls the abundances of heavy elements in the universe. Stars form along with circumstellar disks that are the site of planet formation. Recent observational survey have found more than 700 exoplanets and more than 3000 exoplanet candidates (Wright et al. 2011). However, the Earth is the only planet known to suitable for lives. Properties of these planets must be determined during star formation process. Hence, the origin of lives could trace back to the formation of stars.

1.2 Evolutionary Scenario of Low-Mass Star Formation

How stars form is one of basic questions in astronomy. Shu et al. (1987) reviewed observational and theoretic results of star formation and proposed a four-stages model



of low-mass star formation process, which is currently the most accepted framework of star formation. Stars are formed in molecular clouds, and these molecular clouds are composed of molecular gas and dust with the gas to dust mass ratio of ~ 100 . Molecular clouds typically contain $10^{5-6} M_{\odot}$ gas and have sizes of tens of pc. Through CO observations starting from 1970s, molecular clouds are found to have substructure, clumps. Clumps have sizes of 2–5 pc, masses of $10^{3-4} M_{\odot}$ and densities of $\sim 10^{2-3} \text{ cm}^{-3}$. Within clumps, there are subregions of much higher density, so-called dense cores. The sizes of dense cores are ~ 0.1 pc, and their densities are higher than 10^4 cm^{-3} . On the other hand, the temperatures of dense cores are ~ 10 K. These dense cores are birthplaces of stars (e.g., André et al. 2000; Myers et al. 2000).

Figure 1.1 demonstrates the four-stages model of low-mass star formation. At the beginning, dense cores are supported by the magnetic field or turbulence, and they can contract slowly with leakage of the magnetic or turbulent support (Fig. 1.1a). Besides, these dense cores are slowly rotating (e.g., Goodman et al. 1993). After the dense cores become gravitationally unstable, the dense cores start to collapse dynamically from inside out (Shu 1977), and a protostar surrounded by a disk forms at the center of the dense core (Fig. 1.1b). The material in the dense cores keeps falling toward the center, and the gravitational energy releases during the accretion onto the surface of the protostar and the disk, which is the main energy source of protostellar luminosities. In this conventional picture, the material falls toward the center with a conserved angular momentum, eventually rotates fast enough to reach its Keplerian velocity, and becomes centrifugally supported. Hence, the angular momentum of the infalling material must be removed or transferred outward to have further accretion onto the protostar, and the material would fall onto the disk first rather than onto the surface of the protostar directly. During the accretion, part of material is ejected from the protostar-disk system along the polar axis, which results in collimated jets and bipolar outflows, and the outflowing and infalling motions coexist in the dense core (Fig. 1.1c). Outflows and jets can sweep ambient material to form outflow cavities and shells, and play an important role of removing angular momenta. With evolution, the size of the disk grows. The disk around the protostar is expected to be the site of planetary formation. Eventually, the outflow and the infall terminate, and a newly born star with a circumstellar disk appears

(Fig. 1.1d). In the end, the remnant surrounding material is dissipated, and a star with a planetary system forms.

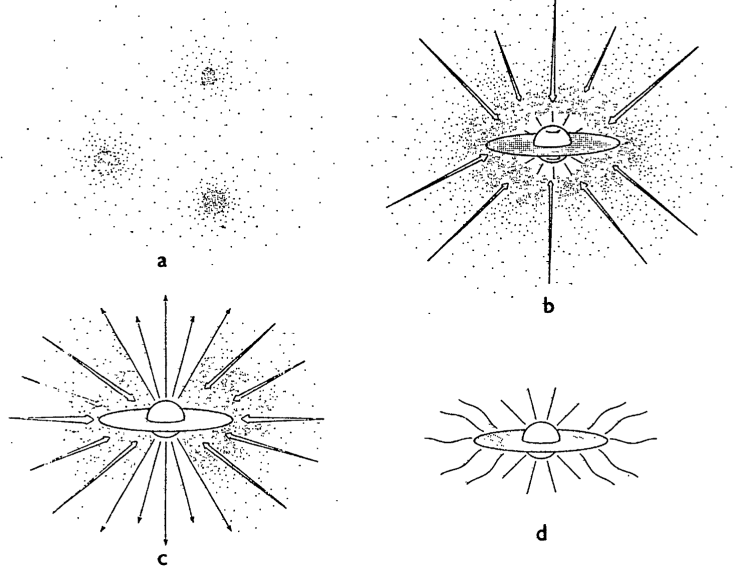


Figure 1.1 Four stages of low-mass star formation of a single star. (a) Dense cores contracts slowly in a clump. (b) A protostar and its surrounding disk form with material infalling dynamically. (c) An outflow launches and sweep ambient material, and the outflow is coexist with the infalling motion. (d) The outflow and the infall terminate. A newly formed star with a circumstellar disk appears. (Shu et al. 1987)

1.3 Classification of Protostellar Sources and Young Stellar Objects

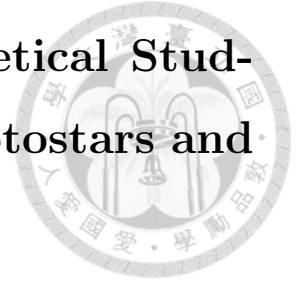
Observationally protostellar sources or young stellar objects (YSOs) can be classified into the Class 0 to III stages with their spectra energy distributions (SEDs), which correspond to the evolutionary stages described above. Class 0 and I stages correspond to Figure 1.1b and c, while Class II and III stages are corresponding to Figure 1.1d. The slope of their SEDs between $2.2 \mu\text{m}$ and $10\text{--}25 \mu\text{m}$ is defined as $\alpha_{\text{IR}} = \frac{d \log(F_{\lambda})}{d \log(\lambda)}$, which has been commonly used to quantify the different classes of protostellar sources or YSOs (Andre et al. 2000). Besides, the evolutionary sequence of protostellar sources or YSOs could be also identified by the bolometric temperature (T_{bol}), which is defined as the temperature of a blackbody having the same mean frequency as that of the SED of protostellar sources or YSOs (Myers &

Ladd 1993).

1. Class III sources are the most evolved YSOs and also called weak-line T-Tauri stars. Class III SEDs can be fitted by a blackbody spectrum and have α_{IR} less than -1.5, and they have $T_{\text{bol}} > 2880$ K. In Class III sources, there is no strong line emission at optical wavelengths, suggesting that most of the surrounding gas has already dissipated in this stage.
2. Class II sources, also called as classical T-Tauri stars, have α_{IR} less than zero but larger than -1.5 and T_{bol} of 650–2880 K. Their SEDs can be fitted by a blackbody spectrum with excess infrared emission. These SEDs suggest that there is a disk around a protostar, and the disk that is heated by the protostar is the source of the infrared excess. Besides, there is more circumstellar material in Class II sources than Class III sources.
3. Class I sources have α_{IR} larger than zero and T_{bol} of 70–650 K, and in their SEDs the mid-infrared emission from the surrounding dusty envelope dominates over the blackbody spectra of the central protostars, suggesting that there is a lot of material around the central protostar-disk systems.
4. Class 0 sources have T_{bol} less than 70 K. In their SEDs there is no significant contribution from the blackbody spectra of the central protostellar sources, different from those of Class I–III sources, and their SEDs are often represented by a single cold blackbody spectrum with a temperature of 15–30 K. Since Class 0 sources are expected to have extended envelopes that are more massive than the central protostellar masses, observationally Class 0 sources can be defined by these properties, i.e., extended submillimeter continuum emission with a central peak, and high ratio of submillimeter to bolometric luminosity.

Protostellar sources in the stage younger than Class 0 are called prestellar or starless cores, and they are in the stage corresponding to Figure 1.1a. Prestellar or starless cores are gravitationally bounded and contracting subsonically (e.g., Tafalla et al. 1998).

1.4 Recent Observational and Theoretical Studies of Keplerian Disks around Protostars and YSOs



With the development of observational techniques, understanding of the star formation process have been improved. Previous interferometric observations have found infalling and rotational gas motions on thousands of AU scale inside dense cores associated with known infrared sources, so-called protostellar envelopes (e.g., Ohashi et al. 1996, 1997b; Momose et al. 1998). Keplerian disks, which are expected to form in the innermost part (~ 100 AU) of protostellar envelopes, have been often observed around T Tauri stars with millimeter interferometric observations (e.g., Guilloteau & Dutrey 1994; Dutrey et al. 1998; Simon et al. 2000; Qi et al. 2003, 2004; Andrews & Williams 2007; Pietu et al. 2007; Guilloteau et al. 2011; Andrews et al. 2012). The radii of those Keplerian disks seen in CO emission range from ~ 100 to ~ 800 AU, and their masses traced by dust continuum emission range from $\sim 10^{-4}$ to $10^{-1} M_{\odot}$. Recent observations with SMA have reported the presence of Keplerian disks around Class I protostars, which are still embedded in protostellar envelopes (Brinch et al. 2007a; Lommen et al. 2008; Jørgensen et al. 2009; Takakuwa et al. 2012). These Keplerian disks around Class I protostars have radii from 100 to 300 AU and masses from 0.004 to 0.06 M_{\odot} , comparable to those around T Tauri stars. Although circumstellar disks around Class 0 protostars are likely deeply embedded in protostellar envelopes and difficult to be observed directly (e.g., Looney et al. 2003; Chiang et al. 2008), previous interferometric observations of millimeter dust continuum emission in B335 (Harvey et al. 2003) and L1157-mm (Chiang et al. 2012) at sub-arcsecond angular resolutions have identified possible disk components with the outer radii < 100 AU and < 40 AU, respectively. Several previous molecular-line observations of Class 0 sources have inferred the inner centrifugal radii to be < 100 AU, from the comparison between the infalling and rotational motions of the protostellar envelopes (e.g., Saito et al. 1999; Lee et al. 2006, 2009). Recently, Tobin et al. (2012a) have reported the detection of a Keplerian disk with a radius of ~ 90 AU around L1527 IRS, a transitional object from the Class 0 to I stages, from their interferometric observations of the ^{13}CO (2–1) emission, and have claimed that L1527 IRS is the youngest protostar surrounded by a Keplerian disk.

These observational results combined with those of Class I protostars and T Tauri stars imply that Keplerian disks around protostars likely increase their radii from <100 AU up to ~ 800 AU as protostars evolve from Class 0 to T Tauri stages.

Many theoretical simulations, including the effect of the magnetic field, have been invested in studying the formation process of Keplerian disks. Classical theoretical calculations of gravitational collapse of dense cores without magnetic field where the angular momentum is conserved show that the radii of Keplerian disks around protostars increase continuously with evolution (e.g., Ulrich 1976; Cassen & Moosman 1981; Terebey et al. 1984; Basu 1998). On the contrary, recent magnetohydrodynamic (MHD) simulations show that the magnetic field can effectively remove the angular momentum of the collapsing material by magnetic braking, and suppress the growth of the outer radii of the Keplerian disks within 10 AU (e.g., Mellon & Li 2008, 2009; Machida et al. 2011; Li et al. 2011; Dapp et al. 2012). After the efficiency of magnetic braking decreases due to the dissipation of protostellar envelopes, the radii of the Keplerian disks could increase to $\gtrsim 100$ AU in the end of the main accretion phase. However, the mass of the formed disk is larger than the protostellar mass by a factor of two to five ($M_{\text{disk}} = 0.2 - 1.0 M_{\odot}$), and the disk is subject to further fragmentation (Machida et al. 2011). Such massive disks around Class I protostars, which are close to the end of the main accretion phase, have not been seen observationally, and thus those MHD simulations have still been unable to reproduce the observationally-identified Keplerian disks.

1.5 Motivation of this Thesis

Despite the recent progress, formation and evolution of Keplerian disks around protostars are still a matter of debate. Observationally formation of Keplerian disks in infalling protostellar envelopes is expected to be initiated from the Class 0 stage, and observational results suggest that the outer radii of Keplerian disks likely increase as protostars evolve from Class 0 to later stages. Formation and evolution of Keplerian disks around protostars are closely related to the mechanism of angular momentum transfer in infalling material from envelope (thousands of AU) to disk (~ 100 AU) scales, and infalling material is considered to supply mass and angular momenta to Keplerian disks. However, observationally it is not well understood how

angular momenta are transferred from large to small scales in infalling protostellar envelope, and direct imaging of envelope material infalling onto Keplerian disks and shocks associated with such accretion has been difficult. These problems motivate this thesis.

In the present thesis, I performed observations of representative protostellar sources to reveal their infalling and rotating gas motions on 100–1000 AU scales, and to compare the kinematics of protostellar envelopes among protostellar sources at different evolutionary stages. As the first step, I have conducted imaging and analysis of the SMA observation in the ^{12}CO (2–1), ^{13}CO (2–1), C^{18}O (2–1), and 1.3 mm continuum emission of B335, a prototypical Class 0 source, to study the kinematics of the inner envelope and outflow on 1000 AU scale. To further trace the innermost part of the protostellar envelope on a few hundred AU scale, I have conducted imaging and analysis of the SMA observation in the submillimeter CS (7–6) and 0.8 mm continuum emission of B335, which selectively traces inner warmer ($\gtrsim 40$ K) and denser ($\gtrsim 10^5 \text{ cm}^{-3}$) regions of protostellar envelopes. To discuss the physical condition of the envelope from large to small scales without suffering from the missing flux problem, I have also made the Submillimeter Telescope (SMT) observations in the C^{18}O (2–1) line and combined the SMA and SMT C^{18}O (2–1) data, as well as the SMA and single-dish CS (7–6) data taken with the Atacama Submillimeter Telescope Experiment (ASTE) by Takakuwa et al. (2007).

In the next step, I have made SMA observations in the C^{18}O (2–1) line toward a sample of Class 0 and I protostars, and measured radial profiles of rotational velocities of the protostellar envelopes with my analytical method. Among the six sample sources, two Class I sources, TMC-1A and L1489 IRS, exhibit rotational profiles of $V_{\text{rot}} \propto r^{-0.5}$ on 100–1000 AU scales, suggesting the presence of Keplerian disks with outer radii of hundreds of AU. Finally, to reveal the connection between the infalling envelope and the Keplerian disk, I have conducted observations of L1489 IRS in the 1.3 mm continuum and the ^{12}CO (2–1), C^{18}O (2–1), and SO (5₆–4₅) lines with the Atacama Large Millimeter/Submillimeter Array (ALMA).

1.6 Outline of this Thesis

In Chapter 2, I present the results of SMA observations in the 1.3 mm continuum, ^{12}CO (2–1), ^{13}CO (2–1), and C^{18}O (2–1) emission of B335. The ^{12}CO and ^{13}CO emission likely traces the outflow in B335, and in particular I discovered a high-velocity ($>160 \text{ km s}^{-1}$) molecular jet in B335. The properties of the molecular jet in B335 are analyzed and compared with those of molecular jets in other protostellar sources. The C^{18}O emission most likely traces a compact protostellar envelope with a size of $\sim 1500 \text{ AU}$ and shows a signature of the infalling motion. On the contrary, there is no signature of the rotational motion in the protostellar envelope seen in the C^{18}O emission. I discuss the absence of detectable rotational motion on hundreds of AU scale in B335 in the context of evolution of protostellar envelopes toward formation of Keplerian disks.

In Chapter 3, I present the results of the combined (SMA + single-dish) data in the C^{18}O (2–1) and CS (7–6) emission of B335. The millimeter C^{18}O emission traces both the extended and compact envelope with sizes of ~ 9000 and $\sim 1500 \text{ AU}$, respectively, while the submillimeter CS emission traces a central compact envelope with a radius of $\sim 400 \text{ AU}$, as well as an east-west elongated outflow with a size of $\sim 3000 \text{ AU}$. The CS emission shows a possible signature of the envelope rotation in the inner envelope, while no signature of the infalling motion is seen in the CS emission. The origins of the different structures and kinematics traced by the millimeter and submillimeter emission are discussed, and their physical conditions are analyzed with a large velocity gradient (LVG) model. With these observations, the radial profile of the specific angular momenta of the rotational motion in B335 is revealed. A possible evolutionary scenario of the profile of the specific angular momenta is proposed.

In Chapter 4, I present the SMA C^{18}O (2–1) observational results of two Class 0, one Class 0/I, and two Class I protostars. The C^{18}O emission in these sources traces the protostellar envelopes with contamination from the associated outflows. I measured radial profiles of the rotational velocities of the protostellar envelopes from the Position–Velocity diagrams perpendicular to the outflow directions passing through the protostellar positions. These results as well as those from literatures demonstrate an evolutionary trend of protostellar envelopes from slow to fast and from $V_{\text{rot}} \propto r^{-1}$ to $\propto r^{-0.5}$ rotational motions on 100–1000 AU scales, as protostars

evolve from the Class 0 to I stages. The observed evolutionary trend is compared with models of the inside-out collapse and discussed in the context of disk formation.

In Chapter 5, I present the ALMA observational results of L1489 IRS in the 1.3 mm continuum, ^{12}CO (2–1), C^{18}O (2–1) and SO (5_6-4_5) emission. The Keplerian disk reported with the previous SMA observations (Brinch et al. 2007a) is clearly identified with ALMA in the ^{12}CO and C^{18}O emission, and its physical parameters are estimated by the fitting of simple geometrically-thin disk models to the observational data. Furthermore, two streams of infalling flows onto the Keplerian disk that follow parabolic trajectories are discovered in the C^{18}O emission. The SO emission primarily traces the transition regions from the infalling flows to the Keplerian disk. I have made a model composed of a Keplerian disk surrounded by a torus and two infalling flows, computed LTE radiative transfer, and generated model images, which can explain and reproduce the main features in the morphologies and kinematics of the C^{18}O and SO emission.

In Chapter 6, I summarize the main results and scientific implications acquired with the present thesis project. In Chapter 7, based on my current observational results, I propose a few new projects for my future work.



Chapter 2

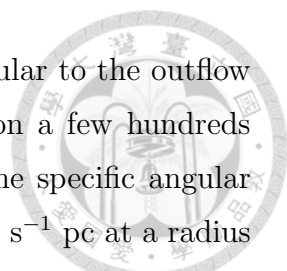
High-Velocity Jets and Slowly Rotating Envelope in B335

This chapter has been published in ApJ.

Hsi-Wei Yen, Shigehisa Takakuwa, and Nagayoshi Ohashi 2010, ApJ, 710, 1786.

2.1 Abstract

We have performed detailed imaging and analyses of the SMA observation in 230 GHz continuum, ^{12}CO (2–1), ^{13}CO (2–1), and C^{18}O (2–1) emissions toward B335, an isolated and nearby (~ 150 pc) Bok globule with an embedded Class 0 source ($L_{\text{bol}} \sim 1.5 L_{\odot}$). We report the first discovery of high-velocity ($V_{\text{propagation}} \sim 160$ km s^{-1}) ^{12}CO (2–1) jets with a size of $\sim 900 \times 1500$ AU along the east-west direction in B335. The estimated mass-loss rate ($\sim 2.3 \times 10^{-7} M_{\odot} \text{ yr}^{-1}$) and the momentum flux ($\sim 3.7 \times 10^{-5} M_{\odot} \text{ yr}^{-1} \text{ km s}^{-1}$) of the ^{12}CO jets in B335 are one order of magnitude lower than those of other ^{12}CO jets in more luminous sources such as HH 211 ($L_{\text{bol}} \sim 3.6 L_{\odot}$) and HH 212 ($L_{\text{bol}} \sim 14 L_{\odot}$). The weaker jet activity in B335 could be due to the lower active accretion onto the central protostar. The C^{18}O emission shows a compact (~ 1500 AU) condensation associated with the central protostar, and it likely traces the protostellar envelope around B335, as in the case of the 230 GHz continuum emission. The envelope exhibits a velocity gradient from the east (blueshifted) to the west (redshifted) that can be interpreted as an infalling motion. The estimated central stellar mass, the mass infalling rate, and the accretion luminosity are $0.04 M_{\odot}$, $6.9 \times 10^{-6} M_{\odot} \text{ yr}^{-1}$, and $2.1 L_{\odot}$, respectively.



On the other hand, there is no clear velocity gradient perpendicular to the outflow axis in the C^{18}O envelope, suggesting little envelope rotation on a few hundreds of AU scale. The upper limits of the rotational velocity and the specific angular momentum were estimated to be 0.04 km s^{-1} and $7.0 \times 10^{-5} \text{ km s}^{-1} \text{ pc}$ at a radius of 370 AU, respectively. The specific angular momentum and the inferred Keplerian radius ($\sim 6 \text{ AU}$) in B335 are one to two orders of magnitude smaller than those in other more-evolved sources. Possible scenarios to explain the lower specific angular momentum in B335 are discussed.

2.2 Introduction

Dense-gas condensations ($\geq 10^{4-5} \text{ cm}^{-3}$) in dark molecular clouds are the sites of low-mass star formation (Andre et al. 2000; Myers et al. 2000). Previous millimeter interferometric observations have revealed rotating and infalling gas motions in dense cores associated with known infrared sources, the so-called “protostellar envelopes” (Ohashi et al. 1996, 1997a,b; Momose et al. 1998). Bipolar molecular outflows associated with protostellar envelopes have also been observed (Bachiller & Tafalla 1999). These molecular outflows are considered to be ambient material entrained by the jet, ejected from the vicinity of the central protostar. Eventually, the infall and the outflow terminate, and a newly born star surrounded by a circumstellar disk appears (Shu et al. 1987).

Details of the physical processes in protostellar envelopes and outflows, however, are still a matter of debate. For example, it is still unclear how the angular momentum of the rotating motion in envelopes is transferred from large to small radii (e.g., Goodman et al.; Ohashi et al. 1997b), and how centrifugally supported disks with radii of a few hundred AU often observed around young stars are formed in envelopes (e.g., Guilloteau et al. 1999; Guilloteau & Dutrey 1998; Qi et al. 2003). In order to address these questions, observations of the rotating motion in a representative envelope, observed from large to small scales, and comparisons with other sources are required. On the other hand, the structure and kinematics of molecular outflows are different from source to source (Lee et al. 2000). In several sources high-velocity (HV; $> 100 \text{ km s}^{-1}$) collimated molecular jets have been found, while in other sources only slow outflow shells with wide opening angles are seen (Bachiller

& Tafalla 1999; Arce et al. 2007). The mechanisms which produce this variety of outflows, and the relation of the mass ejection to the central mass accretion, are still controversial.

B335 is an isolated Bok globule associated with an embedded far-infrared source (IRAS 19347+0727; Keene et al. 1980, 1983), and the distance to B335 was estimated to be ~ 150 pc (Stutz et al. 2008). The central source is a Class 0 source with a bolometric luminosity of $1.5 L_{\odot}$ (Stutz et al. 2008) and a dust temperature of 31 K (Chandler & Sargent 1993). ^{12}CO (1–0) and ^{13}CO (1–0) line observations of B335 have unveiled the presence of a molecular outflow, both on ~ 0.2 pc (Hirano et al. 1988; Cabrit et al. 1988; Moriarty-Schieven & Snell 1989) and ~ 3000 AU scales (Hirano et al. 1992; Chandler & Sargent 1993). The outflow extends along the east-west direction, and shows a conical shape with an opening angle of $\sim 45^\circ$ and an inclination angle of $\sim 10^\circ$ from the plane of the sky. Along the outflow axis there are several HH objects (HH 119 A–F), whose proper motions moving away from the central source have been detected (Reipurth et al. 1992; G  lfalk & Olofsson 2007). The dynamic timescale of the furthest HH object (HH 119 A) is ~ 850 years (Reipurth et al. 1992), and the propagation velocity reaches $140\text{--}170 \text{ km s}^{-1}$ (G  lfalk & Olofsson 2007).

Single-dish observations of B335 have found asymmetric profiles in optically thick CS and H_2CO lines, implying the presence of infalling motions in the envelope around B335 (Zhou et al. 1993; Choi et al. 1995). Direct interferometric imaging of the envelope around B335 in H^{13}CO^+ (1–0) and C^{18}O (1–0) at an angular resolution of $\sim 6''$ supports the presence of infalling motions on a 3000 AU scales (Saito et al. 1999; Chandler & Sargent 1993), although the interferometric imaging of the CS (5–4) emission shows that the asymmetric line profiles are influenced severely by contamination from the outflow (Wilner et al. 2000). Recently, Choi (2007) has suggested that the asymmetric line profile in the H_2CO line arises from both the outflow and the infalling envelope. The envelope around B335 also exhibits a slow rotation at radii of ~ 20000 AU (Frerking et al. 1987; Saito et al. 1999) and ~ 1000 AU (Saito et al. 1999). The density distribution in the envelope around B335 shows an $r^{-1.5}$ dependence between radii of 60 and 3900 AU, while outside this region the radial dependence is r^{-2} (Harvey et al. 2001, 2003a,b), which is consistent with the inside-out collapse model (Shu 1977). B335 has also been observed in submillimeter

molecular lines (Jørgensen et al. 2007; Takakuwa et al. 2007a).

These results indicate that B335 is a prototypical low-mass protostellar source suitable for detailed studies. The observations on 1000–4000 AU scales described above have revealed the core, infalling and rotating envelope, and outflow. In this chapter, we report detailed imaging and analyses of the Submillimeter Array (SMA) observations of the region within 1500 AU in B335 at an angular resolution of $\sim 4''$, to study the inner part of the outflow and the envelope. Through the comparison with previous observations of the envelope around B335 and those of other sources, we will discuss how the angular momentum of the rotating motion in envelopes is transferred. We will also compare the observed properties of the outflow in B335 to those of other sources associated with HV molecular jets, and discuss the relation of the outflow to the central mass-accretion processes.

2.3 Observation

The present observation of B335 was made as a part of a large SMA project (PROSAC: Jørgensen et al. 2007) on 2005 June 24 with the seven SMA antennas. Details of the SMA are described by Ho et al. (2004). The SMA was a double-sideband instrument with a 2 GHz bandwidth each. We observed 230 GHz continuum, ^{12}CO (2–1; 230.5379700 GHz), ^{13}CO (2–1; 220.3986765 GHz), and C^{18}O (2–1; 219.5603568 GHz) emissions in B335 simultaneously. The pointing center was $\alpha(\text{J2000}) = 19^{\text{h}}37^{\text{m}}00^{\text{s}}.89$, $\delta(\text{J2000}) = 7^{\circ}34'10''.0$, and the Field of View was $\sim 55''$ (8300 AU). The lengths of the projected baselines on the sky ranged from 5.5 to 53.5 $k\lambda$, and our observation was insensitive to structures more extended than ~ 4500 AU at the 10% level (Wilner & Welch 1994). The correlator configuration was set to assign 128 channels per one chunk with a 83.3 MHz bandwidth to the ^{12}CO line, and 512 channels per chunk to the ^{13}CO and C^{18}O lines, which results in velocity resolutions of 1.06, 0.26, and 0.28 km s^{-1} , respectively.

The passband calibrator was quasar 3C279, and the flux calibrator was Callisto. Quasar 1749+096 (1.9 Jy) and quasar 2145+067 (2.5 Jy) were observed as gain calibrators. The MIR software package was used to calibrate the data. The calibrated visibility data were Fourier-transformed and CLEANed with MIRIAD to produce images (Sault et al. 1995). The observational parameters are summarized in Ta-

Table 2.1. Summary of the Observational Parameters

Line	Transition	Beam Size (P. A.)	Velocity Resolution (km s ⁻¹)	Noise Level (mJy beam ⁻¹)	Weighting
¹² CO	2–1	3''.8 × 3''.3 (81°7)	1.06	140	Natural
¹³ CO	2–1	4''.0 × 3''.4 (81°8)	0.26	220	Natural
C ¹⁸ O	2–1	3''.7 × 3''.2 (86°5)	0.28	280	Robust = 0.5
Continuum					
1.3 mm	...	3''.9 × 3''.3 (81°7)	...	2	Natural

ble 2.1. In order to improve the signal to noise ratio of the ¹²CO (2–1) data, we smoothed the data cube over two channels, and the noise level reduces to 100 mJy beam⁻¹.

2.4 Results

The images of B335 in the 1.3 mm continuum, ¹²CO (2–1), ¹³CO (2–1), and C¹⁸O (2–1) emissions were first shown in the PROSAC paper (Jørgensen et al. 2007). In this chapter, we present detailed results including velocity structures. Hereafter, the systemic velocity obtained from the single-dish results (Hirano et al. 1991; Evans et al. 2005), 8.3 km s⁻¹, is adopted, and all the velocities are shown as the relative velocity (ΔV) to this systemic velocity.

2.4.1 1.3 mm Continuum Emission

Figure 2.1 shows the 1.3 mm continuum image (contour) overlaid on the ¹²CO (2–1) moment 0 map (gray scale) in B335. The continuum emission shows an elongated structure along the north-south direction, plus two protrusions toward the north-west and south-west directions. The north-south elongation appears to be consistent with the previous single-dish result in the 1.3 mm continuum emission that shows an elongated feature with a size of $\sim 18,000 \times 13,000$ AU along the north-south direction (Motte & André 2001). As will be discussed in the next subsection, the ¹²CO emission most likely traces the molecular outflow along the east-west direction. Hence, the continuum emission is elongated almost perpendicularly to the E-W out-

flow, suggesting that the main component in the 1.3 mm continuum emission traces the circumstellar envelope around B335. On the other hand, the two protrusions abut upon the ^{12}CO emission and delineate the rim of the outflow, which suggests that these components trace the wall of the cavity evacuated by the outflow.

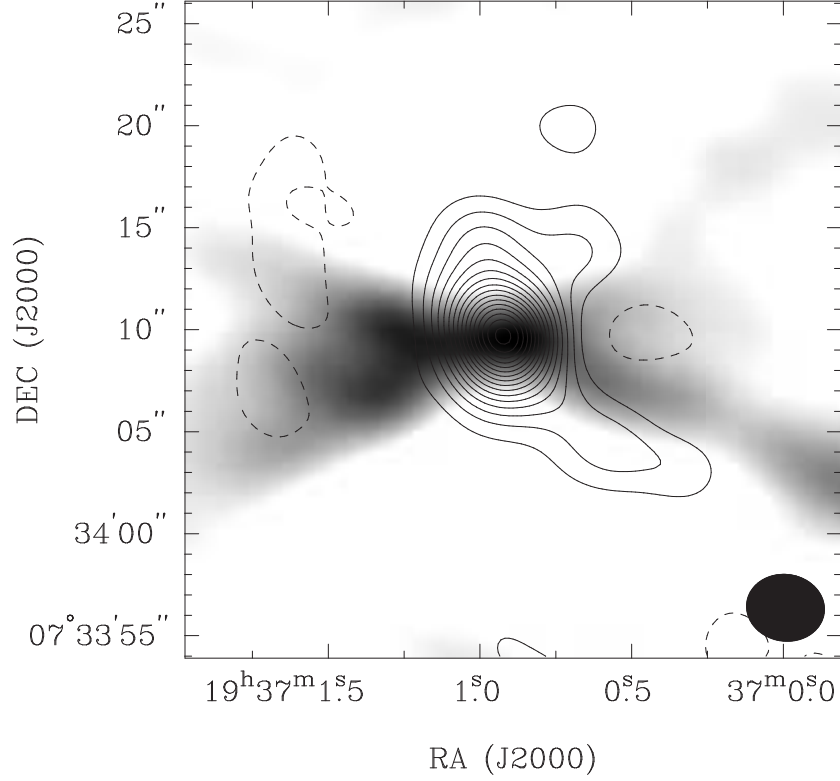


Figure 2.1 1.3 mm continuum map of B335 (contours) overlaid on the ^{12}CO (2–1) outflow map in linear gray scale whose range is from 6 mJy to 98 mJy. Contour levels are from 3 to 48σ in steps of 3σ , where 1σ is 2 mJy. A filled ellipse at the bottom right corner shows the synthesized beam.

By fitting a two-dimensional Gaussian to the continuum image above the 6σ level, which excludes the north-west and south-west protrusions, we obtained the peak position of $\alpha(\text{J2000}) = 19^{\text{h}}37^{\text{m}}0^{\text{s}}.93$, $\delta(\text{J2000}) = 7^{\circ}34'09''.8$, and hereafter we adopted this position as a position of the central protostellar source. The deconvolved size, position angle, and the total flux were estimated to be $4''.9 \times 2''.3$ (740×350 AU), 13° , and 0.18 Jy, respectively. The 1.3 mm continuum flux recovered with the SMA corresponds to $\sim 25\%$ of the integrated flux within a radius of $17''$ measured with the IRAM 30-m telescope (Motte & André 2001). We can estimate the mass of the main dusty component ($\equiv M$) as

$$M = \frac{F_{\nu} D^2}{\kappa_{230\text{GHz}} B(T_{\text{dust}})}, \quad (2.1)$$

where F_ν is the total flux, D is the distance to the source, T_{dust} is the dust temperature, and B is the Planck function. On the assumption that the frequency (ν) dependence of the dust mass opacity ($\equiv \kappa_\nu$) is $\kappa_\nu = 0.1 \times (\frac{\nu}{10^{12}})^\beta$ (Beckwith et al. 1990) with $\beta = 1.2$ (Chandler & Sargent 1993), the mass opacity at 230 GHz ($\equiv \kappa_{230\text{GHz}}$) was estimated to be 0.017 g cm^{-2} . The mass of the central compact component was estimated to be $0.027 M_\odot$ at a dust temperature of 31 K (Chandler & Sargent 1993). Given the uncertainty of the missing flux, the estimated mass is consistent with the mass estimated from the 2.7 mm continuum emission by Owens Valley array observations ($0.08 M_\odot$; Chandler & Sargent 1993).

2.4.2 ^{12}CO (2–1) Emission

Figure 2.2 shows the distribution of the ^{12}CO (2–1) emission in B335 integrated over the following three different velocity ranges: HV ($\Delta V = -37.5$ to -18.5 & 17.5 to 36.5 km s^{-1}), middle velocity (MV; $\Delta V = -16.0$ to -8.7 & 6.9 to 15.3 km s^{-1}), and low velocity (LV; $\Delta V = -5.8$ to -1.6 & 0.6 to 4.8 km s^{-1}). We detected the ^{12}CO (2–1) emission at a much wider velocity range ($\Delta V = -37.5$ to 36.5 km s^{-1}) than the single-dish result ($\Delta V = -5.3$ to 5.7 km s^{-1} ; Hirano et al 1991). In the LV range, the blueshifted and redshifted emissions show a V-shaped geometry opening toward the east and west, respectively, with its apex at the protostellar position. Similar but less significant blueshifted and redshifted V-shaped features are also seen on the other side, and hence the blueshifted and redshifted components are overlapped on each side. The maximum length, width, and opening angle of the V-shaped structures are $\sim 28''$ (4200 AU), $\sim 24''$ (3600 AU), and $\sim 60^\circ$, respectively. From LV to HV, the morphology of the ^{12}CO emission becomes more compact with less overlap between the blueshifted and redshifted components. In the HV range, neither the blueshifted nor the redshifted emission shows the V-shaped morphology, but both show compact condensations with a size of $\sim 1500 \times 900 \text{ AU}$ located near the protostar. The non-detection of the HV ^{12}CO emission in the single-dish observation is probably due to the beam dilution effect since the HV ^{12}CO emission is compact. The peak positions of these HV components are located within $\sim 2''$ ($\sim 300 \text{ AU}$) of the protostar. On the assumption of an outflow inclination angle of 10° from the plane of the sky (Hirano et al. 1988), the mean propagation velocity of the HV ^{12}CO emission reaches $\sim 160 \text{ km s}^{-1}$, which is comparable to the velocity

of the associated HH objects ($140\text{--}170\text{ km s}^{-1}$) (Glfalk & Olofsson 2007), and the dynamic timescale is estimated to be ~ 45 years ($\equiv 1500\text{ AU} / 160\text{ km s}^{-1}$).

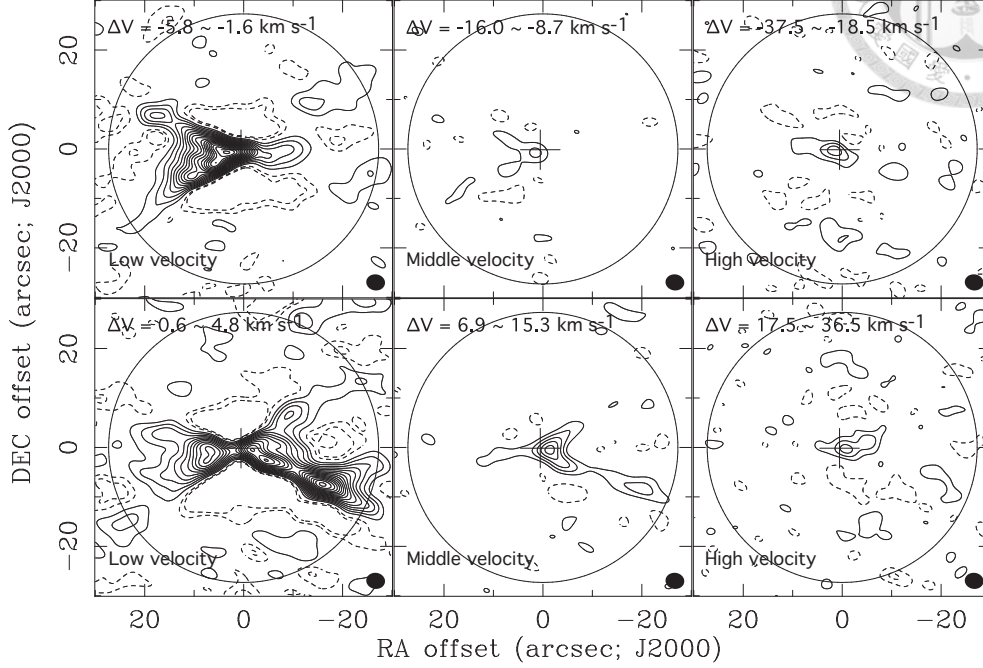


Figure 2.2 Moment 0 maps of the ^{12}CO (2–1) emission in B335 at different velocity ranges. For the HV range, contour levels are from 2 to 6σ in steps of 2σ , where 1σ is 1.3 K km s^{-1} . For the MV range, the contour levels are from 3 to 15σ in steps of 3σ , where 1σ is 1.2 K km s^{-1} . For the LV range, the contour levels are from 3 to 71σ in steps of 4σ , where 1σ is 1.7 K km s^{-1} . Crosses represent the position of the central source, and open circles represent the field of view. A filled ellipse at the bottom right corner in each panel shows the synthesized beam.

Figure 2.3 presents Position–Velocity (P – V) diagrams of the ^{12}CO emission along the east–west direction (P. A. = 90°) in B335. The P – V diagram at a higher velocity resolution (2.1 km s^{-1} ; Figure 2.3 left) exhibits a spatially extended ($\sim 4200 \times 3600\text{ AU}$), narrow-velocity ($\sim 10\text{ km s}^{-1}$) feature of the LV component. The velocity structure of the LV component can be traced with a Hubble-like velocity law ($v = C \times r$) in a geometrically thin conical outflow shell with an opening angle of 60° and an inclination angle of 10° , where the coefficient C was found to be $1.2 \times 10^{-3}\text{ km s}^{-1}\text{ AU}^{-1}$ (orange dotted cross in Figure 2.3). These results suggest that the LV ^{12}CO emission delineates the rim of the east–west outflow with a conical shape, and that the outflow axis is slightly tilted with its eastern part on the near side to us. Previous single-dish observations of B335 in ^{12}CO (2–1 and 1–0) have found that there is an $\sim 0.2\text{ pc}$ conical-shaped outflow along the east–west direction with

an opening angle of $\sim 45^\circ$, and that the eastern outflow axis is tilted toward us by $\sim 10^\circ$ from the plane of the sky (e.g., Hirano et al. 1988, 1991). The Spitzer IRAC image in B335 shows a reflection nebula with its eastern lobe on the near side (Stutz et al. 2008). The single-dish and Spitzer results are consistent with our results, and the LV ^{12}CO (2–1) emission observed with the SMA most likely traces the base of the extended outflow in B335.

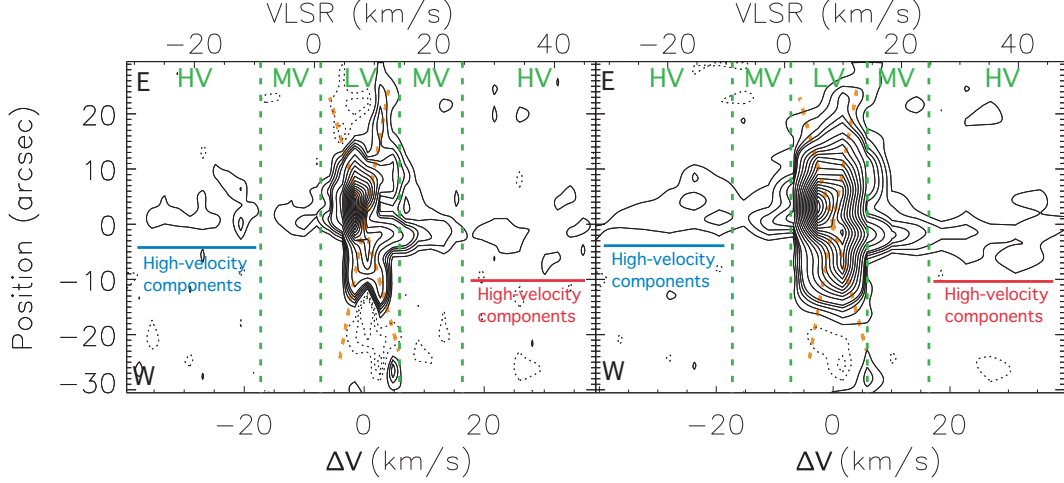


Figure 2.3 P – V diagrams of the ^{12}CO (2–1) emission along the outflow axis in B335, smoothed over the two (left panel) and four velocity (right panel) channels. Green dotted lines divide the ^{12}CO emission into three different velocity components, and the blue and red lines show the velocity range of the HV components. Orange dotted crosses represent our simple model of the ^{12}CO outflow shell. Contour levels are from 2σ in steps of 2σ until 10σ , and then in steps of 6σ , where 1σ is 0.2 K in the left panel and 0.1 K in the right panel.

On the other hand, the P – V diagram at a smoothed velocity resolution (4.2 km s^{-1} ; Figure 2.3 right) with a better sensitivity shows that the kinematics of the HV ^{12}CO is distinct from that of the LV component; the HV component exhibits a much wider velocity width ($\sim 20 \text{ km s}^{-1}$) than the LV component though the spatial extent of the HV component ($\sim 1500 \times 900 \text{ AU}$) is much smaller than that of the LV component. Hence, the HV ^{12}CO emission likely traces distinct outflow components from the LV outflow shell. On the assumption of local thermodynamic equilibrium (LTE) conditions and optically thin ^{12}CO emission with an abundance of 10^{-4} (Frerking et al. 1987; Lucas & Liszt 1998), and an excitation temperature of 50 K (Lee et al. 2007b), the column density at the peaks was estimated to be $6.7 \times 10^{19} \text{ cm}^{-2}$, and the gas masses of the redshifted and blueshifted HV components were estimated to be 2.3×10^{-5} and $2.0 \times 10^{-5} M_\odot$, respectively. While the SMA

^{12}CO observation misses 90% of the total flux observed with James Clerk Maxwell Telescope (JCMT) around the systemic velocity (Hirano et al. 1991), the missing flux decreases to $\leq 30\%$ at a relative velocity of more than 3 km s^{-1} . The flux from the HV component ($\Delta V \gtrsim 18 \text{ km s}^{-1}$), which is compact and not detected by JCMT, is mostly recovered with the present SMA observation. We will discuss the origin of the HV components in section 2.5.1 in more detail.

2.4.3 ^{13}CO (2–1) Emission

Figure 2.4 presents moment 0 maps of the blueshifted ($\Delta V = -2.1$ to 0.0 km s^{-1}) and redshifted ($\Delta V = 0.2$ to 1.9 km s^{-1}) ^{13}CO (2 – 1) emissions in B335. The total velocity range of the ^{13}CO emission ($\Delta V = -2.1$ to 1.9 km s^{-1}) is within the velocity range of the LV ^{12}CO component. We note that the absence of the ^{13}CO counterpart to the HV ^{12}CO component is likely due to the insufficient sensitivity of the observation. Both the blueshifted and redshifted ^{13}CO emissions consist of central compact components with a size of $\sim 1000 \text{ AU}$, and outer extensions, while the blueshifted emission is more intense than the redshifted emission. There are two redshifted “arms” extending toward the south-east and south-west directions and a blueshifted arm toward the south-east direction. These outer extensions, as well as the slight extensions to the north-east and north-west of the protostar at both blueshifted and redshifted velocities, form structures similar to the V-shaped geometry seen in the LV ^{12}CO emission. The interferometric image of B335 in ^{13}CO (1–0) emission shows a similar morphology to that in the ^{13}CO (2–1) emission (Chandler & Sargent 1993), but the V-shaped geometry is less clear in the lower excitation line. The ^{13}CO (2–1) P – V diagram along the outflow axis shows a velocity structure that can be explained as a Hubble-like velocity law in a geometrically thin conical outflow shell on a size scale of $\sim 1500 \text{ AU}$, shown as the solid lines in Figure 2.5. A similar velocity structure was also seen in the ^{12}CO P – V diagram along the outflow axis, but on a size scale of $\sim 2500 \text{ AU}$. The more intense blueshifted emission compared to the redshifted emission could be due to less absorption on the front side of the outflow shell than on the back. In the outflow-envelope configuration, the redshifted outflow lobe is located behind with respect to the blueshifted lobe, and hence will suffer more from absorption by foreground material.

Assuming a ^{13}CO abundance of 1.7×10^{-6} (Frerking et al. 1987), an excitation

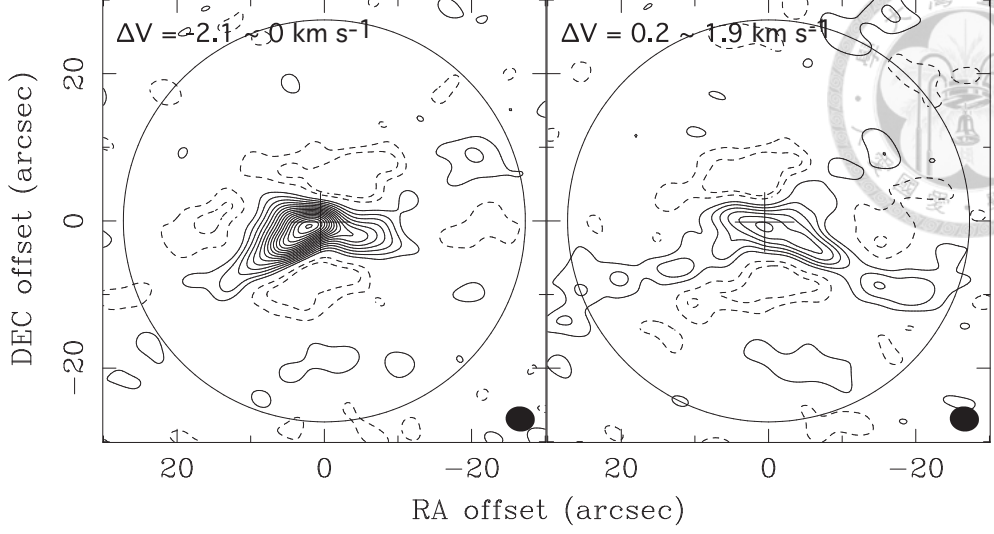


Figure 2.4 Moment 0 maps of the ^{13}CO (2–1) emission in B335 integrated from $V = -2.1$ to 0.0 km s^{-1} (left) and from $V = 0.2$ to 1.9 km s^{-1} (right). Contour levels are from 2σ in steps of 2σ , where 1σ is 0.3 K km s^{-1} . Crosses denote the position of the central source, and open circles represent the field of view. Filled ellipses at the bottom right corner show the synthesized beam.

temperature of 20 K, and LTE and optically thin conditions, the gas masses traced by the blueshifted and the redshifted ^{13}CO emissions were estimated to be $1.9 \times 10^{-3} M_{\odot}$ and $3.2 \times 10^{-3} M_{\odot}$, respectively. The momenta of the blueshifted and redshifted ^{13}CO components were estimated to be 2.3×10^{-3} and $2.1 \times 10^{-3} M_{\odot} \text{ km s}^{-1}$, respectively, using the velocity channel maps ($P_{^{13}\text{CO}} = \sum M_{\text{channel}} \times V_{\text{channel}}$). Here, we assumed that the ^{13}CO emission traces the same geometrically thin conical shell as the LV ^{12}CO component, and we corrected for the inclination to estimate the propagation velocity. The estimated masses and momenta should be considered as lower limits since only $\sim 40\%$ of the total ^{13}CO (2–1) flux obtained with JCMT is recovered with the present SMA observation (Hirano et al. 1991).

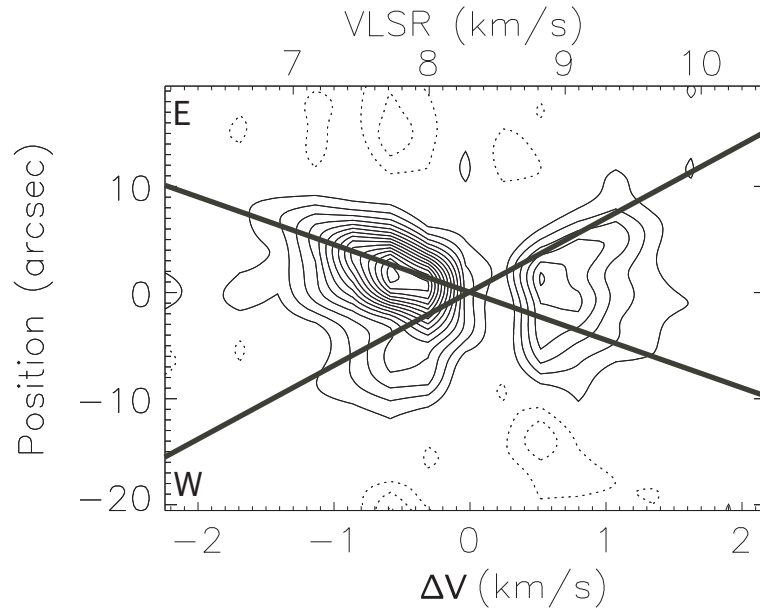


Figure 2.5 P - V diagrams of the ^{13}CO (2-1) emission (left) and the ^{12}CO (2-1) emission (right) along the outflow axis plotted at the same spatial and velocity range. Bold solid lines show our simple model of the outflow shells. In the right panel, contour levels are from 2σ in steps of 2σ , where 1σ is 0.4 K, and in the left panel, contour levels are from 2σ in steps of 2σ until 10σ , and then in steps of 6σ , where 1σ is 0.2 K.

2.4.4 C¹⁸O (2–1) Emission

Figure 2.6 presents the moment 0 map of the C¹⁸O (2–1) emission integrated from $\Delta V = -0.9$ to 0.8 km s^{-1} in B335. In contrast to the ¹²CO and ¹³CO emissions, the C¹⁸O emission shows a $\sim 1500 \text{ AU}$ condensation with a single peak slightly offset from the protostellar position by $\sim 1''$. The condensation shows an almost spherical structure with north-east, south-east, and weak south-west extensions, which is consistent with the C¹⁸O (1–0) map obtained using the Owens Valley millimeter array (Chandler & Sargent 1993). Single-dish observations of B335 in the C¹⁸O (1–0) line show a $\sim 36,000 \times 32,000 \text{ AU}$ envelope with a mass of $2.4 M_{\odot}$ around the protostar with an almost spherical structure (Saito et al. 1999).

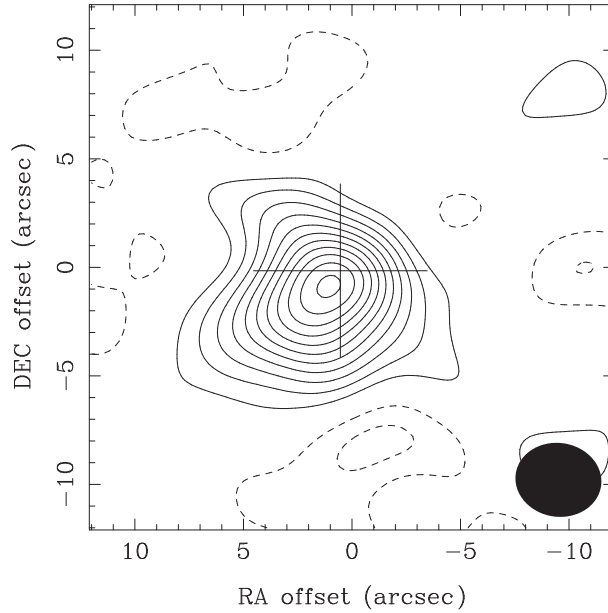


Figure 2.6 Moment 0 map of the C¹⁸O (2–1) emission in B335. The integrated velocity range is $\Delta V = -0.9$ to 0.8 km s^{-1} . Contour levels are from 2 to 20σ in steps of 2σ , where 1σ is 0.5 K km s^{-1} . A cross shows the position of the central source, and a filled ellipse at the bottom right corner shows the synthesized beam.

Figure 2.7 shows the velocity channel maps of the C¹⁸O (2–1) emission overlaid with the 1.3 mm continuum emission (see Figure 2.1). At $\Delta V = -0.9 \text{ km s}^{-1}$, weak C¹⁸O emission elongated along the north-south direction was detected to the east of the protostellar position. At $\Delta V = -0.6 \text{ km s}^{-1}$, C¹⁸O emission is elongated along the outflow axis (P. A. = 90°), and at $\Delta V = -0.3 \text{ km s}^{-1}$ C¹⁸O emission is elongated toward the south-east. Around the systemic velocity ($\Delta V = 0.0$ to 0.2 km s^{-1}),

C^{18}O emission is elongated perpendicularly to the outflow axis, and its distribution is similar to that of the 1.3 mm dust emission. At a redshifted velocity of $\Delta V = 0.5 \text{ km s}^{-1}$, C^{18}O emission shows a compact blob as well as a weak south-west extension with its peak position slightly shifted to the west of the protostar. In the channel maps, the peaks of the C^{18}O emission shift from east to west of the protostar as the velocity changes from blueshifted to redshifted.

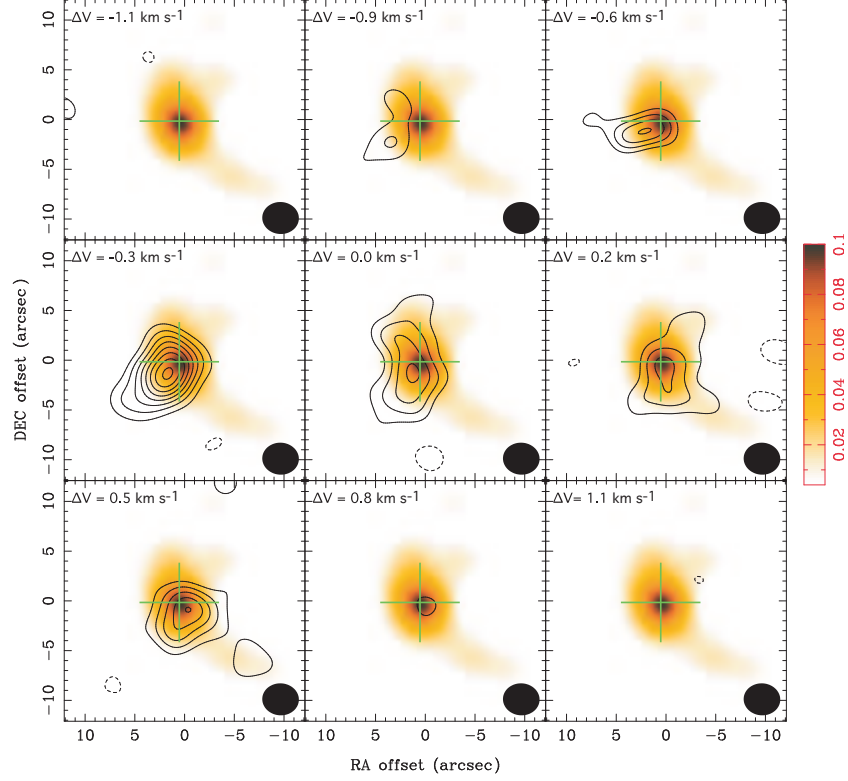


Figure 2.7 Velocity channel maps of the C^{18}O (2–1) emission in B335 overlaid on the 1.3 mm continuum emission in gray scale. Contour levels are from 3σ in steps of 2σ , where 1σ is 0.6 K. Green crosses show the position of the central source, and a filled ellipse at the bottom right corner in each panel shows the synthesized beam.

Figure 2.8 shows P – V diagrams of the C^{18}O emission along (left panel) and across (right panel) the outflow axis passing through the central protostar. Along the outflow axis there appears a velocity gradient: there are blueshifted and redshifted C^{18}O peaks in the east and west of the protostar, respectively. This velocity gradient could be due to the outflow. The P – V diagram, however, does not show the X-shaped velocity structure seen in the ^{12}CO and ^{13}CO emissions. In fact, the model explaining the ^{12}CO emission cannot be applied to the C^{18}O emission (bold solid lines in Figure 2.8 left). On the other hand, there is no clear velocity gradient seen

in the C^{18}O P - V diagram perpendicular to the outflow axis. We will discuss the origin and kinematics of the C^{18}O emission in section 2.5.2.

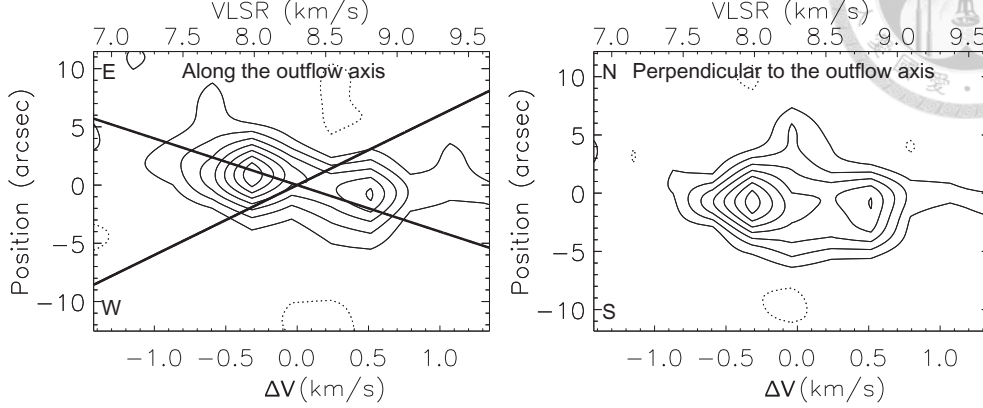


Figure 2.8 P - V diagrams of the C^{18}O (2-1) emission in B335 along the outflow axis (P. A. = 90° , left) and perpendicular to the outflow axis (P. A. = 0° , right), passing through the central protostellar position. In the left panel, bold solid lines represent our simple model of the ^{12}CO outflow shells as shown in Figure 2.3. Contour levels are from 2σ in steps of 2σ , where 1σ is 0.6 K.

The brightness ratio between the C^{18}O (2-1) and C^{17}O (2-1) emissions observed with the Caltech Submillimeter Observatory indicates that the C^{18}O (2-1) emission is optically thin ($\tau_{\text{C}^{18}\text{O} (2-1)} \sim 0.8$; Evans et al. 2005). Assuming LTE conditions, a C^{18}O abundance of 3×10^{-7} (Frerking et al. 1987), and an excitation temperature of 30 K (Chandler & Sargent 1993), we estimated the total gas mass of the C^{18}O condensation to be $5.2 \times 10^{-3} M_\odot$ from the total C^{18}O integrated intensity ($\sim 9400 \text{ K km s}^{-1}$ over $\sim 140 \text{ arcsec}^2$). The derived gas mass is 6 times smaller than the mass estimated from the 1.3 mm dust continuum emission ($\sim 0.03 M_\odot$), although the extent of the C^{18}O emission is approximately 2 times larger than that of the 1.3 mm dust continuum emission. This suggests that the C^{18}O abundance may be approximately one order of magnitude smaller than the value we assumed above, if the molecular gas and dust are well mixed and both the C^{18}O and 1.3 mm emission trace the same structure. The lower C^{18}O abundance in the central region of the envelope could be due to the depletion of CO molecules onto dust grains. In fact, a similar degree of CO depletion has been suggested by modeling the single-dish line profiles of B335 (Evans et al. 2005). Although the missing flux of the SMA C^{18}O data is estimated to be 80% comparing to the single-dish flux of the C^{18}O (2-1) emission (Evans et al. 2005), the above discussion on the lower C^{18}O abundance is still valid because the C^{18}O and 1.3 mm dust continuum emissions miss a similar

amount of flux.



2.5 Discussion

2.5.1 High-velocity ^{12}CO Component


Along with the V -shaped conical outflow shell, we have discovered compact ($\sim 1500 \times 900$ AU) HV ($V_{\text{propagation}} \sim 160 \text{ km s}^{-1}$) ^{12}CO (2–1) components in B335 with our SMA observation. Such an outflow configuration with collimated HV ^{12}CO components plus low-velocity ^{12}CO outflow shells is also seen in other low-mass protostellar sources associated with molecular jets such as HH 211 (Lee et al. 2006), HH 212 (Gueth & Guilloteau 1999), and L1448-mm (Bachiller et al. 1995), and has been explained by the jet-driven bow-shock model (Bachiller et al. 1995; Lee et al. 2006) and the wind-driven model (Shang 2007). In Table 2.2, we compare the kinematical properties of the compact HV ^{12}CO (2–1) components in B335 to those of the three ^{12}CO jets mentioned above. The line width and the propagation velocity of the compact HV ^{12}CO components in B335 are comparable to those in the other sources. In addition, in B335 there are several HH objects (HH 119 A–F) aligned along the outflow axis (G  lfalk & Olofsson 2007), which should trace bow shocks at the leading heads of the episodic mass ejection, and the propagation velocity of the HV ^{12}CO components is consistent with that of these HH objects ($\sim 160 \text{ km s}^{-1}$). These facts suggest that the HV ^{12}CO components found in B335 are most likely molecular jets and counterparts of the HV ^{12}CO jets seen in HH 211, HH 212, and L1448-mm.

We estimated the activity of the HV ^{12}CO jets in B335 with the method adopted by Lee et al. (2007a,b) for the HH 211 and HH 212 jets. On the assumption that the transverse width of the ^{12}CO jets in B335 is 300 AU as in the case of HH 211 (Lee et al. 2007b), the volume gas density in the ^{12}CO jets ($\equiv n_{\text{jet}}$) was estimated to be $\sim 1.5 \times 10^4 \text{ cm}^{-3}$ (from the column density of $\sim 6.7 \times 10^{19} \text{ cm}^{-2}$; see section 2.4.2). By assuming that the jet morphology is cylindrical, the mass-loss rate (\dot{M}_{loss}) can be derived as

$$\dot{M}_{\text{loss}} = r^2 \pi V_{\text{jet}} n_{\text{jet}} \mu, \quad (2.2)$$

where r , V_{jet} , and n_{jet} represent the radius, propagation velocity, and volume gas

Table 2.2. Comparison of Collimated High-velocity ^{12}CO Emissions Among Different Sources



Source	Transition	Inclination Angle($^{\circ}$)	Line Width (km s^{-1})	Velocity ^a (km s^{-1})	Reference
B335	2–1	10	20	160	1, this paper
HH 212	2–1	4	14	120	2, 3
	3–2		14	190	4
HH 211	3–2	5	15	200	5, 6
L1448-mm	1–0	21	20	200	7, 8

References. — (1) Hirano et al. (1988); (2) Claussen et al. (1998); (3) Lee et al. (2006); (4) Lee et al. (2007a); (5) Lee et al. (2007b); (6) Lee et al. (2009); (7) Bachiller et al. (1995); (8) Girart & Acord (2001)

^aThe velocities represent the propagation velocity estimated as $V_{\text{mean}}/\sin(\text{inclination angle})$.

density in jets, respectively, and μ is the mean molecular weight. Then the mass-loss rate was estimated¹ to be $2.3 \times 10^{-7} M_{\odot} \text{ yr}^{-1}$, and the momentum flux ($\equiv F = \dot{M}_{\text{loss}} \times v_{\text{jet}}$) was estimated to be $3.7 \times 10^{-5} M_{\odot} \text{ yr}^{-1} \text{ km s}^{-1}$. In Table 2.3, we compare the estimated jet activity in B335 with those in HH 211 and HH 212. The density, the mass-loss rate, and the momentum flux in B335 are one order of magnitude lower than those in HH 212 and HH 211. In B335, thermal SiO emission, which is considered to be an excellent tracer of bow shocks in protostellar jets (Bachiller 1996), was not detected (Jørgensen et al. 2007), while intense SiO emission was found in HH 211 (e.g., Lee et al. 2007b), HH 212 (e.g., Lee et al. 2007a), and L1448-mm (e.g., Girart & Acord 2001). Moreover, through high- J ^{12}CO line observations in far-infrared, the temperature of the outflow in B335 was estimated to be ~ 350 K with an LVG model, and it is lower than that in the other protostellar jets, such as L1448-mm (~ 1200 K) and HH 211 (350–950 K) (Giannini et al. 2001). In the case of HH 211, HH 212 and L1448-mm, the ^{12}CO jets conform to a chain of knots between the two successive extended bow shocks, while in B335 only one HV ^{12}CO knot located close to the central protostar (~ 1500 AU) is found. These results suggest that the jet phenomena in B335 are less active than those in the other sources.

¹If we estimate \dot{M}_{loss} by $M_{\text{jet}}/T_{\text{dynamic}}$, the value becomes 3 times larger.



Table 2.3. Comparison of ^{12}CO Jet Activities Among Different Sources.

Source	Transition	Beam Size	Distance (pc)	$n_{\text{jet}}^{\text{a}}$ (10^5 cm^{-3})	$\dot{M}_{\text{loss}}^{\text{b}}$ ($10^{-6} M_{\odot} \text{ yr}^{-1}$)	F^{c} ($10^{-4} M_{\odot} \text{ yr}^{-1} \text{ km s}^{-1}$)	ref.
B335	2–1	$3''.8 \times 3''.3$	150	0.2	0.2	0.4	this paper
HH 212	2–1	$2''.8 \times 2''.3$	400	0.7–1.1	0.8–1.3	1.0–1.6	1
	3–2	$1''.2 \times 0''.8$		2.0–2.3	3.7–4.3	7.0–8.2	2
HH 211	3–2	$1''.3 \times 0''.8$	280	1.6–1.8	3.1–3.5	6.2–7.0	3

References. — (1) Lee et al. (2006); (2) Lee et al. (2007a); (3) Lee et al. (2007b)


Note. — n_{jet} , \dot{M}_{loss} , and F are the inferred volume gas density, mass-loss rate, and the momentum flux of the ^{12}CO jets, respectively. The distance to B335 is ~ 2 -3 times smaller than that to HH 211 and HH 212, while the beam size of our observation is ~ 2 -3 times larger than that of the other observations. Therefore, our comparison of the jet activities is not affected much by the difference of the linear beam size.

^aAll the volume densities were estimated from the peak intensity of the most inner knot on the assumption of the same ^{12}CO abundance and the jet diameter of 300 AU.

^bThe mass-loss rate is derived by $r^2 \pi V_{\text{jet}} n_{\text{jet}} \mu$. See section 2.5.1 for details.

^cThe momentum flux is derived by $\dot{M}_{\text{loss}} \times V_{\text{jet}}$.

Table 2.4. Comparison of the Protostellar Properties Between B335 and the Other Sources Associated with SiO Jets



Source	SiO	M_* (M_\odot)	L_{bol} (L_\odot)	T_{bol} (K)	$\frac{L_{\text{bol}}}{M_*}$	Reference
B335	No	0.04	1.5	37	37.5	1,2,3, this paper
HH 212	Yes	0.15	14	70	93.3	1,4,5
HH 211	Yes	0.05	3.6	31	72.0	6,7,8
L1448-mm	Yes	...	8	55	...	9,10,11

Note. — M_* , L_{bol} , and T_{bol} denote the inferred stellar mass, bolometric luminosity, and the bolometric temperature, respectively.

References. — (1) Andre et al. (2000); (2) Jørgensen et al. (2007); (3) Stutz et al. (2008); (4) Lee et al. (2006) (5) Lee et al. (2007a); (6) Lee et al. (2007b); (7) Lee et al. (2009); (8) Froebrich et al. (2003); (9) Bachiller et al. (1995); (10) Dutrey et al. (1997); (11) Motte & André (2001)

In Table 2.4, we compare the protostellar properties of B335 with those of the other driving sources of the jets. It is clear that the bolometric luminosity of B335 is lower than that of HH 212, 211, and L1448-mm, although their bolometric temperatures are similar. The ratio between the bolometric luminosity and the central stellar mass, which should be proportional to the mass accretion rate in the central accretion disk, is more than 2–3 times lower in B335 than in the other sources. Hence, the lower mass-loss rate and the weaker jet activity in B335 compared to the other sources are likely to be linked with the lower mass accretion rate in B335. We suggest that the jet activity is closely related to the properties of the central accretion process.

2.5.2 The Origin and Kinematics of the C¹⁸O Emission

As shown in Figure 2.7, the C¹⁸O emission at $\Delta V = -0.6$ and -0.3 km s⁻¹ shows elongation toward the east and south-east directions, respectively, which is similar to that of the outflow observed in the ¹²CO (2–1) and ¹³CO (2–1) emissions. On the other hand, at around the systemic velocity ($\Delta V = 0.0$ and 0.2 km s⁻¹), the C¹⁸O emission is elongated perpendicularly to the outflow axis. In addition, there is a velocity gradient in the C¹⁸O emission along the outflow axis at around the systemic velocity, while no clear velocity gradient is seen across the outflow axis. In order to study the origin and kinematics of the C¹⁸O emission, in Figure 2.9 we compare the C¹⁸O emission, integrated in four different velocity ranges, with the ¹³CO emission integrated in the same velocity ranges and with the 1.3 mm dust continuum emission. At around the systemic velocity ($\Delta V = 0.0$ and 0.2 km s⁻¹), both the blueshifted and redshifted C¹⁸O emissions show clear elongation perpendicular to the outflow axis and resemble the dust continuum emission in morphology. In contrast, the ¹³CO emission at the same velocity is elongated along the outflow axis and likely traces the outflow. The highly blueshifted C¹⁸O emission ($\Delta V = -0.9$ to -0.3 km s⁻¹) shows elongation toward the south-east with a slight extension toward the north-east, and this morphology is similar to that of the ¹³CO emission at the same velocity. The highly redshifted C¹⁸O emission ($\Delta V = 0.5$ to 1.1 km s⁻¹) shows a central condensation elongated perpendicularly to the outflow axis with a weak extension toward the south-west. Although the C¹⁸O emission shows an extension similar to the ¹³CO outflow shells, the overall structure of the C¹⁸O central condensation is not similar to that of the ¹³CO outflow at the same velocity range. Therefore, the C¹⁸O emission (at least at around the systemic velocity and probably at the highly redshifted velocity) traces structures different from the outflow traced by the ¹³CO emission, and most likely traces the flattened molecular envelope perpendicular to the outflow axis. Such a flattened molecular envelope has often been observed around low-mass protostars (e.g., Ohashi et al. 1997a). Because the molecular outflow associated with B335 is aligned with the plane of sky closely, it is naturally expected for the flattened envelope to have an almost edge-on configuration and to show an elongated structure seen in channel maps.

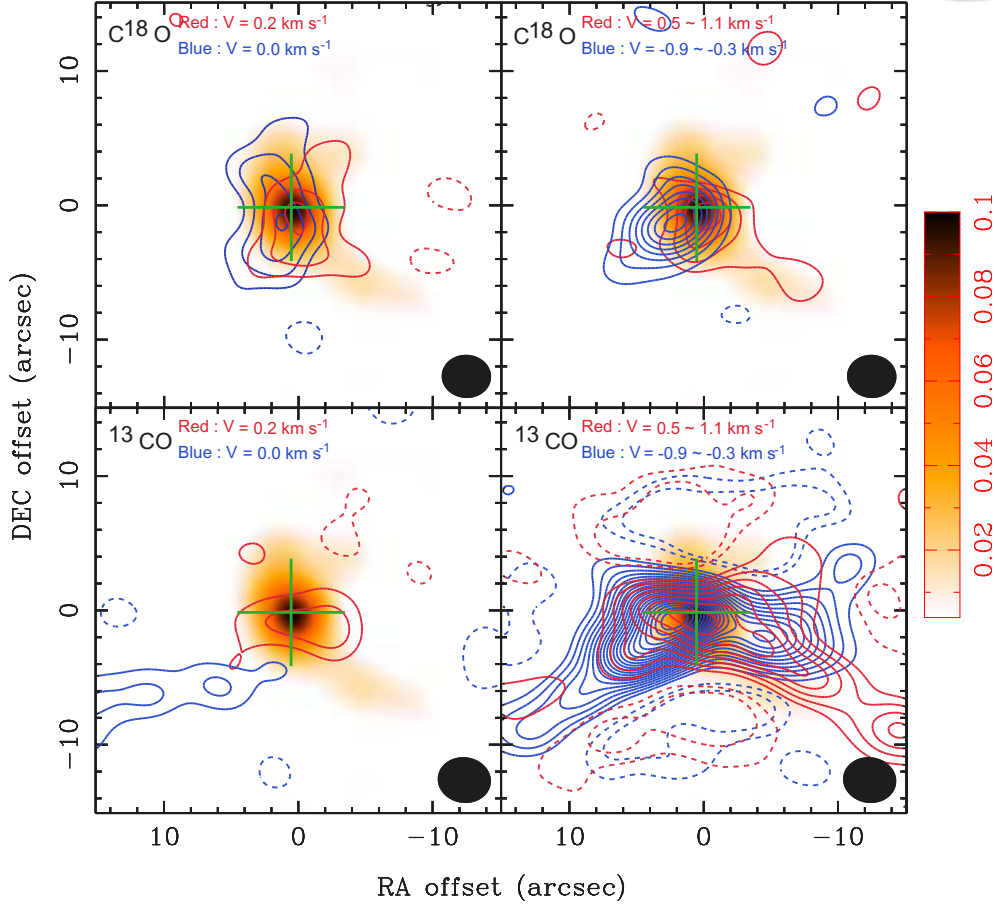
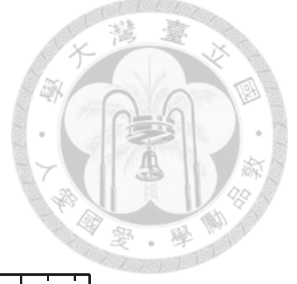


Figure 2.9 Moment 0 maps of the C^{18}O (2–1) (upper panels) and ^{13}CO (2–1) (lower panels) emissions in B335 integrated over four different velocity ranges as written in the Figure, superposed on the 1.3 mm continuum map in gray scale. Contour levels are from 3σ in steps of 2σ , where 1σ corresponds to 0.17 K km s^{-1} in the lower-velocity C^{18}O map, 0.24 K km s^{-1} in the highly redshifted C^{18}O map, 0.29 K km s^{-1} in the highly blueshifted C^{18}O map, 0.11 K km s^{-1} in the lower-velocity ^{13}CO map, 0.16 K km s^{-1} in the highly redshifted ^{13}CO map, and 0.19 K km s^{-1} in the highly blueshifted ^{13}CO map, respectively. Crosses show the position of the central source, and a filled ellipse at the bottom right corner in each panel shows the synthesized beam of the C^{18}O (2–1) (upper) and ^{13}CO (2–1) emissions (lower), respectively.

Since the blueshifted and redshifted outflow emissions arise mostly from the east and west sides of the protostar, respectively, the eastern lobe of the outflow is tilted toward us from the plane of the sky. Hence, the eastern part of the envelope is tilted away from us, while the western part of the envelope is tilted toward us from the plane of the sky. In this configuration, the eastern part of the envelope is the far side, while the western side is the near side. The flattened envelope shows a velocity gradient along its minor axis with the blueshifted emission on the far side and the redshifted emission on the near side. This suggests that the flattened envelope has an infalling motion toward the central protostar. In Figure 2.10, we show a schematic picture of the configuration of the outflow and the infalling flattened envelope described above. From the peak offset between the channels at $\Delta V = 0.0$ and 0.2 km s^{-1} , where the C^{18}O emission most likely traces the flattened envelope, the velocity gradient along the minor axis was measured to be $3.7 \times 10^{-3} \text{ km s}^{-1} \text{ AU}^{-1}$. From this velocity gradient, the infall velocity was estimated to be 0.28 km s^{-1} at a radius of 440 AU on the assumption of an inclination angle of 10° . This infall velocity yields a central stellar mass of $0.02 M_\odot$ in the case of the free-fall motion.

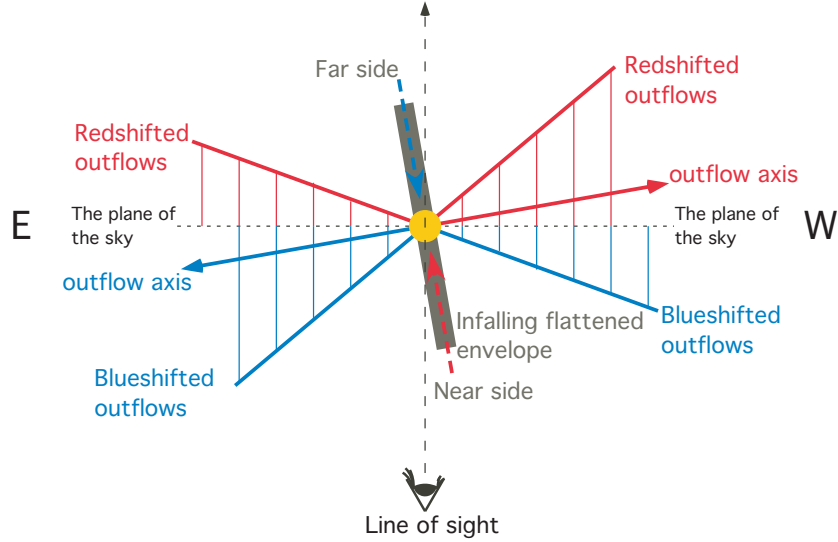


Figure 2.10 Cartoon to show the configuration of the outflow and the infalling flattened envelope viewing from the top. Red and blue solid arrows indicate the redshifted and blueshifted outflow axes, respectively, and red and blue lines show the redshifted and blueshifted outflow. A gray bold line represents the infalling flattened envelope, and red and blue dash arrows on it show the infall motion in the envelope on the near side (redshifted) and on the far side (blueshifted), respectively.

On the other hand, there is no detectable velocity gradient between these two channels ($\Delta V = 0.0$ and 0.2 km s^{-1}) across the outflow axis, suggesting no detectable rotation in the flattened envelope on a few hundreds of AU scale. Although there is no detectable rotation in the envelope on a few hundreds of AU scale, the flattened envelope could be produced by magnetic field (e.g., Galli & Shu 1993). In addition, an outflow can sweep away a part of the material in the envelope along the outflow axis, making the shape of the envelope flattened. Two Class 0 sources, NGC 1333 IRAS 2A (Brinch et al. 2009) and IRAS 16293-2422 (Takakuwa et al. 2007b), show similar cases; their innermost envelopes showing disk-like structures also have no detectable rotation on a few hundreds of AU scale.

In order to study the kinematics of the envelope in more detail, we constructed a simple model of a geometrically thin infalling and rotating envelope with a Gaussian intensity distribution and compared it with the observation. Note that even though the actual envelope has a thickness, we use a model without thickness to make the model simpler. Although the Gaussian intensity distribution is an arbitrary choice, the choice of the intensity distribution does not affect main velocity structures. The radius of the model envelope was set to be 370 AU based on the semi-major axis of the 1.3 mm dust continuum emission (see section 2.4.1). The inclination angle of the outflow was adopted as that of the envelope. The radial motion of the model envelope due to the dynamical infall is described as $v_r(r) = \sqrt{\frac{2GM_*}{r}}$, where M_* is the mass of the central star, while its angular motion due to rotation is described as $v_\phi(r) \propto r^{-1}$ because of the angular momentum conservation. Based on the measurement of the infall velocity using the channel maps described above, the stellar mass was initially set to be $0.02 M_\odot$. The rotational velocity was set to be 0.04 km s^{-1} at $r = 370 \text{ AU}$, which corresponds to the detection limit, because there is no detectable rotation. Then we generated synthesized images of the model envelope with the same u - v sampling as our SMA observation.

For the comparison between the model and the observation, we produced P - V diagrams from both the model and observation as shown in Figure 2.11. Green contours in Figure 2.11 (a) and (g) show the P - V diagrams derived from the model. This simple model can reproduce the main feature of the C^{18}O P - V diagrams both along and across the outflow axis. We note that there is a velocity difference in the redshifted peak between the model and the observation. In order to match the

model redshifted peak with the observed peak, we need to adopt a higher stellar mass in the model. In the case of a model with a stellar mass of $0.04 M_{\odot}$ as shown in Figure 2.11 (b) and (h), the model redshifted peak better matches the observed peak. If we adopt an even higher stellar mass ($0.08 M_{\odot}$; Figure 2.11 (c) and (i)), the model blueshifted peak would be offset from the observed peak due to the larger line width. On the other hand, if we set a higher rotational velocity such as $v_{\phi} = 0.16 \text{ km s}^{-1}$ at $r = 370 \text{ AU}$ in the models (Figure 2.11 (j)–(l)), there is a clear velocity gradient in the model P – V diagrams across the outflow axis, different from the observation which show no detectable velocity gradient across the outflow axis. Therefore, the model with a stellar mass of $0.04 M_{\odot}$ and a rotational velocity of 0.04 km s^{-1} at a radius of 370 AU provides a P – V diagram that matches the observation best. We note that there is a slight positional shift in the blueshifted peak between the model and observation in the P – V diagram along the outflow axis. Although a higher inclination angle could provide a better match of the model blueshifted peak with the observed peak, the difference may be due to contamination of outflowing motions in the observation since part of the blueshifted emission may arise from the outflow.

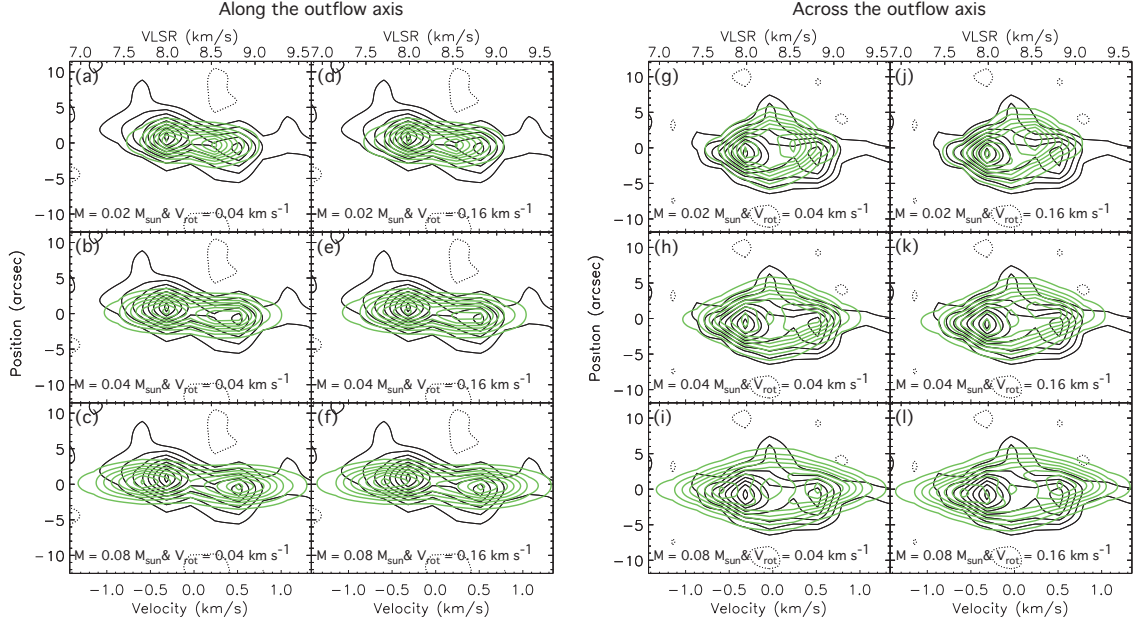
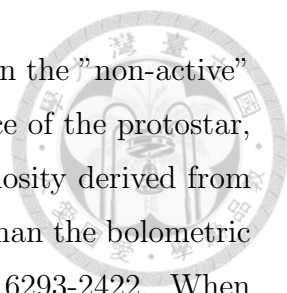


Figure 2.11 P - V diagrams of the C^{18}O ($J = 2-1$) emission in B335 along (P. A. = 90° ; left panel) and across (P. A. = 0° ; right panel) the outflow axis (black contours), overlaid by our simple model P - V diagrams of an infalling and rotating Gaussian disk (green contours). Green contours in panels (a)–(c) and (g)–(i) show the model P - V diagrams along and across the outflow axis with a central stellar mass of 0.02, 0.04, and 0.08 M_\odot and with rotational velocity of 0.04 km s^{-1} at a radius of 370 AU, respectively, and those in panel (d)–(f) and (j)–(l) show the model P - V diagrams along and across the outflow axis with a central stellar mass of 0.02 and 0.04 and 0.08 M_\odot and with rotational velocity of 0.16 km s^{-1} at a radius of 370 AU, respectively. Contour levels are from 12% in steps of 12% of the maximum intensity, where the maximum C^{18}O intensity is 9.1 K.

2.5.3 Infalling Motion in the Envelope

From our simple model of the infalling envelope (see section 2.5.2), the infalling velocity in the envelope around B335 was estimated to be 0.31–0.44 km s^{−1} at a radius of 370 AU, which corresponds to a central stellar mass ($\equiv M_*$) of 0.02–0.04 M_\odot . With an envelope mass ($\equiv M_{\text{env}}$) of 0.027 M_\odot derived from the 1.3 mm continuum emission, the mass infalling rate ($\dot{M}_{\text{inf}} = M_{\text{env}} V_{\text{inf}} / R_{\text{inf}}$) and the accretion luminosity ($L_{\text{acc}} = GM_* \dot{M}_{\text{inf}} / 4R_\odot$) were estimated to be 4.8–6.9 $\times 10^{-6}$ M_\odot yr^{−1} and 0.7–2.1 L_\odot , respectively, where 4 R_\odot is the radius of the protostar (Stahler et al. 1980). Hence, in B335, the mass outflow rate of the ¹²CO jets ($\dot{M}_{\text{out}} = 2.3 \times 10^{-7}$ M_\odot yr^{−1}) is 3%–5% of the mass infalling rate, which is slightly smaller than the results in HH 212 (Lee et al. 2007a) and HH 211 (Lee et al. 2007b), and the accretion luminosity is comparable to or smaller than the bolometric luminosity (1.5 L_\odot).

In B335, the knotty distribution of the associated HH objects along the outflow axis likely suggests episodic jet ejection, and the HV ¹²CO jet components found in our SMA observation are likely to represent the latest ejection event. Episodic jet ejections have been found in a number of protostellar sources, and are often linked to a sudden increase in the mass accretion (Arce et al. 2007). In fact, Dunham et al. (2008) and ? have revealed that many protostellar sources show one order of magnitude lower bolometric luminosities than the accretion luminosities predicted from the steady mass accretion model, and have proposed that the accretion is episodic and sources with lower bolometric luminosities than model predictions are probably in the quiescent stage. Direct observational comparisons between the accretion luminosities derived from the observed infalling motion in the envelopes and the bolometric luminosities also suggest non-steady mass accretion. In HL Tau (Lin et al. 1994; Hayashi et al. 1993), L1551 IRS 5 (Ohashi et al. 1996; Saito et al. 1996), and in IRAS 16293-2422 (Takakuwa et al. 2007b), the estimated accretion luminosities are an order of magnitude higher than the bolometric luminosities, and in HH 212 (Zinnecker et al. 1998; Lee et al. 2006) the accretion luminosity ($\sim 7 L_\odot$) is lower than the bolometric luminosity (14 L_\odot). This mismatch could be reconciled by a picture similar to the FU-Ori phenomenon (Hartmann & Kenyon 1996) and episodic mass accretion. A protostar is surrounded by a disk, and outside of the disk there exists an infalling envelope. The material in the envelope keeps infalling



onto the disk but not directly onto the surface of the protostar. In the "non-active" phase, most material in the disk does not accrete onto the surface of the protostar, and the jet ejection is also quiescent. Hence, the accretion luminosity derived from the mass infalling rate in the infalling envelope could be higher than the bolometric luminosity, as in the case of HL Tau, L1551 IRS5, and IRAS 16293-2422. When the disk becomes massive and unstable, the material accumulated in the disk starts falling onto the surface of the protostar, and then the powerful mass ejection also occurs (Hartmann & Kenyon 1996). This is the "active" phase, when the accretion luminosity estimated from the outer infalling envelope could be lower than the "real" accretion luminosity, as in the case of HH 212 associated with the clear HV jets. Our detection of HV molecular jets with a short dynamic timescale (~ 45 years), and a possibly lower accretion luminosity than the bolometric luminosity in B335, imply a recent burst of mass ejection and accretion. In addition, the [O I] line emission has been detected around the protostar in B335, which could suggest the presence of shocks due to a recent ejection of the jets (Nisini et al. 1999). These results are consistent with the idea that B335 is in an "active" accretion phase.

2.5.4 Non-Conserved Angular Momentum in B335

The infalling envelope traced by C^{18}O (2–1) emission in B335 does not show any clear velocity gradient perpendicular to the outflow axis, suggesting an absence of rotational motion in the envelope on the 300 AU scale. The upper limit of the specific angular momentum was estimated to be $7 \times 10^{-5} \text{ km s}^{-1} \text{ pc}$ (see section 2.5.2), which corresponds to a rotational velocity of 0.04 km s^{-1} at a radius of 370 AU. Since the material within this radius is considered to be dynamically infalling (see section 2.5.3), the specific angular momentum of the material within this radius is supposed to be conserved. If this is the case, the centrifugal force of the rotation becomes balanced with the gravitational force due to the central protostar with a mass of $0.04 M_{\odot}$ at a radius of $\sim 6 \text{ AU}$, which can be considered an upper limit for the radius of the Keplerian rotating disk. The upper limit of the specific angular momentum on the small scale ($\sim 7 \times 10^{-5} \text{ km s}^{-1} \text{ pc}$) is, however, much lower than the measured specific angular momenta at radii of 1000 AU ($\sim 5.4 \times 10^{-4} \text{ km s}^{-1} \text{ pc}$) and 20000 AU ($\sim 4.6 \times 10^{-3} \text{ km s}^{-1} \text{ pc}$) (Saito et al. 1999). If the angular momentum is conserved from large to small scales, the material falling from a radius

of 20000 AU should rotate at a velocity of 2.8 km s^{-1} at a radius of 370 AU, which is 70 times larger than the upper limit of the rotational velocity estimated using the present observation. These results show that the rotational motion in the envelope around B335 is spinning-down toward the inner radii.

This decrease in the specific angular momentum from large to small scales has also been found in other protostellar sources and NH_3 cores by Ohashi et al. (1997b) and Goodman et al. (1993). The specific angular momentum in B335 at a radius larger than 20,000 AU is similar to that of the NH_3 cores, however, the specific angular momentum on the few hundreds of AU scale in B335 is one order of magnitude smaller than that in other protostellar sources (see Table 2.5.4). This lower specific angular momentum on the small scale could be explained by evolutionary effects as follows. A study of velocity gradients in NH_3 cores by Goodman et al. (1993) has shown that the specific angular momentum is larger at a larger radius (i.e., $j \propto r^{1.6}$). If B335 is in an early phase of the inside-out collapse of such a dense core, the material in an outer region with a larger angular momentum has not yet fallen into the central region, and only the material at an inner radius with a smaller angular momentum has fallen in dynamically. Hence, the specific angular momentum on the few hundreds of AU scale in B335 could be still small.

To test this scenario, we estimated the size of the dynamical-infalling region and the maximum amount of the specific angular momentum carried in by the dynamical infall. Based on single-dish observations of the envelope around B335 in C^{18}O (1–0) emission by Saito et al. (1999) and the core rotation profile found by Goodman et al. (1993), we assumed that the initial condition of the core in B335 is a sphere with a rotation profile $\propto r^{0.6}$, a density profile $\propto r^{-2}$, a total mass of $2.4 M_{\odot}$, and a core radius of 20000 AU. Our SMA observation shows that the total mass of the region within a radius of 370 AU is $\sim 0.1 M_{\odot}$ (envelope + protostar). This amount of material was originally enclosed within a radius of 940 AU in the initial core. At this 940 AU radius, the initial core has a specific angular momentum of $\sim 3.5 \times 10^{-5} \text{ km s}^{-1} \text{ pc}$. Therefore, the angular momentum which has been carried in during the inside-out collapse is consistent with our upper limit for the angular momentum in the inner region. Moreover, the timescale of the propagation of the expansion wave to this 940 AU radius is $\sim 2.2 \times 10^4$ years, on the assumption of the sound speed of 0.2 km s^{-1} (Shu 1977). This timescale is smaller than typical Class 0 lifetime (1.7



Table 2.5. Keplerian Radius of the Protostellar Sources

ID	Sources	Class	j (pc km s ⁻¹)	r (AU)	Keplerian Radius (AU)	Reference
1	GG Tau	II	3.5×10^{-3}	460	460	1
2	DM Tau	II	2.2×10^{-3}	630	630	2
3	HL Tau	II	$(6.5-6.8) \times 10^{-4}$	700	30-40	3,4
4	LkCa15	II	2.8×10^{-3}	430	430	5
5	L1527	I	4.9×10^{-4}	2000	110	6
6	L1551 IRS 5	I	$(8.2-10.0) \times 10^{-4}$	700-900	50-320	7,8,9
7	IRS 63	I	8.8×10^{-4}	100	100	10
8	Elias 29	I	3.2×10^{-3}	200	200	10
9	HH 212	0	6.7×10^{-4}	460	70	11
10	HH 211	0	2.9×10^{-4}	80	80	12
11	B335	0	7×10^{-5}	370	6	This paper

Note. — j represents the specific angular momentum derived from disk or envelope rotation at the radius, r . If the Keplerian disk has been observed in the sources, the Keplerian radius represents the outer radius of the disk. If the rotating-supported disk has not been found in the source, the Keplerian radius is inferred from the envelope rotation and the estimated stellar mass.

References. — (1)Guilloteau et al. (1999); (2) Guilloteau & Dutrey (1998); (3) Hayashi et al. (1993); (4) Lin et al. (1994); (5) Qi et al. (2003); (6) Ohashi et al. (1997a); (7) Momose et al. (1998); (8) Saito et al. (1996); (9) Takakuwa et al. (2004); (10) Lommen et al. (2008); (11) Lee et al. (2006); (12) Lee et al. (2009).

$\pm 0.3 \times 10^5$ years; Enoch et al. 2009b). Hence, the small angular momentum in the inner region in B335 can be explained by the early phase of the inside-out collapse, and the material with larger angular momenta at the outer part has not yet fallen in and accumulated in the inner region.

For this scenario, we expect that as the expansion wave propagates outward, a larger amount of the angular momentum will be carried in and accumulated into the inner region, resulting in a larger radius of the Keplerian disk. In Table 2.5.4, we compare the radius of the (inferred) centrifugally supported, Keplerian disk around Class 0, I, and II sources. The sources associated with the observable large-scale Keplerian disks ($r > 400$ AU), GG Tau, DM Tau, and LkCa15, are in the most evolved stage (Class II). On the other hand, the sources in younger evolutionary stages (Class I and 0), such as L1551 IRS5, L1527, HH 212, and HH211, have smaller inferred radii for the Keplerian disks compared to those around the Class II sources. We note that there was no clear direct detection of Keplerian motions around these Class 0 and I sources, although some of them show a hint of Keplerian rotation that is indistinguishable from rotation with an r^{-1} dependence (Lommen et al. 2008; Lee et al. 2009). Nevertheless, jets around these Class 0 and I sources suggest that it is most likely for them to be associated with Keplerian disks (e.g., Shu et al. 1994). We also note that although HL Tau is classified as a Class II source, it is associated with the infalling material, suggesting that it is actually a Class I source. Among these sources, B335 has the smallest inferred Keplerian radius. This result may suggest that the Keplerian disk radius could increase with evolution of the inside-out collapse scenario (Terebey et al. 1984). We should note that in the latest evolutionary stage (Class II) the increase of the disk radius with evolution could be due to the transportation of the angular momentum inside the disk (Hartmann et al. 1998; Kitamura et al. 2002).

If the collapse follows Larson-Penston solution (Larson 1969; Penston 1969), the material at the inner radius with a smaller angular momentum and at the outer radius with a larger angular momentum falls in at almost the same time. Hence, we do not expect a smaller specific angular momentum in the central hundreds of AU region in B335 unless there is a mechanism to effectively remove the angular momentum of the material coming from the large scale, such as magnetic braking. In this case, the difference of the specific angular momentum on a few hundreds of AU

scale between B335 and other protostellar sources could be due to the efficiency of magnetic braking. Simulations have shown that angular momentum can be removed effectively during collapse with a strong magnetic field (Basu & Mouschovias 1994; Hennebelle & Fromang 2008; Mellon & Li 2008, 2009). With this Larson-Penston collapse scenario, it would be difficult to explain the increase of the Keplerian radius with evolution since the majority of the material falls in at almost the same time. If this is the case, the evolution of the Keplerian radius from Class 0 to Class II could be due to the transportation of the angular momentum inside the disk (Hartmann et al. 1998; Kitamura et al. 2002).

2.6 Summary

We have performed detailed imaging and analyses of the SMA Observation of B335 in 1.3 mm continuum, ^{12}CO (2–1), ^{13}CO (2–1), and C^{18}O (2–1) emissions, taken as a part of our large low-mass star formation project, “PROSAC”.

1. In ^{12}CO emission, we found two distinct outflow components associated with B335; one blueshifted ($\Delta V = -5.8$ to -1.6 km s^{-1}) and redshifted ($\Delta V = 0.6$ to 4.8 km s^{-1}) V-shaped structure opening toward the east and west of the protostar, respectively, which probably delineates the conical-shaped outflow shell with the eastern side inclined slightly ($\sim 10^\circ$) toward us, and the other is a compact ($1500 \times 900 \text{ AU}$), HV blueshifted ($\Delta V = -37.5$ to -18.5 km s^{-1}) and redshifted ($\Delta V = 17.5$ to 36.5 km s^{-1}) component to the east and west of the protostar, respectively. The mean propagation velocity ($\sim 160 \text{ km s}^{-1}$) of the HV components is comparable to the velocity of the associated HH objects ($140 - 170 \text{ km s}^{-1}$), and the HV components probably trace molecular jets driven by B335. The ^{13}CO (2–1) emission traces the low-velocity outflow shell.
2. The C^{18}O emission shows a compact ($\sim 1500 \text{ AU}$) condensation with an east (blueshifted) to west (redshifted) velocity gradient. Around the systemic velocity ($\Delta V = 0.0$ to 0.2 km s^{-1}) the C^{18}O emission shows a similar structure to that in the 1.3 mm continuum emission and elongation perpendicular to the direction of the associated outflow. Hence, the C^{18}O emission probably traces

the protostellar envelope around B335. The east-west velocity gradient can be interpreted as an infalling gas motion in the flattened disklike envelope, while there is no clear velocity gradient along the north-south direction or sign of the rotation in the envelope on a few hundreds of AU scale. From our simple modeling of the infalling disklike envelope, the central stellar mass and the mass infalling rate were estimated to be $\sim 0.02\text{--}0.04 M_{\odot}$ and $\sim 4.8\text{--}6.9 \times 10^{-6} M_{\odot} \text{ yr}^{-1}$, respectively, and the accretion luminosity was estimated to be $\sim 0.7\text{--}2.1 L_{\odot}$. The upper limit of the specific angular momentum is estimated as $\sim 7 \times 10^{-5} \text{ km s}^{-1} \text{ pc}$, which corresponds to a rotational velocity of 0.04 km s^{-1} at a radius of 370 AU.

3. The mass-loss rate ($\sim 2.3 \times 10^{-7} M_{\odot} \text{ yr}^{-1}$) and the momentum flux ($\sim 3.7 \times 10^{-5} M_{\odot} \text{ yr}^{-1} \text{ km s}^{-1}$) of the HV ^{12}CO jets in B335 are one order of magnitude lower than those in other protostellar sources such as HH 212 and HH 211. There is no thermal SiO emission found in B335, while intense SiO and H_2 emissions were found in HH 212 and HH 211. These results imply that the jet phenomena in B335 are less active. We suggest that the lower bolometric luminosity and hence the lower mass accretion in B335 are linked to a weaker jet activity than that in the more luminous protostellar sources. The jet activities in B335 are most likely episodic because of the presence of the chain of the discrete HH objects, and it is considered to be linked to the episodic accretion. The short dynamical timescale of the HV jets (~ 45 years) may reflect a recent increase of the mass accretion onto the central protostar.
4. The flattened infalling envelope traced by the C^{18}O emission shows no signature of rotation down to a radius of ~ 370 AU. As compared to the previous single-dish studies of the envelope around B335, we found that the specific angular momentum of the envelope rotation decreases from a radius of 20,000 to 300 AU. The upper limit of the specific angular momentum ($7 \times 10^{-5} \text{ km s}^{-1} \text{ pc}$) in the region within a radius of 370 AU is one order of magnitude smaller than the angular momentum around other protostellar sources, and the estimated size of the centrifugally supported disk (~ 6 AU) around B335 is almost two orders of magnitude smaller than that around young stellar objects in Taurus. Other more evolved sources tend to show higher angular momenta

in the inner region, and a larger size for the centrifugally supported disk. We presume that the low specific angular momentum and the small inferred Keplerian disk around B335 could be due to its young age in the course of the inside-out collapse of the core with the increasing specific angular momentum as a function of the radius or the more efficient magnetic braking.



Chapter 3

Physical Conditions and Kinematics Traced by Millimeter and Submillimeter Lines on a Few Hundreds of AU Scale in B335

This chapter has been published in ApJ.

Hsi-Wei Yen, Shigehisa Takakuwa, and Nagayoshi Ohashi 2011, ApJ, 742, 57

3.1 Abstract

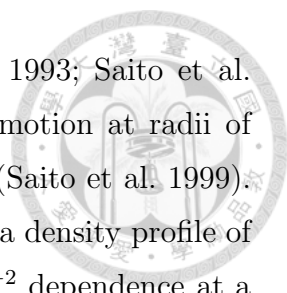
We have performed detailed imaging and analyses of the combined (SMA + single-dish) data in the millimeter C¹⁸O (2–1) and submillimeter CS (7–6) emissions of B335, an isolated nearby (~ 150 pc) Bok globule with an embedded Class 0 sources ($L_{\text{bol}} \sim 1.5 L_{\odot}$). The C¹⁸O emission likely traces both extended and central compact envelopes with sizes of ~ 9000 and ~ 1500 AU, respectively, while the CS emission shows a compact envelope with a radius of ~ 400 AU surrounded by an east-west elongated outflow with a size of ~ 3000 AU. The C¹⁸O inner envelope shows an infalling motion but no signature of envelope rotation. In contrast, the CS envelope shows a rotational motion but no signature of the infalling motion, and the rotational velocity and the specific angular momentum were estimated to be 0.11 km s^{-1} and $5.8 \times 10^{-5} \text{ km s}^{-1} \text{ pc}$ at a radius of 110 AU. The profile of specific angular

momenta of envelope rotation in B335 from radii of $\sim 10^4$ – 10^2 AU is revealed. The specific angular momentum in B335 decreases from radii of 10000 to 370 AU and becomes conserved within 370 AU. The different kinematics traced by the millimeter and submillimeter emissions and the evolution of the profile of the specific angular momentum are discussed, and the physical conditions (density, temperature, optical depth, and excitation) in B335 from 3000 to 300 AU scales were estimated with a LVG model.

3.2 Introduction

Dense-gas ($\geq 10^{4-5}$ cm $^{-3}$) condensations in dark molecular clouds are sites of low-mass star formation (Andre et al. 2000; Myers et al. 2000). Previous millimeter interferometric observations have revealed rotating and infalling gas motions in dense-gas condensations associated with known protostellar sources, so-called “protostellar envelopes” (Ohashi et al. 1996, 1997a,b; Momose et al. 1998). It is still less clear, however, how the infalling motion is terminated and the angular momentum of envelope rotation is transferred from large (~ 10000 AU) to small (\sim few hundred AU) radii in the envelopes (e.g., Goodman et al. 1993; Ohashi et al. 1997b), and how centrifugally supported disks on a few hundred AU scale, often observed around young stars (e.g., Guilloteau et al. 1999; Guilloteau & Dutrey 1998; Qi et al. 2003), are formed around the protostars in those envelopes.

In order to approach these questions, we have performed Submillimeter Array (SMA) observation of B335 (Jørgensen et al. 2007; Chapter 2), an isolated Bok globule at a distance of 150 pc associated with an embedded Class 0 protostar with a bolometric luminosity of $1.5 L_{\odot}$ (IRAS 19347+0727; Keene et al. 1980, 1983; Stutz et al. 2008). B335 is associated with an east-west elongated, conical-shaped molecular outflow with a size of ~ 0.2 pc, an opening angle of $\sim 45^{\circ}$, and an inclination angle of $\sim 10^{\circ}$ from the plane of the sky (Hirano et al. 1988). Along the outflow axis there are also high-velocity (~ 160 km s $^{-1}$), compact ($\sim 1500 \times 900$ AU) molecular jets seen in the ^{12}CO (2–1) emission (Chapter 2), as well as HH objects (HH 119 A–F; Reipurth et al. 1992; Gålfalk & Olofsson 2007). Millimeter interferometric observations of the envelope around B335 in the H^{13}CO^+ (1–0) and C^{18}O (1–0) lines at an angular resolution of $\sim 6''$ have revealed the presence of the



infalling gas motion on a 3000 AU scale (Chandler & Sargent 1993; Saito et al. 1999). The envelope around B335 also exhibits slow rotating motion at radii of ~ 20000 (Frerking et al. 1987; Saito et al. 1999) and ~ 1000 AU (Saito et al. 1999). Millimeter continuum studies of the envelope around B335 show a density profile of an $r^{-1.5}$ dependence between radii of 60 and 3900 AU and an r^{-2} dependence at a radius larger than 3900 AU (Harvey et al. 2003b), which is consistent with the inside-out collapse model (Shu 1977). These results indicate that B335 is a prototypical low-mass protostellar source suitable for detailed studies. Our SMA observation of B335 in the C^{18}O (2–1) emission found a compact (~ 1500 AU) molecular envelope around the protostar, where there is a clear infalling motion. The central stellar mass and the infalling velocity were estimated to be $\sim 0.04 M_{\odot}$ and $\sim 0.44 \text{ km s}^{-1}$ at a radius of 370 AU, respectively. On the other hand, there is no signature of the envelope rotation in the C^{18}O emission on a few hundred AU scale, and the upper limits of the rotational velocity and the specific angular momentum of the envelope rotation were estimated to be $\lesssim 0.04 \text{ km s}^{-1}$ and $\lesssim 7 \times 10^{-5} \text{ km s}^{-1} \text{ pc}$ at a radius of 370 AU, respectively.

Our SMA results in the C^{18}O emission show an infalling motion without any clear signature of a rotational motion at a radius of ~ 400 AU in the envelope around B335. The rotational motion in the infalling envelope within few hundred AU is, however, still a question, and it is unclear how the infalling motion is terminated and the angular momentum of the rotational motion is transferred to the innermost part of the envelope. In fact, structures and kinematics in the innermost part of protostellar envelopes are not well understood with millimeter molecular-line observations, due to the contamination from surrounding low-density and low-temperature gas ($T \sim 10 \text{ K}$ and $n \sim 10^{4-5} \text{ cm}^{-3}$) (e.g., Takakuwa et al. 2007). Physical conditions (temperature, density, optical depth, and excitation conditions) in inner envelopes are also uncertain, and there is little published information on the physical conditions of protostellar envelopes from thousands to hundreds of AU scales with a high angular resolution (\sim a few hundred AU) because interferometric observations suffer from the missing flux problem and cannot directly trace the physical conditions in the inner envelopes, and single-dish observations do not have a sufficient spatial resolution to resolve the inner \sim few hundred AU of envelopes. In order to overcome these problems and to investigate structures, kinematics, and physical conditions

from outer (~ 10000 AU) to innermost (\sim a few hundred AU) parts of protostellar envelopes, combined single-dish and interferometric observations of protostellar envelopes in submillimeter molecular lines and comparison with those in millimeter molecular lines are required.

In this paper, we performed Submillimeter Telescope (SMT) observations in the millimeter C^{18}O (2–1) emission and SMA and Atacama Submillimeter Telescope Experiment (ASTE) observations in the submillimeter CS (7–6) emission of B335, and made the combined SMT + SMA C^{18}O and ASTE + SMA CS images of the protostellar envelope around B335. From the comparison between the combined millimeter C^{18}O (2–1) and the submillimeter CS (7–6) data, we derived physical conditions of the envelope and the outflow in B335 from ~ 3000 to ~ 300 AU scales at an angular resolution of $\sim 4''$. We also found a sign of the spin-up envelope rotation in B335 on a few hundreds AU scale, and studied radial dependence of the specific angular momentum of the envelope rotation in B335.

3.3 Observation

SMA observations of B335 at 230 and 342 GHz were made as a part of a large SMA project (PROSAC: Jørgensen et al. 2007) with the seven antennas on 2005 June 24 and 14, respectively. Details of the SMA were described by Ho et al. (2004). In the 230 GHz observation, ^{12}CO (2–1), ^{13}CO (2–1), C^{18}O (2–1), and 1.3 mm continuum emissions were observed simultaneously, and details of the observation were described in Chapter 2. On the other hand, H_2CO ($5_{1,5}-4_{1,4}$), CS (7–6), and 342 GHz continuum emissions were observed simultaneously in the 342 GHz observation. Parameters for the SMA observations are summarized in Table 1. Our 230 and 342 GHz observations were insensitive to structures more extended than ~ 4500 and ~ 2000 AU at the 10% level (Wilner & Welch 1994). The MIR software package was used to calibrate the data. The calibrated visibility data were Fourier-transformed and CLEANed with MIRIAD (Sault et al. 1995) to produce images. In this paper, we will present the results of the C^{18}O (2–1; 219.56036 GHz), CS (7–6; 342.88295 GHz), and the 1.3 mm and 0.8 mm continuum emissions.

Single-dish observations of B335 in the C^{18}O (2–1) and CS (7–6) line emissions were made with SMT on 2008 November 20 and 26 and with ASTE on 2005 August

16–20, respectively. In the SMT C¹⁸O observations, we made a 7×9 mapping centered on $\alpha(\text{J2000}) = 19^{\text{h}}37^{\text{m}}00^{\text{s}}.90$, $\delta(\text{J2000}) = 7^{\circ}34'08''.8$ with a grid spacing of $15''$, which provides a $90'' \times 120''$ map at Nyquist-sampling. Each position in the map was observed at least twice, and each integration time was 60 seconds in total (on and off position). The central position was adopted to check the relative flux calibration, and the flux uncertainty was estimated to be $\sim 10\% - 20\%$. The telescope pointing was checked every one and half hour by observing Jupiter in the 219 GHz continuum emission. In the ASTE CS observations, the mapping center was the same as that of the SMT observations, and we observed 21 points with a grid spacing of $10''$ to provide Nyquist-sampling. Details of the ASTE observations were described by Takakuwa et al. (2007a). Observational parameter for our single-dish observations are summarized in Table 3.1.

The conversion factors from T_A^* (K) to S (Jy Beam⁻¹) of the SMT C¹⁸O and ASTE CS observations were derived to be 66.3 and 74.8, respectively, as

$$S = \frac{2k_B\Omega_{\text{beam}}}{\lambda^2} \frac{T_A^*}{\eta_{mb}}, \quad (3.1)$$

where k_B is the Boltzmann constant, Ω_{beam} is the solid angle of the beam, λ is the wavelength, and η_{mb} is the main beam efficiency (68% for SMT and 60% for ASTE). We combined these single-dish data with our SMA data, and the spatial resolutions and the noise levels in the combined images are shown in Table 3.1. Details of the combining process are described in Appendix. We also made simulations of the combining process to test the feasibility and the limitation of this technique. We found that there are several sources to cause the miss match of the relative flux between single-dish and interferometric data and hence to distort the final image, as discussed in Appendix. In our combined images, the intensity variation in the outer region ($r > 5''$) due to the distortion is likely less than 1.5σ of our noise levels, while in the inner region ($r < 5''$), the total flux could be suppressed by $\sim 20\%$ due to the distortion, which is comparable to the uncertainty of the flux calibration in our single-dish observations.

3.4 Results

The SMA images of B335 in the 1.3 mm and 0.8 mm continuum, C¹⁸O (2–1), and CS (7–6) emissions were first shown in the PROSAC paper (Jørgensen et al. 2007),



Table 3.1. Summary of the Observational Parameters

	C ¹⁸ O (2–1)	CS (7–6)
Interferometer	SMA	
Coordinate Center	$\alpha(\text{J2000}) = 19^{\text{h}}37^{\text{m}}00^{\text{s}}.89$ $\delta(\text{J2000}) = 7^{\circ}34'10''.0$	
Primary Beam	56''.3	21''.6
Projected Baseline Length (k λ)	5.5 – 53.5	12.5 – 80.0
Synthesized Beam (P. A.)	3''.7 \times 3''.2 (86.5°)	2''.5 \times 2''.3 (69.4°)
Velocity Resolution (km s ^{–1})	0.28	0.18
Noise Level (K)	0.60	0.77
Passband Calibrator	3C 279	3C 454.3
Flux Calibrator	Callisto	Uranus
Gain Calibrator (Flux)	1749+096 (1.9 Jy)	1749+096 (1.0 Jy)
	2145+067 (2.5 Jy)	2145+067 (1.0 Jy)
Single-dish Telescope	SMT	ASTE
Coordinate Center	$\alpha(\text{J2000}) = 19^{\text{h}}37^{\text{m}}00^{\text{s}}.90$ $\delta(\text{J2000}) = 7^{\circ}34'08''.8$	
Beam Size	33''.8	21''.6
Velocity Resolution (km s ^{–1})	0.06	0.11
Main Beam Efficiency	68%	60%
Noise Level (K)	0.22	0.14
Conversion Factors (Jy Beam ^{–1} K ^{–1})	66.3	74.8
Combined Data	SMA + SMA	ASTE + SMA
Coordinate Center	$\alpha(\text{J2000}) = 19^{\text{h}}37^{\text{m}}00^{\text{s}}.89$ $\delta(\text{J2000}) = 7^{\circ}34'10''.0$	
Synthesized Beam (P. A.)	4''.7 \times 4''.0 (82.0°)	2''.7 \times 2''.6 (72.3°)
Velocity Resolution (km s ^{–1})	0.28	0.18
Noise Level (K)	0.63	0.83

and detailed results of the SMA 1.3 mm continuum and C¹⁸O (2–1) data have been presented in Chapter 2. The ASTE data of the CS (7–6) line emission were first published by Takakuwa et al. (2007a). In this paper, we present the results of the combined SMA + single-dish data in the C¹⁸O (2–1) and CS (7–6) emissions, and mainly discuss the combined images. Hereafter, we adopt the peak position of the 1.3 mm continuum emission in the SMA data, $\alpha(\text{J2000}) = 19^{\text{h}}37^{\text{m}}0^{\text{s}}.93$, $\delta(\text{J2000}) = 7^{\circ}34'09''.8$, as the position of the central protostellar source (Chapter 2).

3.4.1 Single-dish, SMA, and the Combined Images in Millimeter C¹⁸O and Submillimeter CS Emissions

Figure 3.1 shows the SMT, SMA, and the combined moment 0 maps of the C¹⁸O (2–1) emission in B335. In the SMT observations, the C¹⁸O (2–1) emission was detected at a level higher than 14σ ($T_{\text{MB}} = 8.4$ K) over the entire observing area of $13500 \text{ AU} \times 18000 \text{ AU}$. In the SMT moment 0 map, the C¹⁸O emission shows a single peak around the protostar and is elongated along the east-west direction at an inner ~ 3000 AU and along the north-south direction at an outer ~ 6000 AU. In the SMA observation, we detected a compact C¹⁸O blob with a size of ~ 1500 AU toward the protostar. In the combined moment 0 map, the C¹⁸O emission shows a compact component surrounded by an extended halo-like component elongated along the east-west direction. Due to the response of the SMA primary beam, the single-dish emission at a radius larger than $\sim 40''$ (~ 6000 AU) is significantly suppressed.

Figure 3.2 shows the ASTE, SMA, and combined moment 0 maps of the CS (7–6) emission. In the ASTE observations, the CS emission was not detected ($< 3\sigma$) toward the observing points of $\pm 20''$ along Declination, and the CS emission toward the observing points of $\pm 20''$ along Right Ascension is one order of magnitude weaker than that at the center. Since the ASTE beam size is $\sim 22''$, in the ASTE moment 0 map, the CS emission is not spatially resolved. On the other hand, in the SMA observation we resolved the CS emission into two peaks. One emission component is coincident with the protostar, and the other is at $5''$ southwest of the protostar. In the combined moment 0 map, the two emission components found in the SMA observation appear to be surrounded by a weaker extended emission with a size of ~ 3000 AU. The outer emission ($r > 900$ AU) shows east-west elongation as in the

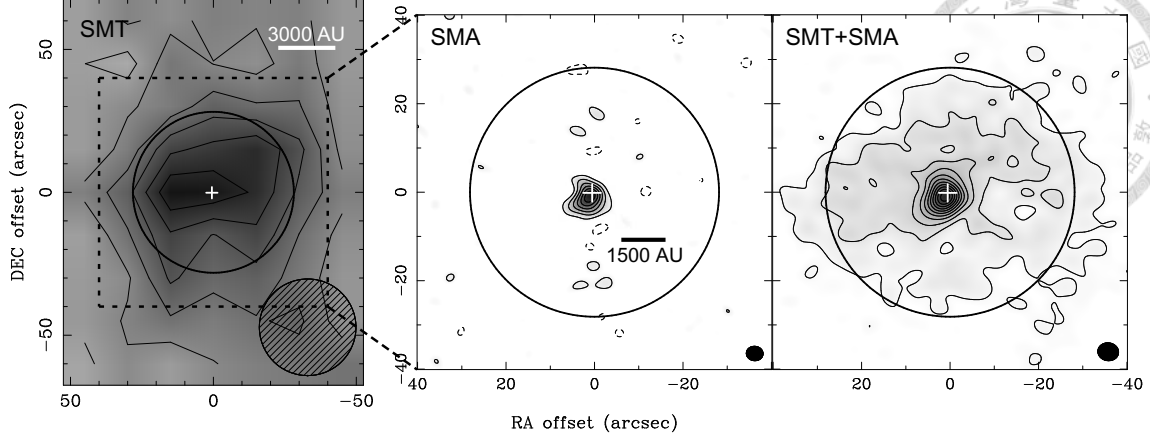


Figure 3.1 The integrated velocity ranges are $V_{\text{LSR}} = 7.95 - 8.92$, $7.29 - 9.23$, and $7.57 - 8.95$ km s^{-1} , respectively. Crosses show the protostellar position, and open circles represent the primary beam of the SMA observation at 230 GHz. Hatched and solid ellipses are the beam sizes of the SMT, SMA, and combined data. Contour levels are from 14σ in steps of 3σ in the SMT map, from 3σ in steps of 3σ in the SMA map, and from 2σ in steps of 2σ in the combined map, where 1σ is 0.05, 0.44, and 0.46 K km s^{-1} , respectively.

case of the C^{18}O emission, while the inner emission ($r < 900$ AU) shows a central compact component plus south-east and south-west protrusions.

In order to compare the distribution of the millimeter C^{18}O (2–1) and submillimeter CS (7–6) emissions, in Figure 3.3 we show the combined moment 0 maps of the C^{18}O and CS emissions on the same spatial scale. The C^{18}O emission is more extended than the CS emission, and there is no CS emission at outer 1500 AU. The absence of the CS emission in the outer region is unlikely due to the response of the SMA primary beam since in the ASTE observations the CS emission is weak in the outer region as compared to the SMT C^{18}O emission. The different spatial extent between the millimeter and submillimeter molecular line emissions is likely to reflect the physical conditions of the envelope around B335, and we will discuss the physical conditions traced by the millimeter C^{18}O (2–1) and submillimeter CS (7–6) emissions in Section 3.5.

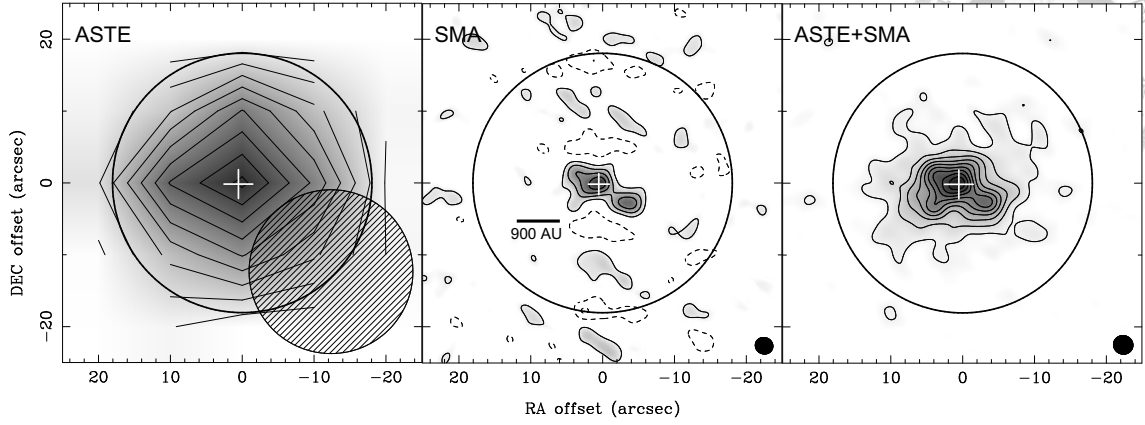


Figure 3.2 Moment 0 maps of the ASTE (left), SMA (middle), and combined (right) data of the CS (7–6) emission in B335. The integrated velocity ranges are $V_{\text{LSR}} = 7.18 - 9.05$, $7.47 - 9.25$, and $7.12 - 9.25$ km s^{-1} , respectively. Crosses show the protostellar position, and open circles represent the primary beam of the SMA observation at 345 GHz. Hatched and solid ellipses are the beam sizes of the SMT, SMA, and combined data. Contour levels are from 3σ in steps of 3σ in the ASTE and SMA maps, and from 2σ in steps of 2σ in the combined map, where 1σ is 0.06, 0.43, and 0.51 K km s^{-1} , respectively.

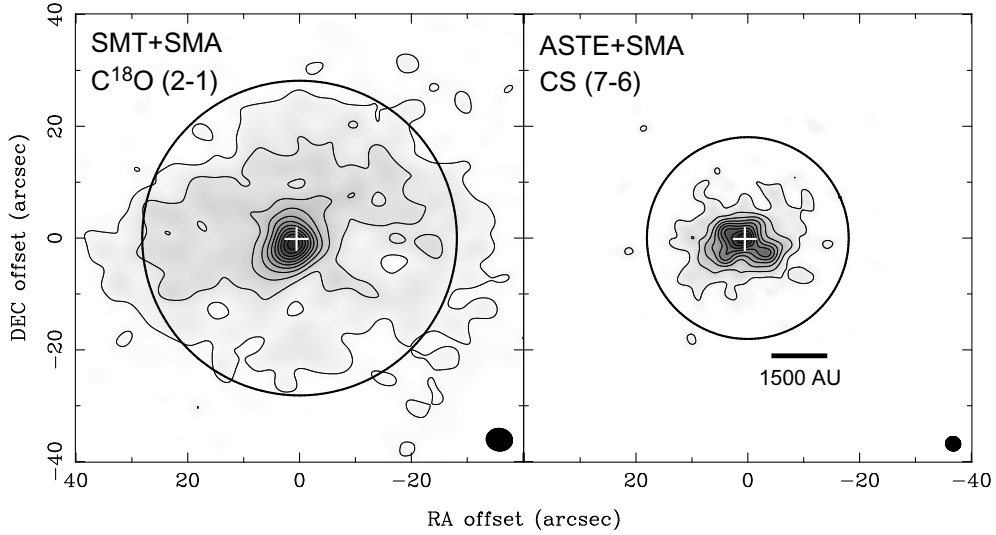


Figure 3.3 Moment 0 maps of the combined data, SMT + SMA in the C^{18}O (2–1) emission and ASTE + SMA in the CS (7–6) emission, on the same spatial scale. The integrated velocity ranges are $V_{\text{LSR}} = 7.57 - 8.95$ and $7.12 - 9.25$ km s^{-1} , respectively. Crosses show the protostellar position, and solid ellipses represent the beam sizes. Open circles in the C^{18}O and CS maps are the primary beam of the SMA observations at 230 and 342 GHz, respectively. Contour levels are from 2σ in steps of 2σ , where 1σ is 0.46 K km s^{-1} in the C^{18}O map and 0.51 K km s^{-1} in the CS map.

3.4.2 Velocity Structures

In Figure 3.4 we compared the single-dish, SMA, and combined C¹⁸O and CS line profiles toward the protostellar position. The SMA and combined spectra are primary-beam corrected and convolved with the relevant single-dish beams (33".8 for the C¹⁸O spectra and 21".6 for the CS spectra). In the SMA C¹⁸O and CS spectra, the missing fluxes were estimated to be ~80% and ~85%, respectively. After we combined the single-dish and SMA data, the missing flux were recovered properly. By fitting a Gaussian function to the C¹⁸O line profile taken with SMT, the central velocity was estimated to be $V_{\text{LSR}} = 8.34 \text{ km s}^{-1}$ (vertical dash line in Figure 3.4). Hereafter, this velocity is adopted as the systemic velocity, and all the velocities in the rest of this paper ($\equiv V$) are shown as relative velocities with respect to this systemic velocity. The full width at half maximum (FWHM) line widths of the single-dish millimeter C¹⁸O and submillimeter CS emissions were estimated to be 0.5 and 1.5 km s^{-1} , respectively, and the submillimeter CS emission is three times broader than the millimeter C¹⁸O emission. In particular, at a velocity higher than $\pm 0.5 \text{ km s}^{-1}$, the submillimeter CS emission is stronger than the millimeter C¹⁸O emission. The physical conditions of the high- and low-velocity components will be discussed in Section 3.5.

In the velocity channel maps of the combined SMT + SMA C¹⁸O data (Fig. 3.5), the extended component seen in the moment 0 map of Figure 3.3 appears around the systemic velocity ($V = -0.08$ and 0.20 km s^{-1}), and there is no clear systematic velocity structure in the extended component. On the other hand, the central compact component appears both at the systemic and higher velocities, and its peak is shifted from east to west of the protostar as the velocity changes from blueshifted to redshifted. Figure 3.6 shows the velocity channel maps of the ASTE + SMA CS data. At higher velocities ($V = -0.96$ to -0.60 and 0.46 to 0.82 km s^{-1}), diffuse CS emission elongated along the east-west direction is seen, while at lower velocities ($V = -0.42$ to 0.46 km s^{-1}) compact CS emission associated with the protostar is evident. At $V = -0.42$ and -0.25 km s^{-1} , a secondary emission peak to the south-west of the protostar is also seen, as already found in the CS (5–4) observation (Wilner et al. 2000). The central compact component associated with the protostar appears to show a systematic velocity gradient along the north-south direction, i.e., the peak is shifted from south to north of the protostar as the velocity

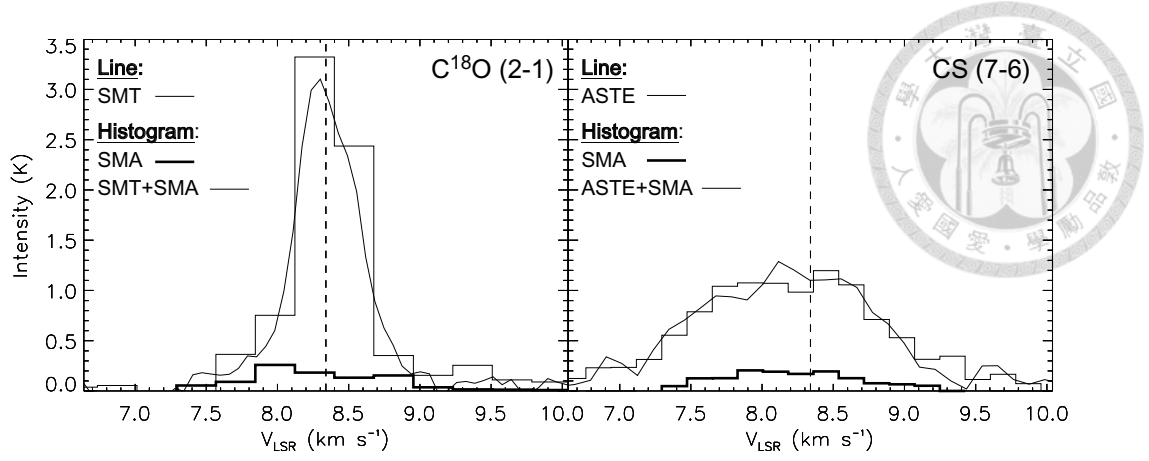


Figure 3.4 Line profiles of the C^{18}O (2–1) emission in the SMT, SMA, and combined data (left) and the CS (7–6) emission in the ASTE, SMA, and combined data (right). The single-dish line profiles are plotted in thin lines, and the line profiles of the SMA and combined data are plotted in thick and thin histograms, respectively. The line profiles are all taken in the central position. In order to compare the line profiles between the single-dish, SMA and combined data, the SMA and combined data are first primary-beam corrected and then convolved with the corresponded single-dish beam sizes. The beam sizes of the SMT and ASTE observations are $33''.8$ and $21''.6$, respectively.

changes from blueshifted to redshifted.

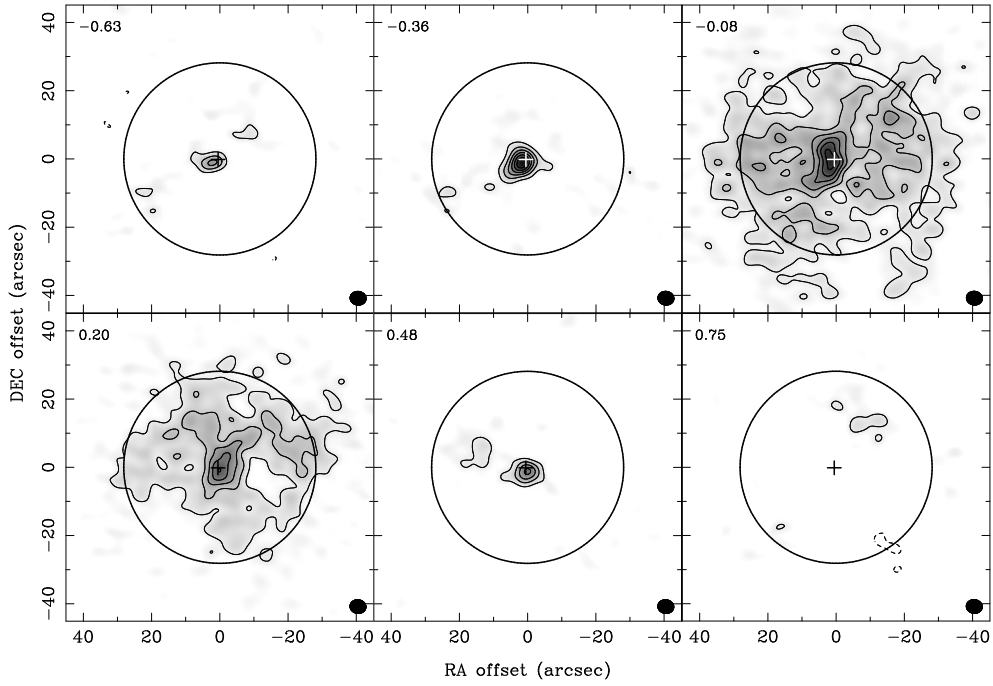


Figure 3.5 Velocity channel maps of the combined C^{18}O (2–1) data. Velocity of each channel is shown in the upper left corner of each panel. Crosses and solid ellipses show the protostellar position and the beam size, respectively, and open circles are the primary beam of the SMA observations at 230 GHz. Contour levels are from 2σ in steps of 2σ , where 1σ is 0.63 K.

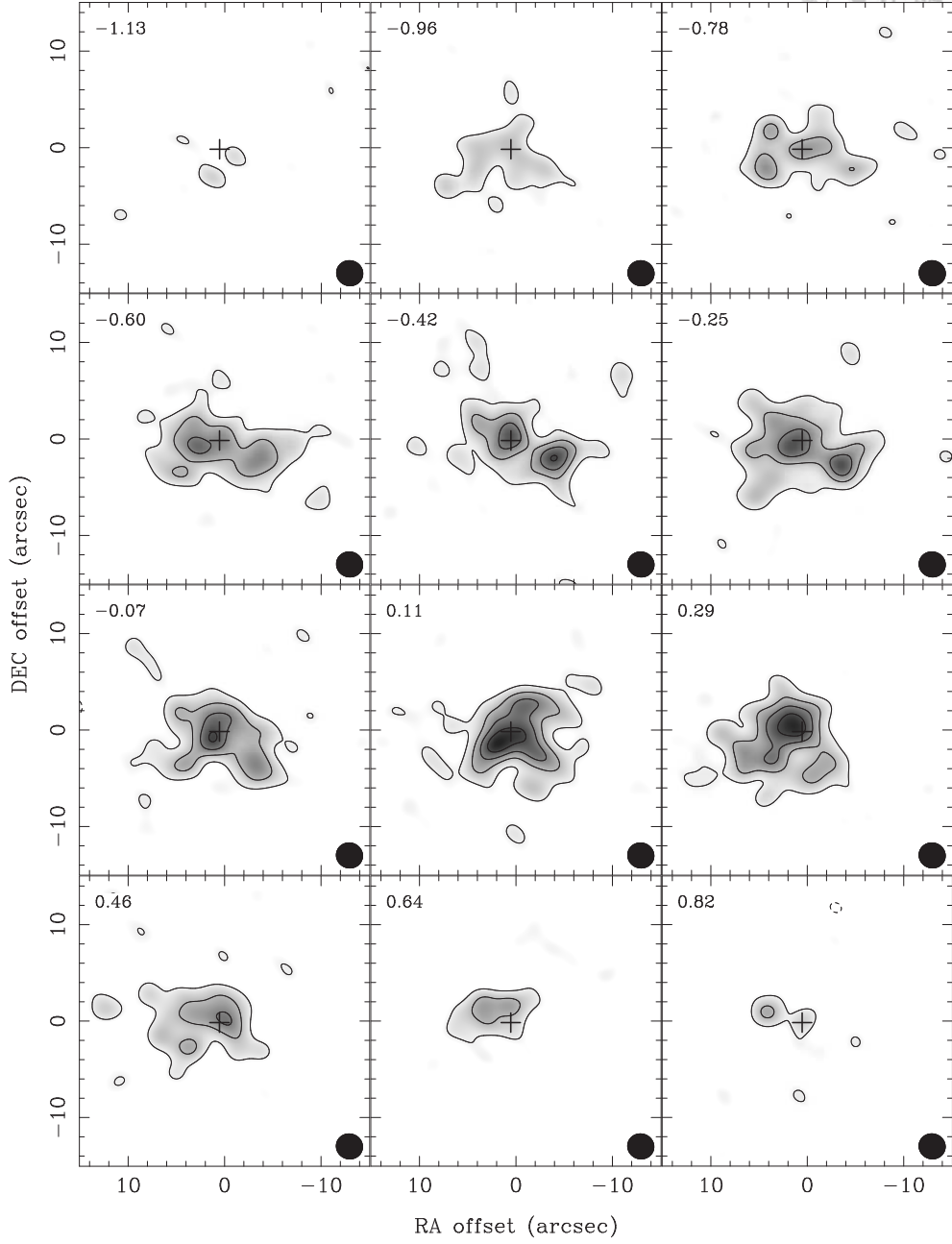


Figure 3.6 Velocity channel maps of the combined CS (7–6) data. Velocity of each channel is shown in the upper left corner of each panel. Crosses and solid ellipses show the protostellar position and the beam size, respectively, and open circles are the primary beam of the SMA observations at 342 GHz. Contour levels are from 2σ in steps of 2σ , where 1σ is 0.83 K.

In order to compare the kinematics traced by the millimeter C¹⁸O (2–1) and submillimeter CS (7–6) emissions, we integrated the emissions into four different velocity regimes; high-velocity blueshifted, low-velocity blueshifted, low-velocity redshifted, and high-velocity redshifted (Fig. 3.7). In the high-velocity regimes ($|V| \gtrsim 0.5 \text{ km s}^{-1}$), the CS emission is stronger and more extended ($\sim 2000 \text{ AU}$) than the C¹⁸O emission, and elongated along the outflow axis. In contrast, in the low-velocity regimes ($|V| \lesssim 0.5 \text{ km s}^{-1}$), the C¹⁸O emission becomes stronger and more extended compared to the CS emission. Both the C¹⁸O and CS emissions show a central compact component associated with the protostar in the low-velocity regimes. The blueshifted and redshifted peaks of the C¹⁸O central compact component are located in east and west of the protostar, respectively, and show a velocity gradient along the outflow axis. On the other hand, the peak of the CS central compact component is shifted from south to north of the protostar as the velocity changes from blueshifted to redshifted, showing a velocity gradient across the outflow axis. The different velocity gradients of the central compact components between the millimeter C¹⁸O and submillimeter CS emissions can be clearly shown in the SMA moment 1 maps of the C¹⁸O and CS emissions (Fig. 3.8).

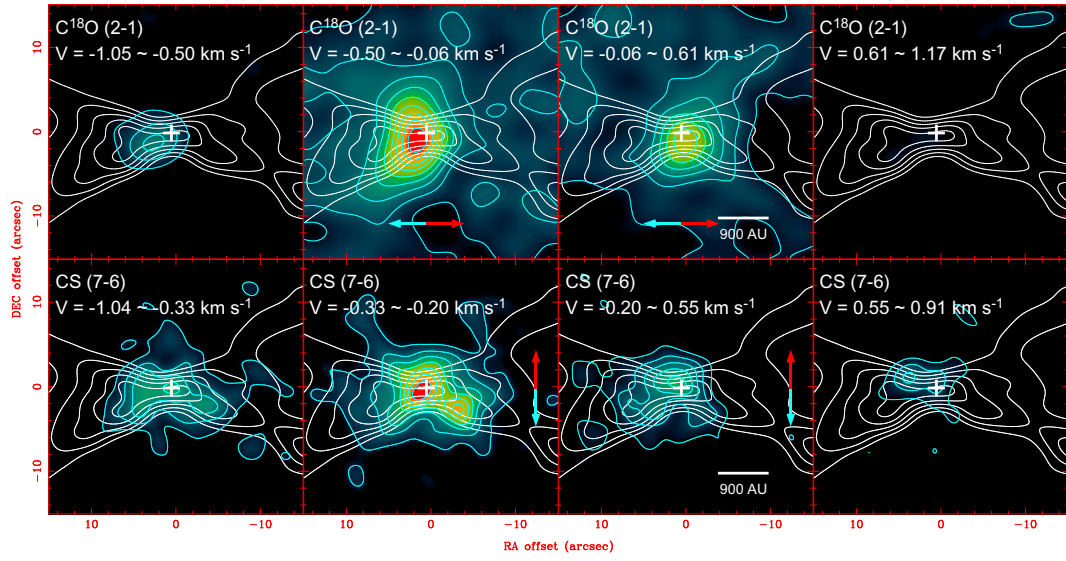


Figure 3.7 Moment 0 maps of the C^{18}O (2–1) (upper panels) and CS (7–6) (lower panels) emissions integrated in different velocity ranges (color scale and blue contours) overlaid on total integrated ^{12}CO (2–1) emission (white contours) taken by SMA (Chapter 2). The integrated velocity range of each map is shown in the upper side of each panel. White crosses show the protostellar position. Blue and Red arrows represent the velocity gradients of the central components traced by the millimeter C^{18}O and submillimeter CS emissions in the middle two panels. Contour levels are from 2σ in steps of 2σ . 1σ in the upper panels is 0.24 K km s^{-1} , and 1σ in the lower panels is $0.25, 0.30, 0.21$, and 0.21 K km s^{-1} in an order from left to right.

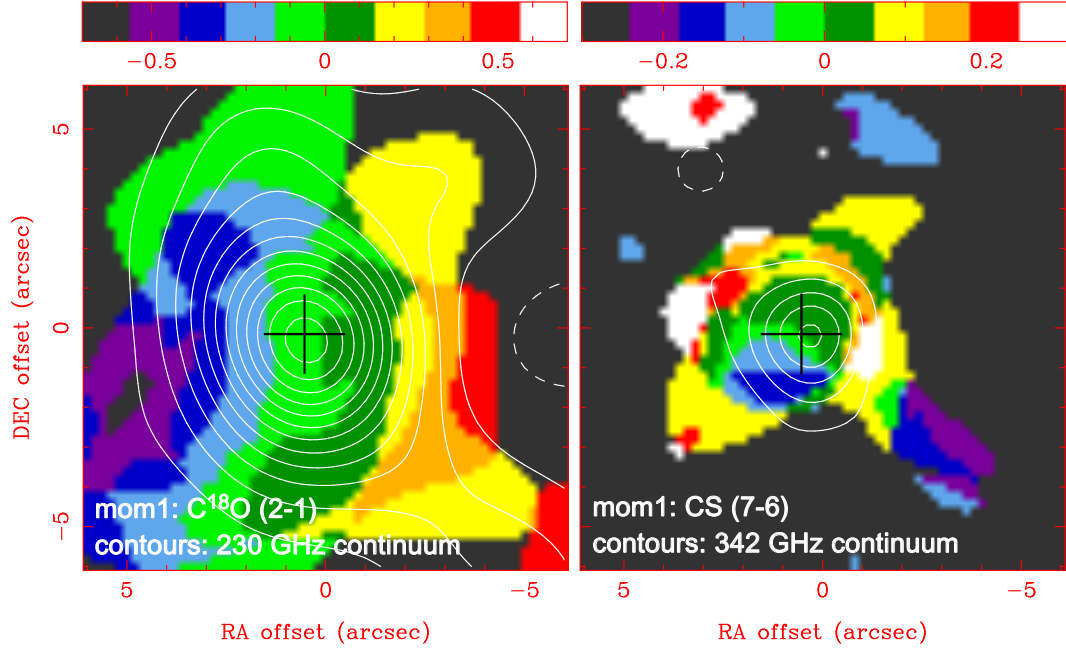


Figure 3.8 Moment 1 maps of the SMA C^{18}O (2–1) and CS (7–6) emissions overlaid on the SMA 230 and 342 GHz continuum emissions, respectively. The continuum emissions are plotted in white contours, and the moment 1 maps are shown in color scale. Crosses show the protostellar position. Note that these images are from the SMA data but not the combined data. Contour levels are from 3σ in steps of 4σ in the 230 GHz continuum map and from 3σ in steps of 3σ in the 342 GHz continuum map, where 1σ is 2 and 8 mJy Beam $^{-1}$, respectively. By fitting a 2-dimensional Gaussian to the continuum images, the deconvolved size, position angle, and the total flux of the 230 GHz continuum emission were estimated to be $4''.9 \times 2''.3$ (740 AU \times 350 AU), 13° , and 0.18 Jy, and of the 342 GHz continuum emission were estimated to be $1''.5 \times 0''.9$ (225 AU \times 135 AU), 3° , and 0.16 Jy.

Figure 3.9 shows the SMT and SMT + SMA position–velocity (P – V) diagrams of the C^{18}O emission in B335, passing through the central protostar along and across the outflow axis. The SMT P – V diagrams trace kinematics of the outer extended component ($r > 1500$ AU), while the combined P – V diagrams focus on the kinematics of the central compact component with a size of ~ 1500 AU. The velocity width of the central compact component ($\sim 1.5 \text{ km s}^{-1}$) is much broader than that of the extended component ($\sim 0.5 \text{ km s}^{-1}$). In the combined P – V diagram along the outflow axis, the central compact component exhibits a clear velocity gradient, and the C^{18}O emission in east and west of the protostar is blueshifted and redshifted, respectively. This velocity gradient corresponds to the velocity feature of the compact C^{18}O emission shown in Figure 3.7 and 3.8. On the other hand, the combined P – V diagram across the outflow axis does not show any clear velocity gradient, while the SMT P – V diagram across the outflow axis exhibits a slight velocity gradient, and the C^{18}O emission in the northern and southern parts is redshifted and blueshifted, respectively.

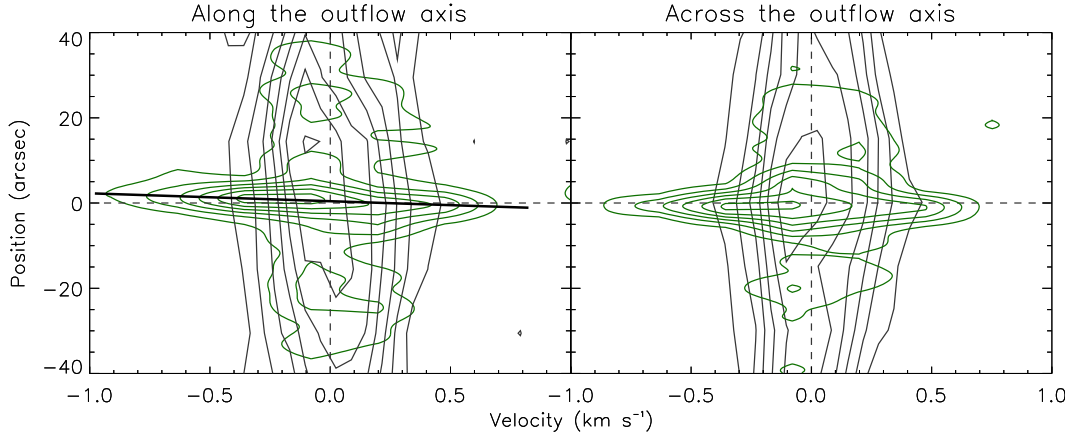


Figure 3.9 SMT and SMT + SMA P – V diagrams of the C^{18}O (2–1) emission along (P. A. = 90° ; left) and across (P. A. = 0° ; right) the outflow axis, passing through the protostellar position. The SMT and SMT + SMA data are plotted in black and green contours, respectively. A solid line shows the velocity gradient along the outflow axis. Contour levels are from 2σ in steps of 2σ , where 1σ is 0.63 K .

Figure 3.10 shows the combined P – V diagrams of the CS (7–6) emission along and across the outflow axis. It is clear that the spatial extent of the submillimeter CS emission is larger along the outflow direction (~ 1200 AU) than across the outflow direction (~ 700 AU). In the CS P – V diagram along the outflow axis, the redshifted

emission mainly arises from the eastern part of the protostar, while the blueshifted emission both from the eastern and western parts. Across the outflow direction, the CS P - V diagram shows a clear velocity gradient in a low-velocity region (-0.3 to 0.6 km s^{-1} ; shown by a solid line in Figure 3.10), but at higher velocities there is no clear velocity gradient. As shown in Figure 6 and 7 the high-velocity CS emission ($|V| > 0.5$ km s^{-1}) is elongated along the east-west direction while the low-velocity CS emission ($|V| < 0.5$ km s^{-1}) shows a compact component associated with the protostar, and the north-south velocity gradient in the compact CS component seen in Figure 3.7 and 3.8 corresponds to this velocity gradient in the P - V diagram. Hence, the CS emission probably originates from two different components with different kinematics. The trend of the velocity gradient across the outflow axis in the compact CS emission is same as that of the SMT C^{18}O emission, i.e., the northern part is redshifted and the southern part is blueshifted, but the amount of the velocity gradient is larger in the CS emission ($\sim 9.7 \times 10^{-4}$ $\text{km s}^{-1} \text{ AU}^{-1}$) than that of the extended C^{18}O emission ($\sim 8.3 \times 10^{-6}$ $\text{km s}^{-1} \text{ AU}^{-1}$).

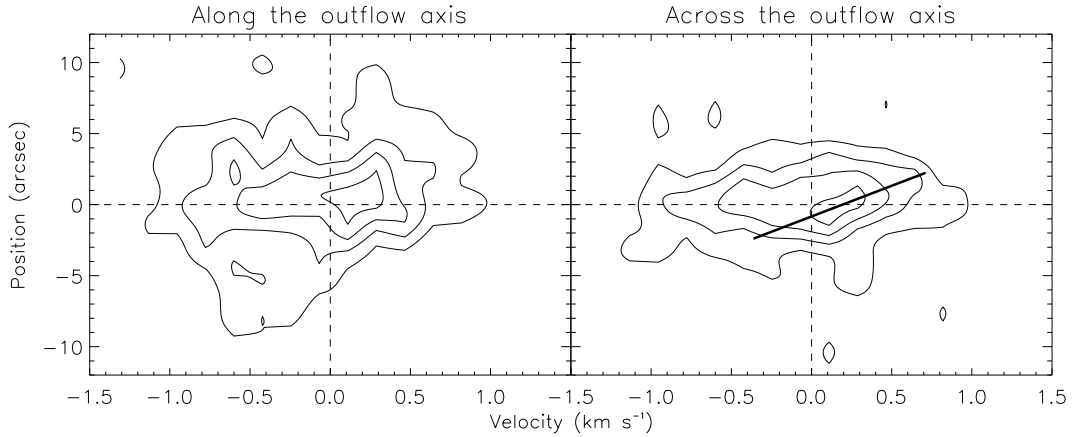
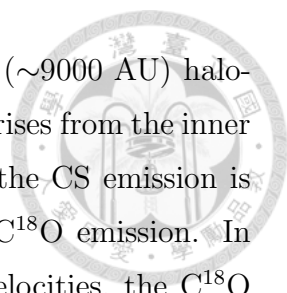


Figure 3.10 ASTE + SMA P - V diagrams of the CS (7-6) emission along (P. A. = 90° ; left) and across (P. A. = 0° ; right) the outflow axis, passing through the protostellar position. A solid line shows the velocity gradient across the outflow axis. Contour levels are from 2σ in steps of 2σ , where 1σ is 0.83 K.

3.5 LVG Analyses

Our combined Single-dish + SMA observations of B335 show that at low velocities ($|V| \lesssim 0.5$ km s^{-1}) the millimeter C^{18}O (2-1) emission shows a compact (~ 1500



AU) component associated with the protostar plus an extended (~ 9000 AU) halo-like component and the submillimeter CS (7–6) emission mainly arises from the inner region (< 1500 AU), while at high velocities ($|V| \gtrsim 0.5 \text{ km s}^{-1}$) the CS emission is east-west elongated and more extended (~ 2000 AU) than the C^{18}O emission. In the compact component associated with the protostar at low velocities, the C^{18}O emission is stronger than the CS emission, and exhibits an east (blueshifted) - west (redshifted) velocity gradient while the CS emission shows a north (redshifted) - south (blueshifted) velocity gradient. On the other hand, at high velocities the submillimeter CS emission is stronger than the millimeter C^{18}O emission. The difference of the relative intensity and the spatial extent between the millimeter and submillimeter emissions among these different velocity components is likely to reflect the physical conditions of these velocity components. In order to derive the physical conditions and to discuss the origin of these different components, we made statistical equilibrium calculations based on the large velocity gradient (LVG) model (Goldreich & Kwan 1974; Surdej 1977).

For our LVG calculations, values of the dipole moment and the rotational and centrifugal constants of the C^{18}O and CS molecules were taken from Winniewisser et al. (1979). The collisional coefficients of the C^{18}O molecule were taken from Flower (2001), on the assumption that the C^{18}O molecule has the same collisional coefficients as the CO molecule. The rotational energy levels up to $J = 28$ (2087 K) were included in our C^{18}O calculations. For the CS molecule, the collisional coefficients were taken from Green & Chapman (1978) and Turner et al. (1992), and the rotational energy levels up to $J = 20$ (447 K) were included. Since we only have one transition of each of the C^{18}O and CS molecules, the physical conditions and the molecular abundances cannot be derived simultaneously. Instead, we estimated typical values of the molecular abundances per unit velocity gradient ($\equiv \frac{X}{dV/dR}$), and adopted those $\frac{X}{dV/dR}$ values to estimate the gas density and temperature in the different velocity components. The molecular abundances per unit velocity gradient were estimated as follows. The FWHM line width of the ASTE CS line profile at the center was measured to be $\sim 1.5 \text{ km s}^{-1}$. In the combined moment 0 map of the CS emission, the size of the CS emitting region was estimated to be ~ 3000 AU (0.015 pc). Therefore, the dV and dR were set to be 1.5 km s^{-1} and 0.015 pc , respectively, and the velocity gradient was estimated to be $100.0 \text{ km s}^{-1} \text{ pc}^{-1}$. For

the C¹⁸O abundance we adopted $X(\text{C}^{18}\text{O}) = 2.5 \times 10^{-8}$, from Table 6 in Evans et al. (2005). This C¹⁸O abundance is the abundance with one order of magnitude depletion compared to the typical C¹⁸O abundance (3×10^{-7} ; Frerking et al. 1987), and in fact a similar amount of the C¹⁸O depletion in the inner region of B335 has been found with our SMA observation (Chapter 2). For the CS abundance we first adopted $X(\text{CS}) = 6 \times 10^{-9}$, again from Table 6 in Evans et al. (2005). Then, the $\frac{X}{dV/dR}$ values are $2.5 \times 10^{-10} \text{ km}^{-1} \text{ s pc}$ and $6 \times 10^{-11} \text{ km}^{-1} \text{ s pc}$ for the C¹⁸O and CS molecules, respectively. We found, however, that the observed peak brightness temperature of the C¹⁸O emission ($\sim 6.1 \text{ K}$) and that of the CS emission ($\sim 4.3 \text{ K}$) toward the center cannot be reproduced simultaneously with these $\frac{X}{dV/dR}$ values. Furthermore, in the outer region at radii from ~ 400 to $\sim 1500 \text{ AU}$ our LVG estimate of the gas kinetic temperature with these $\frac{X}{dV/dR}$ values provides a value lower than 10 K , which is unphysical, since the previous millimeter continuum study of the B335 envelope shows the temperature of 22 to 13 K at radii from ~ 400 to $\sim 1500 \text{ AU}$ (Harvey et al. 2003b). On the other hand, previous observations of B335 in the CS (5–4) emission have found CS depletion by a factor of ~ 10 (Wilner et al. 2000). Evans et al. (2005) have also suggested possible CS depletion by one order of magnitude in B335, based on the modeling of the single-dish line profiles of the CS (2–1, 3–2, & 5–4) emissions with the density and temperature profiles by Harvey et al. (2003b). A similar amount of CS depletion has also been seen toward the Class I protostar of L1551 IRS5 (Takakuwa et al. 2004). Therefore, we adopted the depleted CS abundance of 6×10^{-10} in our LVG analyses, and the adopted $\frac{X}{dV/dR}$ values are $2.5 \times 10^{-10} \text{ km}^{-1} \text{ s pc}$ and $6 \times 10^{-12} \text{ km}^{-1} \text{ s pc}$ for the C¹⁸O and CS molecules, respectively.

To directly compare the millimeter C¹⁸O and submillimeter CS emissions and to derive the physical conditions based on our LVG calculations, the CS image cube was resampled along the velocity axis to match the velocity channels with those of the C¹⁸O image cube, and was convolved with the combined SMT + SMA beam of the C¹⁸O data. Then, both the C¹⁸O and CS image cubes were integrated over the high-velocity ($V = -1.05$ to -0.22 & 0.34 to 0.89 km s^{-1}) and low-velocity ($V = -0.22$ to 0.34 km s^{-1}) ranges, and the image pixels were binned to have a pixel size of $4''8$, comparable to the beam size in the C¹⁸O image cube. Figure 3.11 compares the C¹⁸O and CS brightness temperatures from the resampled image cubes

at the high- (open squares) and low-velocity (open diamonds) ranges. Only the data points with the detected ($\geq 2\sigma$) CS emission are plotted, and for the data points without detectable C¹⁸O counterparts, the 2σ upper limits of the C¹⁸O emission are plotted. The high-velocity data points are mainly located at the left-hand side without detectable C¹⁸O emission since in the high-velocity range the CS emission is more extended and stronger than the C¹⁸O emission (Fig. 3.7), while the low-velocity data points are located in right and top-right corners with respect to the high-velocity data points. Solid and dashed curves in Figure 3.11 show iso-thermal and iso-density contours calculated from our LVG model, respectively. It is clear that in the low-velocity range the temperature is lower than that in the high-velocity range but the density is higher, while in the high-velocity range the temperature is higher. The temperature and density for the low-velocity data points range from 10 to 30 K and from 2×10^6 to 2×10^7 cm⁻³, respectively. The temperature and density for the high-velocity data points are >40 K and $\sim 7 \times 10^5$ to 2×10^6 cm⁻³, respectively, except for one data point with the intense C¹⁸O emission. This data point is originated from the region around the protostar, which suggests that the physical conditions and hence the origins of the central and surrounding east-west elongated CS components are different.

Based on the LVG results shown in Figure 3.11, we made temperature and density maps in the CS emitting region of B335 (Fig. 3.12). As well as the overall difference of the temperature and density between the high- and low-velocity ranges as already shown in Figure 3.11, the spatial distributions of the temperature and density are evident. In the temperature map at the high velocity, it is clear that toward the east-west elongated CS component the temperature is a factor of two higher than that toward the central component. On the other hand, at the low velocity the density monotonically increases by one order of magnitude over the ~ 1500 AU radius toward the central protostellar point. These spatial trends of the temperature and density distributions are also seen in the low-velocity and high-velocity ranges, respectively, while the absolute values are different. The higher temperature (>40 K), higher velocity, and the elongation along the outflow direction in the east-west elongated CS component suggest that the CS component most likely traces the associated outflow. On the other hand, the central dense component seen in both the C¹⁸O and CS emissions probably traces the inner protostellar envelope. In the low velocity

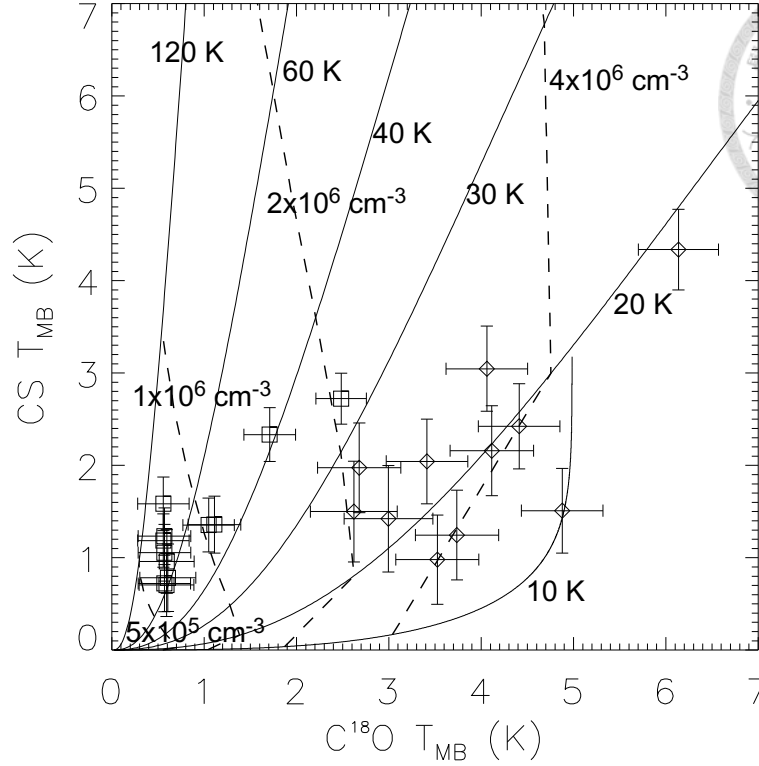


Figure 3.11 Results of our LVG calculations. All the data are taken from the CS emitting region. We integrated the $C^{18}O$ and CS emissions into two velocity ranges, higher velocity ($V = -1.05 - -0.22$ & $0.34 - 0.89$ km s^{-1}) and lower velocity ($V = -0.22 - 0.34$ km s^{-1}). Open Squares are the higher velocity data, and open diamonds are the lower velocity data. Solid and dash lines are iso-temperature and iso-density lines, respectively. Error bars represent a noise level of 1σ . In the CS emitting region, if the $C^{18}O$ emission is not detected ($< 2\sigma$), the intensity of the $C^{18}O$ emission is assigned to be 2σ .

range and at the outer radius larger than ~ 1500 AU, where only the $C^{18}O$ emission was detected, we adopted the 2σ upper limits of the CS emission and estimated the upper limits of the temperature and the density to be ~ 17 K and $\sim 2.3 \times 10^6 \text{ cm}^{-3}$, respectively. In summary, with the millimeter $C^{18}O$ (2–1) and submillimeter CS (7–6) emissions, we found three regions with different physical conditions in B335; the outer envelope with a low temperature and a low density ($T < 17$ K and $n < 2.3 \times 10^6 \text{ cm}^{-3}$), the outflow with a high temperature but a low density ($T = 40$ to 87 K and $n = 0.7$ to $1.6 \times 10^6 \text{ cm}^{-3}$), and the inner envelope with a high density but a low temperature ($T = 10$ to 28 K and $n = 2.3$ to $17 \times 10^6 \text{ cm}^{-3}$).

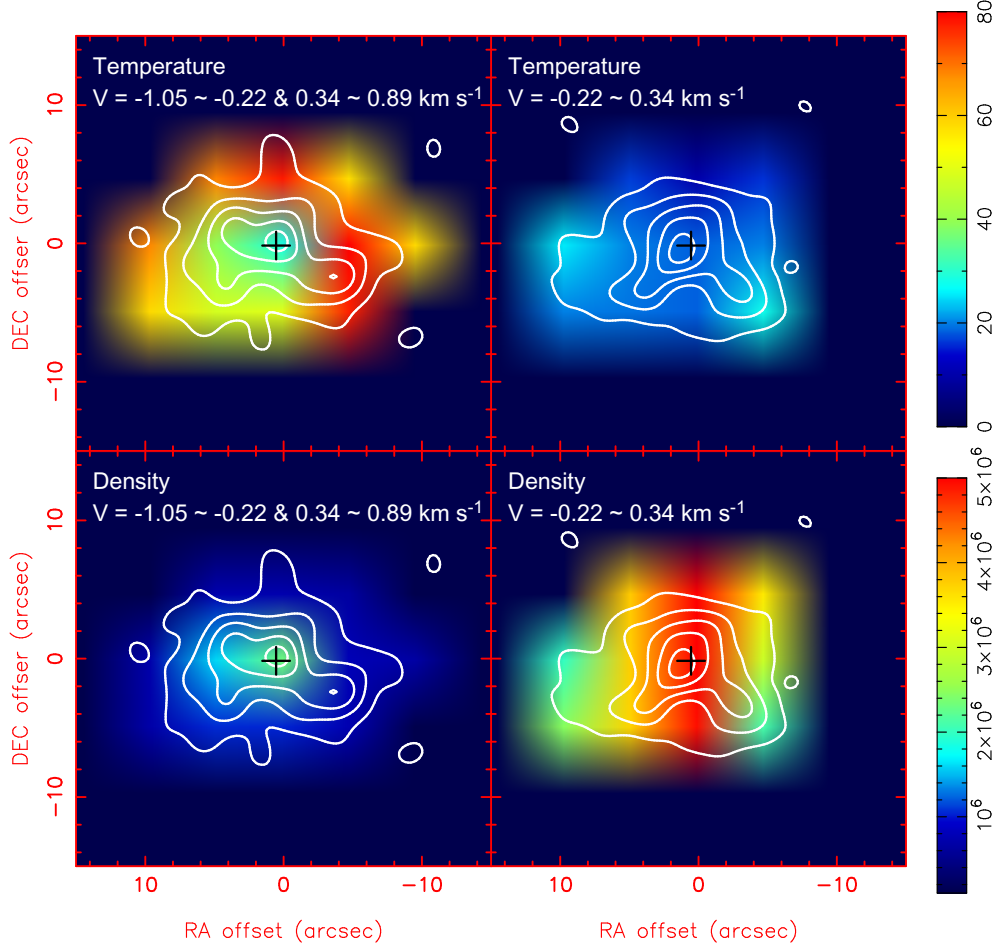


Figure 3.12 Temperature (upper panels) and density (lower panels) maps of the CS emitting region at higher (left panels) and lower (right panels) velocities in color scale, which are based on our LVG calculations shown in Figure 3.11. White contours are the integrated CS emission. The integrated velocity ranges are shown in the upper side of each panel. Crosses represent the protostellar position. Contour levels are from 2σ in steps of 2σ , where 1σ is 0.38 K km s^{-1} in the higher velocity range and 0.24 K km s^{-1} in the lower velocity range.

Table 3.2. Physical Conditions of the Outflow and the Inner Envelope

At the High Velocity	Outer Envelope	Inner Envelope	Outflow
Kinetic Temperature (K)	...	28	40 – 87
Density (10^6 cm^{-3})	...	2.3	0.7 – 1.6
C ¹⁸ O optical depth	...	0.15	0.01 – 0.06
CS optical depth	...	0.4	0.09 – 0.32
C ¹⁸ O excitation temperature (K)	...	27	37 – 83
CS excitation temperature (K)	...	14	15 – 17

At the Low Velocity	Outer Envelope	Inner Envelope	Outflow
Kinetic Temperature (K)	<17	10 – 20	16 – 28
Density (10^6 cm^{-3})	<2.3	3.7 – 17.2	2.0 – 3.5
C ¹⁸ O optical depth	>0.37	0.39 – 4.05	0.15 – 0.71
CS optical depth	<0.14	0.32 – 1.06	0.25 – 0.40
C ¹⁸ O excitation temperature (K)	<16	10 – 19	15 – 26
CS excitation temperature (K)	<10	9 – 14	10 – 13

Note. — These estimated values are based on the velocity gradient of $100 \text{ km s}^{-1} \text{ pc}^{-1}$, the C¹⁸O abundance of 3×10^{-7} , and the CS abundance of 6×10^{-9} . The results of our LVG calculations are dependent on the value of molecular abundance per unit velocity gradient, and there could be fluctuation in the molecular abundances and velocity gradient. Therefore, the estimated values of physical conditions should not be considered as absolute values. However, the qualitative results, showing that the outer and inner envelope and the outflow have different properties of physical conditions, would not be effected by the value of molecular abundance per unit velocity gradient. Note that due to the projection effect both high- and low-velocity emissions could be detected in the low-velocity range. Hence, in the lower-velocity range, the estimated temperature and density could be considered as a lower limit and an upper limit, respectively.

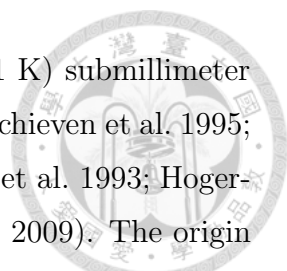
In addition to the temperature and the density, the optical depths and the excitation temperatures of the CS and C¹⁸O emissions were also estimated. In the high-velocity range, both the submillimeter CS (7–6) and the millimeter C¹⁸O (2–1) emissions are optically thin ($\tau_{CS} < 0.06$ and $\tau_{C^{18}O} < 0.15$). In the low-velocity range, both the CS and C¹⁸O emissions are optically thick at the center and optically thin in the surrounding region. In both velocity ranges, the CS emission is sub-thermalized and has an excitation temperature of ~ 10 to 20 K, while the C¹⁸O emission is thermalized. The estimated physical conditions of the outflow and the envelope, and the excitation conditions of the molecular emissions, are summarized in Table 3.2.

3.6 Discussion

3.6.1 Physical Conditions of the Outflow and Envelope

Our combined single-dish + interferometric observations of B335 in the millimeter and submillimeter molecular lines have clearly separated the outflow and the inner and outer envelope components. The estimated gas density and temperature in the envelope components range from $<2.3 \times 10^6 \text{ cm}^{-3}$ to $1.7 \times 10^7 \text{ cm}^{-3}$ and $<17 \text{ K}$ to 28 K , respectively, at the radius from $>1500 \text{ AU}$ to $\sim 400 \text{ AU}$. The estimated range of the gas temperature is approximately consistent with that from the previous millimeter continuum study of the B335 envelope (13 K to 22 K at the radius from $\sim 1500 \text{ AU}$ to $\sim 400 \text{ AU}$; Harvey et al. 2003a,b). Moriarty-Schieven et al. (1995) have made a single-dish survey for a complete flux-limited IRAS sample of protostellar sources in Taurus in the CS ($J = 3-2$, $5-4$, & $7-6$) and H_2CO ($J_{K-1K+1} = 3_{03}-2_{02}$, & $3_{22}-2_{21}$) emissions with the beam size of $\sim 20''$ to $\sim 40''$ (1400 to 2800 AU in radius), and have performed LVG analyses. They have found that the typical temperature and the density of the surrounding protostellar envelopes are 20 to 50 K and a few $\times 10^6 \text{ cm}^{-3}$, approximately consistent with our high-resolution estimate of the envelope physical condition around B335. Moreover, the estimated temperature and density distributions in the protostellar envelope around B335 are also consistent with those derived from an one-dimensional radiative hydrodynamic model of an $1 M_{\odot}$ star-forming dense core by Masunaga & Inutsuka (2000).

The estimated gas density and temperature in the outflow component range from $7.0 \times 10^5 \text{ cm}^{-3}$ to $1.6 \times 10^6 \text{ cm}^{-3}$ and 40 K to 87 K , respectively. The critical density of the submillimeter CS ($7-6$) emission is $\sim 2 \times 10^7 \text{ cm}^{-3}$, much higher than the estimated density in the outflow component on \gtrsim one thousand AU scale. In fact, the excitation temperature of the CS ($7-6$) emission in the outflow component is at most $\lesssim 17 \text{ K}$, much lower than the estimated gas kinetic temperature, and hence the submillimeter CS emission is sub-thermalized. On the other hand, the upper-state rotational energy of the submillimeter CS emission ($\equiv E_{J=7}$) is 66 K , comparable to or lower than the estimated gas temperature in the outflow component. These results suggest that the presence of the submillimeter CS emission on \gtrsim one thousand AU scale toward B335 is not due to the presence of the extended high-density gas but due to the presence of the extended high-temperature gas. Previous single-dish

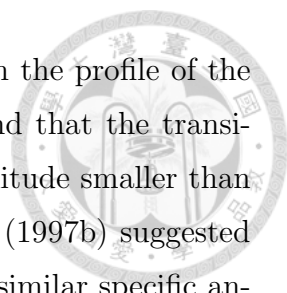


surveys for low-mass protostellar sources have found intense (>1 K) submillimeter molecular emissions such as the CS (7–6), HCN (4–3) (Moriarty-Schieven et al. 1995; Takakuwa et al. 2007b) and CO (7–6 & 6–5) emissions (Schuster et al. 1993; Hogerheijde et al. 1998; van Kempen et al. 2006, 2009; Shinnaga et al. 2009). The origin of the submillimeter molecular-line emissions with an extent of the single-dish beam size (1000 to 3000 AU) has been unclear, and mainly three mechanisms have been proposed to explain the presence of the extended submillimeter molecular emissions toward low-mass protostellar sources; shock heating associated with outflows, heating by ultraviolet (UV) photons from the boundary layer between a protostar and its surrounding disk, and heating by protostellar luminosities (Schuster et al. 1993; Spaans et al. 1995; van Kempen et al. 2009). Our combined single-dish and interferometric observations of the submillimeter CS emission toward B335 have first resolved the distribution of the warm gas component and the thermal structure, and it is possible to distinguish these three mechanisms observationally. The latter two proposed mechanisms predict higher temperatures toward the innermost part of the envelope, inconsistent with our higher-resolution observational results in B335 from 400 to $\gtrsim 1000$ AU scales. We consider that the origin of the $\gtrsim 1000$ AU-scale submillimeter molecular emissions toward low-mass protostellar sources is related to the associated outflows, and that the extended submillimeter molecular emissions trace the shock heating due to the interaction with the surrounding envelope component.

3.6.2 Rotation, Infall, and the Evolution of Protostellar Envelopes Traced by the Millimeter and Submillimeter Line Emissions

The central compact component seen in the millimeter C¹⁸O (2–1) emission traces the envelope with a size of ~ 1500 AU around the protostar and exhibits a velocity gradient along the outflow axis, which has been interpreted as an infalling motion in the envelope (Chapter 2). On the other hand, the central compact component seen in the submillimeter CS (7–6) emission with a size of ~ 900 AU shows a velocity gradient perpendicular to the outflow axis, which is not seen in the compact C¹⁸O (2–1) emission. The sense of this velocity gradient is consistent with that of the envelope rotation at outer radii (Saito et al. 1999), and hence the velocity gradient seen in the submillimeter CS emission most likely traces the rotation in the inner envelope. As a rotational radius, we adopted the semi-major radius of the SMA 342 GHz continuum emission (Fig. 3.8) derived from the two-dimensional Gaussian fitting (~ 110 AU), and the rotational velocity and the specific angular momentum at a radius of 110 AU were estimated to be 0.11 km s^{-1} and $5.8 \times 10^{-5} \text{ km s}^{-1} \text{ pc}$, respectively. The reason for the detection of the rotational motion in the compact submillimeter CS emission and for the absence in the millimeter C¹⁸O emission is likely to be that the rotational velocity increases toward the center since the angular momentum is conserved during dynamical infall, and that the submillimeter CS (7–6) emission traces the inner part of the envelope than the millimeter C¹⁸O emission due to the difference of the excitation conditions.

In Chapter 2, we have shown that the specific angular momentum in B335 decreases from radii of 20000 to 370 AU. With the new measurement of the envelope rotation at a radius of 110 AU traced by the submillimeter CS (7–6) emission, we plot the profile of the specific angular momentum of the envelope rotation in B335 (Fig. 3.13). At a radius larger than 370 AU, the specific angular momentum keeps decreasing toward the center, and at a radius smaller than 370 AU, the specific angular momentum is likely conserved. The two zones of the distribution of the specific angular momentum, a power-law distribution in the outer region and a constant angular momentum in the inner region, have been suggested by Ohashi et al. (1997b) with the observational results of a sample of protostellar sources, and Ohashi et al.



(1997b) estimated the transitional radius to be ~ 6000 AU. With the profile of the specific angular momentum in one single source, B335, we found that the transitional radius is ~ 370 AU, which is more than one order of magnitude smaller than that proposed by Ohashi et al. (1997b). Besides, Ohashi et al. (1997b) suggested that infalling envelopes and rotationally supported disks have a similar specific angular momentum of $\sim 10^{-3} \text{ km s}^{-1} \text{ pc}$, while the specific angular momentum at a radius of 110 AU in B335 is one order of magnitude lower than that suggested by Ohashi et al. (1997b). The different sizes of the transitional radius and values of the specific angular momenta between B335 and the other protostellar sources could be due to an evolutionary effect. In Figure 3.13, we plot specific angular momenta of protostellar sources from Class II to 0 as a function of radius. The values of specific angular momenta of different protostellar sources spread over two order of magnitude, and more evolved sources tend to have higher specific angular momenta than less evolved sources, as already reported in Chapter 2. Moreover, in the case of L1551 IRS 5, a Class I, more evolved source than B335, the envelope rotation at radii between 300 and 1000 AU shows a conserved angular momentum (Momose et al. 1998), and the region with the conserved angular momentum in L1551 IRS 5 is more extended than in B335.

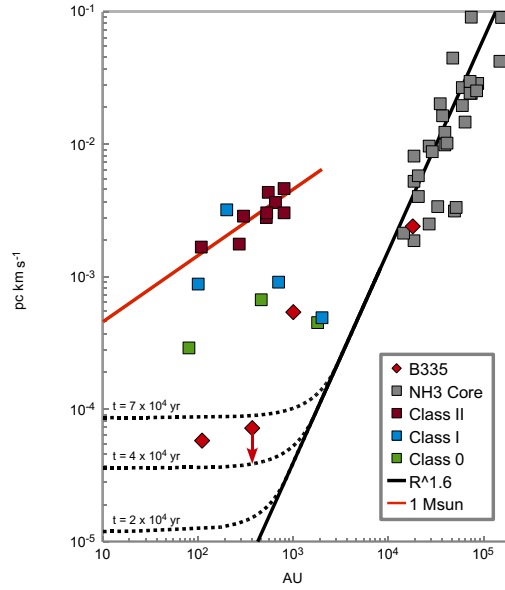


Figure 3.13 Specific angular momentum of rotation plotted as a function of radius. Red diamonds show the measurement of the envelope rotation in B335 (This Chapter; Chapter 2; Saito et al. 1999), and a red arrow show the upper limit of the specific angular momentum of the envelope rotation at a radius of 370 AU in B335 (Chapter 2). Gray squares and a black solid line represent specific angular momenta of rotation in NH₃ cores and the power-law relation between the core sizes and the specific angular momenta, respectively (Goodman et al. 1993). Green, blue, and dark red squares show specific angular momenta of disk or envelope rotation in Class 0, I and II sources, respectively (Simon et al. 2000; Ohashi et al. 1997a; Momose et al. 1998; Lommen et al. 2008; Lee et al. 2006, 2009; Chen et al. 2007). Black dash lines show the expected quantitative evolution of the profiles of specific angular momenta of infalling and rotating envelopes at $t = 2, 4, 7 \times 10^4$ years after the beginning of collapse, and a red line represents the profile of specific angular momenta of a Keplerian disk around a $1 M_{\odot}$ protostar.

In Figure 3.13, we also present the expected evolution of the distribution of the specific angular momenta in protostellar envelopes (black dashed curves), based on the scenario of the inside-out collapse and the assumption that the initial profile of the specific angular momenta (j) in protostellar envelopes follows $j \propto r^{1.6}$ (Shu 1977; Goodman et al. 1993). To obtain the profiles of the specific angular momenta at different time, we calculated the radial position of the infalling material on the equator plane of an isothermal spherical envelope with time evolution, where we assume that the angular momenta of the infalling material are conserved during collapse. The initial density (ρ) profile of the spherical envelope is set to be

$$\rho = \frac{C_s}{2\pi G} r_{\text{rad}}^{-2}, \quad (3.2)$$

where r_{rad} is the radius, C_s is the sound speed, and G is the gravitational constant (Shu 1977). The sound speed is adopted to be 0.2 km s^{-1} as in the case of isothermal envelopes at $\sim 10 \text{ K}$. Note that in reality protostellar envelopes are not isothermal as we discussed in section 4. The gravitational and rotational energy (E_{gra} & E_{rot}) of the material in the envelope are described as,

$$E_{\text{gra}} = \frac{GM}{r_{\text{rad}}}, \quad (3.3)$$

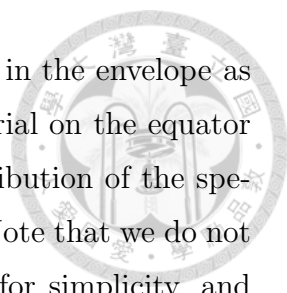
$$E_{\text{rot}} = \frac{j^2}{2r_{\text{rot}}^2}, \quad (3.4)$$

where r_{rot} and M are the rotational radius of the material and the enclosed mass within r_{rad} in the envelope, respectively. The profile of the specific angular momenta is described as,

$$j = 6.1 \times 10^{22} \cdot r_{\text{rot}}^{1.6} \text{ cm}^2 \text{ s}^{-1}, \quad (3.5)$$

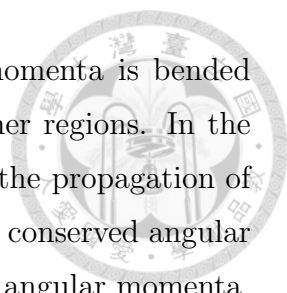
and the rotational radius (r_{rot}) is equivalent to the radius (r_{rad}) if the material is on the equator plane (Goodman et al. 1993). For the material that is located at a radius of 1000 AU on the equator plane in the envelope initially, when the material starts to fall in, its gravitational energy is more than one order magnitude larger than the rotational energy unless the material reaches a radius of 10 AU. Therefore, for simplicity, the collapse of the envelope is assumed to follow free fall, and the motion of the infalling material can be described as,

$$\ddot{r}_{\text{rad}} = -\frac{GM}{r_{\text{rad}}^2}, \quad (3.6)$$



Then we calculated the radial position of each infalling material in the envelope as a function of time. Based on the position of each infalling material on the equator plane and its specific angular momentum, we obtained the distribution of the specific angular momenta in the infalling envelope at a given time. Note that we do not include centrifugal force and pressure gradient in the envelope for simplicity, and that the distribution of the specific angular momenta on the equator plane is only dependent on r_{rad} and not affected by the material outside the equator plane. Although our calculation is not strictly physical, the qualitative trend of the evolution of the profile of the specific angular momenta is still applicable. Inclusion of the centrifugal force and/or pressure gradient in the envelope should make the profile shallower, although the exact calculation must be much more complicated. Besides, we did not calculate the distribution of the specific angular momenta within a radius of 10 AU in the envelope, and the infalling motion is terminated artificially once the material passes $r_{\text{rad}} = 10$ AU. In the calculation, the material was set to fall after the passage of the expansion wave, and we stopped the calculation at $t = 7.2 \times 10^4$ years after the beginning of the collapse. The expansion wave reaches at a radius of ~ 3000 AU at this moment.

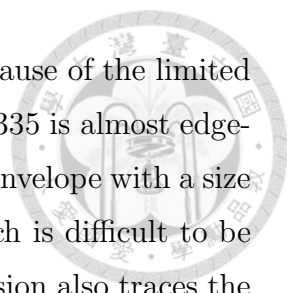
Three black dashed curves in Figure 3.13 represent the profiles of the specific angular momenta on the equator plane of the envelope at $t = 2, 4, 7 \times 10^4$ years after the beginning of collapse in the sequence from bottom to top. The specific angular momenta of the inner envelopes with the constant value increases with evolution (from bottom to top), and there are three zones of the distribution of the specific angular momenta; a power-law relation in an outer region with a radius of thousands of AU, a constant value in an inner region with a radius of hundreds of AU, and a curve in between. The outer region, where the expansion wave has not yet reached and material is still steady, remains its initial condition, and the specific angular momenta of protostellar envelopes show the power-law relation found by Goodman et al. (1993). After the passage of the expansion wave, the material starts to fall and accelerate toward the center of the protostellar envelope, and the profile of the specific angular momenta is shifted away from the initial power-law relation. This is the first transition in the distribution of the specific angular momenta, representing the location of the expansion wave. At the beginning of the infalling motion the infalling velocity is still subsonic, while the expansion wave propagates at sound



speed (Shu 1977). Hence, the profile of the specific angular momenta is bended toward the center and shows a curve between the outer and inner regions. In the inner region, the infalling velocity is supersonic and faster than the propagation of the expansion wave, and this supersonic infalling motion with the conserved angular momenta results in a horizontal line in the profile of the specific angular momenta. This is the second transition of the distribution of the specific angular momenta, representing the transitional radius we discussed above. In this scenario, the infalling radius is larger than the second transitional radius. In B335, the signature of the infalling motion in the envelope has been found at a radius of ~ 1000 AU, while the profile of the specific angular momentum shows constant at a radius less than 370 AU. The transitional radius smaller than the infalling radius in B335 is consistent with our expected evolutionary scenario, and the transitional radius and the specific angular momentum in the inner envelope around B335 could grow and reach the values suggested by Ohashi et al. (1997b) with evolution.

Eventually in the innermost region the rotational motion starts to dominate over the infalling motion and a Keplerian disk is expected to be formed. The sizes of Keplerian disks could grow from less than $\lesssim 10$ to hundreds of AU when protostellar sources evolve from Class 0 to II stages, as discussed in Chapter 2. The profile of the specific angular momenta within Keplerian disks is expected to follow an $r^{1.5}$ dependence as indeed observed in Class II sources with similar protostellar masses (red line in Figure 3.13), and the profile of a constant specific angular momentum in an infalling envelope eventually evolves to the Keplerian profile (from black dashed curves to the red line in Figure 3.13). The transition from the infalling motion with the conserved angular momenta to the Keplerian rotation is, however, still not well understood.

In the compact submillimeter CS emission, there is no clear velocity gradient along the outflow axis, suggesting that there is no detectable infalling motion on a 300 AU scale. The submillimeter CS emission is expected to trace the inner part of the envelope than the millimeter C^{18}O (2–1) emission, where both the infalling and rotational velocities are higher, whereas the CS (7–6) emission does not show any clear signature of the infalling motion in the envelope. There are two possible interpretations of the absence of the infalling signature in the CS emission. The first possibility is that the velocity structure of the infalling motion in the innermost part



of the envelope could not be resolved by our CS observations because of the limited spatial resolution. The orientation of the flattened envelope in B335 is almost edge-on (Hirano et al. 1988), and the projected extent of the flattened envelope with a size of a few hundred AU is less than $1''$ along the outflow axis, which is difficult to be resolved with our spatial resolution of $\sim 3''$. Besides, the CS emission also traces the outflow with a size of ~ 3000 AU. Since the outflow in B335 is almost on the plane of the sky and shows a conical shape with an opening angle larger than 45° (Hirano et al. 1988; Chapter 2), both the blueshifted and redshifted outflows appear in both east and west of the protostar. Therefore, the contamination of the outflow in the CS emission could distort the signature of the infalling motion in the envelope. The infall velocity was estimated to be 0.44 km s^{-1} at a radius of 370 AU (Chapter 2). On the assumption of free-fall motion, the infall velocity is expected to be 0.76 km s^{-1} at a radius of 110 AU, and the expected infall velocity is consistent with the half velocity width of the CS emission ($\sim 1.0 \text{ km s}^{-1}$; Figure 3.10). However, the velocity spread of the CS emission may be due to the outflow whose velocity is expected to be 0.9 km s^{-1} based on the Hubble-like velocity structure found in Chapter 2.

The other possible interpretation is that the infalling motion indeed ceases on a 300 AU scale, and that the gas motion in the envelope is in the transition from the infalling to rotational motions. The rotational centrifugal force on a 300 AU scale, however, cannot support the envelope against the gravitational force by the central protostar of $0.04 M_\odot$ (Chapter 2). In B335 the rotational velocity of the infalling material is expected to reach the Keplerian velocity at a radius of only ~ 4 AU. If the infalling motion in the envelope does cease on a few hundred AU scale in B335, there should be other mechanisms to support the infalling material, such as magnetic field and/or thermal pressure gradient produced by the vertical collapse along the field lines (Mellon & Li 2008).

3.7 Summary

We have performed detailed imaging and analyses of the combined (SMA + single-dish) data of B335 in the millimeter C^{18}O (2–1) and submillimeter CS (7–6) emissions.

1. The C^{18}O emission traces both extended and central compact envelopes with sizes of ~ 9000 AU and ~ 1500 AU, respectively. The CS emission shows a central compact envelope with a radius of ~ 400 AU surrounded by an east-west elongated outflow with a size of ~ 3000 AU, and at $|V| \gtrsim 0.5 \text{ km s}^{-1}$ the CS emission is stronger and more extended than the C^{18}O emission. The C^{18}O and CS inner envelopes exhibit east-west and north-south velocity gradients, respectively. With the millimeter C^{18}O (2–1) and submillimeter CS (7–6) emissions, we detected three regions with different physical conditions in B335, the outer envelope with a low temperature and a density ($T < 17 \text{ K}$ and $n < 2.3 \times 10^6 \text{ cm}^{-3}$), the outflow with a high temperature but a low density ($T = 40$ to 87 K and $n = 0.7$ to $1.6 \times 10^6 \text{ cm}^{-3}$), and the inner envelope with a high density and a low temperature ($T = 10$ to 28 K and $n = 2.3$ to $17 \times 10^6 \text{ cm}^{-3}$).
2. The density and temperature of the inner envelope are consistent with those estimated in the 1.3 mm continuum observations and the one-dimensional radiative hydrodynamic model of an $1 M_{\odot}$ star-forming dense core, and the high temperature of the outflow with a size of 3000 AU could be due to shocks in the outflow but not be caused by protostellar luminosities or the UV photon photons from the boundary layer between a protostar and its disk. In B335, the C^{18}O (2–1) emission is thermalized, and the CS (7–6) emission is sub-thermalized. On the other hand, the C^{18}O (2–1) and CS (7–6) emissions are optically thin at velocities higher than $\sim 0.3 \text{ km s}^{-1}$, while at velocities lower than $\sim 0.3 \text{ km s}^{-1}$ both the emissions are optically thick around the center and optically thin in the surrounding region.
3. In B335, the C^{18}O emission traces the infalling motion in the envelope, but no signature of the envelope rotation is seen in the C^{18}O emission. In contrast, the CS emission shows the envelope rotation but no signature of the infalling motion, and the rotational velocity and the specific angular momentum were estimated to be 0.11 km s^{-1} and $5.8 \times 10^{-5} \text{ km s}^{-1} \text{ pc}$ at a radius of 110 AU. The different kinematics between the millimeter C^{18}O and submillimeter CS emissions is most likely due to different physical conditions traced by these emissions, and the CS emission could trace the inner part of the envelope where

the rotational rotation is higher. No infall signature seen in the CS emission is likely due to the insufficient resolution to resolve the velocity structure in the inner envelope along the outflow axis. The other possible interpretation is that the infalling motion ceases on a few hundred AU scale in B335. However, the infalling material can not be supported by the centrifugal force on this scale, and the Keplerian radius was estimated to be ~ 4 AU. If it is the case, other mechanisms should be included to explain no infall signature seen in the CS emission.

4. We revealed the profile of specific angular momenta of envelope rotation in one single source, B335, from radii of $\sim 10^4$ – 10^2 AU. The specific angular momentum in B335 decreases from radii of 10000 to 370 AU and becomes conserved within 370 AU. The transitional radius and the value of the specific angular momentum in the region with the conserved angular momentum are more than one order of magnitude smaller than those suggested by Ohashi et al. (1997b), and that could be due to an evolutionary effect. Based on the scenario of the inside-out collapse and the assumption of that the initial profile of the specific angular momenta (j) of protostellar envelopes is $j \propto r^{1.6}$, we expected that the transitional radius and the specific angular momentum of the inner envelope increase as the expansion wave propagate outwardly and the infalling radius is larger than the transitional radius, and observationally more evolved sources tend to have higher angular momenta and larger transitional radii.

3.8 Appendix

Combining SMA and Single-dish Data and Imaging Simulation of the Combing Process

We followed the combing process described by Takakuwa et al. (2003), which is based on the description of combining single-dish and interferometric data by Vogel et al. (1984) and the MIRIAD scripts developed by Wilner & Welch (1994). First, we resampled the single-dish data cube along the velocity axis to match the velocity channels of the SMA data. Then we deconvolved the single-dish images by the

single-dish beams and multiplied the deconvolved single-dish images by the response function of the SMA primary beams, which are approximately to be Gaussian. With these deconvolved and primary beam decorrelated images, we generated single-dish visibility data by the Miriad tasks, *uvrandom* and *uvmodel*. Next, the single-dish and SMA visibility data are Fourier-transformed simultaneously by the Miriad task, *invert*, to make combined images.

In order to test the feasibility and the limitation of the combining process described above, we performed simple noise-free imaging simulations and compared an original model image with its final image after the combining process. We generated an image of a single power-law intensity distribution, $I(r) \propto r^{-1}$, which represents as the intensity distribution of an isothermal and optically thin sphere with a density profile of r^{-2} . We set the outer radius of the intensity distribution to be 15000 AU and did not include any velocity structure in the model. The image pixel size and the pixel number of the model image are set to be $0''.2 \times 0''.2$ and 2048×2048 , respectively. We adopted two virtual single-dish telescopes with the dish sizes of 10 and 30 meters and the observing frequency of 219.560357 GHz. The beam sizes of the virtual 10-m and 30-m telescopes are $33''.8$ and $11''.3$, respectively. The virtual 10-m single-dish telescope corresponds to SMT, and the simulation with the virtual 10-m telescope represents our real imaging. First, we convolved this model image with the single-dish beams and resampled the convolved model images onto the Nyquist grids ($15''$ for the 10-m telescope and $5''$ for the 30-m telescope) over our SMT mapping region that is $13500 \text{ AU} \times 18000 \text{ AU}$. After we produced the model single-dish images, we followed the same process described in the last paragraph to create model single-dish visibility data. Next, we multiplied the original model image by the response function of the SMA primary beams and generated model SMA visibility data with the $u-v$ sampling of our SMA observation at 230 GHz. In Figure 3.14, we plot amplitude v.s. $u-v$ distance of our model visibility data. The amplitude of the model 10-m single-dish data is below that of the model SMA data in an $u-v$ distance range of $5 - 6 \text{ k}\lambda$. On the other hand, the amplitude of the model 30-m single-dish data well matches that of the model SMA data in an $u-v$ distance range of $5 - 8 \text{ k}\lambda$, but becomes lower than that of the model SMA data at the longer $u-v$ distances.

To derive the correct solution of the amplitude as a function of the $u-v$ distance

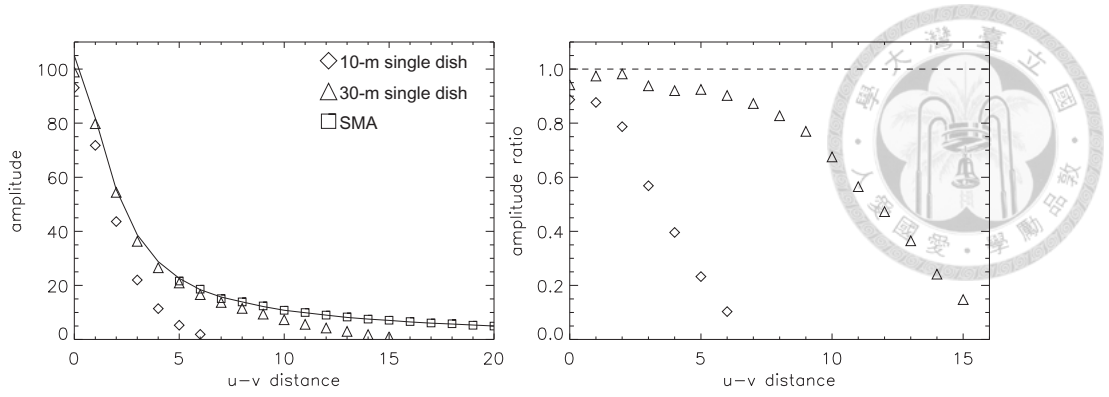


Figure 3.14 Amplitude (left) and amplitude ratio (right) as a function of $u-v$ distance. Open diamonds, triangles, and squares show the model 10-m single-dish, 30-m single-dish, and SMA visibility data, respectively. A solid line represents a correct solution, which is derived from Fourier transforming the original model image with the primary-beam de-correction. Amplitude ratio is calculated by dividing the amplitude function of the model single-dish data by that of the correct solution. Amplitude and $u-v$ distance are plotted in units of Jy and $k\lambda$.

for the original model image, we applied primary-beam de-correction to the original model image and Fourier-transformed the entire de-corrected image (solid line in Figure 3.14). In the right panel of Figure 3.14, we show the amplitude ratio between the model single-dish data and the correct solution as a function of the $u-v$ distance. The amplitude of both simulated 10-m and 30-m single-dish data is a factor of five lower than that of the correct solution at their maximum $u-v$ sampling lengths. Inconsistency between the single-dish visibility and the correct solution at zero $u-v$ distance is likely due to the limited mapping region of the single-dish observations, which does not cover the entire model intensity distribution. On the other hand, the difference at the longer $u-v$ distance is likely due to the finite single-dish beam sizes and the grid-spacing, since the sharpness of the image is diluted. The mismatch between the correct solution and the observed amplitude in the $u-v$ domain is most likely structure-dependent. Therefore, simple scaling of the amplitude cannot fix the discrepancy of the amplitude between single-dish and interferometric data in a longer $u-v$ distance range.

Figure 3.15 compares the combined 10-m single-dish + SMA image to the original model image multiplied by the SMA primary beam and convolved with the same synthesized beam of the combined image. The combined image exhibits a central compact structure plus an extended halo-like component, different from the original single power-law intensity distribution. Figure 3.16 compares the intensity profiles

as a function of the radius along the north-south and the east-west directions. The intensity of the central region at a radius less than $10''$ becomes weaker after the combining process, while that in the outer region is amplified. As a result, the original single power-law intensity distribution appears to be separated into two components. The total intensity in the inner region ($r < 5''$) of the combined image is suppressed to be $\sim 80\%$ of that of the original image, and the difference between the original and combined images is less than 10% of the peak intensity of the combined image at a radius larger than $5''$. In our real observations, there is also miss match of the flux between the single-dish and SMA observations in the common $u-v$ domain, and the apparent two emission components in the C^{18}O (2–1) image may merely be an artifact of the limitations of the combining process. The amount of the intensity suppression in the central $5''$ region ($\sim 20\%$) is comparable to our uncertainty of the single-dish flux calibration, and the maximum difference between the “real” and “observed” images at a radius larger than $5''$ is, however, likely to be 10% of the peak at most as shown in the present simulation, which corresponds to only 1.5σ in our real observations.

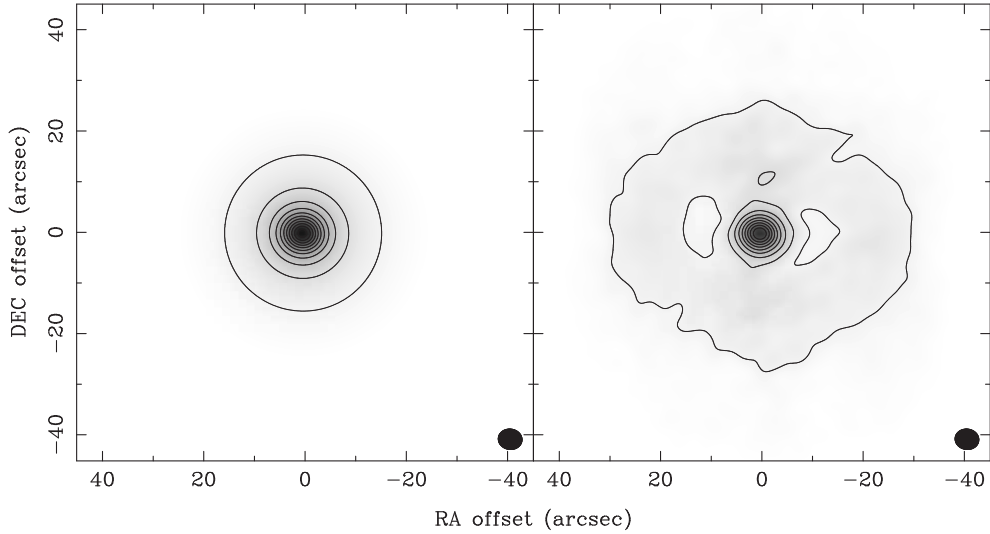


Figure 3.15 Images of the model after the combining process (right) and the original model (left). The combining process is done with the model 10-m single-dish and model SMA data. To compare with the model combined map, the original model is primary-beam decorrected and convolved with a beam that is the same as the model combined data. Contour levels are from 10% in steps of 10% of the maximum intensity in the model combined data. Ellipse in each panel shows the beam size.

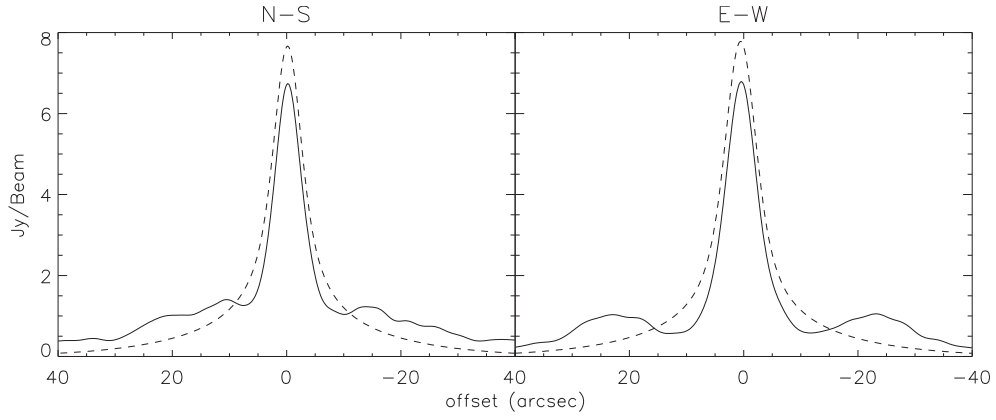


Figure 3.16 Intensity profiles of the model combined map (solid lines) and the original model image (dash lines) along north-south (left) and east-west (right) directions. The combining process is done with the model 10-m single-dish and model SMA data. To compare with the model combined map, the original model is primary-beam deconvolved and convolved with a beam that is the same as the model combined data.



Chapter 4

Unveiling the Evolutionary Sequence from Infalling Envelopes to Keplerian Disks around Low-Mass Protostars

This chapter has been published in ApJ.

Hsi-Wei Yen, Shigehisa Takakuwa, Nagayoshi Ohashi, and Paul P.T. Ho 2013

4.1 Abstract

We performed SMA observations in the C¹⁸O (2–1) emission line toward six Class 0 and I protostars, to study rotational motions of their surrounding envelopes and circumstellar material on 100 to 1000 AU scales. C¹⁸O (2–1) emission with intensity peaks located at the protostellar positions is detected toward all the six sources. The rotational velocities of the protostellar envelopes as a function of radius were measured from the Position–Velocity diagrams perpendicular to the outflow directions passing through the protostellar positions. Two Class 0 sources, B335 and NGC 1333 IRAS 4B, show no detectable rotational motion, while L1527 IRS (Class 0/I) and L1448-mm (Class 0) exhibit rotational motions with radial profiles of $V_{\text{rot}} \propto r^{-1.0 \pm 0.2}$ and $\propto r^{-1.0 \pm 0.1}$, respectively. The other Class I sources, TMC-1A and L1489 IRS, exhibit the fastest rotational motions among the sample, and their rotational mo-

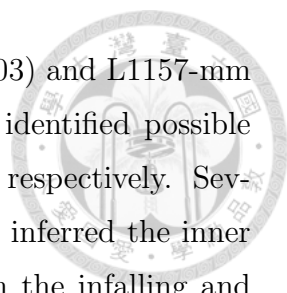
tions have flatter radial profiles of $V_{\text{rot}} \propto r^{-0.6 \pm 0.1}$ and $\propto r^{-0.5 \pm 0.1}$, respectively. The rotational motions with the radial dependence of $\sim r^{-1}$ can be interpreted as rotation with a conserved angular momentum in a dynamically infalling envelope, while those with the radial dependence of $\sim r^{-0.5}$ can be interpreted as Keplerian rotation. These observational results demonstrate categorization of rotational motions from infalling envelopes to Keplerian-disk formation. Models of the inside-out collapse where the angular momentum is conserved are discussed and compared with our observational results.

4.2 Introduction

Protostars are formed through gravitational collapse of dense cores ($n \sim 10^4 - 10^5 \text{ cm}^{-3}$; e.g., André et al. 2000; Myers et al. 2000). Previous interferometric observations have found infalling and rotational components on thousands of AU scale inside dense cores associated with known infrared sources, so-called protostellar envelopes (e.g., Ohashi et al. 1996, 1997b; Momose et al. 1998). In the innermost ($< 500 \text{ AU}$) part of those protostellar envelopes, circumstellar disks are expected to form around protostars when collapsing material rotates fast enough to reach its Keplerian velocity and to become centrifugally supported (e.g., Shu et al. 1987).

Around T Tauri stars, interferometric observations in millimeter molecular lines have identified such Keplerian disks (e.g., Guilloteau & Dutrey 1994; Dutrey et al. 1998; Simon et al. 2000; Qi et al. 2003, 2004; Andrews & Williams 2007; Pietu et al. 2007; Guilloteau et al. 2011; Andrews et al. 2012). The radii of those Keplerian disks seen in CO emission range from ~ 100 to $\sim 800 \text{ AU}$, and their masses traced by dust continuum emission range from $\sim 10^{-4}$ to $10^{-1} M_{\odot}$. Recent observations with the Submillimeter Array (SMA) have reported the presence of Keplerian disks around Class I protostars, which are still embedded in protostellar envelopes (Brinch et al. 2007a; Lommen et al. 2008; Jørgensen et al. 2009; Takakuwa et al. 2012). The Keplerian disks around Class I protostars have radii from 100 to 300 AU and masses from 0.004 to 0.06 M_{\odot} , comparable to those around T Tauri stars.

On the other hand, circumstellar disks around Class 0 protostars are likely deeply embedded in protostellar envelopes, and difficult to be observed directly (e.g., Looney et al. 2003; Chiang et al. 2008). Previous interferometric observations



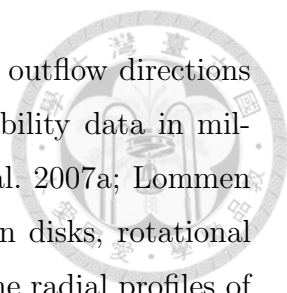
of millimeter dust continuum emission in B335 (Harvey et al. 2003) and L1157-mm (Chiang et al. 2012) at sub-arcsecond angular resolutions have identified possible disk components with the outer radii < 100 AU and < 40 AU, respectively. Several previous molecular-line observations of Class 0 sources have inferred the inner centrifugal radii to be < 100 AU, from the comparison between the infalling and rotational motions of the protostellar envelopes (e.g., Lee et al. 2006, 2009; Chapter 2 and 3). Recently, Tobin et al. (2012a) have reported the detection of a possible Keplerian disk with a radius of ~ 90 AU around L1527 IRS, a transitional object from the Class 0 to I stages, from their interferometric observations of the ^{13}CO (2–1) emission, and have claimed that L1527 IRS is the youngest protostar surrounded by a Keplerian disk. These observational results combined with those of Class I protostars and T Tauri stars imply that Keplerian disks around protostars likely increase their radii from < 100 AU up to ~ 800 AU as protostars evolve from Class 0 to T Tauri stages.

Theoretical calculations of gravitational collapse of dense cores where the angular momentum is conserved suggest that the radii of Keplerian disks around protostars increase continuously with evolution (e.g., Ulrich 1976; Cassen & Moosman 1981; Terebey et al. 1984; Basu 1998). As more material falls toward the center of protostellar envelopes with a conserved angular momentum, more angular momenta travel to the central region. Thus the rotational velocities of the material around protostars and the radii of the Keplerian disks increase. On the contrary, recent magnetohydrodynamic (MHD) simulations show that the magnetic field can effectively remove the angular momentum of the collapsing material by magnetic braking, and suppress the growth of the radii of the Keplerian disks within 10 AU (e.g., Mellon & Li 2008, 2009; Machida et al. 2011; Li et al. 2011; Dapp et al. 2012). After the efficiency of magnetic braking decreases due to the dissipation of protostellar envelopes, the radii of the Keplerian disks could increase to $\gtrsim 100$ AU in the end of the main accretion phase. However, the mass of the formed disk is larger than the protostellar mass by a factor of two to five ($M_{\text{disk}} = 0.2 - 1.0 M_{\odot}$), and the disk is subject to further fragmentation (Machida et al. 2011). Such massive disks around Class I protostars, which are close to the end of the main accretion phase, have not been seen observationally. It is still unclear as to how Keplerian disks are formed out of protostellar envelopes, increase their radii, and evolve to be classical disks

around T Tauri stars.

Formation and evolution of Keplerian disks around protostars should be closely related to the mechanism of angular momentum transfer in collapsing material from envelope (thousands of AU) to disk scales (~ 100 AU). Single-dish observations in NH_3 and N_2H^+ emission lines have found that dense cores and protostellar envelopes exhibit velocity gradients over a 0.1 pc scale with a mean magnitude of $\sim 1-2 \text{ km s}^{-1} \text{ pc}^{-1}$, suggestive of large-scale rotational motions (Goodman et al. 1993; Gaselli et al. 2002; Tobin et al. 2011). Interferometric N_2H^+ observations have shown that the inner part of protostellar envelopes (thousands of AU scale) exhibits a larger amount of velocity gradients with a mean magnitude of $\sim 7-8 \text{ km s}^{-1} \text{ pc}^{-1}$ (Chen et al. 2007; Tobin et al. 2011), suggesting that the inner envelopes rotate faster than the outer envelopes. On the other hand, CARMA N_2H^+ observations of L1157-mm (Chiang et al. 2010) and Very Large Array (VLA) NH_3 observations of HH 211 (Tanner & Arce 2011) have found that the protostellar envelopes on thousands of AU scale around these two Class 0 sources exhibit rigid-body rotation with the magnitudes of 1.5 and 6.3 $\text{km s}^{-1} \text{ pc}^{-1}$, respectively. In reality, the overall velocity gradients seen in the protostellar envelopes should reflect combination of rotational motion and other systematic gas motions such as infalling and/or outflowing motions, as well as the envelope morphologies (Tobin et al. 2012b), and it is not straightforward to disentangle these different motions and envelope morphologies and to extract rotational components. Higher angular-resolution interferometric observations of the innermost parts of protostellar envelopes on hundreds of AU scale are desirable to extract rotational components, because the rotational velocities are expected to be larger in innermost envelopes if the angular momentum is conserved in collapsing envelopes.

To study formation and evolution of Keplerian disks inside protostellar envelopes, it is crucial to observationally identify rotational motions of protostellar envelopes and their radial profiles from envelope to disk scales. In previous observational studies of protostellar envelopes (e.g., Ohashi et al. 1997a; Momose et al. 1998; Takakuwa et al. 2004; Chapter 3), the radial profiles of rotational velocities have been presumed to be either $V_{\text{rot}} \propto r^{-1}$ (rotation conserving its angular momentum) or $V_{\text{rot}} \propto r^{-0.5}$ (Keplerian rotation). On the other hand, previous claims of detection of Keplerian disks around Class I protostars are based on the presence of clear



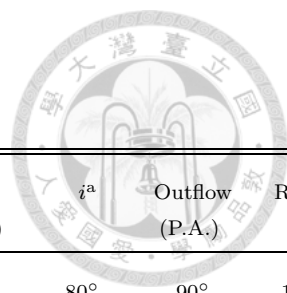
velocity gradients and elongated structures perpendicular to the outflow directions and/or the results of fitting envelope + disk models to the visibility data in millimeter continuum and molecular-line emission (e.g., Brinch et al. 2007a; Lommen et al. 2008; Jørgensen et al. 2009). In these studies of Keplerian disks, rotational motions have been presumed to follow Keplerian rotation, and the radial profiles of rotational velocities were not directly measured from the data. Systematical and unambiguous comparison of radial profiles of angular momenta on 100 to 1000 AU scales among protostellar sources at different evolutionary stages has not been made. In order to directly measure the radial distributions of angular momenta in protostellar sources without any presumption of radial profiles of rotational velocities, we have developed our own analytic method to measure the power-law indices of the rotational profiles. In this paper, we have conducted SMA observations in the C¹⁸O (2–1; 219.560358 GHz) emission line toward six protostars at different evolutionary stages from Class 0 to I, and measured the rotational velocities of their protostellar envelopes as a function of radius on 100 to 1000 AU scales. We have identified three types of the rotational motions on 100 to 1000 AU scales, depending on the protostellar evolutionary stages. We discuss and compare our observational results with models of the inside-out collapse in the context of Keplerian-disk formation (Ulrich 1976; Cassen & Moosman 1981; Terebey et al. 1984; Basu 1998).

4.3 Sample

4.3.1 Overview

The target sources in this project were selected from the sample of the SMA survey project, PROSAC (Jørgensen et al. 2007, 2009). The PROSAC sample was chosen based on the large single-dish survey of submillimeter continuum and molecular-line emission toward low-mass protostars (Jørgensen et al. 2002, 2004a). We selected all the nearby ($d < 250$ pc) sources in the northern hemisphere from the PROSAC sample, except for NGC 1333 IRAS 2A and 4A, which have rather complex outflow morphologies (Jørgensen et al. 2004b, 2007). Table 4.1 presents the summary of our selected sources. The selected sources are surrounded by protostellar envelopes (Hogerheijde et al. 1998; Motte & André 2001), have bipolar molecular outflows (Hogerheijde et al. 1998; Jørgensen et al. 2007), and exhibit signs of rotational

Table 4.1. Sample of Sources



Source	Position (J2000)	Class	Distance (pc)	L_{bol} (L_{\odot})	T_{bol} (K)	V_{sys} (km s $^{-1}$)	i^{a}	Outflow (P.A.)	Reference
B335	19 ^h 37 ^m 00 ^s .93 07°34′09″.8	0	150	1.5	31	8.3	80°	90°	1,2,3,4,5
NGC 1333 IRAS 4B	03 ^h 29 ^m 12 ^s .01 31°13′08″.1	0	250	1.6	54	6.7	77°	151°	1,6,7,8,9
L1527 IRS	04 ^h 39 ^m 53 ^s .91 26°03′09″.8	0/I	140	2.8	59	5.7	85°	90°	1,10,11
L1448-mm	03 ^h 25 ^m 38 ^s .87 30°44′05″.4	0	250	7.5	69	5.0	70°	157°	1,6,12,13,14
TMC-1A	04 ^h 39 ^m 35 ^s .20 25°41′44″.4	I	140	2.4	172	6.6	20°–50° ^b	155°	1,15,16,17
L1489 IRS	04 ^h 04 ^m 42 ^s .85 26°18′56″.3	I	140	3.7	238	7.2	36°–90° ^c	165°	1,15,16,18

^aThe inclination angle (i) is defined as the angle between the disk plane and the plane of the sky, i.e., an inclination angle of 90° corresponds to the edge-on geometry.

^bA medium value of 30° is adopted in this paper.

^cA medium value of 50° is adopted in this paper.

References. — (1) Motte & André 2001; (2) Stutz et al. 2008; (3) Chandler & Sargent 1993; (4) Chapter 3; (5) Hirano et al. 1988; (6) Enoch et al. 2006; (7) Enoch et al. 2009b; (8) Volgenau et al. 2006; (9) Marvel et al. 2008; (10) Tobin et al. 2008; (11) Ohashi et al. 1997a; (12) Tobin et al. 2007; (13) Curiel et al. 1999; (14) Girart & Acord 2001; (15) Furlan et al. 2008; (16) Hogerheijde et al. 1998; (17) Chandler et al. 1996; (18) Brinch et al. 2007a, b.

motions on thousands of AU scale (Ohashi et al. 1997a, b; Curiel et al. 1999; Saito et al. 1999; Hogerheijde 2001) except NGC 1333 IRAS 4B. Hence, these are excellent targets for the study of rotational motions of the inner envelopes on 100 to 1000 AU scales.

Our sample contains three Class 0 (B335, NGC 1333 IRAS 4B, and L1448-mm), one Class 0/I (L1527 IRS), and two Class I (TMC-1A, and L1489 IRS) sources. The 1.3 mm continuum peak positions of these sources, as observed with the SMA, are adopted as the positions of the protostars (Jørgensen et al. 2007, 2009; Brinch et al. 2007a). All the velocities shown in this paper are with respect to the systemic velocity (V_{sys}) of each source. Adopted V_{sys} in the LSR frame are shown in Table 4.1. Inferred inclination angles of the envelope/disk mid-plane from the plane of the sky and position angles of the outflow axes of these sources are listed in Table 4.1.

4.3.2 Individual Sources

B335: This source is an isolated Bok globule associated with a Class 0 protostar having a bolometric luminosity of $1.5 L_{\odot}$ (IRAS 19347+0727; Keene et al. 1980, 1983) at a distance of 150 pc (Stutz et al. 2008). B335 is associated with an east-west elongated, conical-shaped molecular outflow, and the inclination angle of the disk plane is estimated to be $\sim 80^{\circ}$ (Hirano et al. 1988). Along the outflow axis there are also collimated ^{12}CO (2–1) jets (Chapter 2) and Herbig-Haro objects (HH 119 A–F; Reipurth et al. 1992; Galfalk & Olofsson 2007). Millimeter interferometric observations in the C^{18}O (2–1) and $\text{H}^{13}\text{CO}^{+}$ (1–0) emission lines have revealed the infalling motion of the envelope around B335, and the protostellar mass is estimated to be $\sim 0.04 M_{\odot}$ from the infalling velocity (Saito et al. 1999; Chapter 2). The rotational motion of the envelope around B335 has been detected at radii from $\sim 20,000$ to ~ 1000 AU (Saito et al. 1999; Chapter 3), while the previous SMA observations did not detect clear rotational motion on hundreds of AU scale, and the upper limit of the rotational velocity is estimated to 0.04 km s^{-1} at a radius of 370 AU (Chapter 2). The radius of the central circumstellar disk has been estimated to be less than 100 AU from the interferometric observations of the millimeter continuum emission in B335 (Harvey et al. 2003). V_{sys} of B335 is 8.3 km s^{-1} as measured by the single-dish observations in the C^{18}O (2–1; 1–0) emission (Saito et al. 1999; Chapter 3).

NGC 1333 IRAS 4B: This source is a Class 0 protobinary system with a bolometric luminosity of $1.6 L_{\odot}$ (Enoch et al. 2009b) in the Perseus molecular cloud ($d = 250$ pc; Enoch et al. 2006). The separation of the binary companions, named 4B and 4B', is ~ 2750 AU ($\sim 11''$; Jorgensen et al. 2007). In the present paper, we refer the primary component 4B to as IRAS 4B and discuss the molecular emission associated with the primary component. IRAS 4B is associated with a bipolar ^{12}CO outflow along the north-south direction (e.g., Jorgensen et al. 2007) as well as a collimated jet seen in the H_2O maser emission (e.g., Marvel et al. 2008). The position angle of the H_2O jet is different from that of the ^{12}CO outflow by $\sim 30^{\circ}$. From the proper motions of the H_2O maser spots, the inclination angle of the disk plane of IRAS 4B is estimated to be $\sim 77^{\circ}$ (Marvel et al. 2008). Interferometric observations of the H_2CO (3_{12} – 2_{11}) emission in IRAS 4B show an inverse P Cygni profile, suggesting the presence of infalling motion (Di Francesco et al. 2001). V_{sys}

of IRAS 4B is 6.7 km s^{-1} as measured from the combined BIMA+FCRAO C^{18}O (1–0) spectrum (Volgenau et al. 2006). The NGC 1333 IRAS 4 region is complex and contains a small cluster of protostars within a radius of $\sim 30''$ (7500 AU), and no systematic velocity gradient corresponding to rotational motion on thousands of AU scale was observed (Volgenau et al. 2006).

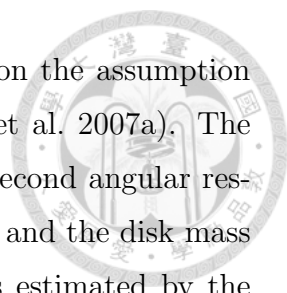
L1527 IRS (IRAS 04368+2557): This source is a protostar with a bolometric luminosity of $2.8 L_{\odot}$ (Tobin et al. 2008) in the Taurus molecular cloud ($d = 140 \text{ pc}$). The source exhibits a Class 0 type spectrum, but could be an obscured Class I protostar because of its high inclination angle (Ohashi et al. 1997a). The inclination angle of the disk plane is estimated to be 85° from the infrared images (Tobin et al. 2008). Previous millimeter interferometric observations show that the ^{12}CO (1–0) outflow associated with L1527 IRS exhibits a bipolar conical shape along the east-west direction, and that there are infalling and rotational motions in the C^{18}O (1–0) flattened envelope on a 2000 AU scale (Ohashi et al. 1997a). From the mass infalling rate ($\sim 1 \times 10^{-6} M_{\odot} \text{ yr}^{-1}$) estimated by Ohashi et al. (1997a) and the bolometric luminosity ($2.8 L_{\odot}$) measured by Tobin et al. (2008), the protostellar mass is estimated to be $0.2 M_{\odot}$. Recently the presence of a possible Keplerian disk with a radius of 90 AU and a mass of $0.007 M_{\odot}$ around L1527 IRS has been reported from the CARMA observations in the ^{13}CO (2–1) emission line, and the protostellar mass has been estimated to be $0.2 M_{\odot}$ from the observed Keplerian rotation (Tobin et al. 2012a). V_{sys} of L1527 IRS is measured to be 5.7 km s^{-1} from the Nobeyama 45-m telescope observations in the C^{18}O (1–0) emission line (Ohashi et al. 1997a), while that is measured to be 5.9 km s^{-1} by the N_2H^+ and NH_3 single-dish observations (Goodman et al. 1993; Caselli et al. 2002; Tobin et al. 2011). As will be presented below, our SMA results show that the distribution of the C^{18}O (2–1) emission is symmetric with respect to $V_{\text{LSR}} = 5.7 \text{ km s}^{-1}$, and hence V_{sys} of 5.7 km s^{-1} is adopted in this paper.

L1448-mm: This source is also known as L1448 C, a Class 0 protostar with a bolometric luminosity of $7.5 L_{\odot}$ (Tobin et al. 2007) in the Perseus molecular cloud. L1448-mm is associated with an active molecular outflow along the northwest-southeast direction, and several high-velocity ($> 50 \text{ km s}^{-1}$) ^{12}CO and H_2O "bullets" along the outflow axis and collimated SiO jets have been observed (e.g., Bachiller 1996; Hirano et al. 2010; Kristensen et al. 2011). From the proper motions of the

SiO jets, the inclination angle of the disk plane is estimated to be $\sim 70^\circ$ (Girart & Acord 2001). Based on the mass loss rate of the outflow and the bolometric luminosity, the protostellar mass of L1448-mm is inferred to be $0.03 - 0.09 M_\odot$ (Hirano et al. 2010). VLA observations in the NH_3 emission lines of this source show that the envelope around L1448-mm exhibits velocity gradients both along and perpendicular to the outflow direction, which are interpreted as infalling and rotational motions on thousands of AU scale, respectively (Curiel et al. 1999). V_{sys} of L1448-mm is 5.0 km s^{-1} as measured by the VLA NH_3 observation (Curiel et al. 1999).

TMC-1A (IRAS 04365+2535): This source is a Class I protostar with a bolometric luminosity of $2.4 L_\odot$ (Furlan et al. 2008) in the Taurus molecular cloud. TMC-1A is associated with a conical-shaped, bipolar molecular outflow along the northwest-southeast direction, and the inclination angle of the disk plane is estimated to be $40^\circ - 70^\circ$ (Chandler et al. 1996). Interferometric observations of the C^{18}O (1–0) emission in TMC-1A (Ohashi et al. 1997b) show that the envelope exhibits a velocity gradient perpendicular to the outflow direction only, suggesting that the rotational motion is more dominant than the infalling motion on a 1500 AU scale. V_{sys} of TMC-1A is 6.6 km s^{-1} as estimated by the IRAM 30-m telescope and the James Clerk Maxwell Telescope (JCMT) observations in the C^{18}O and ^{12}CO emission lines at multiple transitions (Hogerheijde et al. 1998).

L1489 IRS (IRAS 04016+2610): This source is a Class I protostar with a bolometric luminosity of $3.7 L_\odot$ (Furlan et al. 2008) in the Taurus molecular cloud. In L1489 IRS, there is a faint molecular outflow along the northwest-southeast direction as observed by the JCMT in the ^{12}CO (3–2) emission line (Hogerheijde et al. 1998). Estimates of the inclination angle of the disk plane range from 36° to 90° from the model fitting of the spectral energy distribution, scatter light and millimeter continuum images, and molecular-line spectra (Kenyon et al. 1993; Padgett et al. 1999; Eisner et al. 2005; Brinch et al. 2007a; Eisner 2012). The infalling and rotational motions of the envelope on a 2000 AU scale have been revealed by interferometric observations at millimeter wavelengths, and the rotational motion is more dominant than the infalling motion (Hogerheijde 2001). The SMA observations in the millimeter continuum and HCO^+ (3–2) line emission have reported the presence of a Keplerian disk with a radius of 200 AU and a mass of $0.004 M_\odot$ embedded in the

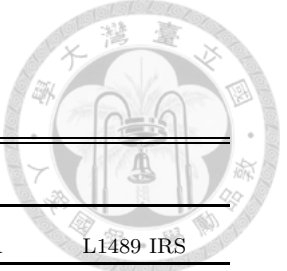


envelope, and the protostellar mass is estimated to be $1.4 M_{\odot}$ on the assumption that the inclination angle of the Keplerian disk is 40° (Brinch et al. 2007a). The 1.3 mm continuum observations with the CARMA at a sub-arcsecond angular resolution ($\sim 0''.8$) have shown that the disk radius is $250 - 450$ AU and the disk mass is $0.005 M_{\odot}$ (Eisner 2012). V_{sys} of L1489 IRS is 7.2 km s^{-1} as estimated by the single-dish observations in several molecular lines at multiple transitions (Brinch et al. 2007b).

4.4 Observations

The data in this work were taken from both the SMA data archive and new SMA observations. Details of the SMA are described by Ho et al. (2004). We conducted SMA observations in the C^{18}O (2–1) line with the compact configuration toward TMC-1A and L1489 IRS and with the subcompact configuration toward all the sample sources except B335. The SMA C^{18}O (2–1) data of IRAS 4B with the extended configuration are obtained from the SMA data archive, and the PI of this observation is Jørgensen, J. K.. Details of these observations are shown in Table 4.2. The SMA C^{18}O (2–1) data of B335, IRAS 4B, L1448-mm, and L1527 IRS with the compact configuration are obtained from the SMA data archive, and the details of these observations are described in the PROSAC paper (Jørgensen et al. 2007). The 1.3 mm continuum emission was observed simultaneously in all of these observations. The maximum and minimum uv lengths after the compilation of all the available data are listed in Table 4.3. In the observations with the compact and extended configurations, the correlator configuration was set to assign 512 channels to one chunk with a 83.3 MHz bandwidth for the C^{18}O (2–1) line, resulting in a velocity resolution of 0.28 km s^{-1} . In the observations with the subcompact configuration, 1024 channels were assigned to the chunk for the C^{18}O (2–1) line, resulting in a velocity resolution of 0.14 km s^{-1} . MIR software package (Scoville et al. 1993) was used to calibrate all the data. The calibrated visibility data were Fourier-transformed and CLEANed with MIRIAD (Sault et al. 1995) to produce images. Two types of images with different velocity and angular resolutions were produced: images made only with the subcompact data and combined images made with all the available data. The resolutions and noise levels of the images are summarized in

Table 4.2. Summary of Observations



Subcompact Configuration					
Source	IRAS 4B	L1527 IRS	L1448-mm	TMC-1A	L1489 IRS
Observing Date	2012 Jan 7	2012 Jan 8	2012 Jan 7	2012 Jan 8	2012 Jan 7
Pointing Center (J2000)	03 ^h 29 ^m 12 ^s .00 31°13′08″.0	04 ^h 39 ^m 53 ^s .90 26°03′10″.0	03 ^h 25 ^m 38 ^s .80 30°44′05″.0	04 ^h 39 ^m 35 ^s .01 25°41′45″.5	04 ^h 04 ^m 42 ^s .95 26°18′56″.3
225 GHz Opacity			0.03 – 0.12		
System Temperature			70 – 130 K		
Bandpass Calibrator			3c84 and 3c279		
Flux Calibrator			Uranus		
Gain Calibrator		3c111 (2.1 Jy) and 3c84 (8.8 Jy)			
<i>uv</i> Coverage			3 – 34 <i>kλ</i>		

Compact Configuration		Extended Configuration
Source	TMC-1A L1489 IRS	IRAS 4B
Observing Date	2012 Oct 28	2006 Jan 17
Pointing Center (J2000)	04 ^h 39 ^m 35 ^s .01 04 ^h 04 ^m 42 ^s .95 25°41′45″.5 26°18′56″.3	03 ^h 29 ^m 12 ^s .00 31°13′08″.0
225 GHz Opacity	0.1 – 0.2	~ 0.07
System Temperature	100 – 300 K	80 – 250 K
Bandpass Calibrator	3c279 and 3c454.3	3c273
Flux Calibrator	Uranus	Callisto
Gain Calibrator	3c111 (1.9 Jy)	3c84 (2.8 Jy) and 3c111 (3.3 Jy)
<i>uv</i> Coverage	8 – 57 <i>kλ</i>	17 – 134 <i>kλ</i>

Table 4.3. The combined images with the higher angular resolutions can show finer structures, while the subcompact images with more weights on the short-spacing data and the higher velocity resolution can trace more extended structures and slower motions. In the present paper results of the C¹⁸O (2–1) data are primarily discussed, and detailed discussion of the 1.3 mm continuum data will be the subject to the forthcoming papers. The continuum images are shown in Section 4.9.1.



Table 4.3. Resolutions and Noise Levels of the C¹⁸O (2–1) Images

Source	u – v coverage ($k\lambda$)	Subcompact Image		Combined Image	
		Beam (P.A.)	RMS (Jy Beam ^{−1})	Beam (P.A.)	RMS (Jy Beam ^{−1})
B335	6 – 54	3''7 × 3''2 (87°)	0.20
IRAS 4B	3 – 134	8''5 × 4''8 (73°)	0.19	2''6 × 2''2 (47°)	0.09
L1527 IRS	4 – 102	8''5 × 5''1 (68°)	0.17	4''2 × 2''5 (80°)	0.10
L1448-mm	3 – 102	8''5 × 4''9 (72°)	0.18	5''1 × 3''2 (78°)	0.11
TMC-1A	4 – 57	8''6 × 5''1 (67°)	0.17	3''6 × 3''2 (−84°)	0.16
L1489 IRS	3 – 57	8''5 × 4''9 (72°)	0.18	3''7 × 3''3 (78°)	0.16
Velocity Resolution		0.14 km s ^{−1}		0.28 km s ^{−1}	

4.5 Spatial and Kinematics Structures of the C¹⁸O (2–1) Emission

Figure 4.1 shows integrated-intensity (i.e., moment 0) maps (contours) overlaid on the intensity-weighted mean velocity (i.e., moment 1) maps (color) of all the sources in the C¹⁸O (2–1) emission made from the combined (left) and subcompact data (right). In the moment 1 maps a common color scale is adopted to compare the amount of the velocity gradients among the different sources directly. In all the sources the C¹⁸O (2–1) emission shows \sim a few thousand AU scale envelope features approximately centered on the protostellar sources, but the velocity structures are remarkably different as described below.

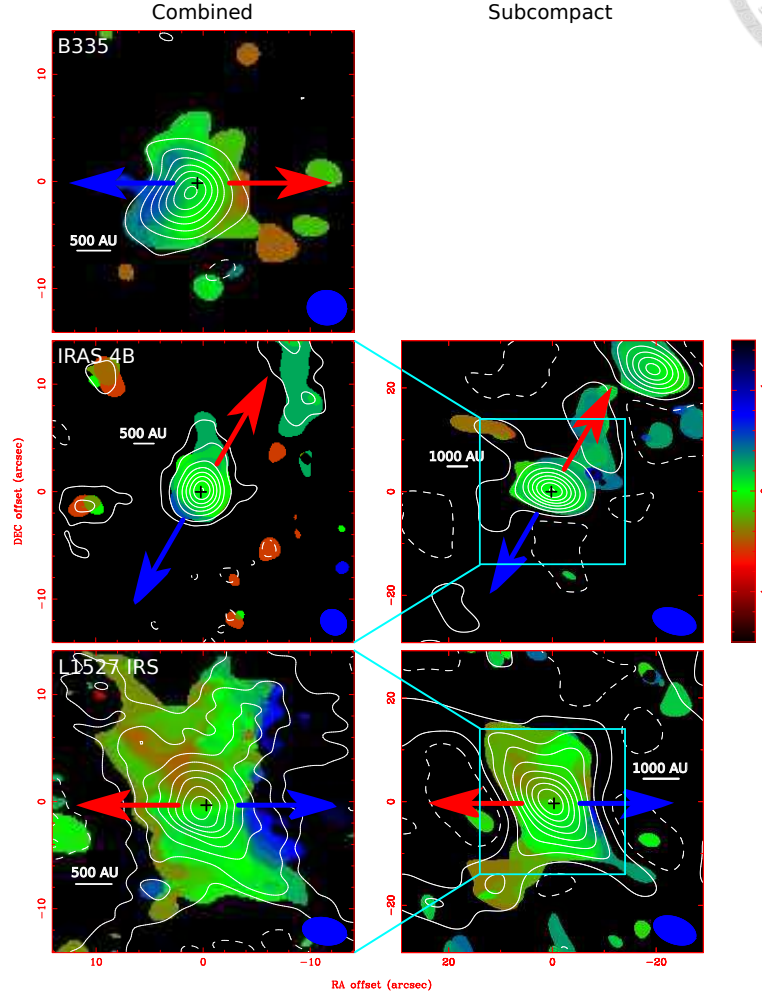


Figure 4.1 Moment 0 maps (contours) overlaid on the moment 1 maps (color scale) of the C^{18}O (2–1) emission in B335, IRAS 4B, L1527 IRS, L1448-mm, TMC-1A, and L1489 IRS. The maps in the left and right columns are produced with the combined and subcompact data, respectively. Light blue boxes in the subcompact maps show the area of the combined maps. Crosses present the protostellar positions derived from the 1.3 mm continuum emission (Jørgensen et al. 2007, 2009; Brinch et al. 2007a), and blue and red arrows show the directions of the blueshifted and redshifted outflows, respectively. A blue filled ellipse at the bottom-right corner in each panel denotes the beam size. Contour levels start from 3σ in steps of 3σ in the combined maps and in steps of 7σ in the subcompact maps. The 1σ noise levels of the combined moment 0 maps of B335, IRAS 4B, L1527 IRS, L1448-mm, TMC-1A, and L1489 IRS are 0.14, 0.07, 0.1, 0.09, 0.16, and 0.18 $\text{Jy beam}^{-1} \text{ km s}^{-1}$, respectively, and those of the subcompact moment 0 maps of IRAS 4B, L1527 IRS, L1448-mm, TMC-1A, and L1489 IRS are 0.08, 0.12, 0.1, 0.12, and 0.12 $\text{Jy beam}^{-1} \text{ km s}^{-1}$, respectively. The beam sizes are summarized in Table 4.3.

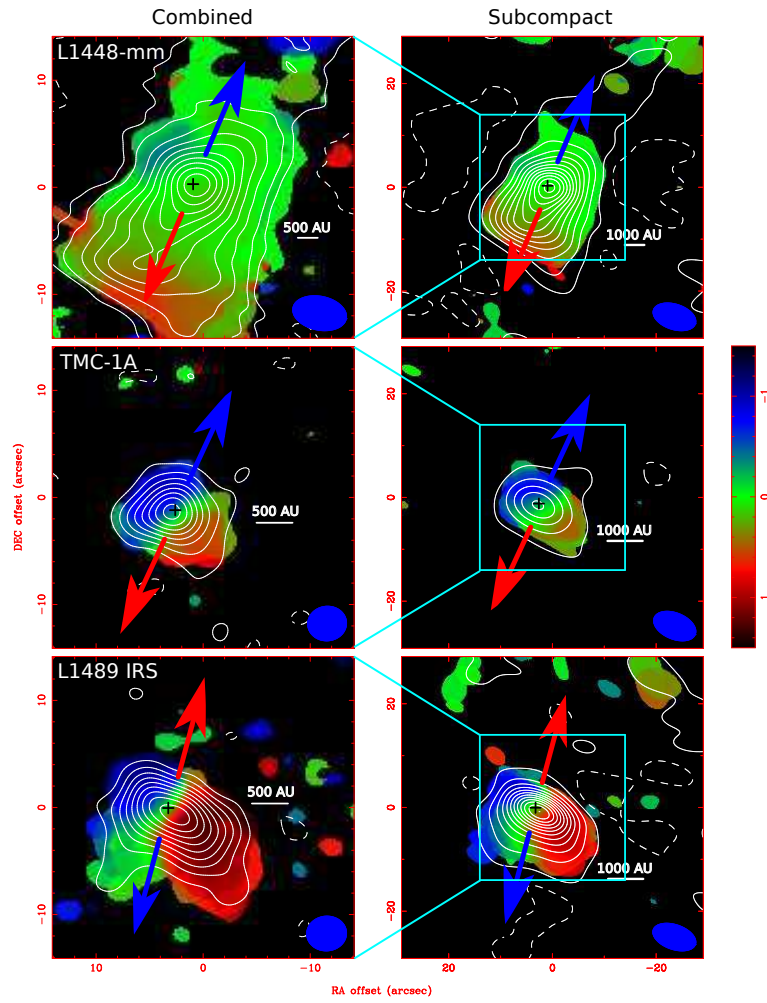


Fig. 4.1.— Continued.

4.5.1 B335

The SMA results of B335 in the C^{18}O (2–1) emission have been presented in detail in Chapter 2 and 3. The C^{18}O (2–1) emission shows a compact (~ 1500 AU) blob approximately centered on the protostar (Fig. 4.1). A velocity gradient along the outflow axis in the east-west direction is clearly seen in the moment 1 map (Fig. 4.1). The velocity gradient of the C^{18}O (2–1) emission has been compared with that of the associated outflow traced by the ^{12}CO (2–1) emission, and is unlikely originated from the outflow. Through the comparison between the observed C^{18}O (2–1) results and models of infalling envelopes, we have found that the velocity gradient of the C^{18}O (2–1) emission can be explained by the infalling motion in the flattened envelope (see Chapter 2 for details). On the other hand, there is no clear velocity gradient perpendicular to the outflow direction, and hence the rotational velocity of the envelope is likely below the detection limit of our SMA observations (Chapter 2 and 3).

4.5.2 IRAS 4B

In the combined moment 0 map of IRAS 4B (Fig. 4.1), the C^{18}O (2–1) emission shows a compact (~ 2000 AU) condensation centered on the protostar, plus an extension toward the direction of the redshifted outflow. The relevant moment 1 map of IRAS 4B shows that the southeastern part of the condensation is slightly ($\sim 0.3 \text{ km s}^{-1}$) blueshifted than the northwestern part. The direction and the sense of the velocity gradient are the same as those of the associated molecular outflow. This velocity gradient is more clearly seen in the velocity channel maps shown in Figure 4.2. At velocities from -0.81 to -0.53 km s^{-1} , the centroid position of the C^{18}O (2–1) emission is shifted to southeast from the protostellar position, while at velocities from 0.02 to 0.58 km s^{-1} the emission peak appears to be located to the northwest. The origin of this velocity gradient could be either infalling motion in the flattened envelope as in the case of B335 (e.g., Chapter 2 and 3), or the outflow itself. On the other hand, there is no detectable velocity gradient perpendicular to the outflow direction.

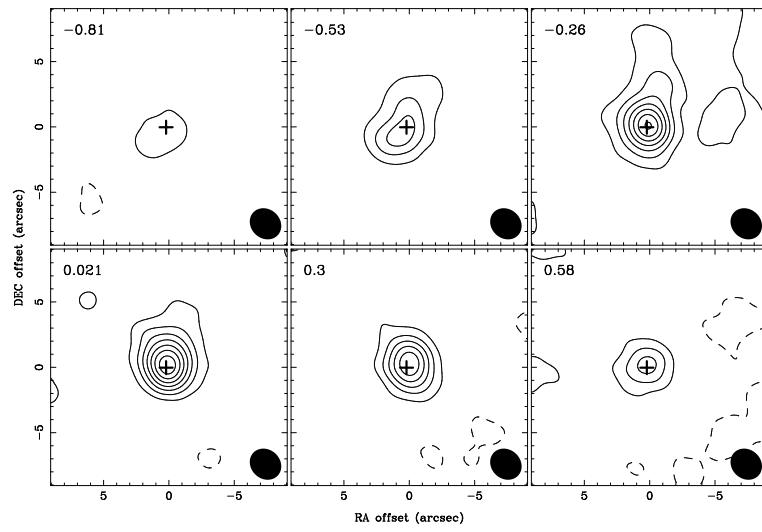


Figure 4.2 Velocity channel maps of the C^{18}O (2–1) emission in IRAS 4B made with the combined data. Crosses and filled ellipses show the protostellar position and the beam size, respectively. The velocity at each channel is shown at the upper-left corner in each panel. Contour levels start from 3σ in steps of 4σ . The noise level and the beam size are summarized in Table 4.3.

The northwestern extension appears in the blueshifted velocities (-0.53 to -0.26 km s $^{-1}$) and is coincident with the redshifted outflow. This component may trace a shell of the northwestern outflow, whose axis is close to the plane of the sky ($\sim 13^\circ$). In the moment 0 map of the subcompact data, there is a secondary component toward the northwest, which is associated with NGC 1333 IRAS 4A. In the moment 0 map of the combined data, toward the east there appears a weak component associated with 4B'.

4.5.3 L1527 IRS

In the moment 0 maps of L1527 IRS (Fig. 4.1), the C 18 O (2–1) emission shows a central component plus an extended structure delineating the conical shell of the outflow. The velocity channel maps of the combined data shown in Figure 4.3 also exhibits a central component plus an X-shaped structure (e.g., at velocities of -0.23 , 0.05 , and 0.88 km s $^{-1}$). A similar morphological feature has also been observed in the 13 CO (1–0) emission with the Nobeyama Millimeter Array (Ohashi et al. 1997a), which is interpreted as the protostellar envelope plus the outflow shell (see Figure 7 in Ohashi et al. 1997a). The peak position of the central component shifts from south to north at blueshifted to redshifted velocities, suggesting that there is a velocity gradient perpendicular to the outflow direction. This velocity gradient perpendicular to the outflow direction is also seen in the moment 1 maps (Fig. 4.1). The same sense of the velocity gradient has also been identified in interferometric observations of L1527 IRS in the C 18 O (1–0) emission line at an angular resolution of $\sim 6''$ (Ohashi et al. 1997a) and in the 13 CO (2–1) emission line at an angular resolution of $\sim 1''$ (Tobin et al. 2012a). The extended X-shaped structure exhibits a velocity gradient consistent with that of the large-scale outflow (e.g., Ohashi et al. 1997a).

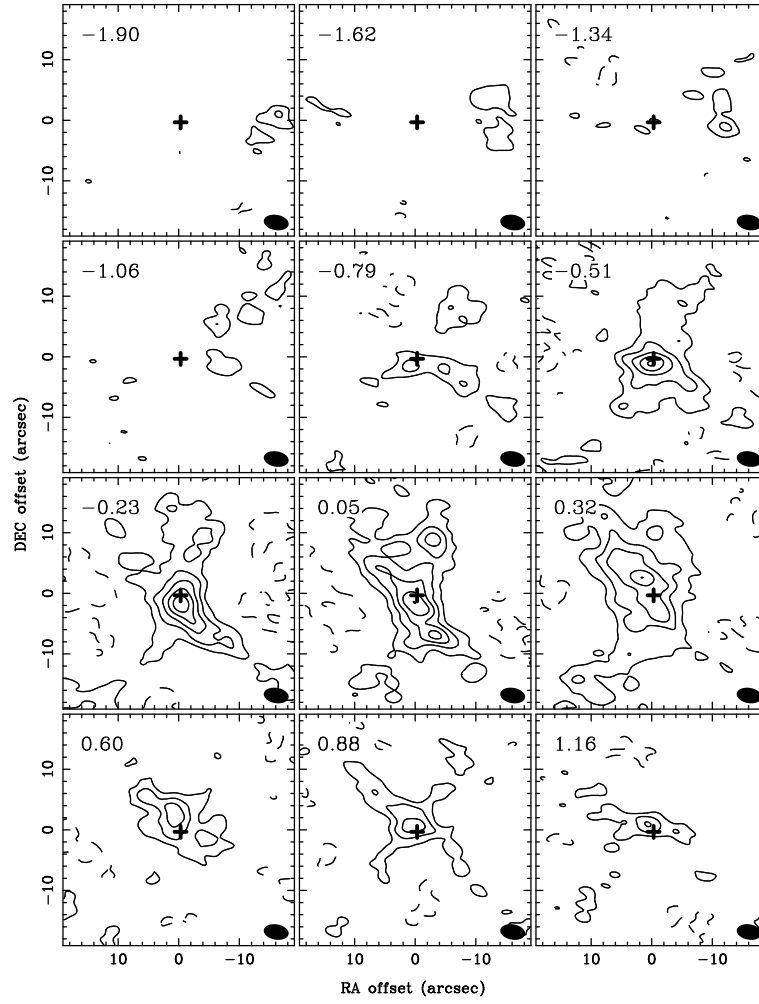


Figure 4.3 Same as Fig. 4.2 but for L1527 IRS. Contour levels start from 3σ in steps of 3σ .

4.5.4 L1448-mm

In the C^{18}O (2–1) velocity channel maps of the combined data of L1448-mm (Fig. 4.4), there appears a central compact (~ 1500 AU) component associated with the protostar as well as an extended (~ 5000 AU) component elongated along the outflow direction from northwest to southeast, plus a secondary component at velocities from 0.52 to 1.07 km s^{-1} . The extended and secondary components are most likely related to the powerful molecular outflow driven from L1448-mm (e.g., Bachiller 1996; Hirano et al. 2010; Kristensen et al. 2011). On the other hand, the central compact emission associated with L1448-mm exhibits a velocity gradient along northeast (blueshifted) to southwest (redshifted), suggesting a velocity gradient perpendicular to the outflow direction. The moment 0 maps of the C^{18}O (2–1) emission in L1448-mm (Fig. 4.1) primarily shows the extended component elongated along the outflow direction, and the central component seen in the velocity channel maps appears embedded in the extended component. As a result, the velocity gradient of the central compact component is not clear in the moment 1 maps. The moment 1 maps show that the southern part of the emission is redshifted, which arises from the secondary component seen in the velocity channel maps.

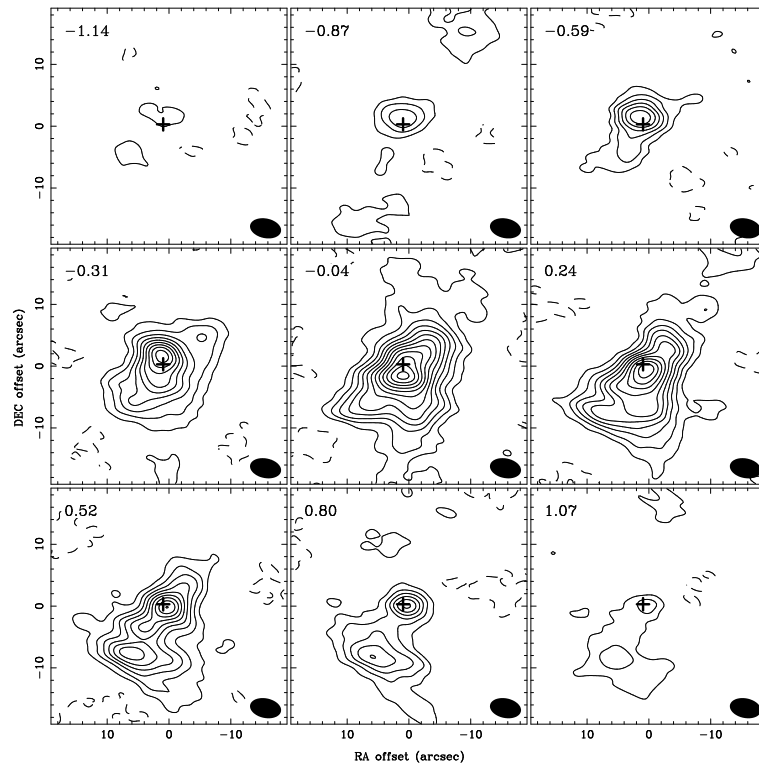


Figure 4.4 Same as Fig. 4.2 but for L1448-mm. Contour levels start from 3σ in steps of 3σ .

4.5.5 TMC-1A

Figure 4.5 presents the velocity channel maps of the combined data in TMC-1A. The peak positions of the C^{18}O (2–1) emission in TMC-1A are shifted from northeast to southwest of the protostar from blueshifted to redshifted velocities, suggesting the presence of a velocity gradient perpendicular to the outflow direction. The high-velocity components ($|V| \gtrsim 1.4 \text{ km s}^{-1}$) are more compact and closer to the protostar than the low-velocity components ($|V| \lesssim 0.8 \text{ km s}^{-1}$). In the moment 0 maps (Fig. 4.1), the peak position of the total integrated C^{18}O (2–1) emission is coincident with the position of the protostar. The velocity gradient perpendicular to the outflow direction seen in the velocity channel maps is clearly identified in the moment 1 maps.

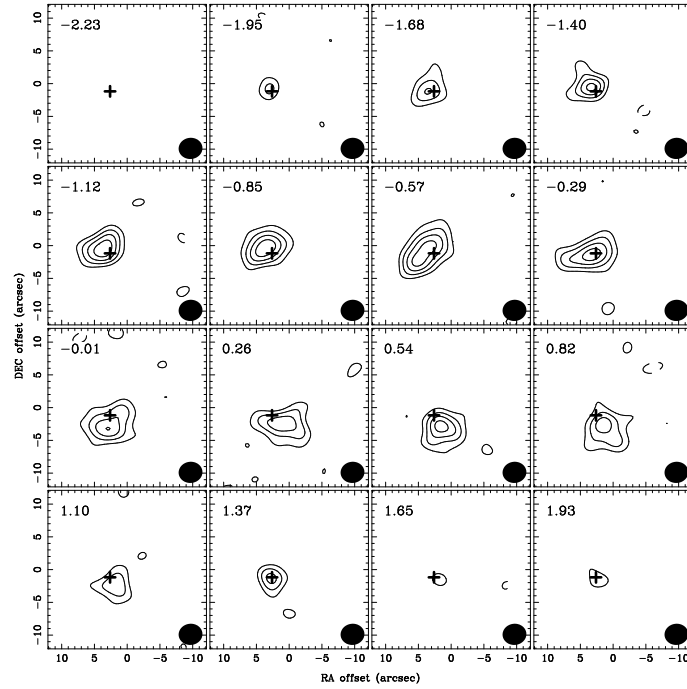


Figure 4.5 Same as Fig. 4.2 but for TMC-1A. Contour levels start from 3σ in steps of 2σ .

4.5.6 L1489 IRS

Figure 4.6 presents the velocity channel maps of the combined data in L1489 IRS. In the blueshifted velocities the C^{18}O (2–1) emission is located to the northeast of the protostar, while in the redshifted velocities to the southwest. Thus, there is a clear velocity gradient perpendicular to the outflow direction. The moment 0 and I maps show an elongation and a clear velocity gradient perpendicular to the outflow direction (Fig. 4.1), respectively, and the peak position of the moment 0 maps is coincident with the position of the protostar.

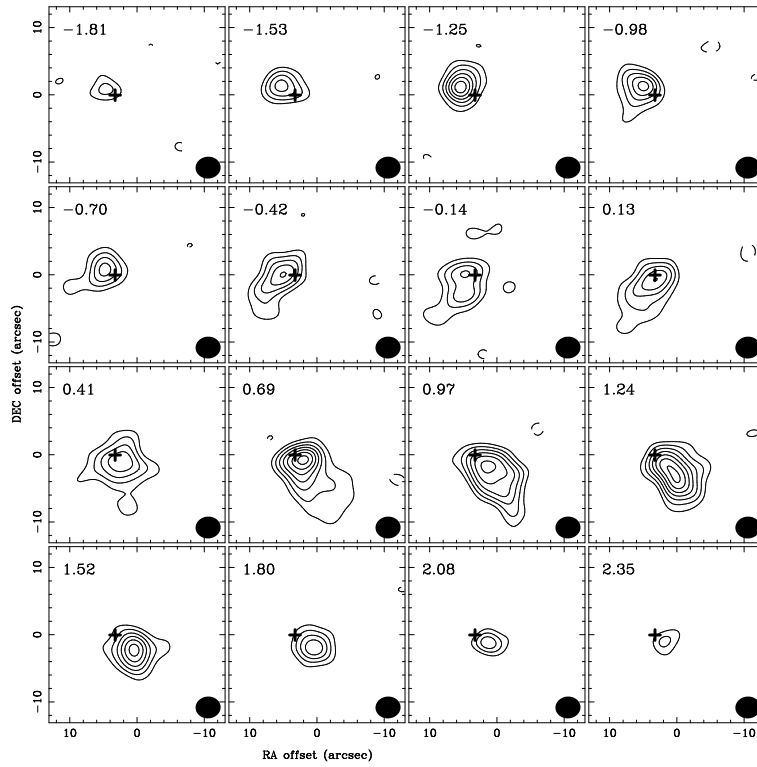
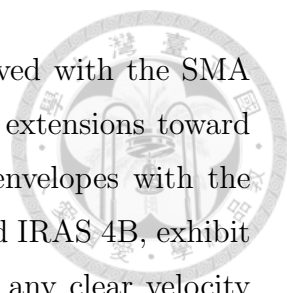


Figure 4.6 Same as Fig. 4.2 but for L1489 IRS. Contour levels start from 3σ in steps of 2σ .



In summary, the C^{18}O (2–1) emission in these sources observed with the SMA shows central condensations associated with the protostars plus extensions toward the outflow directions, and most likely traces the protostellar envelopes with the contaminations from the outflows. Two Class 0 sources, B335 and IRAS 4B, exhibit velocity gradients along the outflow directions but do not show any clear velocity gradient perpendicular to the outflow directions. In the other four sources (L1527 IRS, L1448-mm, TMC-1A, and L1489 IRS) there are clear velocity gradients perpendicular to the outflow directions, and the magnitudes of the velocity gradients in the Class I sources (TMC-1A and L1489 IRS) are the largest, as shown by the contrast of the color scales in Figure 4.1. The sources with the smaller amounts of the velocity gradients perpendicular to the outflow directions (B335, IRAS 4B, L1527 IRS, and L1448-mm) all have high inclination angles ($i > 70^\circ$), and thus their smaller amounts of the velocity gradients are unlikely due to the projection effects. Our observed samples demonstrate that on an 1000 AU scale, Class 0 sources tend to exhibit velocity gradients along the outflow directions clearer than those perpendicular to the outflow directions, while Class I sources tend to exhibit dominant velocity gradients perpendicular to the outflow directions. Such a tendency has also been identified in the interferometric C^{18}O (1–0) observations on thousands of AU scale around protostars by Arce & Sargent (2006).

4.6 Analysis

4.6.1 Method to Derive Rotational Profiles

The variety of the velocity gradients in the protostellar envelopes along and perpendicular to the outflow directions found with the present SMA observations are intriguing. However, it is in general not straightforward to attribute an observed velocity gradient to a certain systematic gas motion (i.e., rotation, infall, or outflow), because a velocity gradient often consists of multiple systematic motions and depends on the envelope morphologies. For simplicity, in the rest of this paper, we assume that the protostellar envelopes are axisymmetric around the outflow axes. On this assumption, the observed velocity gradients perpendicular to the outflow directions should primarily trace the rotational motions of the envelopes around the protostars. In contrast, the velocity gradients along the outflow directions should

be originated either from the outflows or the infalling motions of the envelopes, or both. Thus, for our analysis we adopt the C^{18}O (2–1) position–velocity (P–V) diagrams perpendicular to the outflow directions passing through the protostellar positions, produced from the combined and subcompact image cubes (Fig. 5.11). Such diagrams can provide velocity structures of rotational motions with the least contamination from outflows, and infalling motions do not induce any velocity gradient in such diagrams (see Appendix 4.9.2).

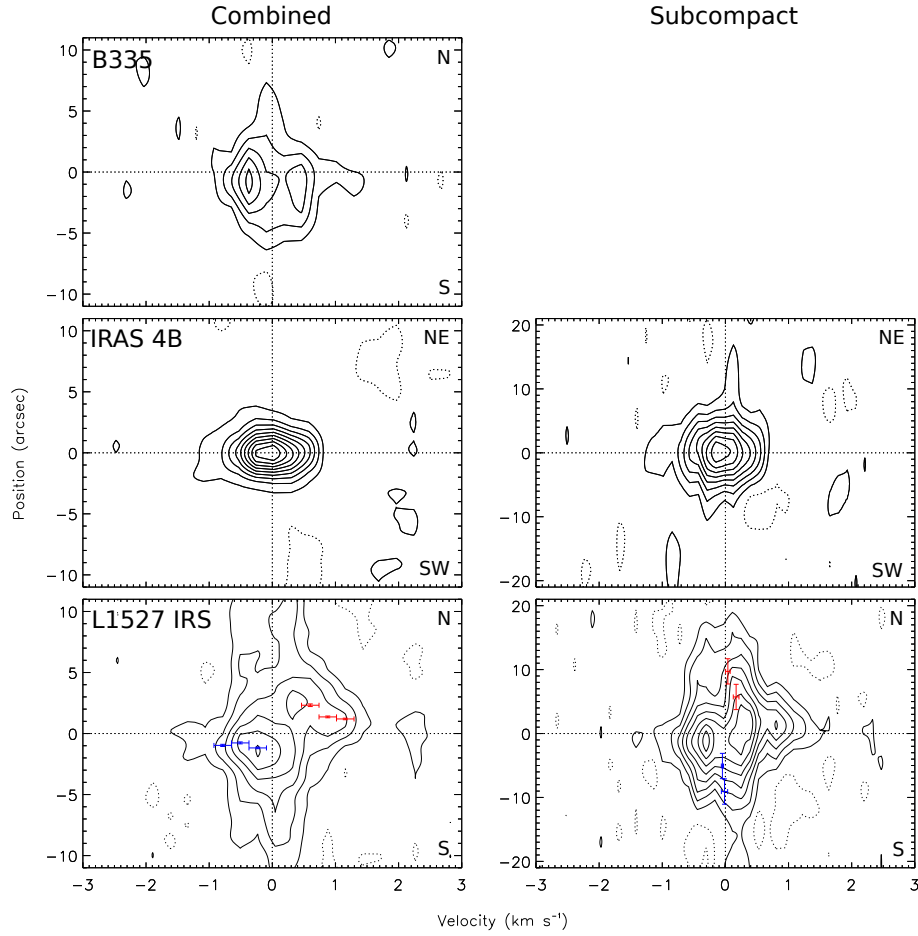


Figure 4.7 P–V diagrams perpendicular to the outflow directions in the C^{18}O (2–1) emission of B335, IRAS 4B, L1527 IRS, L1448-mm, TMC-1A, and L1489 IRS. The diagrams in the left and right columns are produced with the combined and subcompact data, respectively. Note that the spatial scales of the combined and subcompact P–V diagrams are different. Horizontal and vertical lines in each panel denote the protostellar position and the systemic velocity of each source, respectively. Blue and red data points with error bars show the measured rotational velocities as a function of radius at the blueshifted and redshifted velocities, respectively. Contour levels start from 3σ in steps of 3σ , where the noise levels are summarized in Table 4.3.

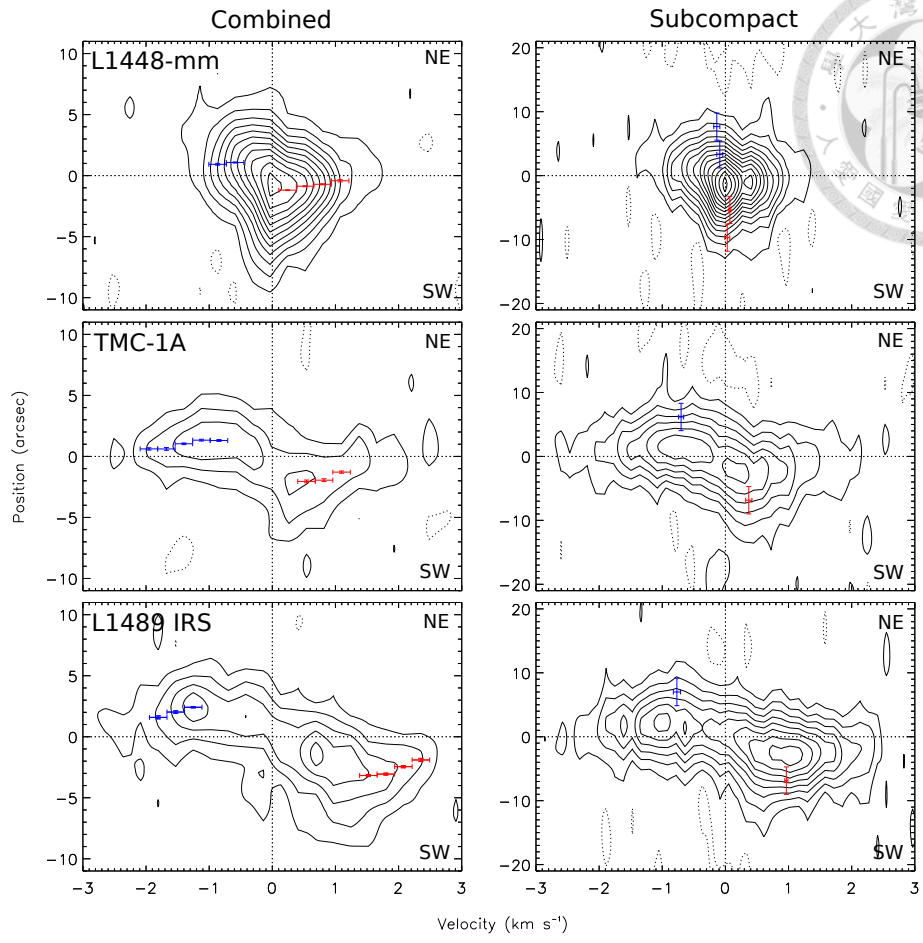


Fig. 4.7.— Continued.

In the P–V diagram of B335, there is no clear positional offset between the blueshifted and redshifted peaks. In both the combined and subcompact P–V diagrams of IRAS 4B, a single peak at the central position around the systemic velocity is seen. These results show the absence of detectable rotational motions in these two sources. For the rest of the sources, velocity gradients are clearly seen in their P–V diagrams. In these sources, the emission at higher velocities ($|V| > 0.5 - 1 \text{ km s}^{-1}$) appears closer to the protostellar positions while the emission at offsets larger than $\sim 3''$ from the protostars shows lower velocities ($|V| < 0.5 - 1 \text{ km s}^{-1}$). This feature implies that the rotational velocities increase as the radii decrease, i.e., spin-up rotation, which has been observed around other protostellar sources such as L1551 IRS 5 (Momose et al 1998; Takakuwa et al. 2004) and L1551 NE (Takakuwa et al. 2012).

For the sources with the detectable velocity gradients perpendicular to the outflow directions, the rotational velocities as a function of radius are measured from the P–V diagrams. Figure 4.8 demonstrates our method. We adopt different fitting methods to the emission distributions in the P–V diagrams at the inner ($r < 500 \text{ AU}$) and outer ($r > 500 \text{ AU}$) parts. The borderline between the inner and outer parts ($r = 500 \text{ AU}$) is chosen to be roughly the turning point of the trajectory of the spin-up rotation. For the inner part, a Gaussian function is fitted to the intensity distribution at each velocity channel in the combined P–V diagrams, to measure its peak position and hence the rotational radius at that rotational velocity (Fig. 4.8 (a) & (b)). For the outer part, a Gaussian function is fitted to the spectrum at a given position in the P–V diagrams of the subcompact data with the higher velocity resolution, to measure its centroid velocity thus the rotational velocity at that rotational radius (Fig. 4.8 (c) & (d)). The spatial interval to perform the spectrum fitting is chosen to be the half of the beam size. To minimize the possible effect of the missing flux, the fitting is only performed at radii $\lesssim 10''$ since our observations are insensitive to structures larger than $20''$ scale at a 50% level (Wilner & Welch 1994). The measured data points with the error bars are shown in the P–V diagrams of L1527 IRS, L1448-mm, TMC-1A, and L1489 IRS (Fig. 4.7). The rotational velocities as a function of radius after the correction of the inclination effects, as well as the results of the power-law fitting to the measured data points (i.e., $V_{\text{rot}} \propto r^p$), are presented in Figure 4.9. The best-fit power-law indices and their uncertainties

are listed in Table 4.4. The estimation of the uncertainties of the data points in the P–V diagrams and the best-fit power-law indices is described in the next subsection. Among the four sources with the detectable velocity gradients, TMC-1A and L1489 IRS exhibit flatter rotational profiles on an 1000 AU scale than L1527 IRS and L1448-mm, and the rotational velocities in TMC-1A and L1489 IRS are higher than those in L1527 IRS and L1448-mm at the same radii.

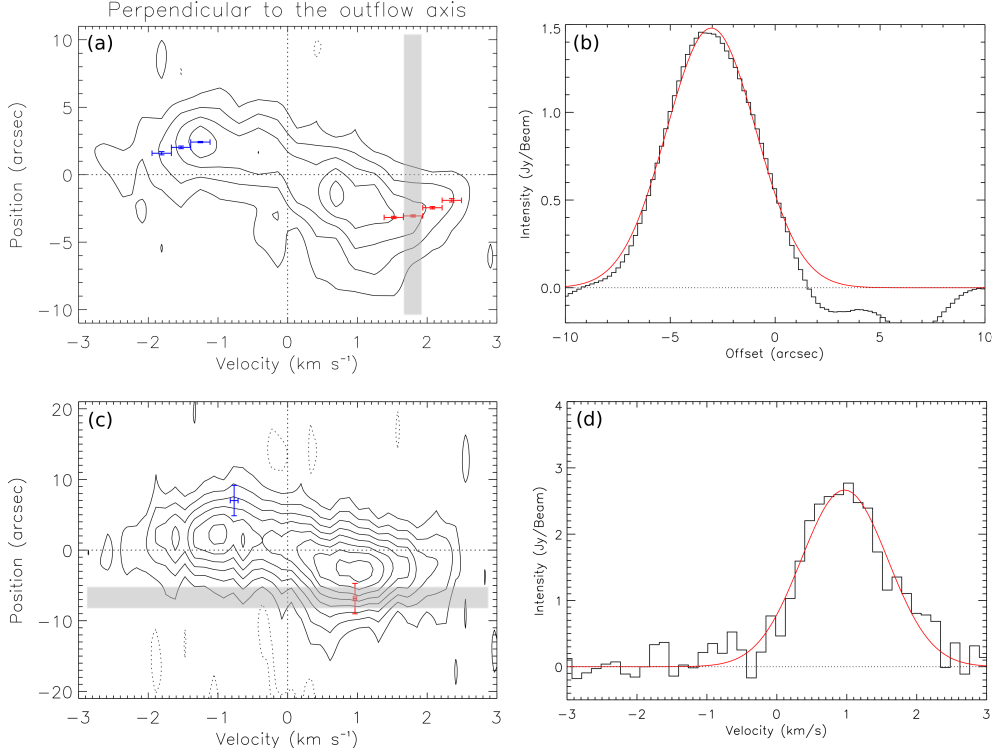


Figure 4.8 Schematic representation of our method to derive rotational velocities as a function of radius. (a) P–V diagram of L1489 IRS in the C¹⁸O (2–1) emission perpendicular to the outflow direction produced with the combined data (same as Figure 4.7). A hatched line represents the region where a Gaussian fitting to the intensity distribution at a given velocity channel is performed. (b) Intensity distribution (black histogram) along the hatched line and the result of the Gaussian fitting (red curve). Here the centroid position of the Gaussian function is regarded as the rotational radius at that rotational velocity. (c) P–V diagram of L1489 IRS perpendicular to the outflow direction produced with the subcompact data (same as Figure 4.7). A hatched line denotes the region where a Gaussian fitting to the spectrum at a given position is made. (d) Spectrum (black histogram) in the hatched region and the result of the Gaussian fitting (red curve). The centroid velocity of the Gaussian function is regarded as the rotational velocity at that rotational radius.

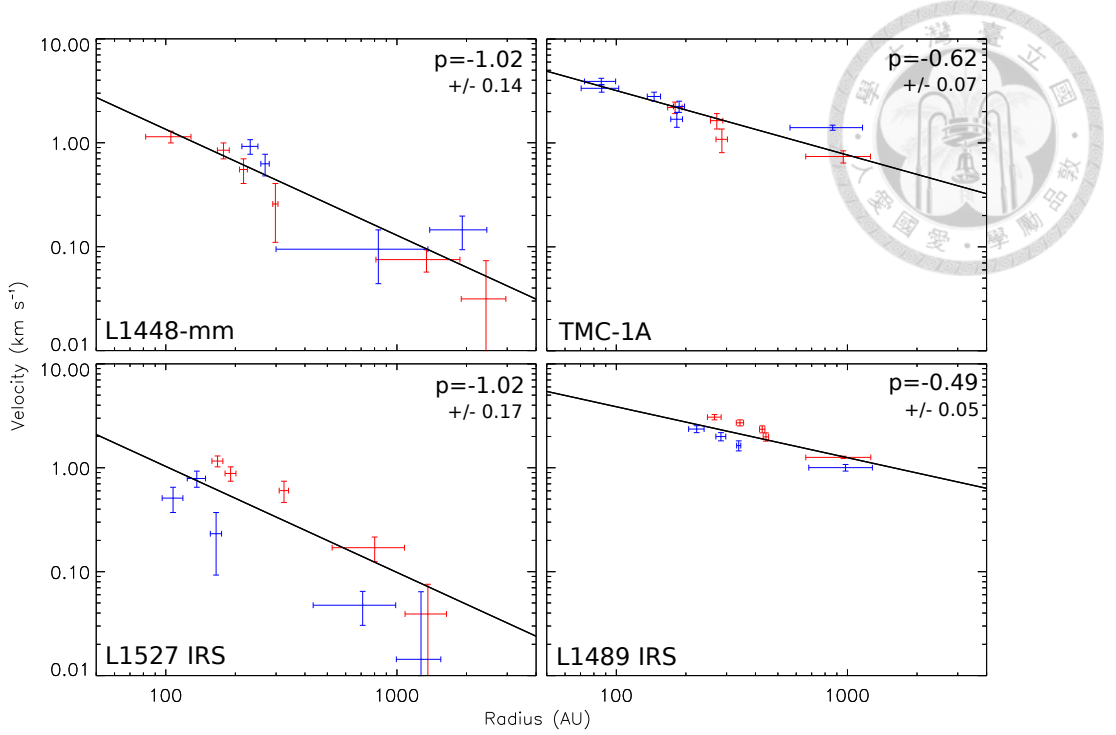



Figure 4.9 Plots of the derived rotational velocities as a function of radius in L1527 IRS, L1448-mm, TMC-1A, and L1489 IRS. Blue and red data points are taken from Figure 4.7 after the correction of the inclination angles. Solid lines show the best-fit power-law rotational profiles ($v \propto r^p$). The best-fit power-law index is shown in the upper-right corner of each panel.

4.6.2 Uncertainties of the Measured Rotational Profiles

Before we discuss the variety of the rotational profiles of the protostellar envelopes and the interpretation, it is necessary to quantitatively assess the possible errors of the rotational profiles derived from our method. The sources of errors should be both the over-simplification of our method to derive rotational profiles, and the finite observational resolutions and noises. In this subsection, the uncertainty of the rotational profiles derived from our method, due to both the over-simplification of our method and the observational limitations, will be discussed.

To examine the possible effect of the over-simplification of our method, we constructed axisymmetric models of protostellar envelopes (e.g., Shirley et al. 2000; Harvey et al. 2003; Brinch et al. 2007b), and performed radiative transfer calculations of the model envelopes and SMA observing simulations of the model image cubes. Then, our method to derive the rotational profiles was applied to the model P–V diagrams and the resultant rotational profiles were compared to the “genuine”

Table 4.4. Power-law Indices of the Rotational Profiles and the Estimated Protostellar Mass

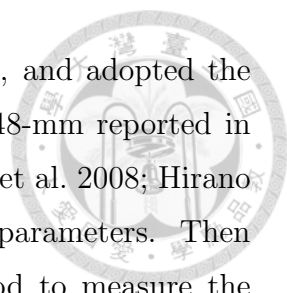


Source	p	Protostellar Mass (M_{\odot})
B335
IRAS 4B
L1527 IRS	-1.02 ± 0.17	...
L1448-mm	-1.02 ± 0.14	...
TMC-1A	-0.62 ± 0.07	1.1 ± 0.1^a
L1489 IRS	-0.49 ± 0.05	1.8 ± 0.2^a

^aThe estimated protostellar mass is sensitive to the inclination angle by $1/\sin^2(i)$.

rotational profiles. Details of these model calculations and simulations are described in Appendix 4.9.2. First, a model of an infalling envelope without any rotational motion was tested, and it is confirmed that in this case our method does not deduce any "artificial" rotational profile. Second, a model of a rotating envelope without any infalling motion was tested, and it is verified that the rotational power-law index derived from our method is consistent with the "real" power-law index. Third, several cases of envelopes with both infalling and rotational motions were tested. In these cases, the synthetic vectors of the rotational and infalling motions can contribute to the line-of-sight velocities along the envelope major axes, and thus the P–V diagrams along the major axes do not reflect only the rotational motions but also the infalling motions. In these cases our method could produce artificially shallower rotational power-law indices than the genuine rotational power-law indices (i.e., $p_{\text{ob}} > p_{\text{real}}$). The magnitude of the distortion of the rotational power-law indices depends on the vertical structures ("thickness") of the envelopes, inclinations, ratios between the infalling and rotating motions, and the observational angular resolutions.

In the case of L1527 IRS and L1448-mm there are velocity gradients along the outflow directions (see Fig. 4.1, 4.3, and 4.4), which could be due to the infalling motions of the envelopes. Thus, the "genuine" rotational power-law indices in these sources could be steeper than those listed in Table 4.4. To estimate the level of the possible distortion of the rotational profiles of L1527 IRS and L1448-mm, we



constructed models of infalling and rotating flattened envelopes, and adopted the protostellar masses and the inclinations of L1527 IRS and L1448-mm reported in the literatures (Ohashi et al. 1997a; Girart & Acord 2001; Tobin et al. 2008; Hirano et al. 2010) and the rotational profiles we measured as model parameters. Then we generated the model P–V diagrams and applied our method to measure the rotational power-law indices. These simulations show that the magnitude of the possible distortion of the rotational power-law indices of L1527 IRS and L1448-mm ranges from 2σ (i.e., $p_{\text{real}} = p_{\text{ob}} - 2\sigma$) to no distortion, where 1σ is the uncertainty of the power-law indices due to the finite observational resolutions and noises. On the other hand there are no clear velocity gradients along the outflow directions in L1489 IRS and TMC-1A, and thus these sources are likely close to the "pure rotation" case. In conclusion, although the contaminations from the infalling motions could distort the rotational power-law indices of L1527 IRS and L1448-mm to artificially shallower values, the differences of the rotational profiles among our sources, i.e., no detectable rotation in B335 and IRAS 4B, $V_{\text{rot}} \propto r^{-1}$ or steeper in L1527 IRS and L1448-mm, and $V_{\text{rot}} \propto r^{-0.5}$ in L1489 IRS and TMC-1A, are still valid.

Next, we will examine the effects of the observational limitations on the rotational profiles deduced from our method. In our method either an intensity distribution at a given velocity channel or a spectrum at a given position in the P–V diagrams is fitted with a Gaussian function. In the former case the velocity channel width can be regarded as the uncertainty of the rotational velocity, while in the latter case the observational spatial resolution as the uncertainty of the rotational radius. The uncertainties of the rotational radius in the former case and the rotational velocity in the later case were estimated by a Monte-Carlo method. Artificial random noises at the same level as that of our real observational noises were added to the observational P–V diagrams, and then our method was applied to the modified P–V diagrams with the additional artificial random noises. This process was repeated for 10,000 times, and the probability distributions of the rotational radius and velocity were obtained. The widths of the probability distributions demonstrate how sensitive the measurement of the rotational radius and velocity are to the noises, and provide the 1σ uncertainties. To derive the errors of the power-law indices of the rotational profiles, we varied each data point (i.e., the rotational radius and velocity) randomly within its uncertainty, performed the power-law fitting to these varied measurements

with weights by their uncertainties, and repeated this process for 10,000 times. Then a Gaussian function was fitted to the obtained probability distribution of the power-law index, and the peak position and the 1σ width were adopted as the best-fit value and the uncertainty of the power-law index, respectively. We also varied the number of the repetitions by a factor of five, and we confirmed that 10,000 times are sufficiently large to ensure the statistical significance.

Our analysis is based on the two-dimensional P–V diagrams, and an error of the adopted position angles of the outflow axes may also introduce an additional source of uncertainties to our analysis. To examine the uncertainty due to the error of the outflow directions, the position angles of the P–V diagrams were changed by 10° , and the same method was applied. We found that the variation of the best-fit power-law indices due to the 10° error of the outflow directions is less than the uncertainty due to the random noises. Indeed, the differences between the adopted outflow directions and the minor axes of the millimeter continuum emission observed with the SMA at an angular resolution $\lesssim 1''$ (Brinch et al. 2007a) are less than 10° . We also note that errors of the adopted V_{sys} could influence the fitting results. It is found that an error of 0.1 km s^{-1} in V_{sys} varies the best-fit value of the power-law indices by $10\% - 15\%$, comparable to the uncertainty due to the random noise. V_{sys} of our target sources were measured at velocity resolutions ranging from ~ 0.1 to $\sim 0.3 \text{ km s}^{-1}$ (Ohashi et al. 1997a; Hogerheijde et al. 1998; Curiel et al. 1999; Chapter 3), except for that of L1448-mm, which was measured at a velocity resolution of $\sim 0.6 \text{ km s}^{-1}$ (Volgenau et al. 2006). The accuracy of the measured V_{sys} can be expressed as $\sim \Delta V/(S/N)$, where ΔV denotes the velocity resolution and S/N the signal-to-noise ratio of the line emission, and is found to be better than 0.1 km s^{-1} for all of our sources. In L1527 IRS, the adopted V_{sys} ($= 5.7 \text{ km s}^{-1}$) is in between the central two peaks at $V \sim -0.3$ and 0.2 km s^{-1} in the subcompact P–V diagram. In L1448-mm, V_{sys} is coincident with the velocity of the emission peak in the P–V diagram. In TMC-1A and L1489 IRS, the mean velocities of the C^{18}O (2–1) emission at the protostellar positions are consistent with V_{sys} (Fig. 4.1). These results suggest that V_{sys} measured by the single-dish observations match those of the inner regions observed with the SMA, and that the errors of the adopted V_{sys} are unlikely to affect the estimates of the rotational power-law indices.

Finally, we note the present method is based on the assumption that the pro-

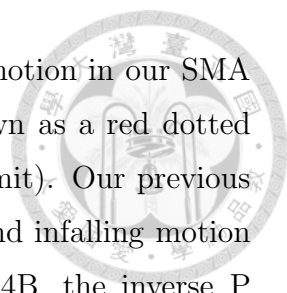
protostellar envelopes are axisymmetric around their rotational axes. If protostellar envelopes are non-axisymmetric and filamentary for example, the velocity gradients in the P–V diagrams perpendicular to the outflow directions could be caused by other kinematics instead of rotational motions, such as infalling flow along the filaments (Tobin et al. 2012b).

4.7 Discussion

4.7.1 Variations of the Rotational Motions around the Protostellar Sources

Our SMA observations of six representative protostellar sources and the data analysis have unveiled the variations of the rotational motions of the envelopes on the 100 to 1000 AU scales. Toward B335 and IRAS 4B no detectable velocity gradients perpendicular to the outflow directions are seen, suggesting absence of the rotational motions in the envelopes. It is possible that in these sources CO depletion occurs in the envelope mid-planes and thus the rotational motions are not detected with the present C¹⁸O (2–1) observations. However, in B335 the C¹⁸O (2–1) emission is elongated perpendicularly to the outflow direction around the systemic velocity, similar to the 1.3 mm dust continuum emission (Chapter 2 and 3). Furthermore, the temperature of the envelope mid-plane in B335 is estimated to be higher than 20 K, the CO sublimation temperature (Chapter 3), and the envelope around IRAS 4B has been identified as a "hot corino" ($T_k \sim 100$ K; Bottinelli et al. 2007). Therefore, it is unlikely that CO depletion occurs and affects the observed kinematics in the envelopes around B335 and IRAS 4B. Although there is possible distortion of the rotational power-law indices of L1527 IRS and L1448-mm due to the contamination from the infalling motions as discussed above, the difference of the rotational profiles from those around the other sources is likely real. In the case of L1489 IRS and TMC-1A no infalling motion is identified in our data and thus the derived rotational power-law indices are probably valid. In this subsection, the variations of the rotational motions in the protostellar envelopes and their possible interpretation will be discussed.

Figure 4.10 plots of our measured rotational velocities and radii. The envelopes



around B335 and IRAS 4B do not show any sign of rotational motion in our SMA data, and the detection limit of the rotational velocities is drawn as a red dotted line in Figure 4.10 (see Chapter 2 for details of the detection limit). Our previous SMA observations of B335 in the C^{18}O (2–1) emission have found infalling motion in the 1000 AU scale envelope (Chapter 2 and 3). In IRAS 4B, the inverse P Cygni profile seen in the H_2CO ($3_{12}-2_{11}$) emission suggests the presence of infalling motion (Di Francesco et al. 2001). Therefore, in the envelopes around B335 and IRAS 4B there are infalling motions but little rotation. The envelopes around the other sources (L1527 IRS, L1448-mm, TMC-1A, and L1489 IRS) show detectable rotational motions. The rotational velocities around L1489 IRS and TMC-1A are higher than those around L1527 IRS and L1448-mm at the same radii, and the rotational profiles of L1489 IRS and TMC-1A ($p \sim -0.5$) are flatter than those of L1527 IRS and L1448-mm ($p \sim -1$ or steeper). A rotational profile with $p = -1$ denotes rotational motion with a conserved angular momentum in a dynamically infalling envelope (Ulrich 1976; Cassen & Moosman 1981; Terebey et al. 1984; Basu et al. 1998). In fact, previous interferometric molecular-line observations of L1527 IRS (Ohashi et al. 1997a) and L1448-mm (Curiel et al. 1999) have identified the infalling motions in the envelopes. On the other hand, a rotational profile with $p = -0.5$ implies Keplerian rotation, and the presence of a Keplerian disk in L1489 IRS has been reported by Brinch et al. (2007a).

For comparison, rotational velocities around the other Class 0 and I protostars taken from the literatures are also plotted in Figure 4.10. Around Class I protostars IRS 63, Elias 29, and L1551 NE, the presence of Keplerian disks has been reported with the SMA observations (Lommen et al. 2008; Takakuwa et al. 2012), and the rotational velocities at the disk outer radii appear to be consistent with those around L1489 IRS and TMC-1A. Around a Class I protostar HH 111, Lee (2010) measured the rotational velocities of the surrounding envelope and claimed the presence of the transition of the rotational profile from $V_{\text{rot}} \propto r^{-1}$ to $V_{\text{rot}} \propto r^{-0.5}$ (black solid lines in Figure 4.10). The reported Keplerian rotation at inner radii around HH 111 also appears to be consistent with the Keplerian rotation around L1489 IRS and TMC-1A. On the other hand, the presence of a possible Keplerian disk around L1527 IRS has been reported (Tobin et al. 2012a), and the rotational velocity at the disk outer radius is consistent with that from the extrapolation of our derived rotational pro-

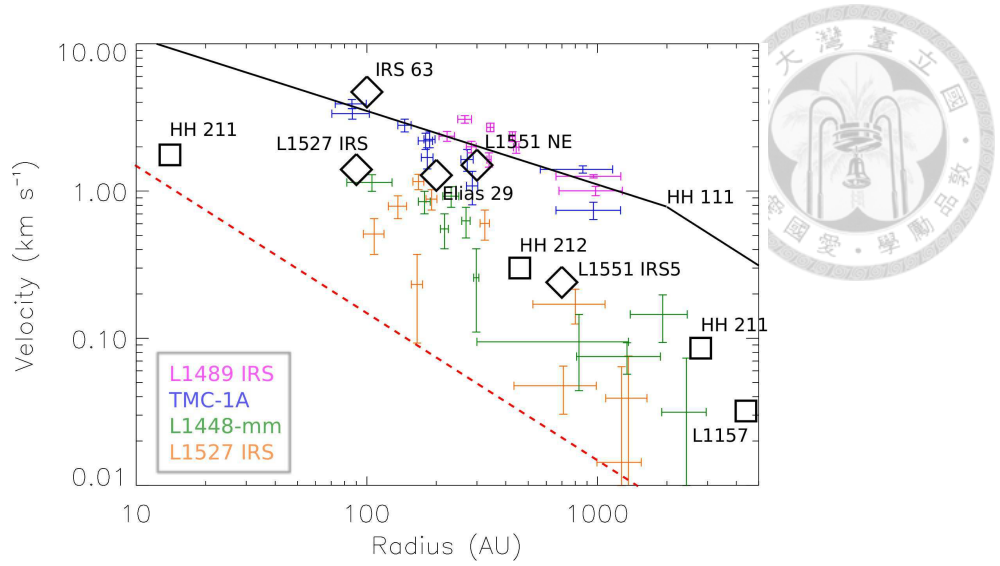


Figure 4.10 Plots of the rotational velocities as a function of radius in L1527 IRS, L1448-mm, TMC-1A, and L1489 IRS, and comparison with those of other Class 0 and I protostars taken from the literatures. The data points of L1527 IRS, L1448-mm, TMC-1A, and L1489 IRS are shown in orange, green, blue, and magenta colors, respectively. A red dotted line shows the detection limit of our SMA observations (Chapter 2), and rotational velocities around B335 and IRAS 4B are likely below this line. A black solid line presents the rotational profile of HH 111, a Class I protostellar source (Lee 2010). Open squares and diamonds show rotational velocities at the representative radii in Class 0 and I protostellar sources, respectively (Momose et al. 1998; Belloche et al. 2002; Lee et al. 2006, 2009; Lommen et al. 2008; Chiang et al. 2010; Tanner & Arce 2011; Takakuwa et al. 2012; Tobin et al. 2012a).

file of L1527 IRS to the inner radii. Infalling motions in the surrounding envelopes have been identified around Class I protostar L1551 IRS 5 (Momose et al. 1998) and Class 0 protostar HH 212 (Lee et al. 2006), and their rotational velocities are consistent with those around L1448-mm and L1527 IRS. Around Class 0 protostars HH 211 and L1157-mm, rigid-body rotation on thousands of AU scale in the protostellar envelopes have been proposed (Chiang et al. 2010; Tanner & Arce 2011), while their rotational velocities at radii of few thousand AU appear to be consistent with those around L1448-mm and L1527 IRS. Thus, the rotational velocities of the Keplerian disks around the Class I sources are higher than those around the Class 0 and I sources exhibiting non-Keplerian rotation on hundreds of AU scales. Our measured rotational profiles combined with the rotational velocities reported in the literatures demonstrate that the rotational motions of the envelopes on the 100 to 1000 AU scales around the protostars can be classified into the three categories; 1) no detectable rotation but infalling motions (Class 0 protostars, B335 and IRAS

4B), 2) rotational motions with $V_{\text{rot}} \propto r^{-1}$ in the infalling envelopes (Class 0 and I protostars, L1527 IRS, L1448-mm, L1551 IRS 5, and HH 212), 3) Keplerian rotation (Class I protostars, L1489 IRS, TMC-1A, IRS 63, Elias 29, HH 111, and L1551 NE), and the protostellar sources in the later evolutionary stages exhibit faster rotational motions.

In the following, we will show that the three categories of the rotational motions of the envelopes can be interpreted with a conventional, analytical picture of evolution of a protostellar envelope into Keplerian-disk formation (e.g., Shu et al. 1987). In the conventional picture of an infalling envelope, each infalling material conserves its angular momentum, and its rotational velocity (v_ϕ) is described as,

$$v_\phi = \sqrt{\left(\frac{GM}{r}\right)\left(1 - \frac{\cos \theta}{\cos \theta_0}\right)} \frac{\sin \theta_0}{\sin \theta}, \quad (4.1)$$

and

$$r = \frac{r_d \cos \theta_0 \sin^2 \theta_0}{\cos \theta_0 - \cos \theta} = \frac{r_d \sin^2 \theta_0}{1 - \cos \theta / \cos \theta_0}, \quad (4.2)$$

where G is the gravitational constant, M is the central protostellar mass, r_d is the centrifugal radius in mid-plane, and θ_0 is the initial polar angle of the infalling material (see Equation 9 & 10 in Ulrich 1976). Therefore, the rotational velocity can be expressed as $v_\phi = \sqrt{GM r_d} (\sin^2 \theta_0 / \sin \theta) r^{-1}$, which yields a rotational profile with a power-law index of -1 close to the mid-plane (i.e., $\sin^2 \theta_0 / \sin \theta \sim 1$). The rotational velocity of the infalling material increases as the material approaches to the central protostar, and eventually becomes comparable to the infalling velocity. At this point, the infalling material becomes centrifugally supported and forms a Keplerian disk. The presence of such a rotational profile, $p = -0.5$ at the inner radii and $p = -1$ at the outer radii, has been reported in HH 111 (Lee 2010). When the inside-out collapse takes place in an initial dense core with rigid-body rotation as seen in the NH_3 cores (Goodman et al. 1993), the innermost part of the dense core with the smallest angular momentum collapses first. Because of the smallest angular momentum, the rotational velocity of the infalling material is small even though it becomes larger in the vicinity of the central protostar. As a result, most of the infalling materials accrete onto the central protostar without forming a Keplerian disk. As the expansion wave propagates outward in the dense core, an outer part of the dense core with a larger angular momentum starts to collapse. Because of the larger angular momentum, the rotational velocity becomes large enough to form

a Keplerian disk before the infalling material accretes onto the central protostar. When the expansion wave propagates further, materials with even larger angular momenta start to collapse, and they become centrifugally supported at larger radii, expanding the size of the Keplerian disk.

To present this scenario analytically, we followed the calculation by Terebey et al. (1984) and Basu et al. (1998), and calculated the expected rotational profiles at different evolutionary stages of the collapse of a dense core. The initial condition is assumed to be an isothermal singular sphere with a rigid-body rotation. The initial density profile of the sphere $\rho(r)$ is

$$\rho(r) = \frac{c_s^2}{2\pi G} r^{-2}, \quad (4.3)$$

where c_s is the sound speed (Shu 1977). The enclosed mass as a function of radius $M(r)$ is given by

$$M(r) = \frac{2c_s^2}{G} r. \quad (4.4)$$

The initial distribution of the specific angular momenta $j(r)$ is

$$j(r) = \omega r^2, \quad (4.5)$$

where ω is the angular velocity of the rigid-body rotation. On the assumption that the angular momentum is conserved during the collapse, the Keplerian radius (r_d) of each mass shell initially at a radius of r can be expressed as,

$$\frac{j(r)^2}{r_d^3} = \frac{GM(r)}{r_d^2}. \quad (4.6)$$

On the assumption of the steady mass accretion ($\equiv \dot{M}$), the Keplerian radius as a function of time t can be derived from Equation 4.6 as

$$r_d = \frac{j(r)^2}{GM(r)} = \frac{\omega^2 G^3 M(r)^3}{16c_s^8} = \frac{\omega^2 G^3 \dot{M}^3}{16c_s^8} t^3. \quad (4.7)$$

This is the solution by Terebey et al. (1984). Basu et al. (1998) performed the same calculation with the initial rotation of a constant velocity, and their solution is $r_d \propto t$. Equation 4.7 implies that when a central protostar + disk system increases its mass to $M(r)$ after a time interval of $t = M(r)/\dot{M}$, the material initially at a radius of r has collapsed and carried an angular momentum of $j(r)$ toward the center, and the rotational velocity of the material reaches its Keplerian velocity at a radius

of r_d . On the assumption that the gravity is dominated by the central protostar, the rotational profile follows $V_{\text{rot}} \propto r^{-0.5}$ inside r_d , i.e., Keplerian rotation. In the dynamically infalling region and outside the Keplerian radius (i.e., $r_d < r < c_s t$), the infalling material is accelerated to supersonic, and the initial profile of the specific angular momentum shown by Equation 4.5 is altered. Then, the radial profile of the specific angular momentum becomes constant asymptotically toward the inner radii (see Figure 2 in Terebey et al. 1984), and the rotational profile of the infalling material becomes $V_{\text{rot}} \propto r^{-1}$ as derived from Equation 4.1 and 4.2. Therefore, the rotational profile as a function of time can be described as

$$V_{\text{rot}}(r) = \sqrt{\frac{G\dot{M}t}{r_d^2}} \times \begin{cases} \left(\frac{r}{r_d}\right)^{-0.5} & r \leq r_d \\ \left(\frac{r}{r_d}\right)^{-1.0} & r_d \leq r < r_{\text{infall}} \end{cases}, \quad (4.8)$$

where r_d is evaluated by Equation 4.7 and r_{infall} is the location of the expansion wave ($= c_s t$; Shu 1977). Note that the material located closer to the polar axis possesses a smaller angular momentum, and the calculated rotational profile is applied to the material on the equatorial plane. Also note that the effect of the magnetic field and outflows, and the mass distribution inside r_d are not considered in this calculation.

The expected rotational profiles at different collapse stages calculated from Equation 4.8 are shown as solid lines in Figure 4.11. Here the sound speed c_s is assumed to be $\sim 0.2 \text{ km s}^{-1}$ (i.e., the gas kinematic temperature is 10 K), and thus the mass accretion rate \dot{M} ($= c_s^3/G$) is $\sim 2 \times 10^{-6} M_\odot \text{ yr}^{-1}$ (Shu 1977). The angular velocity ω is assumed to be $6.5 \times 10^{-14} \text{ s}^{-1}$, which corresponds to $2 \text{ km s}^{-1} \text{ pc}^{-1}$ and is similar to the mean magnitude of the large-scale rotational motions of dense cores and protostellar envelopes within a factor of two (Goodman et al. 1993; Gaselli et al. 2002; Tobin et al. 2011). Note that the expected rotational profile is sensitive to the initial conditions, and these parameters are adopted with an intent to demonstrate the evolutionary trend rather than to constrain the initial conditions of star formation. As long as the initial rotational profile shows an increasing specific angular momentum with the increasing radius, the overall evolutionary trend deduced here is valid, although the time dependence should be different. In the calculation the steady mass accretion is assumed, although the mass accretion is likely episodic and its rate may change with time (e.g., Evans et al. 2009). A time-dependent mass accretion rate do not affect the evolutionary trend of the rotational profile described by Equation 4.8.

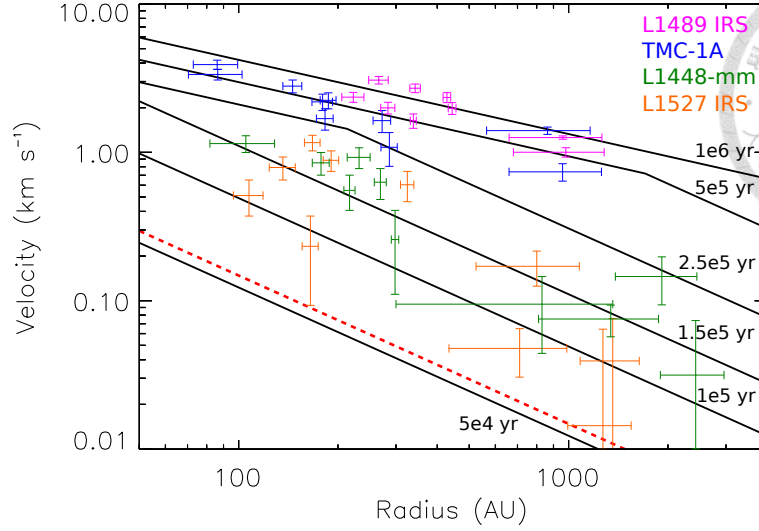


Figure 4.11 Same as Figure 4.10 but for comparison with the expected rotational profiles calculated from our analytical model (see texts for details). Solid lines show the expected rotational profiles at different evolutionary stages of the collapse of a dense core. The breaking points in the expected rotational profiles at $t = 2.5 \times 10^5$ and 5×10^5 yr, where the power-law indices change from -0.5 to -1 , present the radii of the Keplerian disks at those evolutionary stages. At $t < 1.5 \times 10^5$ yr, the radii of the Keplerian disks are smaller than 45 AU, and the breaking points are not seen in the plots.

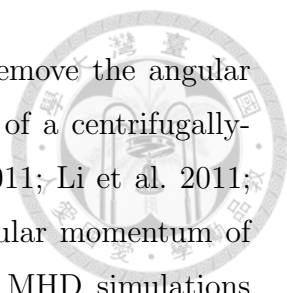
As shown in Figure 4.11, the rotational velocities of our model increase with time. At $t < 5 \times 10^4$ yr, the rotational velocities are slow and below our detection limit. This applies to the case of B335 and IRAS 4B, where their rotational motions are not detected but the infalling motions are likely present. At $t < 1.5 \times 10^5$ yr, the radius of the Keplerian disk is less than 45 AU and cannot be seen in this plot, and the material at radii between 45 and 6000 AU exhibits a rotational profile with a power-law index of -1 . L1527 IRS and L1448-mm, which exhibit steep rotational profiles on the 100 to 1000 AU scales, are fit to this stage. Recent observations of L1527 IRS in the C^{18}O (2–1) emission line with the Atacama Large Millimeter/Submillimeter Array (ALMA) have revealed that the rotational profile with a power-law index of -1 extends down to ~ 50 AU (Ohashi et al. 2013 in prep.), consistent with the expected rotational profile at $t \sim 1.5 \times 10^5$ years. On the other hand, recent CARMA observations of L1527 IRS have found a possible Keplerian disk with a radius of ~ 90 AU (Tobin et al. 2012a). Although the reason for the possible discrepancy between the ALMA and CARMA results is unclear, the presence of the Keplerian disk with the radius of ~ 90 as well as our measured rotational profile with the SMA can be

explained by our model with a factor of two to three larger ω . At $t = 2.5 \times 10^5$ yr, the radius of the Keplerian disk, shown as a breaking point in the rotational profile, grows to ~ 200 AU. The power-law index of the rotational profile at radii less than 200 AU has changed from -1 to -0.5 , and that at radii larger than 200 AU remains -1 . At $t = 5 \times 10^5$ yr, the radius of the Keplerian disk grows to more than 1000 AU, which is consistent with the data points of L1489 IRS and TMC-1A. Thus, the evolutionary sequence of the rotational profile predicted by our simple calculations matches the observed rotational profiles.

We stress here that the time scales shown in our analytical calculation are merely an indicator of the collapse stages, and do not represent the real ages of the individual sources. As discussed above, the evolutionary time scale is sensitive to the initial conditions of dense cores, such as the initial angular velocity, the initial rotational profile, and the sound speed and hence the mass accretion rate. In fact, among our sample L1448-mm is a factor of two to five more luminous than the other sources and drives energetic molecular outflows (Bachiller 1990; Hirano et al. 2010), suggesting that the mass accretion rate onto L1448-mm is higher than that onto the other sources. Furthermore, the locations of our target sources span different types of star-forming regions from an isolated Bok globule, an isolated star-forming region in Taurus, to a cluster-forming region in Perseus. The different environments are likely to affect the initial conditions of the dense cores and hence the real time scale of the evolution of the protostellar envelopes. On the other hand, we have unveiled three categories of the envelope kinematics from our target sources as well as the sources from the literatures as described above. It is unlikely that these categories merely reflect the "individuality" of each source. We suggest that the three types of the envelope kinematics reflect evolution of the protostellar envelopes, and that our simple analytical model provides at least a qualitative guideline of evolution of protostellar envelopes to Keplerian-disk formation.

4.7.2 Observations and MHD Simulations of Disk Formation

Recent MHD simulations of disk formation in a collapsing dense core have shown that if the mass-to-flux ratio is less than 10 times of the critical value ($1/2\pi\sqrt{G}$;



Nakano & Nakamura 1978), the magnetic field can efficiently remove the angular momentum of the collapsing material and suppress the growth of a centrifugally-supported disk (e.g., Mellon & Li 2008, 2009; Machida et al. 2011; Li et al. 2011; Joos et al. 2012; Dapp et al. 2012). Because a part of the angular momentum of the collapsing material is removed by magnetic braking, these MHD simulations predict a shallower ($p > -1$) rotational profile of infalling envelopes, and its power-law index depends on the efficiency of magnetic braking (e.g., Mellon & Li 2008, 2009). Observations of the Zeeman splitting of the OH line toward 34 dark cloud cores show that the mean mass-to-flux ratio is $\sim 4 - 5$ (Troland & Crutcher 2008), which probes the outer parts of the cores with a mean gas density of $10^3 - 10^4 \text{ cm}^{-3}$. Observations of the Zeeman splitting of the CN line toward massive star-forming regions have shown that the mean mass-to-flux ratio is 1–4 in the denser regions ($n_{\text{H}_2} \sim 10^4 - 10^6 \text{ cm}^{-3}$), but the result may not be applied to the case of low-mass star-forming regions where the physical conditions are likely different from those in the massive star-forming regions. In the MHD simulations adopting these observed mass-to-flux ratios, efficient magnetic braking restricts the radii of Keplerian disks to be less than 10 AU. Incorporation of non-ideal MHD effects in the simulations cannot reduce the efficiency of magnetic braking to the level that Keplerian disks with radii of hundreds of AU can form (e.g., Mellon & Li 2009; Li et al. 2011; Dapp et al. 2012). The dissipation of protostellar envelopes due to outflows or mass accretion, which reduces the efficiency of magnetic braking, is proposed to enable the formation of large-scale Keplerian disks (e.g., Mellon & Li 2008; Machida et al. 2011). Machida et al. (2011) have calculated the evolution of magnetized collapsing cores until the stage when most of the mass of the envelopes are ejected or accreted, and have formed centrifugally-supported disks with radii more than 100 AU. However, in their simulations, the centrifugally-supported disks are more massive than the protostars by a factor of two to five. Such massive disks have not been observed around Class I protostars, and their rotational motions deviate from Keplerian rotation and show $p > -0.5$ due to the self-gravity. The other possible mechanism to reduce the efficiency of magnetic braking is the misalignment between the direction of the magnetic field and the rotational axes of dense cores (e.g., Joos et al. 2012). Recent CARMA survey of polarized dust continuum emission at 1.3 mm shows that the inferred directions of the magnetic field in low-mass protostellar

sources are not tightly aligned with the outflow directions on an 1000 AU scale (Hull et al. 2012), which could support this scenario to reduce the efficiency of magnetic braking.

Our SMA observations of L1448-mm, L1527 IRS, TMC-1A, and L1489 IRS found that the angular momenta of the collapsing cores are conserved and efficiently transferred to the inner radii, and the centrifugally-supported disks with radii of hundreds of AU have been formed in the Class I stage. These results suggest that magnetic braking has already become minimal in the Class 0 to Class I stages. On the other hand, the absence of detectable rotational motions in B335 and IRAS 4B, which are in the early collapse stage, could suggest the presence of magnetic braking in the early collapse stage. The efficiency of magnetic braking and its time evolution in protostellar envelopes are still controversial, and currently there is no direct measurement of the mass-to-flux ratio of protostellar envelopes on an 1000 AU scale around low-mass protostars. The magnetic fields toward low-mass protostellar sources are mostly measured with single-dish observations at an angular resolution of $\sim 10''$ (> 1400 AU; e.g., Attard et al. 2009; Davidson et al. 2011), insufficient to resolve the structures of the magnetic fields on the 1000 AU scale. The magnetic field in NGC 1333 IRAS 4A, a low-mass protobinary system with a separation of $\sim 2''$ (500 AU), has been observed at a high angular resolution of $1''.6$ (400 AU; Girart et al. 2006). However, NGC 1333 IRAS 4A drives two outflows in different directions (e.g., Choi 2005), and hence the relation between the kinematics of the inner envelope and the magnetic field is likely complicated. To investigate the role of the magnetic field in the formation of Keplerian disks, observations revealing the structure and strength of the magnetic field on hundreds of AU scale around low-mass protostars as well as precise measurements of envelope rotational profiles for a statistically significant sample are crucial. Recently Koch et al. (2012a, b) developed a method to measure the mass-to-flux ratio by the gradients of polarization directions and intensity distributions by using the SMA data of high-mass star-forming regions. Such studies can be applied to inner envelopes around low-mass protostars with future ALMA observations.

4.7.3 Keplerian Disks around Class I Protostars

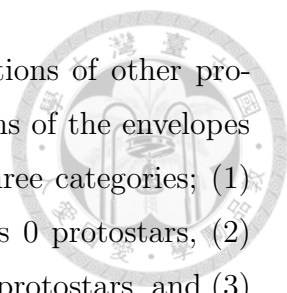
Our measured rotational power-law indices suggest that TMC-1A and L1489 IRS are surrounded by Keplerian disks. From the Keplerian rotational profile ($V_{\text{rot}} = \sqrt{GM_*}r^{-0.5}$), the central protostellar masses are estimated to be $1.1 \pm 0.1 M_{\odot}$ in TMC-1A and $1.8 \pm 0.2 M_{\odot}$ in L1489 IRS on the assumption that the inclination angles of the Keplerian disks are 30° and 50° , respectively (Table 4.1). From the total flux of the 1.3 mm continuum emission, the masses of the Keplerian disks around TMC-1A and L1489 IRS are estimated to be $0.06 - 0.025 M_{\odot}$ and $0.02 - 0.007 M_{\odot}$ with dust temperatures of $15 - 30$ K (Appendix 4.9.1). The estimated masses are approximately consistent with previous estimates of the disk masses in TMC-1A ($0.035 - 0.005 M_{\odot}$; Jørgensen et al. 2009; Eisner 2012) and L1489 IRS ($0.018 - 0.004 M_{\odot}$; Brinch et al. 2007a; Jørgensen et al. 2009; Eisner 2012). The disk masses around TMC-1A and L1489 IRS are orders of magnitude lower than the protostellar masses, and hence the disk self-gravity is indeed negligible. Keplerian disks around more evolved sources (i.e., T Tauri stars) have masses ranging from 10^{-1} to $10^{-4} M_{\odot}$ (e.g., Guilloteau et al. 2011) and radii ranging from 100 to 800 AU (e.g., Simon et al. 2000). Our results of TMC-1A and L1489 IRS suggest that Keplerian disks with sizes and masses comparable to those of classical disks have formed in the Class I stage. The presence of similar Keplerian disks around other Class I protostars has also been reported (Brinch et al. 2007a; Lommen et al. 2008; Jørgensen et al. 2009; Takakuwa et al. 2012).

If the mass accretion rate is constant ($\sim c_s^3/G$; Shu 1977) in TMC-1A and L1489 IRS, their ages ($\equiv M_*/\dot{M}$) are estimated to be 6×10^5 and 9×10^5 yr, respectively. In the MHD simulations made by Machida et al. (2011), at $\sim 10^5$ yr, the radii of centrifugally-supported disks increase to $100 - 1000$ AU (depending on the mass-to-flux ratio), which are comparable to the radii of the Keplerian disks in TMC-1A and L1489 IRS. However, the masses of the centrifugally-supported disks in the MHD simulations grow to $\gtrsim 0.1 M_{\odot}$ and are larger than the protostellar mass by a factor of two to five. Further theoretical efforts are required to reproduce the observationally-identified Keplerian disks around Class I protostars.

4.8 Summary

We have performed imaging and analysis of the SMA observations in the C^{18}O (2–1) emission line toward three Class 0 (B335, IRAS 4B, and L1448-mm), one Class 0/I (L1527 IRS), and two Class I protostars (TMC-1A, and L1489 IRS). The aim of the present research is to study the rotational motions of the protostellar envelopes on 100 to 1000 AU scales, and to investigate formation process of Keplerian disks. Our main results are summarized below.

1. The C^{18}O (2–1) emission shows $\sim 1500 - 2000$ AU scale, centrally-peaked condensations associated with the protostars plus extensions toward the outflow directions, and likely traces the protostellar envelopes with the contamination from the outflows. The protostellar envelopes around the two Class 0 protostars, B335 and IRAS 4B, show no detectable velocity gradient perpendicular to the outflow directions. The protostellar envelopes around L1527 IRS (Class 0/I) and L1448-mm (Class 0) show substantial velocity gradients, and those around the Class I protostars, TMC-1A and L1489 IRS, show the largest velocity gradients among the sample. The velocity gradients perpendicular to the outflow directions most likely trace the rotational motions of the protostellar envelopes around the protostars.
2. We developed a simple analytical method to measure the rotational velocities of the protostellar envelopes as a function of radius ($V_{\text{rot}} \propto r^p$) over the 100 – 1000 AU scales from the observed P–V diagrams perpendicular to the outflow directions. Possible systematic errors of the measured rotational profiles due to the over-simplification of our method are evaluated with models of infalling and rotating envelopes and the observing simulations of the model images. With a Monte-Carlo method errors of the derived rotational profiles due to the observational noises and resolutions are also estimated. We found that L1527 IRS and L1448-mm exhibit rotational profiles with the power-law indices $p = -1.0 \pm 0.2$ and -1.0 ± 0.1 , respectively, or steeper if the contamination from the infalling motions affects the P–V diagrams perpendicular to the outflow directions. TMC-1A and L1489 IRS exhibit flatter rotational profiles with the power-law indices $p = -0.6 \pm 0.1$ and -0.5 ± 0.1 , respectively. B335 and IRAS 4B do not show any detectable rotational motion. These results,



as well as previous observational results of rotational motions of other protostellar envelopes, demonstrate that the rotational motions of the envelopes on the 100 to 1000 AU scales can be classified into the three categories; (1) infalling motion with little rotational motion around Class 0 protostars, (2) both infalling and rotational motions around Class 0 and I protostars, and (3) rotational motion without clear infalling motion around Class I protostars

3. We demonstrated that the three categories of the rotational motions of the protostellar envelopes can be reproduced with analytical calculations of the inside-out collapse model combined with rigid-body rotation and a conserved angular momentum. At the initial onset of the collapse the innermost part of the dense core with smaller angular momenta collapses first. As the expansion wave propagates outward, the envelope materials with larger angular momenta start to collapse. At the late stage of the collapse, more angular momenta transfer to the center, and Keplerian disks around protostars are formed. In reality the individual evolutions of the protostellar envelopes depend on the environmental conditions such as the magnitude of the initial rotational motion and sound speed, and it is difficult to sort the various protostellar sources along a common evolutionary track of a protostellar envelope. On the other hand, the three categories of the envelope kinematics found from our observations as well as from the literatures are unlikely to be explained merely by the "individuality" of each source. We suggest that the three types of the envelope kinematics reflect evolution of the protostellar envelopes, and that our simple analytical model provides at least a qualitative guideline of evolution of protostellar envelopes into Keplerian-disk formation.
4. Around TMC-1A and L1489 IRS Keplerian disks with the radii of hundreds of AU, comparable to those around T-Tauri stars, are present. The protostellar masses of TMC-1A and L1489 IRS are estimated to be 1.1 ± 0.1 and 1.8 ± 0.2 M_{\odot} , respectively, and the disk masses are estimated to be $0.005 - 0.035$ M_{\odot} and $0.007 - 0.02$ M_{\odot} . These results as well as results from recent millimeter and submillimeter interferometric observations of other Class I sources imply that Keplerian disks are already well developed in the Class I stage. Theoretical studies of disk formation including the realistic magnetic fields have trouble

reproducing these observationally-identified disks around Class I protostars, because magnetic breaking efficiently suppresses the disk formation. Sensitive observational measurements of strength and structures of the magnetic field are essential to refine theoretical studies of disk formation and to explain an increasing number of Keplerian disks around Class I protostars.

4.9 Appendix

4.9.1 1.3 mm Continuum Images

Figure 4.12 shows the 1.3 mm continuum images of our sample sources. The continuum images of IRAS 4B, L1527 IRS, L1448-mm, TMC-1A, and L1489 IRS were taken with the SMA compact and subcompact configurations, and that of B335 was taken with the SMA compact configuration. The spatial resolutions and the noise levels of these images are summarized in Table 4.5. 1.3 mm dust continuum emission is detected toward all the sources. In IRAS 4B, two dusty components, one associated with the primary source of the binary to the west (4B) and the other with the secondary (4B'), are seen. In L1448-mm, in addition to the central compact component associated with the protostellar source there are a secondary peak to the southeast and an extended emission component elongated along the outflow direction. The secondary peak is coincident with the redshifted C¹⁸O (2–1) clump to the southeast seen in the velocity channel maps (Fig. 4.4).

Two-dimensional Gaussian fittings were performed to the central components associated with the protostellar sources, and the total fluxes, deconvolved sizes, and the position angles are derived (Table 4.5). In IRAS 4B, B335, and L1489 IRS, the central components are elongated perpendicular to the outflow directions. In L1527 IRS, L1448-mm, and TMC-1A, the aspect ratios of the central components are larger than 0.75, and hence the elongation of the central components is not clear.

Toward TMC-1A and L1489 IRS Keplerian disks have been identified from the C¹⁸O (2–1) data. Assuming that the 1.3 mm dust continuum emission in TMC-1A and L1489 IRS arise from the Keplerian disks, the masses of the Keplerian disks can be estimated from the total 1.3 mm fluxes as;

$$M_d = \frac{F_\nu d^2}{\kappa_{1.3\text{mm}} B(T_{\text{dust}})}, \quad (4.9)$$

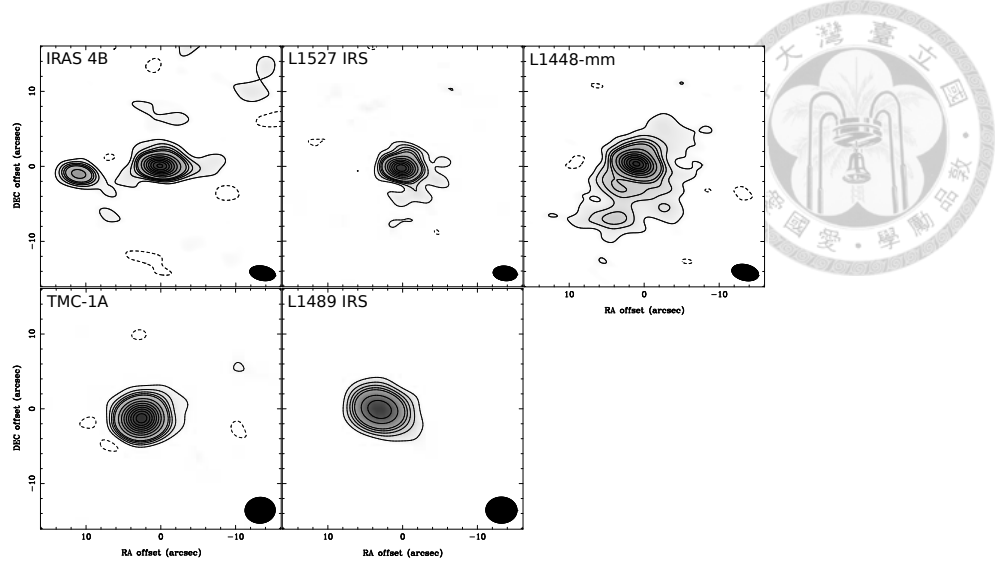


Figure 4.12 1.3 mm continuum images of B335, IRAS 4B, L1527 IRS, L1448-mm, TMC-1A, and L1489 IRS, made with the combined SMA data. A filled ellipse at the bottom-right corner in each panel presents the beam size. Contour levels are 3σ , 6σ , 9σ , 12σ , 15σ , and then in steps of 10σ . Table 4.5 summarizes the 1σ noise values.

Table 4.5. Summary of the 1.3 mm Continuum Observations

Source	Beam (P.A.)	RMS (mJy Beam ⁻¹)	Total Flux (Jy)	Deconvolved Size (P.A.)
B335	$3''.9 \times 3''.3$ (82°)	2	0.18	$4''.9 \times 2''.3$ (13°)
IRAS 4B	$3''.4 \times 1''.9$ (79°)	9	1.11	$2''.3 \times 1''.2$ (-77°)
L1527 IRS	$3''.2 \times 1''.9$ (84°)	2	0.21	$1''.4 \times 1''.2$ (-8°)
L1448-mm	$3''.6 \times 2''.1$ (77°)	2	0.26	$2''.1 \times 2''.0$ (-79°)
TMC-1A	$4''.0 \times 3''.5$ (-87°)	2	0.23	$1''.6 \times 1''.2$ (-71°)
L1489 IRS	$4''.2 \times 3''.5$ (89°)	1	0.07	$3''.7 \times 2''.0$ (67°)

where F_ν is the total flux, $\kappa_{1.3\text{mm}}$ is the dust mass opacity at 1.3 mm, T_{dust} is the dust temperature, and B is the Planck function. On the assumption that the frequency (ν) dependence of the dust mass opacity ($\equiv \kappa_\nu$) is $\kappa_\nu = 0.1 \times (\nu/10^{12})^\beta$ (Beckwith et al. 1990), the mass opacity at 1.3 mm is $0.023 \text{ cm}^2 \text{ g}^{-1}$ with $\beta = 1.0$ (e.g., Jørgensen et al. 2007). The masses of the Keplerian disks in TMC-1A and L1489 IRS are estimated to be $0.025 - 0.06 M_\odot$ and $0.007 - 0.02 M_\odot$ with $T_{\text{dust}} = 15 - 30 \text{ K}$, which are typical temperatures of circumstellar disks on hundreds of AU scale around T Tauri stars (e.g., Isella et al. 2009; Guilloteau et al. 2011).

4.9.2 Measuring Rotational Profiles from Position–Velocity Diagrams

To investigate the feasibility and limitation of our method to derive rotational profiles from the observed P–V diagrams perpendicular to the outflow directions, model images of infalling and rotating protostellar envelopes in the C¹⁸O (2–1) emission were constructed, and the SMA observing simulations with the model images were performed. Then, our method to derive rotational profiles was applied to the simulated P–V diagrams, and the outputs were compared to the "genuine" rotational profiles of the model envelopes. In the model envelopes the density and temperature profiles are assumed to be $\rho(r) \propto r^{-1.5} \cdot \sin^f \theta$ and $T(r) = 10 \times (r/5000 \text{ AU})^{-0.4}$, respectively (Shirley et al. 2000; Harvey et al. 2003; Brinch et al. 2007b). Here, $\sin^f \theta$ represents the "flatness" of the model envelopes, and $f = 4, 8$, and infinity (geometrically-thin disk) are adopted. In the geometrically-thin case a two-dimensional Gaussian intensity distribution is adopted as the moment 0 map. The distance to the model envelopes is adopted to be 140 pc, same as that to our targets in the Taurus region. The outer radius of the model envelopes is adopted to be 4200 AU ($= 30''$), similar to the radius of the SMA primary beam. For simplicity, the infalling motion is assumed to follow radial free fall, $v_{\text{in}} = \sqrt{2GM_*/r}$, while the rotational motion is assumed to have a power-law profile, $v_{\text{rot}} = v_0 \cdot (R_{\text{rot}}/100 \text{ AU})^p$, where G is the gravitational constant, M_* is the protostellar mass, and R_{rot} is the rotational radius (i.e., the distance to the rotational axis). The model image cubes in the C¹⁸O (2–1) emission were generated with a three-dimensional radiative transfer code, LIME (Brinch & Hogerheijde 2010), and those of the geometrically-thin envelopes were generated with MIRIAD tasks, *velmodel* and *velimage*. The generated image cubes were sampled with the same uv points and velocity resolution as those of our real observations with a MIRIAD task *uvmodel*, to produce the simulated visibility data. Then the simulated images were created from the simulated visibility data, and our method to derive rotational profiles was applied to the simulated P–V diagrams, which includes random noises to match the signal-to-noise ratios of the simulated P–V diagrams with those of the real observations.

A series of simulations with $M_* = 0, 0.05, 0.1$, and $0.2 M_\odot$, $v_0 = 0, 1$, and 4 km s^{-1} , $p = -0.5, -0.7, -1.0$, and -1.3 , an inclination angle of $45^\circ, 60^\circ$, and 90° , and $f = 4, 8$, and infinity, were performed. The parameter space was chosen

to approximately cover the anticipated ranges of those parameters of our target sources. Here we show three representative cases with $f = 4$ and an inclination angle of 60° ; 1) no rotation but infalling motion ($M_* = 0.2 M_\odot$ and $v_0 = 0$); 2) rotation without infalling motion ($M_* = 0$, $v_0 = 1 \text{ km s}^{-1}$, and $p = -1$); and 3) rotating and infalling envelope ($M_* = 0.2 M_\odot$, $v_0 = 1 \text{ km s}^{-1}$, and $p = -1$). Figure 4.13 shows the model moment 0 and 1 maps, P–V diagrams, and the data points of the rotational velocities deduced from our method on the P–V diagrams. In Case 1, the moment 1 map exhibits a clear velocity gradient along the outflow direction but no velocity gradient perpendicular to the outflow direction (Fig. 4.13 (a)). The P–V diagrams perpendicular to the outflow direction with the SMA compact and subcompact configurations (Fig. 4.13 (b)) and with the subcompact configuration only (Fig. 4.13 (c)) do not show any velocity gradient as expected. In Case 2 there is a clear velocity gradient perpendicular to the outflow direction but no velocity gradient along the outflow direction (Fig. 4.13 (d)). There are clear peak offsets between the blueshifted and redshifted emission in the P–V diagrams perpendicular to the outflow direction (Fig. 4.13 (e) & (f)). In Case 3, the moment 1 map shows that the direction of the velocity gradient is from northeast to southwest (Fig. 4.13 (g)), and hence there are velocity gradients both along and perpendicular to the outflow direction (Fig. 4.13 (h) & (i)).

Figure 4.14 (a) and (b) show the measured rotational velocities as a function of radius derived from the simulated P–V diagrams in Case 2 and 3, respectively. In Case 2 (pure rotation case), the measured power-law index of the rotational profile is consistent with the input value within the 1σ error, and the measured rotational velocity at a radius of 100 AU is consistent with the input value within 10%. We found that over the parameter ranges we surveyed, in the pure rotation cases the measured power-law indices are consistent with the input values within 2σ uncertainty, and that the rotational velocities at a radius of 100 AU within 30%. On the other hand, Figure 14 (b) shows that in Case 3 the measured power-law index of the rotational profile ($p = -0.76 \pm 0.1$) is larger than the input value ($p = -1$). We tested several cases of the rotating and infalling envelopes and found that in these cases our method could produce artificially shallower rotational power-law indices than the genuine rotational power-law indices. This is because the synthetic vectors of the rotating and infalling motions can contribute to the line-of-sight velocities

along the envelope major axes, and the P–V diagrams along the major axes do not reflect only the rotational motions but also the infalling motions. The magnitude of the distortion of the rotational power-law indices depends on the flatnesses of the envelopes, inclinations, ratios between the infalling and rotating motions, and the observational angular resolutions. For the parameters we have studied, cases of higher resolutions, flatter envelopes, higher ratios of the rotational to infalling motions, higher inclination angles (closer to the edge-on case), provide better results.

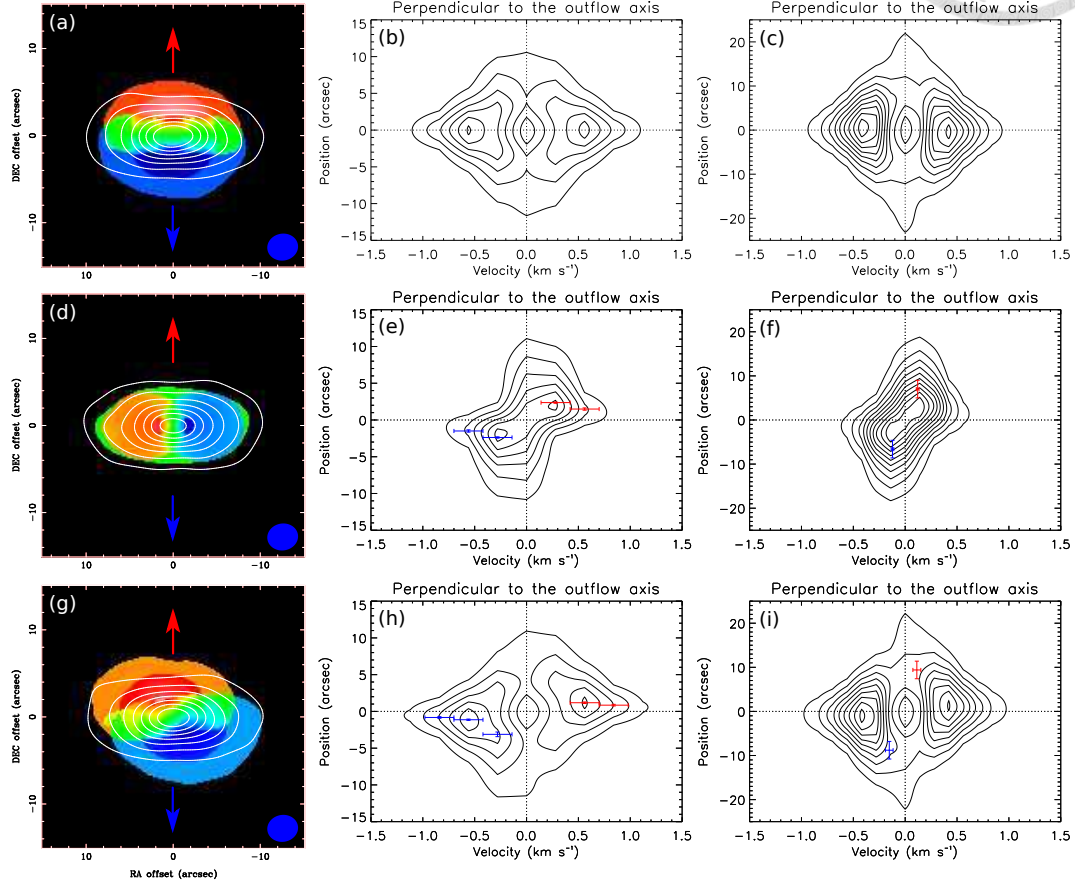


Figure 4.13 Results of our simulations to assess the feasibility and the limitation of our method; (a) – (c) an infalling envelope without any rotational motion; (d) – (f) a rotating envelope without any infalling motion; and (g) – (i) an infalling and rotating envelope. The left column shows the moment 0 maps (contours) overlaid on the moment 1 maps (color scale), produced by combining the simulated compact and subcompact data. Red and blue arrows present the outflow direction, and filled ellipses show the beam size. The middle column shows the P–V diagrams perpendicular to the outflow direction, produced with the combined data. The right column shows P–V diagrams perpendicular to the outflow direction, produced with the subcompact data. Note that the spatial scales of the combined and subcompact P–V diagrams are different. The zero position in each panel corresponds to the protostellar position. Blue and red data points with error bars show the measured rotational velocities as a function of radius.

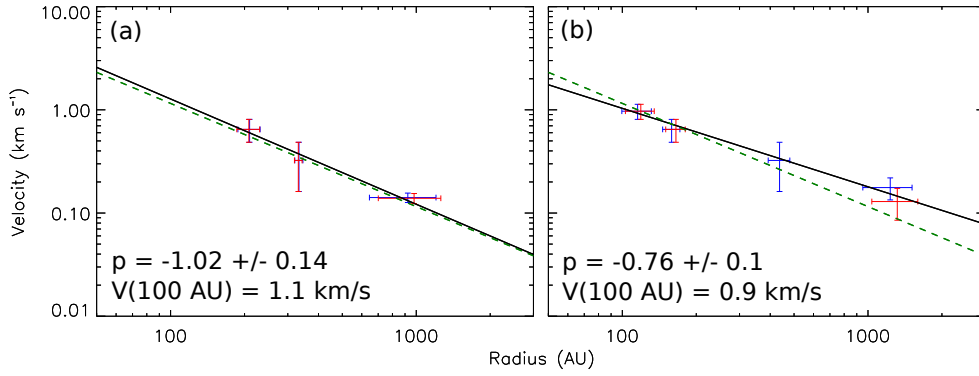


Figure 4.14 Rotational velocities as a function of radius measured from the simulated P–V diagrams of (a) an rotating envelope without infalling motion and (b) an infalling and rotating envelope. Solid lines show the best-fit power-law rotational profiles ($v \propto r^p$). The best-fit power-law index and rotational velocity at a radius of 100 AU are shown at the bottom-left corner of each panel. Green dotted lines present the input rotational profile having $p = -1$ and a rotational velocity of 1 km s^{-1} at a radius of 100 AU.



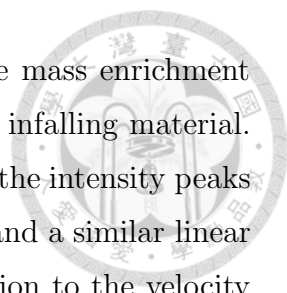
Chapter 5

ALMA Observation of Accretion Flows onto the Keplerian Disk around a Class I protostar L1489 IRS

This chapter is in preparation for submission to ApJ.

5.1 Abstract

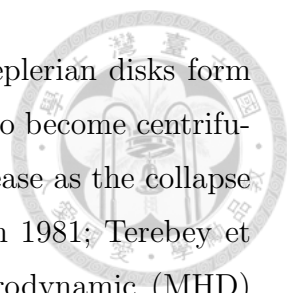
We have conducted ALMA observations in the 1.3 mm continuum and ^{12}CO (2–1), C^{18}O (2–1) and SO (5_6-4_5) lines toward L1489 IRS, a Class I protostar surrounded by a Keplerian disk and an infalling protostellar envelope. The Keplerian disk is clearly identified in the high-velocity ($\gtrsim 2.5 \text{ km s}^{-1}$) ^{12}CO and C^{18}O emission but not seen in the SO emission, and the protostellar mass is estimated to be $2.0 M_{\odot}$. At lower velocities ($\lesssim 2.5 \text{ km s}^{-1}$), the C^{18}O emission shows blueshifted and redshifted intensity peaks located outside the Keplerian disk, and blueshifted and redshifted protrusions pointing toward the north and south, respectively. The curvature and kinematics of the protrusions can be interpreted as infalling gas flows with a conserved angular momentum following parabolic trajectories toward the Keplerian disk, suggesting the presence of non-isotropic infalling motion, and the mass infalling rate is estimated to be $< 5 \times 10^{-7} M_{\odot} \text{ yr}^{-1}$. The intensity peaks outside the



Keplerian disk and connected to the protrusions could trace the mass enrichment at the centrifugal radius (~ 300 AU) due to the accumulation of infalling material. The SO emission primarily trace the components associated with the intensity peaks and exhibit a linear velocity gradient along the disk major axis, and a similar linear velocity gradient is also identified in the C^{18}O emission in addition to the velocity gradient of the Keplerian rotation. The linear velocity gradient and intensity peaks outside the Keplerian disk can be reproduced with a Keplerian-rotating torus at a radius of ~ 320 AU surrounding the central Keplerian disk. The torus could be formed by the mass enrichment around the centrifugal radius and is the transitional region between the infalling gas flows and the Keplerian disk, and the SO emission primarily traces the transitional region. The observational results are discussed in the context of evolution of protostellar envelopes and Keplerian disks.

5.2 Introduction

Protostars form along with Keplerian disks through gravitational collapse of dense cores ($n \sim 10^4 - 10^5 \text{ cm}^{-3}$) in molecular clouds (e.g., Shu et al. 1987; André et al. 2000; Myers et al. 2000). Previous interferometric observations have found infalling and rotational gas motions on thousands of AU scale inside dense cores associated with known infrared sources, so-called protostellar envelopes (e.g., Ohashi et al. 1997; Momose et al. 1998). Keplerian disks have often been observed around T Tauri stars with millimeter interferometric observations (e.g., Guilloteau & Dutrey 1994; Dutrey et al. 1998; Simon et al. 2000; Qi et al. 2003, 2004; Andrews & Williams 2007; Pietu et al. 2007; Guilloteau et al. 2011; Andrews et al. 2012). The outer radii of those Keplerian disks seen in CO emission range from ~ 100 to ~ 800 AU, and their masses traced by dust continuum emission range from $\sim 10^{-4}$ to $10^{-1} M_{\odot}$. Recent observations with the Submillimeter Array (SMA) have reported the presence of Keplerian disks around Class I protostars, which are still embedded in protostellar envelopes (Brinch et al. 2007a; Lommen et al. 2008; Jørgensen et al. 2009; Takakuwa et al. 2012). The Keplerian disks around Class I protostars have outer radii from 100 to 300 AU and masses from 0.004 to 0.06 M_{\odot} , comparable to those around T Tauri stars. How these large-scale (>100 AU) Keplerian disks form in infalling and rotating protostellar envelopes is still controversial. Theoretical models



of collapsing dense cores without magnetic field suggest that Keplerian disks form around protostars when collapsing material rotates fast enough to become centrifugally supported, and that the outer radii of Keplerian disks increase as the collapse proceeds toward outer regions (Ulrich 1976; Cassen & Moosman 1981; Terebey et al. 1984; Basu 1998). On the other hand, recent magnetohydrodynamic (MHD) simulations show that the magnetic field can effectively remove the angular momentum of collapsing material by magnetic braking, and suppress the outer radii of Keplerian disks within 10 AU (e.g., Mellon & Li 2008, 2009; Machida et al. 2011; Li et al. 2011; Dapp et al. 2012). In the MHD simulations, large-scale Keplerian disks cannot form until the efficiency of magnetic braking decreases due to the dissipation of protostellar envelopes (Machida et al. 2011).

In order to study the evolution from infalling and rotating envelopes to the formation of large-scale Keplerian disks, we have conducted Submillimeter Array (SMA) observations of the inner part (100–1000 AU) of protostellar envelopes around a sample of Class 0 and I protostars (Chapter 2, 3, and 4). Our observations combined with previous observations of protostellar envelopes (e.g., Arce & Sargent 2006) show that the kinematics of protostellar envelopes can be categorized into three groups, (1) infalling motion with little rotational motion around Class 0 protostars (e.g., B335 and NGC 1333 IRAS 4B), (2) both infalling and rotational motions around Class 0 and I protostars (e.g., L1448-mm and L1527 IRS), and (3) rotational motion without clear infalling motion around Class I protostars (e.g., TMC-1A and L1489 IRS). The three categories demonstrate the evolution from infalling envelopes to Keplerian disks, and can be explained with the scenario of the inside-out collapse of a rotating dense core where the angular momentum is conserved (Chapter 4). In the early collapse stage, the envelope material with a small angular momentum in the vicinity of the protostar collapses first, and hence the protostellar envelope on 100–1000 AU scale shows infalling motion but little rotational motion. As the expansion wave propagates outwardly, the envelope material with a larger angular momentum in the outer region start to collapse and forms a Keplerian disk at the center. As more angular momenta travel to the central region with the infalling motion, rotational velocities of the envelope on 100–1000 AU scale and the size of the central Keplerian disk increase. Eventually, the protostellar envelope is dissipated via the mass accretion onto the central disk+protostar system and/or the mass ejection.

tion by the outflow, and the central Keplerian disk with a radius of hundreds of AU becomes apparent.

However, it is still unclear as to how and when the kinematics of protostellar envelopes on 100–1000 AU scale evolves from infall-dominant to rotation-dominant, and how infalling material feeds angular momenta to central disks and expands disk sizes. Previous observations in the HCO^+ and C^{18}O lines toward those Class I protostars surrounded by Keplerian disks primarily trace the Keplerian rotations of the disks but are unable to reveal the detailed kinematics of their surrounding envelopes because of the limited sensitivity and angular resolutions (e.g., Brinch et al. 2007a; Lommen et al. 2008; Chapter 4). Thus, observationally the connection between protostellar envelopes and central Keplerian disks is still unknown, and it is still unclear how infalling material transforms into Keplerian disks.

To approach these questions, observations revealing the kinematics and structures of protostellar envelopes surrounding Keplerian disks around Class I protostars are essential. We have conducted observations with the Atacama Large Millimeter/Submillimeter Array (ALMA) in the 1.3 mm continuum and the ^{12}CO (2–1; 230.538 GHz), C^{18}O (2–1; 219.560358 GHz), and SO (5_6-4_5 ; 219.949433 GHz) lines toward L1489 IRS, a Class I protostar with a bolometric luminosity of $3.7 L_{\odot}$ (Furlan et al. 2008) in the Taurus molecular cloud ($d = 140$ pc). L1489 IRS is associated with a faint molecular outflow along the north-south direction on thousands of AU scale as observed by the JCMT in the ^{12}CO (3–2) line (Hogerheijde et al. 1998). Single-dish continuum observations at 1.3 mm show that L1489 IRS is surrounded by a compact protostellar envelope with a size of $\sim 30''$ (~ 4200 AU), and the envelope has a mass of $0.03 M_{\odot}$ (Motte & André 2001). Both infalling and rotational motions are present in the envelope on a 2000 AU scale, as observed by interferometric observations in millimeter molecular lines, and the rotational motion is more dominant than the infalling motion (Hogerheijde 2001). The SMA observations in the millimeter continuum and HCO^+ (3–2) line emission have reported the presence of a Keplerian disk with a radius of 200 AU and a mass of $0.004 M_{\odot}$ embedded in the envelope, and the protostellar mass is estimated to be $1.4 M_{\odot}$ on the assumption that the inclination angle of the Keplerian disk is 40° (Brinch et al. 2007aa). The 1.3 mm continuum observations with the CARMA at a sub-arcsecond angular resolution ($\sim 0''.8$) have shown that the disk radius is 250 – 450 AU and the disk

mass is $0.005 M_{\odot}$ (Eisner 2012). The radial profile of the rotational motion on 100–1000 AU scale is $V \propto r^{-0.5 \pm 0.1}$ as measured by the SMA C¹⁸O (2–1) observations, and is consistent with Keplerian rotation (Chapter 4). From the observed Keplerian rotation, the protostellar mass is estimated to be $1.8 \pm 0.2 M_{\odot}$ on the assumption that the inclination angle of the Keplerian disk is 50° (Chapter 4). These observational results show that L1489 IRS is an excellent target to study the kinematics and structures of a protostellar envelope surrounding a Keplerian, and to reveal the connection between a protostellar envelope and a Keplerian disk.

In the present paper, we report the imaging and analysis of our ALMA observations of L1489 IRS. Our previous SMA C¹⁸O (2–1) observations at an angular resolution of $\sim 4''$ have shown that the overall gas motion on 100–1000 AU scale around L1489 IRS follows Keplerian rotation, whereas the observed intensity distributions and kinematics cannot be entirely explained by the Keplerian disk. These results suggest that there are likely non-Keplerian components in addition to the Keplerian disk, and that the spatial and velocity structures of the non-Keplerian components are not fully resolved by our SMA observations. With the ALMA observations, providing angular resolutions ($\sim 1''$) and sensitivity four times better than those of our SMA observations, the previously reported Keplerian disk is clearly identified in the ¹²CO (2–1) and C¹⁸O (2–1) emission, and the kinematics and structures of the additional non-Keplerian components are unveiled in the C¹⁸O (2–1) and SO (5₆–4₅) emission. In the present paper, we propose a model comprising a Keplerian disk surrounding by a torus + two infalling gas flows onto the disk, to explain the observed intensity distributions and velocity structures. The observational results are compared with our model and discussed in the context of the evolution of protostellar envelopes and circumstellar disks.

5.3 Observations

The ALMA observations of L1489 IRS was conducted in its cycle 0 operation on 2013 August 9 with the 23 antennas. The pointing center is $\alpha(\text{J2000}) = 4^{\text{h}}04^{\text{m}}42^{\text{s}}.85$, $\delta(\text{J2000}) = 26^{\circ}18'56''.3$. The primary beam of ALMA at 1.3 mm is $\sim 28''$ (~ 3900 AU). In the observation, the 1.3 mm continuum and the ¹²CO (2–1), C¹⁸O (2–1), and SO (5₆–4₅) emission lines were observed simultaneously. The spectral resolution

for the emission lines is 122 kHz, resulting in velocity resolutions of $\sim 0.17 \text{ km s}^{-1}$ for the C^{18}O and SO lines and $\sim 0.16 \text{ km s}^{-1}$ for the ^{12}CO line. Callisto, J0522+364 ($\sim 4.7 \text{ Jy}$), and J0325+226 ($\sim 0.3 \text{ Jy}$) were observed as flux, bandpass, and gain calibrators. The visibility data were calibrated, Fourier-transformed, and CLEANed using Common Astronomy Software Applications (CASA) with the robust parameter of +0.5. The synthesized beams of the CLEANed images are $0''.92 \times 0''.71$ for the 1.3 mm continuum, $0''.85 \times 0''.72$ for the ^{12}CO line, $0''.96 \times 0''.75$ for the C^{18}O line, and $0''.96 \times 0''.74$ for the SO line. The rms noise levels are $\sim 0.15 \text{ mJy}$ in the 1.3 mm continuum image and $\sim 8 \text{ mJy}$ in the images of the emission lines.

5.4 Results

The systemic velocity (V_{sys}) of L1489 IRS has been estimated to be $V_{\text{LSR}} = 7.2 \text{ km s}^{-1}$ with the single-dish observations in several molecular lines at multiple transitions (Brinch et al. 2007b). As will be shown in Section 5.5.1, from our fitting of the disk model to the observed Keplerian disk, V_{sys} of L1489 IRS is estimated to be $V_{\text{LSR}} = 7.4 \text{ km s}^{-1}$, approximately consistent with the systemic velocity measured on thousands of AU scale with the single-dish observations. In the present paper, $V_{\text{LSR}} = 7.4 \text{ km s}^{-1}$ is adopted as V_{sys} of L1489 IRS, and all the velocities shown in this paper are the relative velocities ($\equiv V$) with respect to V_{sys} .

5.4.1 1.3 mm Continuum Emission

Figure 5.1a shows the 1.3 mm continuum image of L1489 IRS. The continuum emission is elongated from northeast to southwest, and its intensity distribution can be described by a combination of a point source and a Gaussian intensity distribution (Figure 5.1b) derived by the fitting program of MIRIAD, *imfit*. The point source has a total flux of $\sim 7.6 \text{ mJy}$ and is located at $\alpha(\text{J2000}) = 4^{\text{h}}04^{\text{m}}43^{\text{s}}.07$, $\delta(\text{J2000}) = 26^{\circ}18'56''.3$. In the present paper, this position is adopted as the position of the central protostar. The center of the Gaussian intensity distribution is at $\alpha(\text{J2000}) = 4^{\text{h}}04^{\text{m}}43^{\text{s}}.09$, $\delta(\text{J2000}) = 26^{\circ}18'56''.3$, consistent with the position of the point source within $0''.2$. The Gaussian intensity distribution has a total flux of $\sim 42 \text{ mJy}$, a deconvolved size of $3''.5 \times 1''.1$ ($500 \text{ AU} \times 150 \text{ AU}$), and a position angle of 69° . The elongation of the Gaussian intensity distribution is perpendicular to the outflow axis

with a position angle of 165° (Hogerheijde et al. 1998).

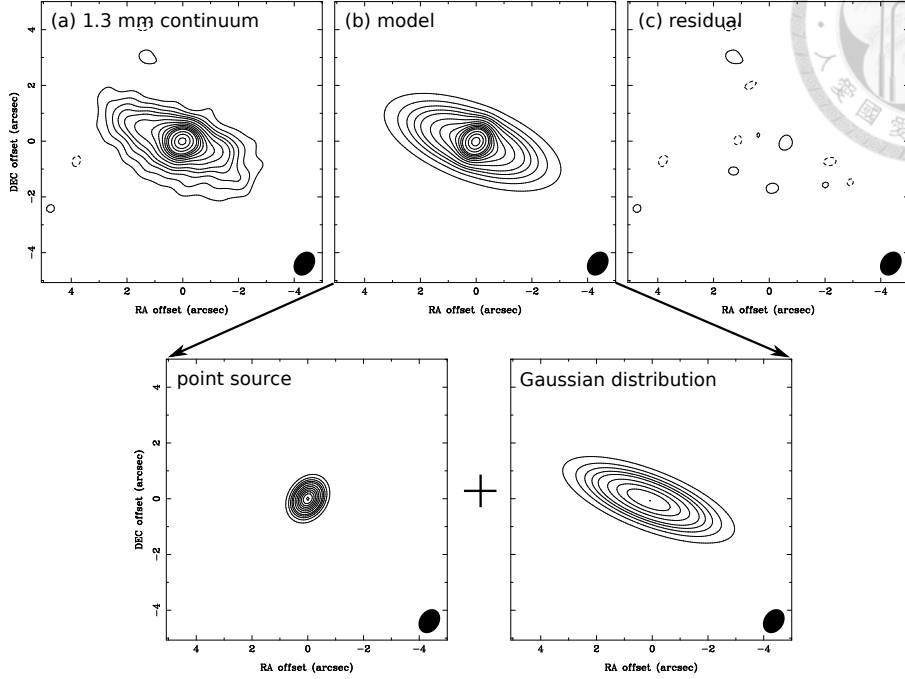


Figure 5.1 (a) 1.3 mm continuum image of L1489 IRS. (b) Model image of the 1.3 mm continuum emission in L1489 IRS, which is composed of a point source and a Gaussian intensity distribution. (c) Residual image after subtracting the model image from the observed continuum image. A filled ellipse at the bottom-right corner in each panel denotes the beam size. Contour levels are from 3σ to 15σ in steps of 3σ , from 15σ to 50σ in steps of 5σ , and then from 50σ to 80σ in steps of 10σ , where 1σ is $0.15 \text{ mJy Beam}^{-1}$.

5.4.2 ^{12}CO (2–1) Emission

Figure 5.2 shows the integrated-intensity (i.e., moment 0) map and the intensity-weighted mean velocity (i.e., moment 1) maps of the ^{12}CO (2–1) emission in L1489 IRS. The ^{12}CO emission shows blueshifted and redshifted V-shaped structures with the apices coincident with the protostellar position in the south and the north, respectively. The direction and velocity gradient of the ^{12}CO emission are consistent with those of the large-scale outflow observed with JCMT in the ^{12}CO (3–2) line (Hogerheijde et al. 1998). We consider that the V-shaped features seen in the ^{12}CO ALMA observations trace the shell of the bipolar outflow. In addition to the outflow lobes, there is a central compact component with a size of $\sim 1''.7$ ($\sim 240 \text{ AU}$) and a positional angle of $\sim 79^\circ$ associated with the protostar. The central component is elongated and exhibit a velocity gradient perpendicular to the outflow axis, as clearly

seen in the moment 0 map integrated over the high-velocity ranges ($|V| \gtrsim 5 \text{ km s}^{-1}$; Figure 5.2b). The high-velocity ^{12}CO emission shows blueshifted and redshifted compact blobs with sizes of $\sim 0''.5\text{--}0''.6$ ($\sim 70\text{--}80 \text{ AU}$) and positional offsets of $\sim 0''.2$ ($\sim 30 \text{ AU}$) to the east and the west of the protostar, respectively. The position angle of the axis passing through the blueshifted and redshifted peak positions of the high-velocity ^{12}CO emission is $\sim 87^\circ$, perpendicular to the outflow axis. The direction of the velocity gradient of the central component is consistent with that of the rotational motion on hundreds of AU scale around the protostar as observed with SMA in the HCO^+ (3–2) and C^{18}O (2–1) lines (Brinch et al. 2007a; Chapter 4).

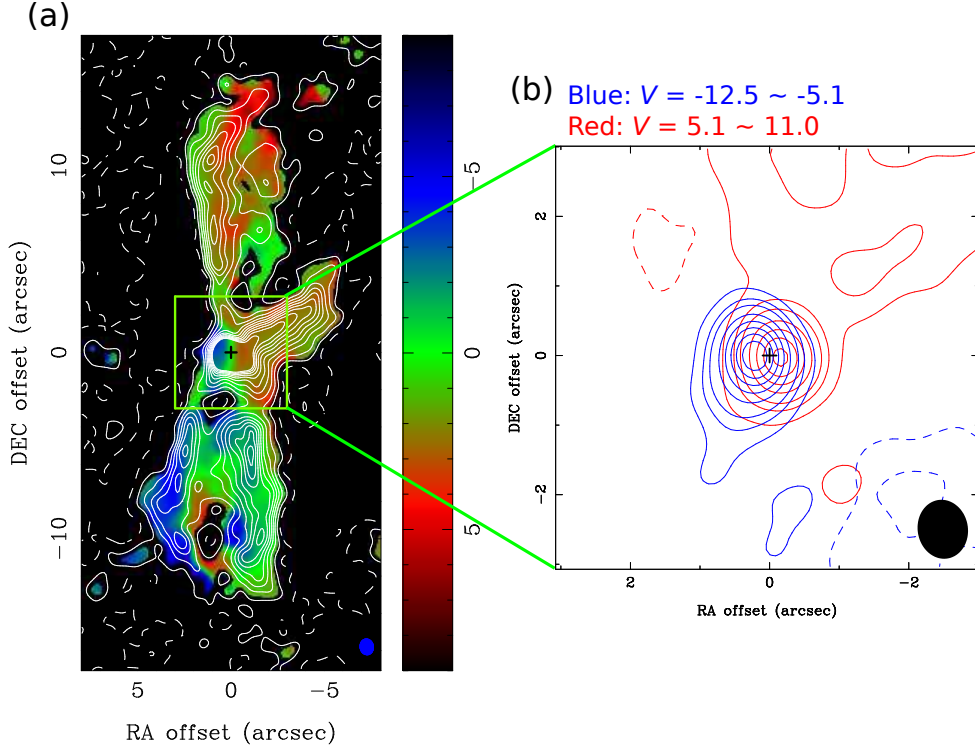


Figure 5.2 (a) Moment 0 map (contour) overlaid on the moment 1 map (color) of the ^{12}CO (2–1) emission in L1489 IRS. (b) Moment 0 maps of the high-velocity ^{12}CO (2–1) emission in L1489 IRS. Blue contours show the ^{12}CO (2–1) emission integrated from $V = -12.5 \text{ km s}^{-1}$ to $V = -5.1 \text{ km s}^{-1}$, and red contours from $V = 5.1 \text{ km s}^{-1}$ to $V = 10.8 \text{ km s}^{-1}$. A green box in (a) shows the area of the high-velocity ^{12}CO map. A filled ellipse at the bottom-right corner in each panel denotes the beam size. Crosses show the protostellar position. Contour levels are from 5σ in steps of 10σ in (a), where 1σ is $20 \text{ mJy Beam}^{-1} \text{ km s}^{-1}$, and are 5σ , 15σ , 25σ , and then in steps of 20σ in (b), where 1σ is $9 \text{ mJy Beam}^{-1} \text{ km s}^{-1}$.

5.4.3 C¹⁸O (2–1) Emission

Figure 5.3 shows the moment 0 and 1 maps of the C¹⁸O (2–1) emission in L1489 IRS. The C¹⁸O emission is elongated from northeast to southwest and exhibits a velocity gradient along its major axis (blueshifted to the northeast and redshifted to the southwest), which is consistent with the previous SMA observational results in the HCO⁺ (3–2) line at an angular resolution of $\sim 1''$ (Brinch et al. 2007a) and in the C¹⁸O (2–1) line at an angular resolution of $\sim 4''$ (Chapter 4). Around the protostar, the C¹⁸O emission shows two peaks, one blueshifted to the east and one redshifted to the west, and exhibits a zero mean velocity at the protostellar position. At the tips of the elongated structure, there are protrusions of the blueshifted and redshifted emission pointing toward the north and south, respectively. These off-axis protrusions of the blueshifted and redshifted C¹⁸O emission have also been identified in our previous SMA images of L1489 IRS (Chapter 4).

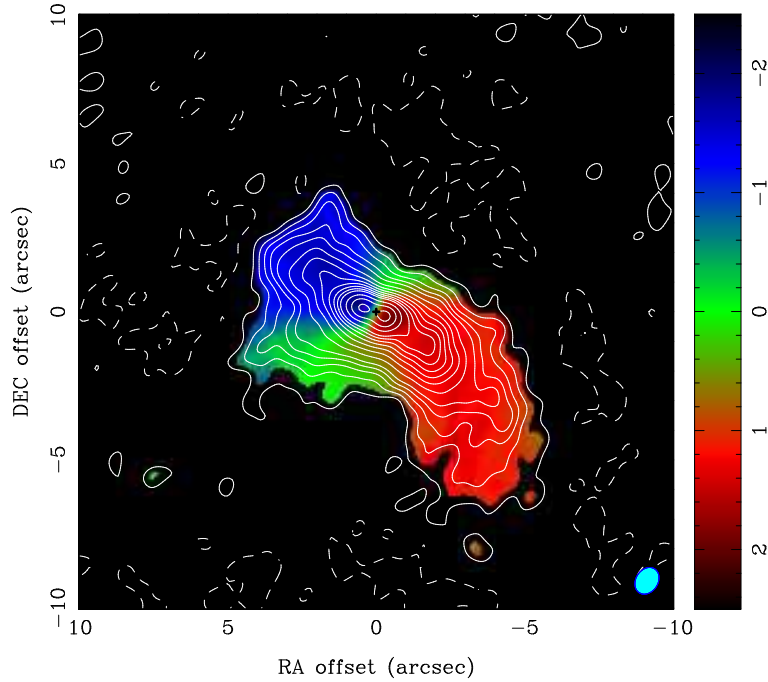


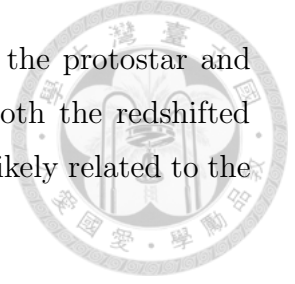
Figure 5.3 Moment 0 map (contour) overlaid on the moment 1 map (color) of the C¹⁸O (2–1) emission in L1489 IRS. A filled ellipse at the bottom-right corner denotes the beam size. A cross shows the protostellar position. Contour levels are from 3σ to 15σ in steps of 3σ , from 15σ to 50σ in steps of 5σ , and then from 50σ to 90σ in steps of 10σ , where 1σ is $9 \text{ mJy Beam}^{-1} \text{ km s}^{-1}$.

Figure 5.4 shows the velocity channel maps of the C¹⁸O emission. The C¹⁸O emission is detected at 3σ levels at 62 channels from $V = -5.1 - 5.0 \text{ km s}^{-1}$.

Here we binned 3 channels together to reduce the total number of the channels for presentation. At $|V| \geq 2.5 \text{ km s}^{-1}$, the C^{18}O emission shows a single-peaked blob close to the protostar, and the blobs at $V = -2.5$ and 2.5 exhibit protrusions toward the northeast and southwest, respectively. At $|V| = 1.5 - 2 \text{ km s}^{-1}$, the C^{18}O emission exhibits two peaks, suggesting the presence of two components, and the two components are spatially connected. The inner component is weaker and coincident with the positions of the high-velocity blobs, while the outer component at the blueshifted velocities extends toward the north, and that at the redshifted velocities toward the southeast. At $V = 0.52 - 1 \text{ km s}^{-1}$, the C^{18}O emission show extensions from the center toward the south, and an arm-like structure is seen at $V = 0.52 \text{ km s}^{-1}$. At $V = -0.48 - 0.025 \text{ km s}^{-1}$, the C^{18}O emission exhibits a central component elongated along the outflow direction and coincident with the protostellar position, as well as extensions toward the direction of the blueshifted outflow, and similar extensions are also seen at $V = -0.98 \text{ km s}^{-1}$.

To present the main features of the C^{18}O emission observed at different velocities, we integrated the C^{18}O emission over three velocity regimes, high velocities ($|V| = -5.1 - -2.6$ and $2.4 - 5.0 \text{ km s}^{-1}$), medium velocities ($V = -2.5 - -1.1$ and $0.5 - 2.2 \text{ km s}^{-1}$), and low velocities ($V = -1.0 - 0.4 \text{ km s}^{-1}$), shown in Figure 5.5. The high-velocity C^{18}O emission shows blueshifted and redshifted compact blobs with sizes of $\sim 0''.7$ ($\sim 100 \text{ AU}$) and positional offsets of $\sim 0''.6$ ($\sim 80 \text{ AU}$) to the east and the west of the protostar, respectively. The position angle of the axis passing through the peak positions of these two blobs is $\sim 70^\circ$, consistent with the elongation of the 1.3 mm continuum emission. Both the high-velocity ^{12}CO and C^{18}O emission shows similar structures, position angles, and the directions of the velocity gradients, and likely trace the inner part ($\lesssim 200 \text{ AU}$) of the rotational motion seen on hundreds of AU scale. In addition, the high-velocity ^{12}CO emission is closer to the center and has a smaller size and higher velocities than the high-velocity C^{18}O emission, suggesting that in L1489 IRS the circumstellar material closer to the protostar rotates faster. The medium-velocity C^{18}O emission exhibits blueshifted and redshifted peaks located at $\sim 2''$ ($\sim 280 \text{ AU}$) to the northeast and to the southwest, respectively, and shows an elongation with a position angle of $\sim 55^\circ$. At the tip of the elongated structure, there are blueshifted and redshifted protrusions pointing to the north and south, respectively, as seen in Figure 5.3. The

low-velocity C^{18}O emission shows a central component close to the protostar and extensions toward the direction of the blueshifted outflow at both the redshifted and blueshifted velocities. The extension at the low velocities is likely related to the outflow.



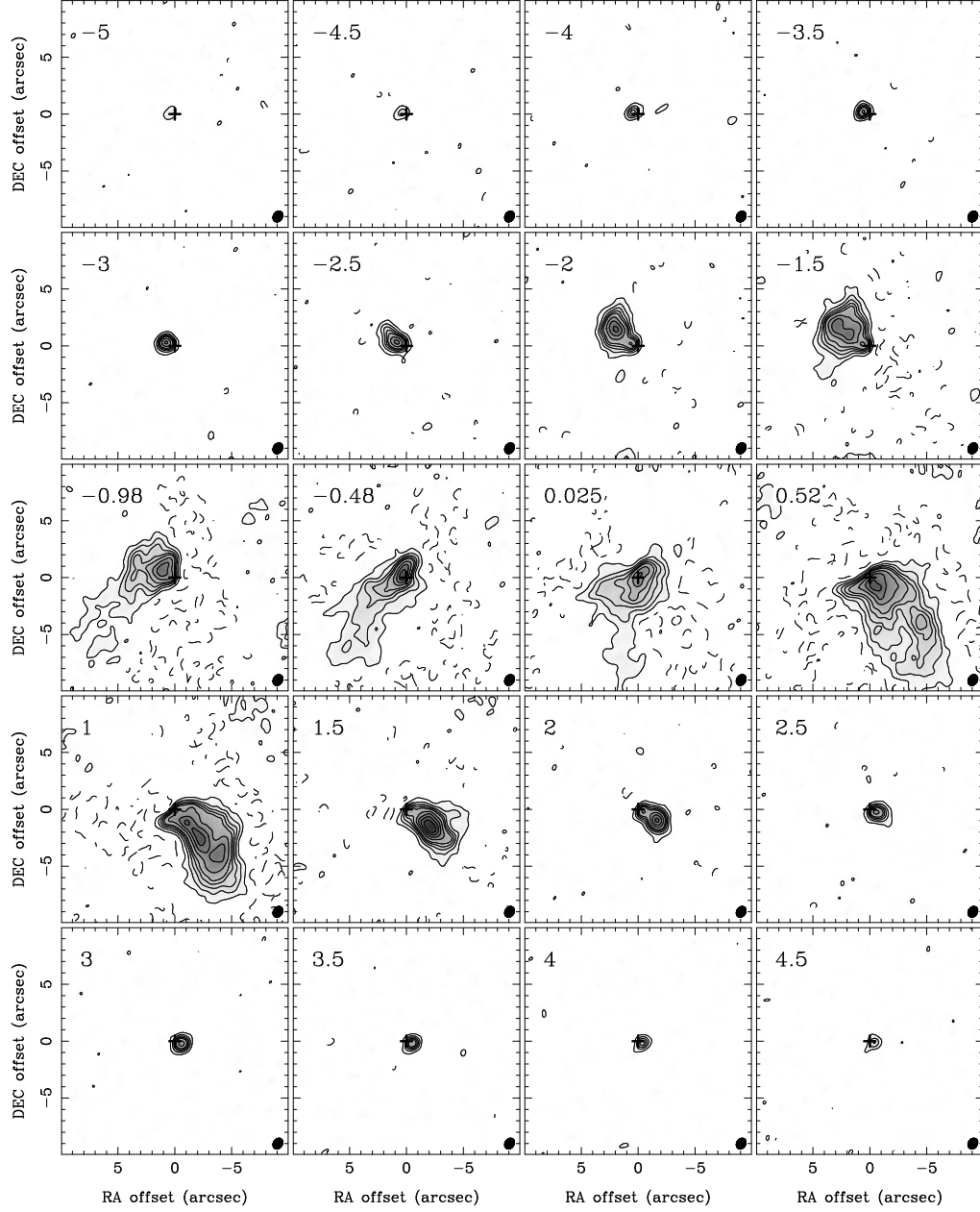


Figure 5.4 Velocity channel maps of the C^{18}O (2–1) emission in L1489 IRS (3 channel binned). The velocity at each channel are shown at the upper left corner in each panel. A filled ellipse at the bottom-right corner in each panel denotes the beam size. Crosses show the protostellar position. Contour levels are 3σ , 6σ , 11σ , 16σ , and then in steps of 10σ , where 1σ is 5 mJy Beam^{-1} .

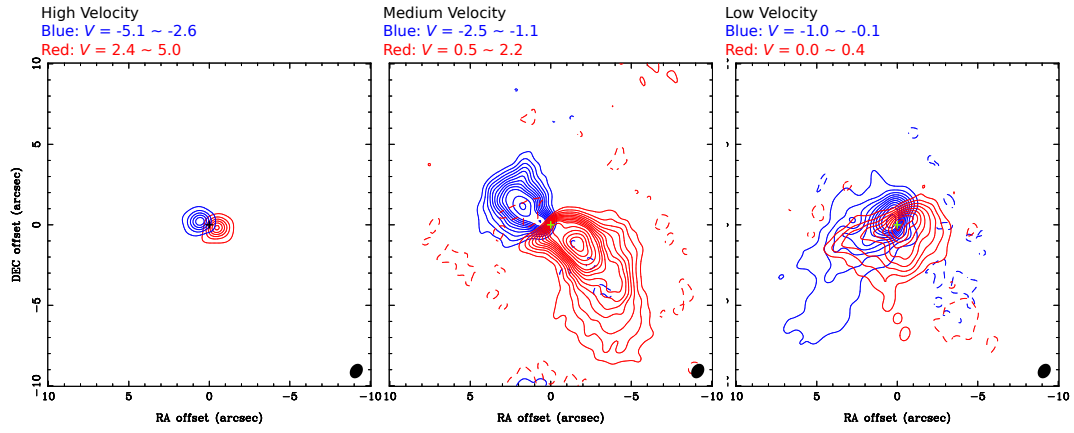


Figure 5.5 Moment 0 map of the high-velocity, medium-velocity, and low-velocity C^{18}O (2-1) emission in L1489 IRS. The integrated velocity ranges are shown above the relevant panels. A filled ellipse at the bottom-right corner in each panel denotes the beam size. Crosses show the protostellar position. Contour levels are from 5σ in steps of 10σ in the high-velocity map, and those are from 5σ to 50σ in steps of 5σ and then in steps of 10σ in the medium- and low-velocity maps. 1σ is 5, 6, 4, 5, 3 and 2 $\text{mJy Beam}^{-1} \text{ km s}^{-1}$ in the high-velocity blueshifted, high-velocity redshifted, medium-velocity blueshifted, medium-velocity redshifted, low-velocity blueshifted, and low-velocity redshifted maps, respectively.

5.4.4 SO (5₆–4₅) Emission

Figure 5.6 shows the moment 0 and 1 maps of the SO (5₆–4₅) emission in L1489 IRS. The SO emission exhibits the northeast–southwest elongation and the clear velocity gradient along the major axis as in the case of the C¹⁸O emission, while multiple SO peaks are present, different from the C¹⁸O emission. Figure 5.7 shows the velocity channel maps of the SO emission. The SO emission is detected at 3 σ levels at 35 channels from $V = -2.6 - 3.1$ km s⁻¹. Here we binned 3 channels together to reduce the total number of the channels for presentation. At $V = 2.6 - 3.1$ km s⁻¹, the SO emission shows a single-peaked blob close to the protostar, as the case of the high-velocity C¹⁸O emission. At $V = -2.4 - -1.9$ and $1.6 - 2.1$ km s⁻¹, the SO emission also shows a single-peaked blob, which is different from the C¹⁸O emission exhibiting two peaks at similar velocities. The peak positions of the SO emission at $V = -2.4 - -1.9$ and $1.6 - 2.1$ km s⁻¹ are coincident with those of the outer components of the C¹⁸O emission at $|V| = 1.5 - 2$ km s⁻¹, while the inner components seen in the C¹⁸O emission are not identified in the SO emission. The SO emission at $V = -1.9 - -1.4$ km s⁻¹ exhibits protrusions toward the north, similar to the C¹⁸O emission at $V = -2 - -1.5$ km s⁻¹. At $V = 0.6 - 1.1$ km s⁻¹, the SO emission is elongated along the northeast–southwest direction, and there is an intensity peak at the southwest tip of the elongation. The southwest peak is spatially coincident with the arm-like structure seen in the C¹⁸O emission at $V = 0.52$ km s⁻¹. At $V = -0.9 - 0.1$ km s⁻¹, the SO emission show a central component elongated along the outflow direction as well as well extensions toward the direction of the blueshifted outflow.

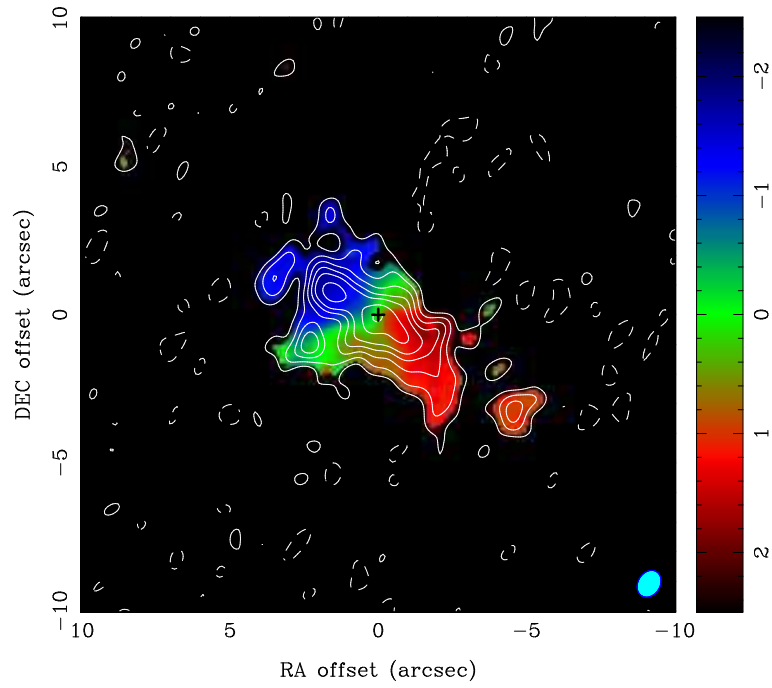


Figure 5.6 Moment 0 map (contour) overlaid on the moment 1 map (color) of the SO (5_6-4_5) emission in L1489 IRS. A filled ellipse at the bottom-right corner denotes the beam size. A cross shows the protostellar position. Contour levels are from 3σ to 15σ in steps of 3σ and then in steps of 5σ , where 1σ is $8 \text{ mJy Beam}^{-1} \text{ km s}^{-1}$.

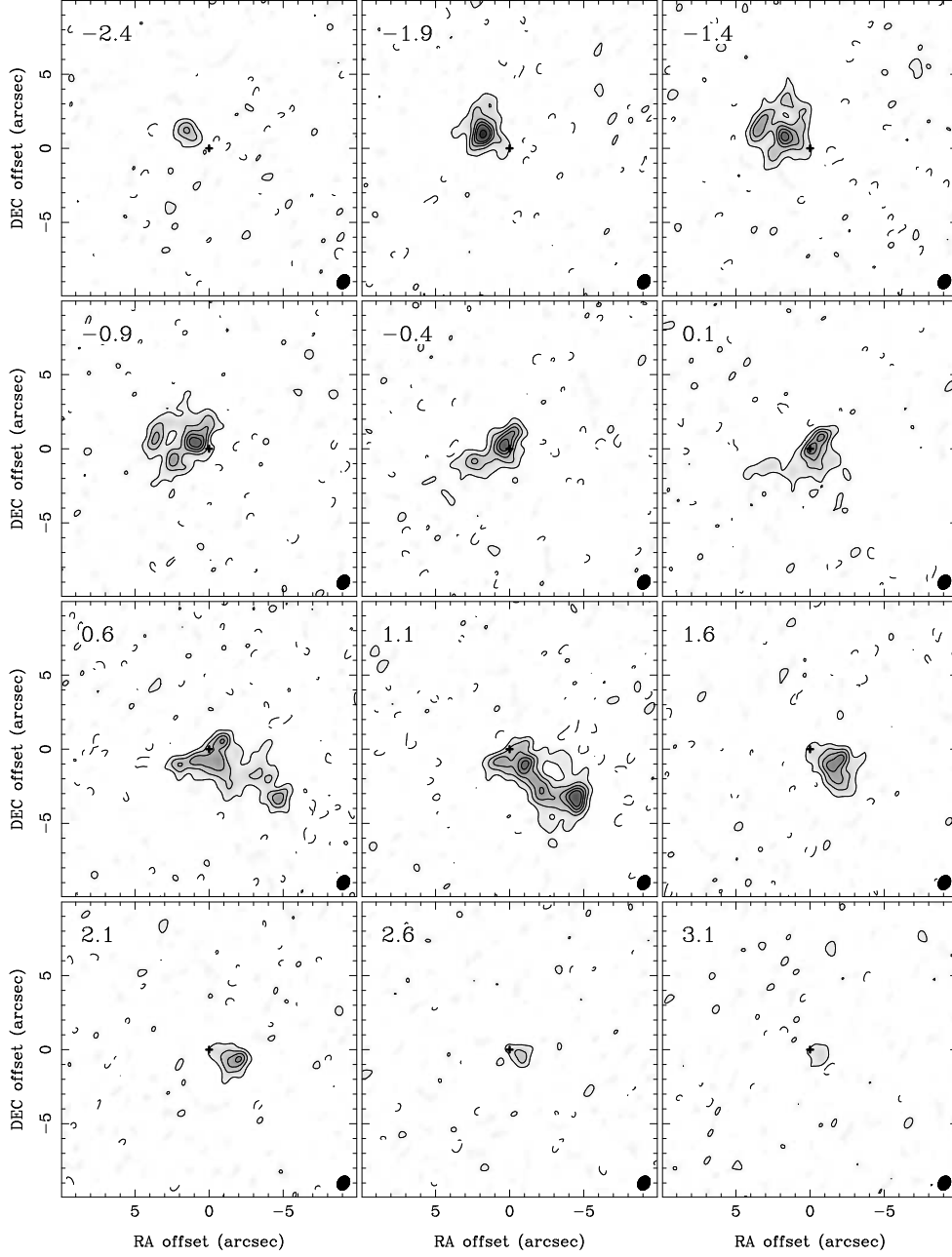
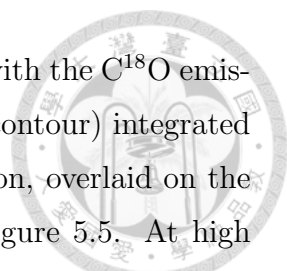


Figure 5.7 Velocity channel maps of the SO (5_6-4_5) emission in L1489 IRS (3 channel binned). The velocity at each channel are shown at the upper left corner in each panel. A filled ellipse at the bottom-right corner in each panel denotes the beam size. Crosses show the protostellar position. Contour levels are 3σ , 6σ , 11σ , 16σ , and then in steps of 10σ , where 1σ is 5 mJy Beam^{-1}



To present the main feature of the SO emission and compare with the C¹⁸O emission, Figure 5.8 shows the moment 0 maps of the SO emission (contour) integrated over three velocity regimes, similar to those for the C¹⁸O emission, overlaid on the moment 0 maps of the C¹⁸O emission (gray scale) shown in Figure 5.5. At high velocities ($|V| \gtrsim 2.5 \text{ km s}^{-1}$) no blueshifted SO emission is detected, while the redshifted SO emission shows a weak compact blob with a size of $\sim 1''.1$ ($\sim 150 \text{ AU}$) and a positional offset of $\sim 0''.9$ ($\sim 130 \text{ AU}$) to the west. As compared to the high-velocity ¹²CO and C¹⁸O emission, the high-velocity SO emission is less compact and located further away from the protostar. At medium velocities (V), the SO emission shows blueshifted and redshifted peaks to the northeast and the southwest, respectively, coincident with the peak positions of the medium-velocity C¹⁸O emission within $0''.1$, plus an additional redshifted peak further away to the southwest. The elongation of the medium-velocity SO emission is consistent with that of the medium-velocity C¹⁸O emission. The redshifted protrusion seen in the medium-velocity C¹⁸O emission is not identified in the SO emission. At the low-velocities, the SO emission also shows a central component close to the protostar as well as extensions toward the blueshifted outflow at both the blueshifted and redshifted velocities, as the case of the low-velocity C¹⁸O emission, while the SO emission is less extended than the C¹⁸O emission.

5.5 Analysis

5.5.1 Keplerian Disk Surrounded by a Torus in L1489 IRS

The high-velocity C¹⁸O and ¹²CO emission show velocity gradients along the northeast (blueshifted) to southwest (redshifted) direction. The direction of the velocity gradients is along the major axis of the 1.3 mm continuum emission. Previous SMA observations of L1489 IRS in the HCO⁺ (3–2) (Brinch et al. 2007a) and C¹⁸O (2–1) lines (Chapter 4) have found a 100 – 1000 AU scale Keplerian disk around the protostar, and the high-velocity C¹⁸O and ¹²CO emission taken with ALMA most likely trace the same Keplerian disk. On the contrary, the C¹⁸O emission at the medium and low velocities, showing asymmetric intensity distributions, cannot be fully explained by a simple Keplerian disk model. In this section, we will first reproduce the high-velocity C¹⁸O emission with a geometrically-thin Keplerian disk

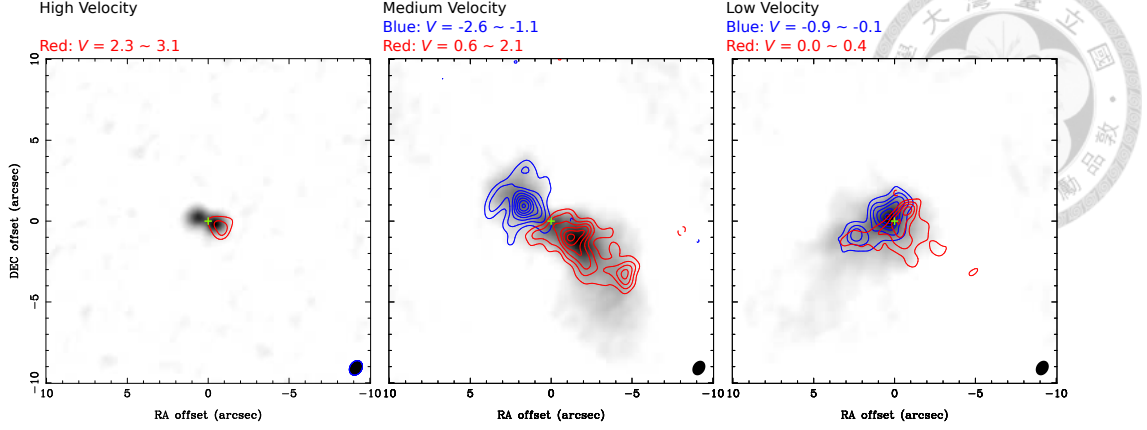


Figure 5.8 Moment 0 map of the high-velocity, medium-velocity, and low-velocity SO (5_6-4_5) emission (contour) in L1489 IRS overlaid on the moment 0 maps of the $C^{18}O$ emission integrated over almost the same velocity ranges (gray scale). The integrated velocity ranges are shown above the relevant panels. A filled ellipse at the bottom-right corner in each panel denotes the beam size. Crosses show the protostellar position. Contour levels are from 5σ in steps of 5σ , where 1σ is 3, 5, and 3 $\text{mJy Beam}^{-1} \text{ km s}^{-1}$ in the high-velocity, medium-velocity, and low-velocity maps, respectively.

model, and constrain the physical condition of the central Keplerian disk. Then we will discuss the nature of the $C^{18}O$ ($2-1$) emission at lower velocities and the SO emission.

To derive the physical parameters of the Keplerian disk around L1489 IRS, we have built axisymmetric geometrically-thin disk models as.

$$\Sigma(r) = \Sigma_0 \cdot \left(\frac{r}{100 \text{ AU}}\right)^p, \quad (5.1)$$

$$T(r) = T_0 \cdot \left(\frac{r}{100 \text{ AU}}\right)^q, \quad (5.2)$$

and

$$V_{\text{rot}}(r) = \sqrt{\frac{GM_*}{r}}, \quad (5.3)$$

where

$$r = \sqrt{x^2 + y^2}, \quad (5.4)$$

$$x = \Delta\alpha \cdot \sin \text{PA} + \Delta\delta \cdot \cos \text{PA}, \quad (5.5)$$

$$y = (-\Delta\alpha \cdot \cos \text{PA} + \Delta\delta \cdot \sin \text{PA}) / \cos i, \quad (5.6)$$

$\Delta\alpha$ and $\Delta\delta$ are RA and Dec offsets with respect to the gravitational center, and x and y are positional offsets along disk major and minor axes, respectively. The

line-of-sight velocity ($\equiv V_{\text{los}}$) is given by,

$$V_{\text{los}} = V_{\text{rot}} \sin i \cdot \frac{x}{r} + V_{\text{sys}}. \quad (5.7)$$

The line profile (ϕ_v) of the C¹⁸O line are assumed to be a Gaussian function as,

$$\phi_v \propto \exp\left(-\frac{(v - V_{\text{los}})^2}{2\sigma_v^2}\right), \quad (5.8)$$

where

$$\sigma_v = \sqrt{\frac{2kT(r)}{m} + \sigma_{\text{turb}}^2}, \quad (5.9)$$

and m is the C¹⁸O molecular mass and k is the Boltzmann constant. Here, $\sqrt{2kT(r)/m}$ is the thermal dispersion, and σ_{turb} is the turbulent dispersion. On the assumption of the LTE condition, which is likely valid for C¹⁸O emission in protostellar envelopes because of their high density (e.g., Chapter 3), the C¹⁸O (2–1) line intensity of our model disks is computed with the radiative transfer equation,

$$I_\nu = B_\nu(T) \cdot (1 - e^{-\tau_\nu}), \quad (5.10)$$

where

$$\tau_\nu = \Sigma(r) \kappa_\nu \phi_v, \quad (5.11)$$

$B_\nu(T)$ is the Planck function at a temperature T , and τ_ν and κ_ν are the optical depth and absorption coefficient of the C¹⁸O (2–1) line, respectively. The model parameters are the gravitational center (dX and dY , defined as RA and Dec offsets with respect to the 1.3 mm continuum peak position), the protostellar mass (M_*), the inclination angle of the disk plane (i), the position angle of the disk major axis (PA), the outer radius of the disk (R_d), the radial profile of the surface number density (Σ_0 and p), the radial profile of the temperature (T_0 and q), V_{sys} , and the turbulent line width (v_{turb}).

Because we apply our disk model only to the high-velocity C¹⁸O emission, which should trace the inner part ($r \lesssim 200$ AU) of the Keplerian disk, R_d cannot be estimated in this analysis. Previous observations of the Keplerian disk around L1489 IRS have estimated R_d to be larger than 200 AU (Brinch et al. 2007a; Eisner 2012). Thus, in our disk models, R_d is fixed to be 200 AU. In addition, we fixed $p = -1.5$ and $q = -0.4$, which are surface density and temperature profiles commonly adopted for modeling disks around T Tauri stars (e.g., Guilloteau & Dutrey 1994; Dutrey et

al. 1998; Guilloteau et al. 2011). Therefore, there are nine fitting parameters in our disk model (dX , dY , M_* , i , PA, Σ_0 , T_0 , V_{sys} , and v_{turb}). To reduce further the number of free parameters, we first adopted the 1.3 mm continuum peak position as the gravitational center ($dX = dY = 0$), the elongation of the high-velocity C¹⁸O emission as the disk major axis (PA = 70°), and the previous reported $V_{\text{sys}} = 7.2 \text{ km s}^{-1}$ (Brinch et al. 2007b). Then we performed χ^2 fitting with M_* , i , Σ , T_0 , and v_{turb} as fitting parameters over the parameter ranges of $1.2 \leq M_* \leq 2.4 M_\odot$, $30^\circ \leq i \leq 80^\circ$, $1.5 \times 10^{16} \leq \Sigma_0 \leq 2.4 \times 10^{17} \text{ cm}^{-2}$, $10 \leq T_0 \leq 60 \text{ K}$, and $0.2 \leq v_{\text{turb}} \leq 0.6 \text{ km s}^{-1}$, respectively. The parameter ranges cover the previous reported M_* (1.4 and $1.8 M_\odot$; Brinch et al. 2007a; Chapter 4) and i (36°–74°; Padgett et al. 1999; Eisner et al. 2005; Brinch et al. 2007a; Eisner 2012) of L1489 IRS and typical temperature of disks on 100 AU scale around T Tauri stars (e.g., Isella et al. 2009; Guilloteau et al. 2011). After we had initial estimates of M_* , i , Σ_0 , T_0 , and v_{turb} , we fixed these parameters and adopted dX , dY , PA, and V_{sys} as free parameters to repeat the fitting with parameter ranges of $dX = 0 \pm 0''.3$, $dY = 0 \pm 0''.3$, PA = 70° ± 6°, and $V_{\text{sys}} = 7.2\text{--}7.5 \text{ km s}^{-1}$. After we obtained new estimates of dX , dY , PA, and V_{sys} , we fixed these parameters and returned to adopt M_* , i , Σ_0 , T_0 and v_{turb} as free parameters to repeat the fitting. After few iterations, we found the best-fit values of dX , dY , PA, and Σ_0 barely change. Then, we adopted M_* , i , T_0 , V_{sys} , and v_{turb} as free parameters for the final iterations to obtain the best-fit values of all the model parameters. The best-fit results are shown in Figure 5.9, and the best-fit parameter values are listed in Table 5.1. We have also tested the fitting by adopting different p (−1.2 – −1.8) and q (−0.2 – −0.6), and found that the best-fit results except for T_0 are consistent, suggesting our estimates would not be affected by the initial assumptions of p and q . Our fitting results show that the channel at $V = -2.8$, the lowest blueshifted velocity included in the fitting, has significant residuals at levels of $\sim 6\sigma$, suggesting that the C¹⁸O emission at this channel cannot be explained by a simple geometrically-thin disk. In the other channels, the levels of residuals are all $\lesssim 4\sigma$ and mostly $\lesssim 3\sigma$, suggesting the high-velocity C¹⁸O emission likely traces the inner Keplerian disk where its thickness is negligible compared to our angular resolutions.



Table 5.1. Best-Fit Physical Parameters of the Keplerian disk

Parameter	Best-Fit Value
Gravitational Center	$4^h 04^m 43^s 05, 26^\circ 18' 56'' 2$
Protostellar Mass	$2 M_\odot$
Inclination	54°
Position Angle	68°
Temperature at a Radius of 100 AU	32 K
C ¹⁸ O Surface Number Density at a Radius of 100 AU	$3 \times 10^{16} \text{ cm}^{-3}$
Systemic Velocity (V_{LSR})	7.4 km s^{-1}
Turbulent Line Width	0.5 km s^{-1}

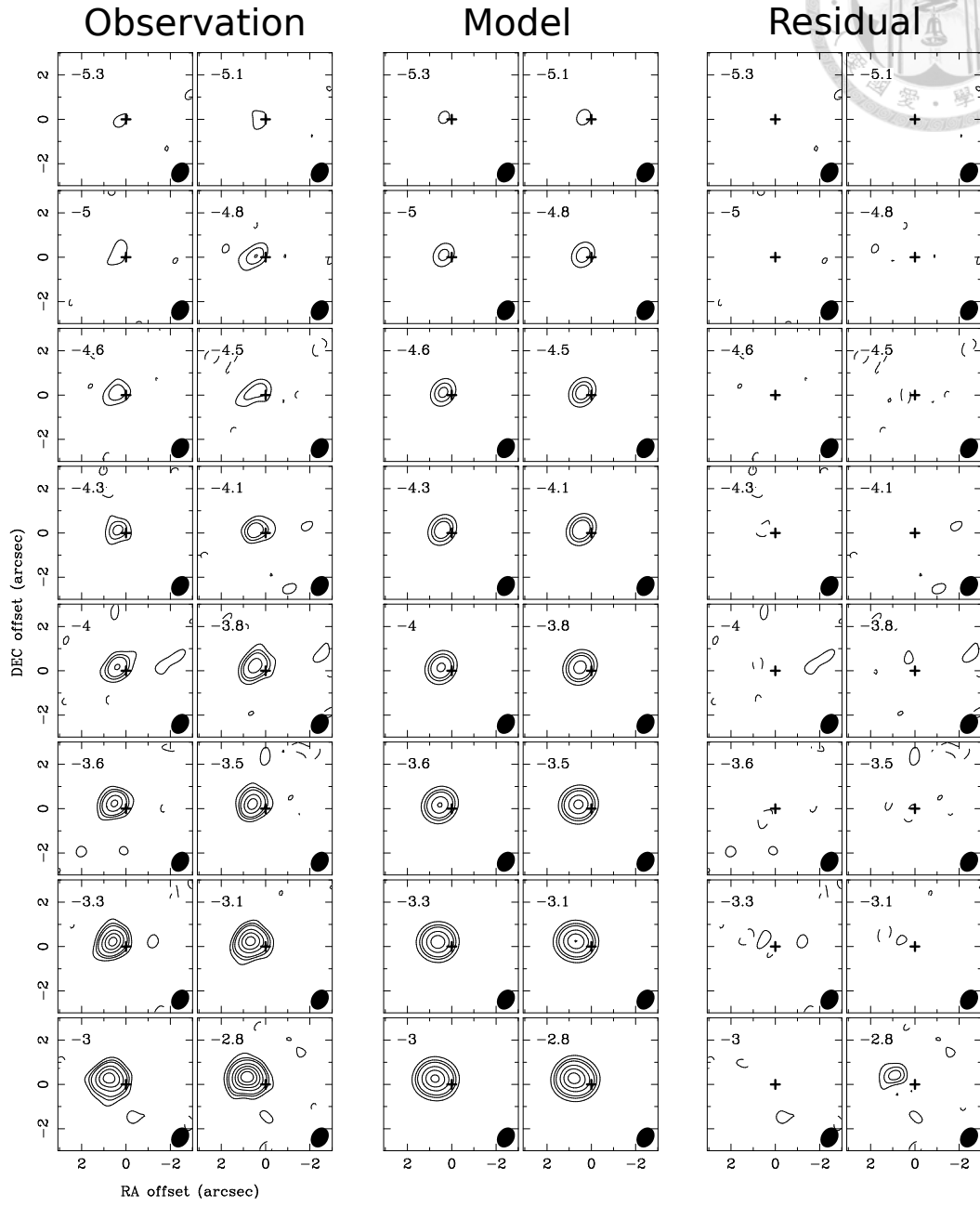


Figure 5.9 Left columns: velocity channel maps of the high-velocity C^{18}O (2-1) emission in L1489 IRS. Middle columns: model velocity channel maps of the Keplerian disk traced by the high-velocity C^{18}O (2-1) emission. Right columns: residual maps after subtracting the model velocity channel maps from the C^{18}O velocity channel maps. The velocity at each channel is shown at the upper-left corner in each panel. Crosses show the protostellar position. Contour levels are from 2σ to 6σ in steps of 2σ and then in steps of 5σ , where 1σ is 8 mJy Beam^{-1} .

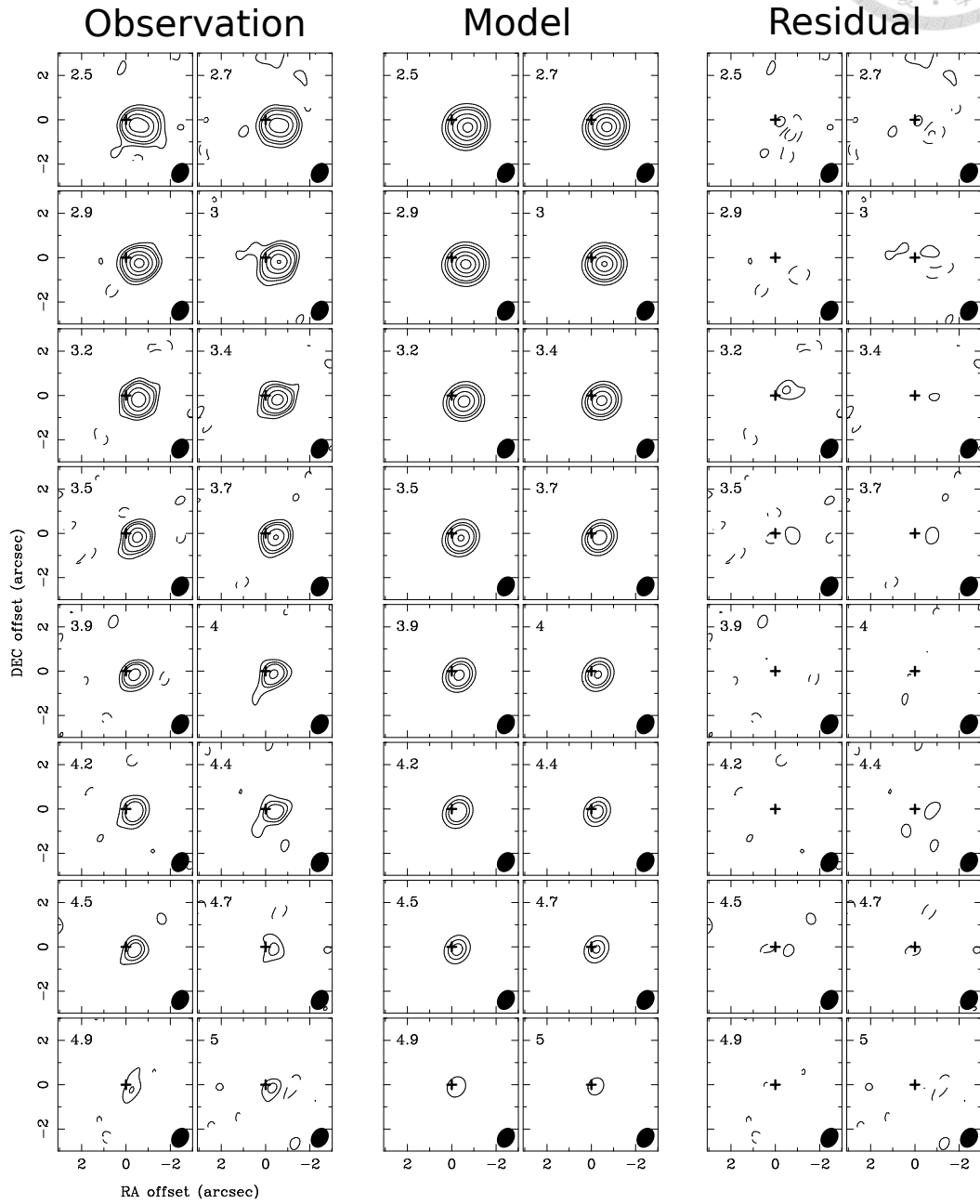


Figure 5.9. (Continued)

Figure 5.10 presents the comparison between the 1.3 mm continuum emission with the high-velocity C^{18}O emission, which likely traces the inner Keplerian disk, and with the best-fit disk model. The elongated component of the 1.3 mm continuum emission with the same position angle and similar extent as those of the model Keplerian disk most likely traces the Keplerian disk. On the other hand, the nature of the point source of the 1.3 mm continuum emission is not clear, which could arise from the very inner part of the disk ($r < 50$ AU), where the density or the temperature may be much higher than that of the outer disk. The mass of the Keplerian disk can be estimated from the total 1.3 mm flux as;

$$M_d = \frac{F_{1.3\text{mm}} d^2}{\kappa_{1.3\text{mm}} B(T_{\text{dust}})}, \quad (5.12)$$

where $F_{1.3\text{mm}}$ is the total flux, $\kappa_{1.3\text{mm}}$ is the dust mass opacity at 1.3 mm, T_{dust} is the dust temperature. On the assumption that the wavelength (λ) dependence of the dust mass opacity ($\equiv \kappa_\lambda$) is $\kappa_\lambda = 0.1 \times (0.3 \text{ mm}/\lambda)^\beta \text{ cm}^2 \text{ g}^{-1}$ (Beckwith et al. 1990), the mass opacity at 1.3 mm is $0.023 \text{ cm}^2 \text{ g}^{-1}$ with $\beta = 1.0$ (e.g., Jørgensen et al. 2007). The mass of the Keplerian disk is estimated to be $\sim 0.013\text{--}0.003 M_\odot$ with the dust temperature of 15–45 K derived from our disk fitting.

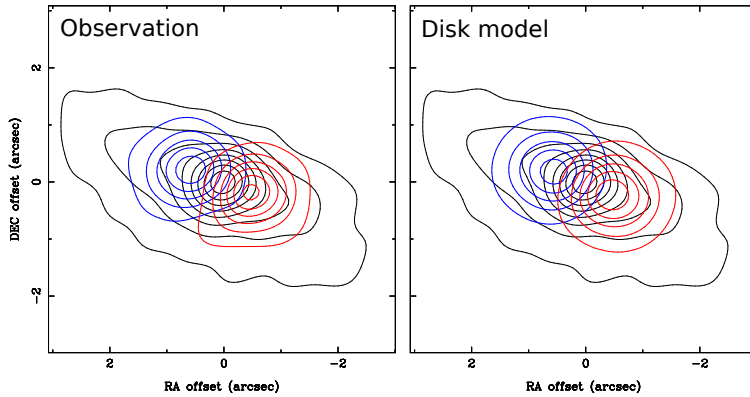


Figure 5.10 Comparison between the 1.3 mm continuum emission (black) with the high-velocity blueshifted and redshifted C^{18}O emission (left), same as Figure 5.5 left, and with the best-fit disk model integrated over the same velocity ranges (right). Contour levels are from 5σ in steps of 5σ .

To compare the velocity structures of the ^{12}CO and SO emission and the C^{18}O emission at the lower velocities with the derived Keplerian rotation, we made position–velocity (P–V) diagrams along the disk major axis passing through the gravitational center (Figure 5.11). Blue and red curves in the P–V diagrams present the expected

velocities of the Keplerian rotation. The velocity structure of the ^{12}CO emission can be explained by the Keplerian rotation. There is deviation between the observed velocity structure and the Keplerian rotation appears at $V \sim -2 \text{ km s}^{-1}$, which could be due to the effects of the opacity and missing flux. The velocity structure of the C^{18}O emission at lower velocities, which is not included in the disk fitting, can also be explained by the Keplerian rotation, suggesting the disk size could be more extended than the extent of the high-velocity C^{18}O emission. Due to the effect of the missing flux ($\sim 80\%$ at $|V| \sim 0 \text{ km s}^{-1}$ and $\sim 50\%$ at $|V| \sim 0.5 \text{ km s}^{-1}$; Hogerheijde et al. 1998), however, the velocities and the extents of the C^{18}O emission are likely distorted to be higher and smaller, and thus it is difficult to unambiguously identify the outer radius of the Keplerian disk. In addition to the Keplerian-rotating component, in the P–V diagram of the C^{18}O emission there appears a linear velocity gradient at $V \sim -2 - 2 \text{ km s}^{-1}$ and radii of $\sim -2'' - 2''$, indicated by a green segment, and the Keplerian-rotating component and the component exhibiting the linear velocity gradient are located along the same lines of sights with the different velocities. A similar linear velocity gradient is also seen in the P–V diagram of the SO emission. The velocity structure of the SO emission along the disk major axis primarily traces this linear velocity gradient, and only a part of the SO emission shows the velocity structure following the Keplerian rotation, e.g., the redshifted emission at $V \sim 2 - 3.5 \text{ km s}^{-1}$. The presence of the two components can also be identified in the velocity channel maps of the C^{18}O emission at $|V| = 1.5 - 2 \text{ km s}^{-1}$ (Figure 5.4), where two intensity peaks are present. The inner intensity peak most likely traces with the Keplerian disk identified in the high-velocity C^{18}O emission, while the outer intensity peak could be associated with the component exhibiting the linear velocity gradient. On the other hand, the velocity channel maps of the SO emission at similar velocities ($V = -1.9 - -1.4$ and $1.6 - 2.1 \text{ km s}^{-1}$; Figure 5.7) is weaker close to the protostar and exhibits an intensity peak corresponding to the outer intensity peak seen in the C^{18}O emission.

One hypothesis of the nature of the two components, the Keplerian rotation and the linear velocity gradient, in the P–V diagrams is that the Keplerian disk around L1489 IRS is surrounded by a Keplerian-rotating torus, and that the C^{18}O emission traces both the inner Keplerian disk and the outer torus, while the SO emission primarily traces the outer torus. Theoretical models of infalling protostellar

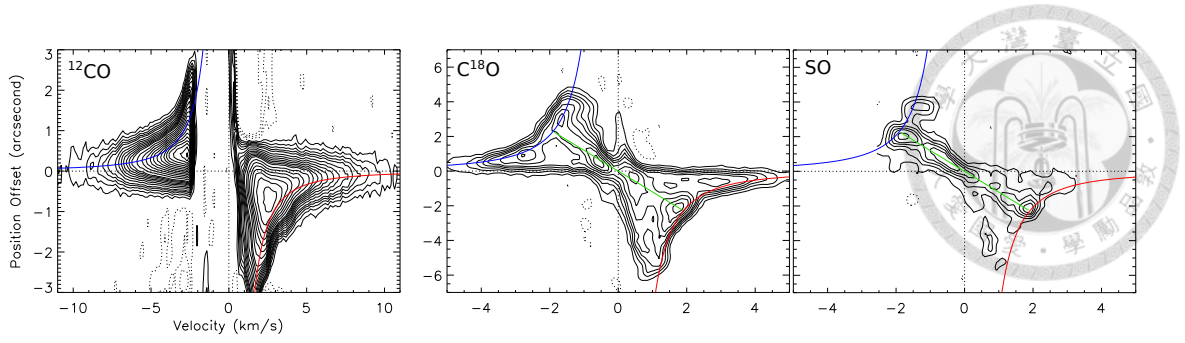
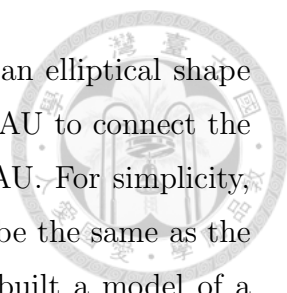


Figure 5.11 P–V diagrams of along the disk major axis in the ^{12}CO (left), C^{18}O (middle), and SO (right) emission. Blue and red curves show the expected velocities of the Keplerian rotation around a $2.0 M_{\odot}$ protostar at an inclination angle of 54° . Green segments delineate the linear velocity gradient seen in the C^{18}O and SO emission. Contour levels are from 3σ to 15σ in steps of 3σ and then in 5σ .

envelopes have shown that infalling material would accumulate at the centrifugal radius (Ulrich 1976; Cassen & Moosman 1981; Terebey et al. 1984). The proposed torus could be formed by the mass enrichment around the centrifugal radius. The intensity peaks outside the inner Keplerian disk seen in the moment 0 map of the medium-velocity C^{18}O emission (Figure 5.5 middle) could trace the mass enrichment at the centrifugal radius, and the radii of the blueshifted and redshifted peaks are estimated to be ~ 300 AU after correcting the inclination angle. Because the torus has a large thickness and narrow ranges of radii and rotational velocities, its emission be projected into the same lines of sight as the inner disk and show a linear velocity gradient along the disk major axis (i.e., x axis in Equation 5.7). From the position and magnitude of the linear velocity gradient, the radius of the torus is estimated to be ~ 320 AU with Equation 5.7, similar to those of the intensity peaks seen in the medium-velocity C^{18}O emission, suggesting the component exhibiting the linear velocity gradient (i.e., the torus) is likely associated with the mass enrichment at a radius of ~ 300 AU. From the geometry of the torus and the inclination of the disk plane, the scale height of the torus at a radius of 320 AU is estimated to be ~ 170 AU.

To demonstrate this hypothesis, we built a model of a geometrically-thin disk surrounded by a torus to compare with the C^{18}O data, and a model of a torus without an inner disk to compare with the SO data. We adopted our best-fit disk model as the model of the inner disk, which has an outer radius of 200 AU. The model torus is located at a radius of 320 AU as estimated from the observed linear



velocity gradient, and the tube of the torus is assumed to have an elliptical shape with a semi-major axis of 170 AU and a semi-minor axis of 120 AU to connect the inner disk. Thus, the entire model has an outer radius of 440 AU. For simplicity, the density of the model torus is assumed to be uniform and to be the same as the density of the inner disk at a radius of 200 AU. We have also built a model of a geometrically-thin disk with an outer radius of 440 AU to compare with the model of the inner disk surrounded by the torus, and a geometrically-thin uniform ring at $200 \leq r \leq 440$ AU to compare with the model of the torus. We computed the model images of the four models in the C^{18}O (2–1) line using Equation 5.7–5.11. Because the excitation and abundance of SO molecules in protostellar sources can be complicated (e.g., Bachiller & Pérez Gutiérrez 1997; Wakelam et al. 2005), the model images of the torus model and the ring model in the SO emission are made by artificially scaling the model C^{18}O images with the observed SO/ C^{18}O peak intensity ratio. Figure 5.12 show the comparison between the model and the C^{18}O and SO P–V diagrams. The main features in the C^{18}O and SO P–V diagrams can be reproduced by the disk+torus model and by the torus model, respectively (Figure 5.12a and b). The P–V diagram of the disk model without the surrounding torus does not show a linear velocity gradient at $r = -2''$ – $2''$ as the C^{18}O P–V diagram (Figure 5.12c), and that of the ring model shows two separated components and no linear velocity gradient, which are distinct from the SO P–V diagram (Figure 5.12d). The comparison shows that the two components seen in the velocity channel maps of C^{18}O emission at $|V| = 1.5 - 2 \text{ km s}^{-1}$, the missing high-velocity components in the SO emission, and the linear velocity gradients seen in the C^{18}O and SO P–V diagrams cannot be explained by a simple disk, but can be reproduced with the model of a inner geometrically-thin Keplerian disk surrounding by a Keplerian-rotating torus, and that the C^{18}O emission traces both the disk and the torus, while the SO emission primarily traces the torus.

5.5.2 Infalling Gas Flows onto the Keplerian Disk

The high-velocity C^{18}O emission likely traces the Keplerian disk (Figure 5.5 left). On the other hand, the two off-axis protrusions of the blueshifted and redshifted C^{18}O emission at the medium velocities (Figure 5.5 middle) cannot be explained by any axisymmetric disk model. We consider two possibilities of the nature of

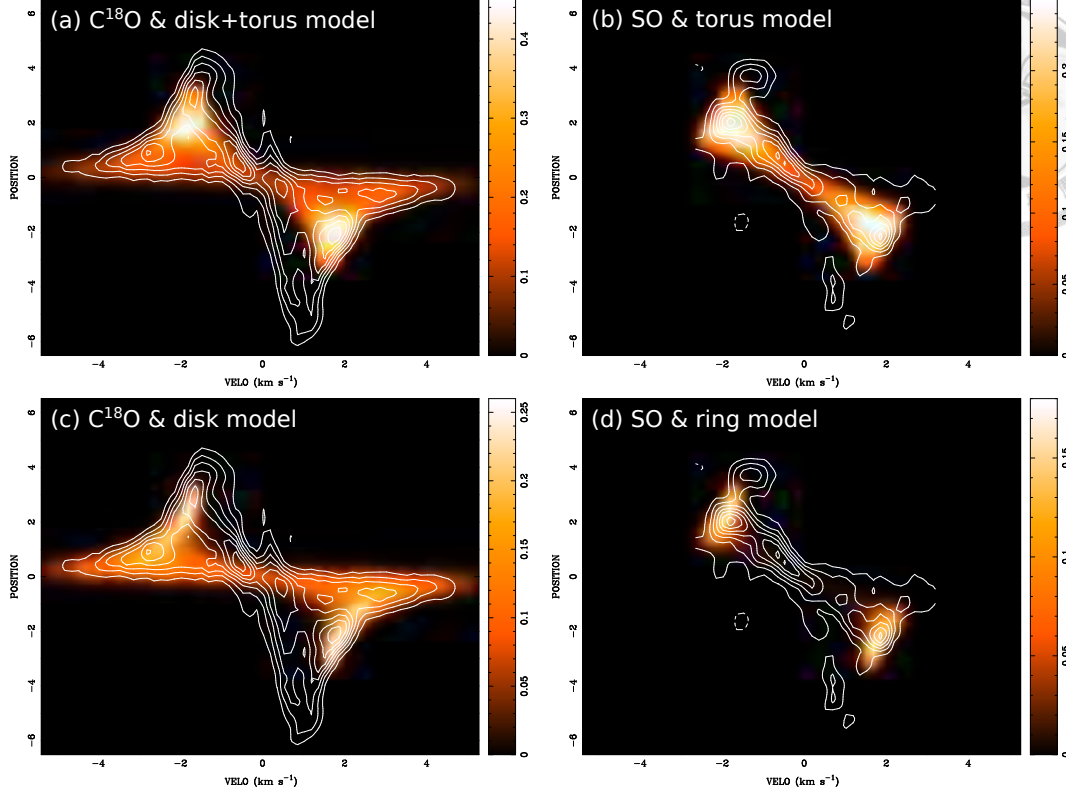


Figure 5.12 P–V diagrams along the disk major axis in the C^{18}O (left column) and SO (right column) emission (contours) overlaid on the model P–V diagrams (color), (a) disk+torus model, (b) torus model, (c) disk model without a torus, and (d) ring model. Contour levels are from 5σ in steps of 5σ in the C^{18}O P–V diagram, and are from 3σ in steps of 3σ in the SO P–V diagram.

these protrusions. The first possibility is that the protrusions could trace infalling flows toward the Keplerian disk. Free-falling material with a conserved angular momentum and zero total energy would follow a parabolic trajectory toward the center, and the protrusions in the medium-velocity C^{18}O emission trace infalling material with a conserved angular momenta from a certain incoming direction (i.e., non-isotropic infalling motion), which may not be located on the same plane as the Keplerian disk. In this scenario, the two intensity peaks of the blueshifted and redshifted C^{18}O emission at the medium velocities, connected to the protrusions (Figure 5.5 middle), could trace the mass enrichment at the centrifugal radius. The other possibility is that the protrusions trace the spiral structures of the Keplerian disk.

First, we examine whether the curvature and kinematics of the protrusions can be explained by infalling flows with a conserved angular momentum. We measured

the peak positions of the intensity profiles along the RA or Dec directions across the protrusions, shown as green filled squares in Figure 5.13, to delineate their curvatures, where the spatial interval between the measured point is taken to be the half of the beam size. Then we fitted parabolic trajectories of material free-falling toward a $2.0 M_{\odot}$ protostar to the measured peak positions. On the assumption that the gravity is dominated by the central protostar, the parabolic trajectories and the expected velocities along the trajectories are given by Ulrich (1976) as,

$$r = \frac{R_c \cos \theta_0 \sin^2 \theta}{\cos \theta_0 - \cos \theta} \quad (5.13)$$

where

$$\cos \theta = \cos \theta_0 \cos \alpha, \quad (5.14)$$

$$\tan(\phi - \phi_0) = \tan \alpha \sin \theta_0, \quad (5.15)$$

R_c is the centrifugal radius, and θ_0 and ϕ_0 are the initial polar and azimuthal angles of infalling material, which defined as the angle between the rotational axis and the line connecting the infalling material and the protostar. We adopted θ_0 and ϕ_0 as free parameters and the centrifugal radius of 300 AU (i.e., the radius of the intensity peaks of the medium-velocity C^{18}O emission), computed infalling trajectories and velocities, and performed χ^2 fitting to the measured peak positions. The curvature of the redshifted protrusion can be explained by a parabolic trajectory of material free-falling from $\theta_0 = 133^\circ$ and $\phi_0 = 263^\circ$ (red curve in Figure 5.13a), and that of the blueshifted bent protrusion $\theta_0 = 43^\circ$ and $\phi_0 = 76^\circ$ (blue curve in Figure 5.13b). Notice that the derived infalling trajectories of the redshifted and blueshifted protrusion are not coplanar, and are below and above the disk plane, respectively.

To demonstrate this interpretation, we built a model of two infalling flows and attached the infalling flow model to our disk+torus model. The velocities and density distributions of the infalling flows are given by Ulrich (1976) as,

$$V_r = -\sqrt{\frac{GM_*}{r}} \cdot \sqrt{1 + \frac{\cos \theta}{\cos \theta_0}}, \quad (5.16)$$

$$V_\theta = \sqrt{\frac{GM_*}{r}} \cdot (\cos \theta_0 - \cos \theta) \cdot \sqrt{\frac{\cos \theta_0 + \cos \theta}{\cos \theta_0 \sin \theta}}, \quad (5.17)$$

$$V_\phi = \sqrt{\frac{GM_*}{r}} \cdot \frac{\sin \theta_0}{\sin \theta} \cdot \sqrt{1 - \frac{\cos \theta}{\cos \theta_0}}, \quad (5.18)$$

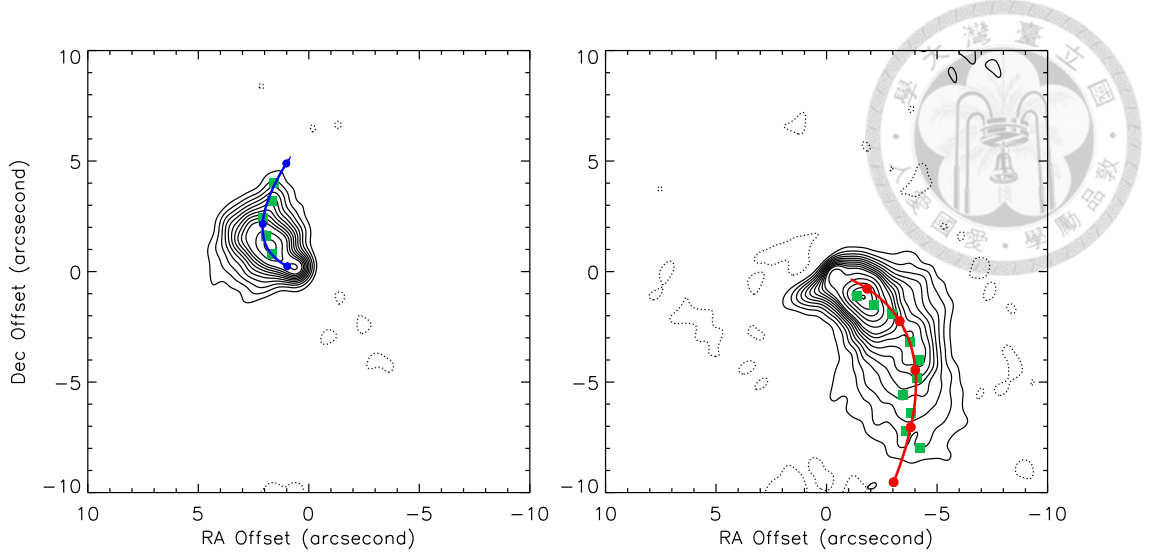


Figure 5.13 Trajectories of the blueshifted (left) and redshifted (right) infalling flows. Contours show moment 0 maps of the blueshifted (left) and redshifted (right) medium-velocity C^{18}O (2–1) emission in L1489 IRS (same as Figure 5.5 middle). Green filled squares present the measured peak positions of the intensity distributions along RA or DEC directions across the protrusions in the medium-velocity C^{18}O emission, which are used to derive the infalling trajectories. Red and blue curves show the trajectories of the redshifted and blueshifted infalling flows derived from the model fitting, respectively. Red filled circles on the red trajectory denote the positional offset of $2''$, $4''$, $6''$, $8''$, and $10''$ from the center, and blue filled circles on the blue trajectory $1''$, $3''$, and $5''$. Contour levels are from 5σ to 50σ in steps of 5σ and then in steps of 10σ , where 1σ is $4 \text{ mJy Beam}^{-1} \text{ km s}^{-1}$ at the blueshifted velocities and $5 \text{ mJy Beam}^{-1} \text{ km s}^{-1}$ at the redshifted velocities.

$$n = n_1 \cdot \left(\frac{r}{R_c}\right)^{-1.5} \left(1 + \frac{\cos \theta}{\cos \theta_0}\right)^{-0.5} \left(\frac{\cos \theta}{2 \cos \theta_0} + \frac{R_c}{r} \cos^2 \theta_0\right)^{-1}. \quad (5.19)$$

, and R_c is adopted to be 300 AU, as the radius of the intensity peaks in the medium-velocity C^{18}O emission (Figure 5.5 middle). In reality the infalling flows must have certain characteristic widths (Figure 5.13), which depends on the mass distribution as a function of θ_0 and ϕ_0 . However, it is not straightforward to unambiguously determine the widths of the infalling flows and hence the mass distribution of the initial infalling material as a function of θ_0 and ϕ_0 due to the contamination from the outflow and from the remnant envelope and/or disk components on the disk plane. For simplicity and the purpose of demonstration, in our model we assumed the redshifted infalling flow has $\theta_0 = 133^\circ \pm 4^\circ$ and $\phi_0 = 263^\circ \pm 4^\circ$, and the blueshifted infalling flow $\theta_0 = 43^\circ \pm 4^\circ$ and $\phi_0 = 76^\circ \pm 4^\circ$, such that the model infalling flows have sufficiently wide widths for comparison of their morphologies and kinematics with those in the real observation. We have made several model images in the C^{18}O

(2–1) line with different n_1 and outer radii of the infalling flows using Equation 5.7–5.11, and found that model images with n_1 of $6 \times 10^7 \text{ cm}^{-3}$ and outer radii of 6000 and 2000 AU for the redshifted and blueshifted infalling flows, respectively, can approximately reproduce the extent and intensity of the observed protrusions in the medium-velocity C^{18}O emission. The density distribution of the model is shown in Figure 5.14.

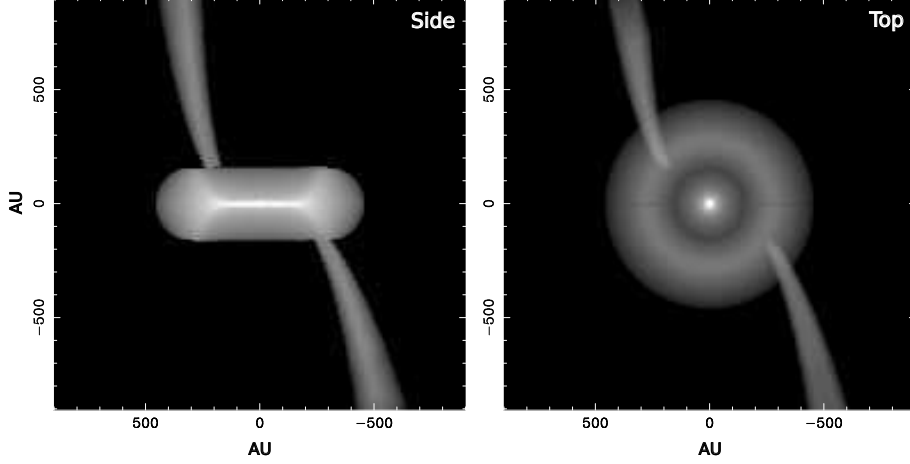


Figure 5.14 Edge-on (right) and face-on (left) view of the model comprising an central geometrically-thin Keplerian disk surrounded by a Keplerian-rotating torus and two infalling flows.

Figure 5.15a and b show the moment 0 maps of the medium-velocity C^{18}O emission and the model. The infalling flow model can explain the curvature of the protrusions in the medium-velocity C^{18}O emission, while the observed intensity distribution is more extended than the model intensity distribution, which could be due to the contamination from the outflow and from the remnant envelope and/or disk component on the disk plane. Figure 5.15c and d present the comparison between the C^{18}O and model P–V diagrams along the derived infalling trajectories (the red and blue curves in Figure 5.13a and b). The infalling flow model can reproduce the main velocity structures of the protrusions. There is excess of high-velocity components ($|V| \sim 2\text{--}3 \text{ km s}^{-1}$) and lack of low-velocity components ($|V| < 1 \text{ km s}^{-1}$) at positional offsets of $1.5''\text{--}3''$ in the blueshifted infalling flow (Figure 5.15c) and of $2''\text{--}4''$ in the redshifted infalling flow (Figure 5.15d). This discrepancy is likely due to that in our model, there are sharp boundaries between the infalling flows and the central disk. In reality the infalling flows likely decelerate and transform into the Keplerian disk as approaching the disk. As a result, our model predicts more

high-velocity components but less low-velocity components.

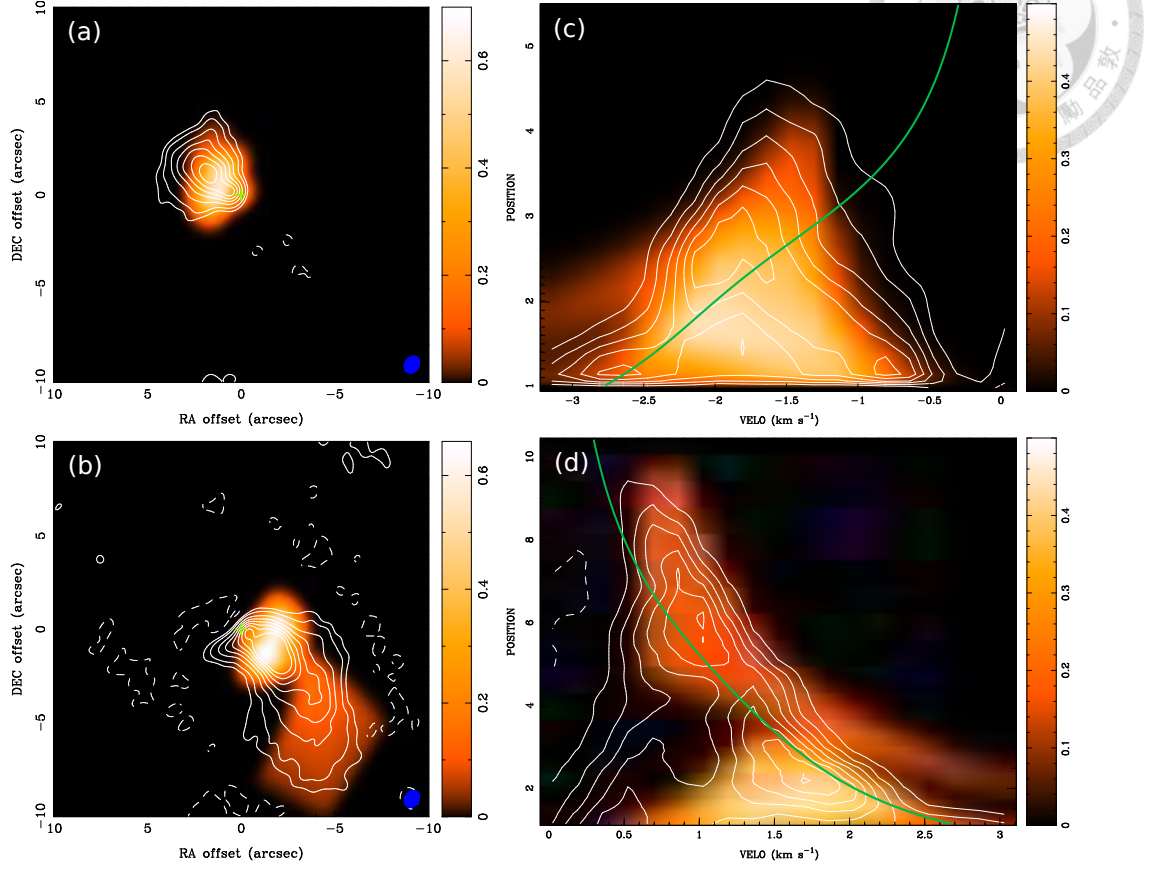


Figure 5.15 (a) & (b) Moment 0 maps of the blueshifted and redshifted medium-velocity C^{18}O (2–1) emission (contour), same as Figure 5.5 middle, overlaid on the moment 0 maps of the infalling flow model integrated over the same velocity ranges (color). Crosses show the protostellar position. Filled ellipses denote the beam size. Contour levels are from 5σ , 10σ , and then in steps of 10σ , where 1σ is 4 mJy Beam^{-1} . (c) & (d) C^{18}O (2–1) P–V diagrams along the curvature of the blueshifted and redshifted protrusions (blue and red curves in Figure 5.13), overlaid on the model P–V diagrams. The calculated Keplerian velocities along the curvature of the protrusions are shown in green curves on the assumption that the protrusions are located on the disk plane. Contour levels are from 5σ in steps of 5σ , where 1σ is 8 mJy .

Next, we discuss the second possibility, the protrusions seen in the medium-velocity C^{18}O emission are the coplanar spiral structures of the Keplerian disk. The Keplerian velocities along the protrusions can be computed with Equation 5.7 and 5.3, which are shown as green curves in Figure 5.15c and d. In the P–V diagrams along the curvature of the protrusions the velocities of the blueshifted protrusions at positional offsets $\gtrsim 3''$ and those of the redshifted protrusion at positional offsets $\gtrsim 5''$ are faster than the Keplerian velocities, suggesting the presence of other systemic motions, while the inner parts of the protrusions could follow the Keplerian rotation. Hence, the kinematics of the protrusions cannot be purely explained by the Keplerian rotation. The velocities of the outer parts of blueshifted and redshifted protrusions are more blueshifted and redshifted than the Keplerian velocities, respectively, and the northern and southern parts of the disk plane are tilted toward and away from us, respectively, suggesting the outer parts of the protrusions are expanding and moving away from the central disk if they are coplanar component of the Keplerian disk. However, the mechanism to induce the expanding spirals on the Keplerian disk is not clear. Therefore, we consider that the infalling flow model is a more natural interpretation of the protrusions seen in the medium-velocity C^{18}O emission.

5.6 Discussion

As shown by the results of our disk fitting (Figure 5.9), the high-velocity C^{18}O emission most likely traces the inner part of the Keplerian disk ($r \lesssim 200$ AU), and the central protostellar mass is estimated to be $2.0 M_{\odot}$. The derived Keplerian rotation can also explain the velocity structures of the high-velocity ^{12}CO emission (Figure 5.11), and hence the high-velocity ^{12}CO emission likely traces the innermost part of the Keplerian disk ($r \lesssim 45\text{--}70$ AU). In addition to the signature of the Keplerian rotation seen in the C^{18}O P–V diagram, both the C^{18}O and SO emission lines exhibit a linear velocity gradient in their P–V diagrams along the disk major axis (Figure 5.11). This linear velocity gradient can be explained by the emission from a torus surrounding the Keplerian disk (Figure 5.12). and the SO emission primarily trace the torus. On the other hand, the C^{18}O emission at the medium velocities shows the intensity peaks at radii of ~ 300 AU and the two protrusions pointing toward the north and south (Figure 5.5 middle). Through the comparison

with our proposed model (Figure 5.14), we found the protrusions can be interpreted as parabolic infalling flows toward the Keplerian disk (Figure 5.13 and 5.15), and the intensity peaks could trace the mass enrichment at the centrifugal radius, caused by the accumulation of infalling material. The torus surrounding the Keplerian disk is likely associated with the mass enrichment around the centrifugal radius. Therefore, our analysis of the ALMA observational results suggests that L1489 IRS is likely surrounded by an inner Keplerian disk with a outer radius ~ 200 AU and an outer torus at radius of ~ 320 AU, and that there are two infalling flows toward the Keplerian disk.

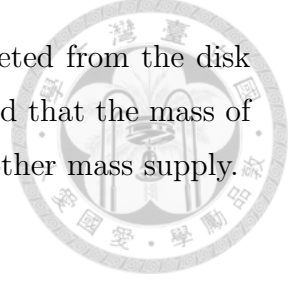
In Class 0 and I protostellar sources without large-scale (> 100 AU) Keplerian disks, the kinematics of their protostellar envelopes can often be explained by axisymmetric models of infalling and rotating envelopes, such as B335 (Chapter 3), HH 212 (Lee et al. 2006), L1527 IRS (Ohashi et al. 1997), and L1551 IRS 5 (Momose et al. 1998). On the contrary, the infalling material in L1489 IRS follows two parabolic flows and cannot be explained by any axisymmetric models. The difference in the infalling motions between L1489 IRS and the other Class 0 and I sources could be due to the different evolutionary stages of the protostellar envelopes. Previous observations have found that protostellar envelopes around more evolved sources tend to exhibit less mass (e.g., Ladd et al. 1998; Arce & Sargent 2006, Jørgensen et al. 2009), and that the opening angle of outflow cavities increases as protostellar sources evolve to later stages (Velusamy & Langer 1998; Arce & Sargent 2004, 2006), suggesting that the majority of protostellar envelopes is distorted and cleared away by outflows in later evolutionary stages (see Figure 8 in Arce & Sargent 2006 for schematic demonstration). Therefore, it is likely that L1489 IRS is in the later evolutionary stage, and that the envelope around L1489 IRS is partially dissipated and becomes asymmetric due to the interaction with the outflow. Thus, the infalling motion of the remnant asymmetric envelope appears as two parabolic flows.

The presence of the infalling flows onto the Keplerian disk around L1489 IRS suggests that as protostellar sources evolve from Class I to II stage, when protostellar envelopes are partially dissipated, remnant envelopes can still feed mass and angular momenta to central Keplerian disks. In addition, the angular momentum of the infalling flows in L1489 IRS is likely conserved, which is consistent with the expectation of recent MHD simulations for infalling material in dissipated envelopes

(e.g., Mellon & Li 2008; Machida et al. 2011). The results of these MHD simulations have suggested that in an early evolutionary stage, magnetic braking can effectively remove the angular momentum of infalling material in protostellar envelopes and hence suppress the outer radii of Keplerian disks ($\gtrsim 10$ AU; e.g., Dapp et al. 2012). The efficiency of magnetic braking decreases as protostellar envelopes are dissipated through the mass accretion onto central protostar+disk systems or the mass ejection by outflows in a later evolutionary stage, allowing large-scale disks to form. Our results of L1489 IRS, which is likely in the later evolutionary stage, could support such a scenario. On the other hand, the role of magnetic braking in the early evolutionary stage is still unclear.

We have estimated the mass infalling rate of the infalling flows in L1489 IRS as described below. The integrated flux of the medium-velocity C^{18}O emission is $1300 \text{ Jy Beam}^{-1} \text{ km s}^{-1}$ (Figure 5.5 middle). Because it is not straightforward to unambiguously distinguish the infalling flows, the contamination from the outflow, and the disk or remnant envelope components from our observational results, the integrated flux includes the flux of the infalling flows as well as the contamination. Therefore, the mass infalling rate, estimated with the integrated flux of the medium-velocity C^{18}O emission, should be considered as an upper limit. On the assumption of an excitation temperature of 10 K and the C^{18}O abundance of 3×10^{-7} (Frerking et al. 1982), the total gas mass traced by the medium-velocity C^{18}O emission is estimated to be $\sim 5 \times 10^{-3} M_{\odot}$. The infalling time scale is estimated to be $\sim 10^4$ yr based on the lengths and mean radial infalling velocities of the infalling flows (Equation 5.13 and 5.16). Thus, the upper limit of the mass infalling rate is estimated to be $5 \times 10^{-7} M_{\odot} \text{ yr}^{-1}$. The mass infalling rate in L1489 IRS is an order of magnitude lower than those often observed in Class 0 and I protostellar sources exhibiting axisymmetric envelopes but without large-scale Keplerian disks (e.g., Ohashi et al. 1997; Momose et al. 1998; Lee et al. 2006; Chapter 3). The lower mass infalling rate in L1489 IRS could be the consequence of the dissipation of the protostellar envelope. On the assumption that the bolometric luminosity ($3.7 L_{\odot}$) is fully generated by the gravitational energy released by material accreted on the surface of the protostar ($M_{\star} \sim 2M_{\odot}$), the mass accretion rate onto the protostar is estimated to be $\sim 2 \times 10^{-6} M_{\odot} \text{ yr}^{-1}$ with a protostellar radius of $3R_{\odot}$. The estimated mass accretion rate is higher than the mass infalling rate onto the Keplerian

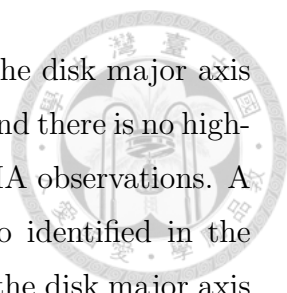
disk by a factor of five, suggesting that there is more mass accreted from the disk onto the protostar than that from the envelope onto the disk, and that the mass of the Keplerian disk likely decreases with evolution if there is no other mass supply.



5.7 Summary

We have performed detailed imaging and analysis of the ALMA observations of L1489 IRS in the 1.3 mm continuum and the ^{12}CO (2–1), C^{18}O (2–1), and SO (5_6-4_5) lines. The main results are summarized below.

1. The C^{18}O and SO emission and the central component of the ^{12}CO emission are elongated along the northeast–southwest direction and exhibit velocity gradients along their major axes. The velocity gradients most likely trace the rotational motion around L1489 IRS. The Keplerian rotation is clearly identified in the high-velocity ($\gtrsim 2.5 \text{ km s}^{-1}$) ^{12}CO and C^{18}O emission. We have built an axisymmetric geometrically-thin disk model and performed χ^2 fitting to the high-velocity C^{18}O emission. The protostellar mass and the inclination angle of the disk plane are estimated to be $2 M_{\odot}$ and 54° , respectively. The 1.3 mm continuum emission shows the elongation and extent similar to those of the Keplerian disk and most likely traces the Keplerian disk. The disk mass is estimated to be $0.003\text{--}0.013 M_{\odot}$.
2. The C^{18}O emission at medium velocities ($\sim 0.5\text{--}2.5 \text{ km s}^{-1}$) exhibits blueshifted and redshifted peaks located at $\sim 2''$ ($\sim 300 \text{ AU}$) to the northeast and to the southwest, respectively. At the tip of the elongated structure in the C^{18}O emission, there are blueshifted and redshifted protrusions pointing to the north and south, respectively, which cannot be reproduced by any axisymmetric disk model. We have built a model of infalling gas flows with a conserved angular momentum following parabolic trajectories toward the Keplerian disk, and found the curvature and kinematics of the protrusions can be reproduced with the infalling flow model, and that the intensity peaks at the medium velocities connected to the protrusions could trace the mass enrichment at the centrifugal radius and the transitional region from the infalling flow to the Keplerian disk. The mass infalling rate is estimated to $< 5 \times 10^{-7} M_{\odot} \text{ yr}^{-1}$.

- 
3. The SO emission exhibits a linear velocity gradient along the disk major axis and does not show any signature of the Keplerian rotation, and there is no high-velocity ($\gtrsim 2.5\text{--}3\text{ km s}^{-1}$) SO emission detected in our ALMA observations. A similar velocity gradient along the disk major axis is also identified in the C^{18}O emission. We have compared the P–V diagrams along the disk major axis in the C^{18}O and SO emission with models of a geometrically-thin Keplerian disk, a geometrically-thin Keplerian ring, and a Keplerian torus, and the linear velocity gradient and the signature of the Keplerian rotation seen in the P–V diagrams can be reproduced simultaneously with a model of the Keplerian disk surrounding by a Keplerian-rotating torus. The radius of the torus is estimated to be $\sim 320\text{ AU}$, close to the centrifugal radius. The torus could be associated with the mass enrichment caused by the accumulation of infalling material around the centrifugal radius. The SO emission primarily traces the torus and is not clearly detected toward the Keplerian disk, while the C^{18}O emission traces both the torus and the Keplerian disk. The enhancement in the SO intensity in the transitional region from the infalling flows to the Keplerian disk could be due to the enhancement in the SO abundance by accretion shocks.
 4. Our ALMA observational results suggest that the infalling motion in L1489 IRS is not isotropic and appears as two streams of infalling flows. The presence of the non-isotropic infalling motion could be due to that the protostellar envelope around L1489 IRS has been partially dissipated by the outflow, and the dissipating protostellar envelope can still feed mass and angular momenta to the Keplerian disk as the protostar evolves from the Class I to II stages. The angular momentum of the infalling flows is found to be conserved, which is consistent with the expectation of the MHD simulations that magnetic braking is ineffective in the end of the main accretion phase as protostellar envelopes are dissipated.



Chapter 6

Summary of this Thesis

In this thesis project, I have conducted systematic observations and data analyses of six representative protostellar sources in several (sub)millimeter molecular lines and continuum emission with the SMA, SMT, ASTE, and ALMA. The primary goal of my thesis is to unveil the evolutionary sequence of protostellar envelopes toward Keplerian-disk formation, and to observationally understand the formation mechanism of Keplerian disks. The main results are summarized below.

1. SMA + SMT and ASTE observations of a Class 0 protostar B335 show that the millimeter C^{18}O (2–1) emission exhibits both extended (~ 9000 AU) halo-like feature and the central compact (~ 1500 AU) envelope, while the submillimeter CS (7–6) emission exhibits even more compact feature with a size of ~ 800 AU, surrounded by an east-west elongated outflow with a size of ~ 3000 AU. The compact C^{18}O envelope shows elongation perpendicular to the outflow direction, and a velocity gradient along the minor axis. The velocity gradient seen in the C^{18}O emission can be interpreted as an infalling gas motion toward the central protostar with the mass of $0.04 M_{\odot}$. On the other hand, the absence of the velocity gradient along the envelope major axis implies little rotational motion ($V_{\text{rot}} < 0.04 \text{ km s}^{-1}$ at a radius of 370 AU) in the infalling envelope. In contrast, the CS emission shows a sign of a rotational motion ($V_{\text{rot}} = 0.11 \text{ km s}^{-1}$ at a radius of 110 AU) but no signature of the infalling motion. These results indicate that the submillimeter CS emission traces innermost part of the envelope where the infalling gas motion is terminated and formation of the circumstellar disk is initiated.

2. I have performed SMA survey observations of three Class 0 (B335, NGC 1333 IRAS 4B, and L1448-mm), one Class 0/I (L1527 IRS), and two Class I sources (TMC-1A and L1489 IRS) in the C^{18}O (2–1) emission. I have developed a new method to measure the radial profiles of the rotational motions from the observed P–V diagrams perpendicular to the outflow directions, and derived the rotational profiles (i.e., $V_{\text{rot}} = v_0(r/r_0)^{-p}$) on 100 – 1000 AU scales. L1527 IRS (Class 0/I) and L1448-mm (Class 0) have rotational profiles with the power-law indices $p = -1.0 \pm 0.2$ and -1.0 ± 0.1 , respectively. Class I protostars TMC-1A and L1489 IRS exhibit higher rotational velocities with the power-law indices $p = -0.6 \pm 0.1$ and -0.5 ± 0.1 , respectively. On the contrary, Class 0 protostars B335 and NGC 1333 IRAS 4B do not show any detectable rotational motion. The rotational motions with the radial dependence of $\sim r^{-1}$ can be interpreted as rotation with a conserved angular momentum in a dynamically infalling envelope, while those with the radial dependence of $\sim r^{-0.5}$ can be interpreted as Keplerian rotation. These results, as well as previous observational results of rotational motions of other protostellar envelopes, demonstrate that the kinematics of the protostellar envelopes on 100–1000 AU scales can be classified into the three categories; (1) infalling motion with little rotational motion around Class 0 protostars (e.g., B335 and NGC 1333 IRAS 4B), (2) infalling and rotational motions around Class 0 and I protostars (e.g., L1527 IRS, L1448-mm, HH 212, and L1551 IRS 5), and (3) Keplerian rotation around Class I protostars (e.g., TMC-1A, L1489 IRS, L1551 NE, IRS 63 and Elias 29). This classification demonstrates the evolution from infalling envelopes to Keplerian disks, and can be reproduced with analytical calculations of the inside-out collapse model where the angular momentum of collapsing material is conserved.
3. With the ALMA observation, a Keplerian disk around L1489 IRS is clearly identified in the ^{12}CO (2–1) and C^{18}O (2–1) emission, and the central protostellar mass is estimated to be $2.0 M_{\odot}$. In addition to the central Keplerian disk, two stream-like features that connect to the Keplerian disk from outside are seen in the C^{18}O emission. The SO emission is seen around the "connection points" between the streams and the disk. To interpret these results, I have constructed a non-axisymmetric model that comprises a Keplerian disk

surrounded by a torus and outer gas components, performed the radiative transfer calculations on the LTE assumption, and generated model images that can be compared to the observed ALMA image. My model shows that the two streams can be reproduced by non-isotropic infalling-gas flows that follow parabolic trajectories toward the central Keplerian disk. The mass infalling rate of the infalling flows in L1489 IRS is estimated to be less than $5 \times 10^{-7} M_{\odot} \text{ yr}^{-1}$. Furthermore, my model shows that the SO emission primarily traces the transitional regions from the infalling flows to the Keplerian disk, which is likely due to the enhancement of the SO abundance caused by the accretion shock. The presence of the non-isotropic infalling gas flows suggests that the protostellar envelope around L1489 IRS has been partially dissipated by the outflow, and the remnant envelope material can still infall and feed mass and angular momenta to the Keplerian disk in the late Class I stage.

Figure 6.1 shows a schematic figure of the evolution of the protostellar envelopes into Keplerian disk formation, which the present thesis has revealed

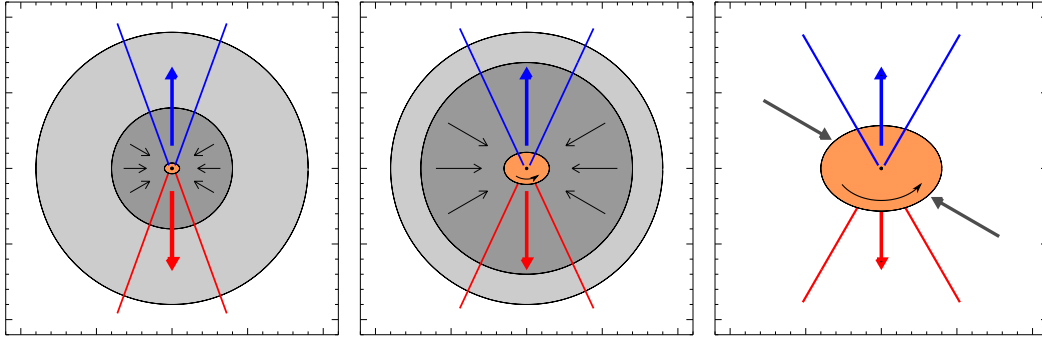


Figure 6.1 In the early collapse stage (left), the envelope material with a small angular momentum in the vicinity of the protostar collapses first, and hence the protostellar envelope on 100–1000 AU scale shows infalling motion but little rotational motion. As the expansion wave propagates outwardly (middle), the envelope material with a larger angular momentum in the outer region start to collapse and forms a large-scale (~ 100 AU) Keplerian disk at the center. Eventually (right), the protostellar envelope is dissipated via the mass accretion onto the central disk+protostar system and/or the mass ejection by the outflow. The central Keplerian disk with a radius of hundreds of AU becomes apparent, and the infalling motion becomes non-isotropic and is along few streams of parabolic flows.



Chapter 7

Future Work

My SMA survey observations of protostellar sources have revealed a systematic evolutionary sequence of protostellar envelopes toward form of Keplerian disk. One still unclear point is the effect of magnetic fields on the disk formation. Whereas presence of protostellar jets and outflows unambiguously proves the presence of the magnetic fields in protostellar sources (see Chapter 2), the effect of the magnetic fields on disk formation has been still controversial. Thorough theoretical simulations by Mellon & Li (2008, 2009) and Li et al. (2011) show that large-scale (>100 AU) Keplerian disks cannot be formed due to the effective magnetic braking. On the contrary, a series of theoretical simulations by Machida et al. (2011) show that large-scale, self-gravitating disks can form at the stage when the bulk of the protostellar envelopes has been dissipated, although the disk masses are a few times higher than the protostellar masses. It is still an unresolved, important astrophysical issue how Keplerian disks form in the presence of magnetic fields.

It is also still unclear how infalling gas is transformed into a central Keplerian disk. My ALMA observations of a Class I protostar L1489 IRS have identified infalling flows to the central Keplerian disk. The presence of the SO emission peaks at the apparent landing points of the flows onto the Keplerian disk may suggest the presence of the accretion shock. However, the structure and kinematics at the landing points are not resolved, and it is not clear how abrupt the deceleration of the infalling motion and the change of the angular momentum are.

I hereby propose the following projects as my future works, to expand my thesis project and to deepen our understanding of disk formation.



1. **Direct Imaging of the Magnetic Field Structures in the Disk-Forming Regions**

I propose to conduct submillimeter polarimetric observations of dust continuum emission and observations of Zeeman splitting of submillimeter molecular lines toward a few Class 0 and I sources with ALMA. These ALMA observations should be able to unveil the configuration and the strength of the magnetic fields in the disk-forming region. I will compare the measured field strengths and configurations to the gas motions in the disk-forming regions revealed with the present thesis project, and discuss the effect of the magnetic field in the disk formation processes.

2. **Resolving the Transitional Region from Infalling Envelopes to Keplerian Disks**

My ALMA results of L1489 IRS suggest that the SO emission could trace transitional regions between infalling envelopes and Keplerian disks. I also have the SMA data in the SO (5_6-4_5) line toward several Class 0 and I protostars, and currently I am working on the analyses of the SO data. From the SMA data I will identify promising candidates to study the transitional regions between the envelopes and the disks, and then propose the ALMA observations with higher spatial and velocity resolutions in the multi-transitional SO lines. With the ALMA observations I aim to reveal the deceleration of the infalling motion, the change of the angular momentum, and the physical conditions of the accretion shock in the transitional regions.

3. **Mapping Dissipating Protostellar Envelopes from the Envelope to Disk Scales**


Dissipation of protostellar envelopes may be one of the key phenomena to promote disk formation, because the envelopes anchor the magnetic field and cause magnetic braking that suppresses the formation of Keplerian disks. Envelope dissipation is considered to be driven by the interaction with the protostellar winds and outflows, but observationally the physics of the interaction is still unclear. To reveal the physical process of the envelope dissipation, I plan to propose single-dish mapping and SMA mosaic observations of Class I protostars which already possess Keplerian disks, such as L1489 IRS and TMC-1A.

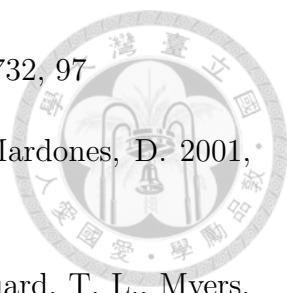
By combining the single-dish and SMA data it is possible to study the kinematics and structure of the entire dissipating envelopes on thousands of AU scale at an angular resolution of few arcsecond. I will also study the relation between the non-isotropic infalling flows in L1489 IRS found by my ALMA observations and the dissipation of the envelope.





Bibliography

- Andre, P., Ward-Thompson, D., & Barsony, M. 2000, in *Protostars and Planets IV*, ed. V., Mannings, A. P., Boss, & S. S., Russell (Tucson, AZ: Univ. of Arizona Press), 59 Q2
- Andrews, S. M., Wilner, D. J., Hughes, A. M., et al. 2012, *ApJ*, 744, 162
- Andrews, S. M., & Williams, J. P. 2007, *ApJ*, 659, 705
- Arce, H. G., Shepherd, D., Gueth, F., Lee, C.-F., Bachiller, R., Rosen, A., & Beuther, H. 2007, in *Protostars and Planets V*, ed. B. Reipurth, D. Jewitt, & K. Keil (Tucson: Univ. of Arizona Press), 245
- Arce, H. G., & Sargent, A. I. 2006, *ApJ*, 646, 1070
- Arce, H. G., & Sargent, A. I. 2004, *ApJ*, 612, 342
- Attard, M., Houde, M., Novak, G., et al. 2009, *ApJ*, 702, 1584
- Bachiller, R. 1996, *ARA&A*, 34, 111
- Bachiller, R., Guilloteau, S., Dutrey, A., Planesas, P., & Martin-Pintado, J. 1995, *A&A*, 299, 857
- Bachiller, R., & Perez Gutierrez, M. 1997, *ApJ*, 487, L93
- Bachiller, R., & Tafalla, M. 1999, in *NATO ASIC Proc. 540, The Origin of Stars and Planetary Systems*, ed. C. J. Lada & N. D. Kylafis (Dordrecht: Kluwer), 227
- Basu, S. 1998, *ApJ*, 509, 229
- Basu, S., & Mouschovias, T. C. 1994, *ApJ*, 432, 720
- Beckwith, S. V. W., Sargent, A. I., Chini, R. S., & Guesten, R. 1990, *AJ*, 99, 924

- 
- Bottinelli, S., Ceccarelli, C., Williams, J. P., & Lefloch, B. 2007, *A&A*, 463, 601
- Brinch, C., Crapsi, A., Jørgensen, J. K., Hogerheijde, M. R., & Hill, T. 2007a, *A&A*, 475, 915
- Brinch, C., Crapsi, A., Hogerheijde, M. R., & Jørgensen, J. K. 2007b, *A&A*, 461, 1037
- Brinch, C., Jørgensen, J. K., & Hogerheijde, M. R. 2009, *A&A*, 502, 199
- Cabrit, S., Goldsmith, P. F., & Snell, R. L. 1988, *ApJ*, 334, 196
- Caselli, P., Benson, P. J., Myers, P. C., & Tafalla, M. 2002, *ApJ*, 572, 238
- Cassen, P., & Moosman, A. 1981, *ICARUS*, 48, 353
- Chandler, C. J., & Sargent, A. I. 1993, *ApJ*, 414, L29
- Chandler, C. J., Terebey, S., Barsony, M., Moore, T. J. T., & Gautier, T. N. 1996, *ApJ*, 471, 308
- Chen, X., Launhardt, R., & Henning, T. 2007, *ApJ*, 669, 1058
- Chiang, H.-F., Looney, L. W., Tassis, K., Mundy, L. G., & Mouschovias, T. C. 2008, *ApJ*, 680, 474
- Chiang, H.-F., Looney, L. W., & Tobin, J. J. 2012, *ApJ*, 756, 168
- Chiang, H.-F., Looney, L. W., Tobin, J. J., & Hartmann, L. 2010, *ApJ*, 709, 470
- Choi, M. 2005, *ApJ*, 630, 976
- Choi, M. 2007, *PASJ*, 59, L41
- Choi, M., Evans, N. J., II, Gregersen, E. M., & Wang, Y. 1995, *ApJ*, 448, 742
- Claussen, M. J., Marvel, K. B., Wootten, A., & Wilking, B. A. 1998, *ApJ*, 507, L79
- Curiel, S., Torrelles, J. M., Rodríguez, L. F., Gómez, J. F., & Anglada, G. 1999, *ApJ*, 527, 310
- Dapp, W. B., Basu, S., & Kunz, M. W. 2012, *A&A*, 541, A35


- 
- Davidson, J. A., Novak, G., Matthews, T. G., et al. 2011, *ApJ*, 732, 97
- Di Francesco, J., Myers, P. C., Wilner, D. J., Ohashi, N., & Mardones, D. 2001, *ApJ*, 562, 770
- Dunham, M. M., Crapsi, A., Evans, N. J., II, Bourke, T. L., Huard, T. L., Myers, P. C., & Kauffmann, J. 2008, *ApJS*, 179, 249
- Dutrey, A., Guilloteau, S., & Bachiller, R. 1997, *A&A*, 325, 758
- Dutrey, A., Guilloteau, S., Prato, L., et al. 1998, *A&A*, 338, L63
- Eisner, J. A. 2012, *ApJ*, 755, 23
- Eisner, J. A., Hillenbrand, L. A., Carpenter, J. M., & Wolf, S. 2005, *ApJ*, 635, 396
- Enoch, M. L., Corder, S., Dunham, M. M., & Duchêne, G. 2009a, *ApJ*, 707, 103
- Enoch, M. L., Evans, N. J., II, Sargent, A. I., & Glenn, J. 2009b, *ApJ*, 692, 973
- Enoch, M. L., Young, K. E., Glenn, J., et al. 2006, *ApJ*, 638, 293
- Evans, N. J., II, Dunham, M. M., Jørgensen, J. K., et al. 2009, *ApJS*, 181, 321
- Evans, N. J., II, Lee, J.-E., Rawlings, J. M. C., & Choi, M. 2005, *ApJ*, 626, 919
- Falgarone, E., Troland, T. H., Crutcher, R. M., & Paubert, G. 2008, *A&A*, 487, 247
- Furlan, E., McClure, M., Calvet, N., et al. 2008, *ApJS*, 176, 184
- Flower D. R. 2001, *J. Phys. B: At. Mol. Opt. Phys.*, 34, 2731
- Frerking, M. A., Langer, W. D., & Wilson, R. W. 1987, *ApJ*, 313, 320
- Froebrich, D., Smith, M. D., Hodapp, K.-W., & Eislöffel, J. 2003, *MNRAS*, 346, 163
- Gålfalk, M., & Olofsson, G. 2007, *A&A*, 475, 281
- Galli, D., & Shu, F. H. 1993, *ApJ*, 417, 220
- Giannini, T., Nisini, B., & Lorenzetti, D. 2001, *ApJ*, 555, 40
- Girart, J. M., & Acord, J. M. P. 2001, *ApJ*, 552, L63


- 
- Girart, J. M., Rao, R., & Marrone, D. P. 2006, *Science*, 313, 812
- Goldreich, P., & Kwan, J. 1974, *ApJ*, 189, 441
- Goodman, A. A., Benson, P. J., Fuller, G. A., & Myers, P. C. 1993, *ApJ*, 406, 528
- Green, S., & Chapman, S. 1978, *ApJS*, 37, 169
- Gueth, F., & Guilloteau, S. 1999, *A&A*, 343, 571
- Guilloteau, S., & Dutrey, A. 1998, *A&A*, 339, 467
- Guilloteau, S., Dutrey, A., & Simon, M. 1999, *A&A*, 348, 570
- Guilloteau, S., Dutrey, A., Piétu, V., & Boehler, Y. 2011, *A&A*, 529, A105
- Guilloteau, S., & Dutrey, A. 1994, *A&A*, 291, L23
- Hartmann, L., Calvet, N., Gullbring, E., & D'Alessio, P. 1998, *ApJ*, 495, 385
- Hartigan, P., Kenyon, S. J., Hartmann, L., Strom, S. E., Edwards, S., Welty, A. D., & Stauffer, J. 1991, *ApJ*, 382, 617
- Hartmann, L., & Kenyon, S. J. 1996, *ARA&A*, 34, 207
- Harvey, D. W. A., Wilner, D. J., Lada, C. J., Myers, P. C., Alves, J. F., & Chen, H. 2001, *ApJ*, 563, 903
- Harvey, D. W. A., Wilner, D. J., Myers, P. C., & Tafalla, M. 2003a, *ApJ*, 596, 383
- Harvey, D. W. A., Wilner, D. J., Myers, P. C., Tafalla, M., & Mardones, D. 2003b, *ApJ*, 583, 809
- Hayashi, M., Ohashi, N., & Miyama, S. M. 1993, *ApJ*, 418, L7
- Hennebelle, P., & Fromang, S. 2008, *A&A*, 477, 9
- Hirano, N., Ho, P. P. T., Liu, S.-Y., et al. 2010, *ApJ*, 717, 58
- Hirano, N., Kameya, O., Kasuga, T., Hawegawa, T., Hayashi, S.S., Umemoto, T. 1991, in *Molecular Clouds*, ed.R.A. James & T.J. Miller (Cambridge: Cambridge Univ. Press), 115

- 
- Hirano, N., Kameya, O., Kasuga, T., & Umemoto, T. 1992, *ApJ*, 390, L85
- Hirano, N., Kameya, O., Nakayama, M., & Takakubo, K. 1988, *ApJ*, 327, L69
- Hirano, N., & Taniguchi, Y. 2001, *ApJ*, 550, L219
- Ho, P. T. P., Moran, J. M., & Lo, K. Y. 2004, *ApJ*, 616, L1
- Hogerheijde, M. R. 2001, *ApJ*, 553, 618
- Hogerheijde, M. R., van Dishoeck, E. F., Blake, G. A., & van Langevelde, H. J. 1998, *ApJ*, 502, 315
- Hull, C. L. H., Plambeck, R. L., Bolatto, A. D., et al. 2013, *ApJ*, 768, 159
- Isella, A., Carpenter, J. M., & Sargent, A. I. 2009, *ApJ*, 701, 260
- Jørgensen, J. K., van Dishoeck, E. F., Visser, R., et al. 2009, *A&A*, 507, 861
- Jørgensen, J. K., Bourke, T. L., Myers, P. C., Schoier, F. L., van Dishoeck, E. F., & Wilner, D. J. 2005, *ApJ*, 632, 973
- Jørgensen, J. K., Bourke, T. L., Myers, P. C., Di Francesco, J., van Dishoeck, E. F., Lee, C.-F., Ohashi, N., Schöier, F. L., Takakuwa, S., Wilner, D. J., Zhang, Q. 2007, *ApJ*, 659, 479
- Jørgensen, J. K., Schöier, F. L., & van Dishoeck, E. F. 2004a, *A&A*, 416, 603
- Jørgensen, J. K., Hogerheijde, M. R., van Dishoeck, E. F., Blake, G. A., & Schöier, F. L. 2004b, *A&A*, 413, 993
- Joos, M., Hennebelle, P., & Ciardi, A. 2012, *A&A*, 543, A128
- Keene, J., Davidson, J. A., Harper, D. A., Hildebrand, R. H., Jaffe, D. T., Loewenstein, R. F., Low, F. J., & Pernic, R. 1983, *ApJ*, 274, L43
- Keene, J., Hildebrand, R. H., Whitcomb, S. E., & Harper, D. A. 1980, *ApJ*, 240, L43
- Kenyon, S. J., Calvet, N., & Hartmann, L. 1993, *ApJ*, 414, 676
- Kitamura, Y., Momose, M., Yokogawa, S., Kawabe, R., Tamura, M., & Ida, S. 2002, *ApJ*, 581, 357

- Kenyon, S. J., Calvet, N., & Hartmann, L. 1993, *ApJ*, 414, 676
- Larson, R. B. 1969, *MNRAS*, 145, 271
- Lee, C.-F. 2010, *ApJ*, 725, 712
- Lee, C.-F., Hirano, N., Palau, A., Ho, P. T. P., Bourke, T. L., Zhang, Q., & Shang, H. 2009, *ApJ*, 699, 1584
- Lee, C.-F., Ho, P. T. P., Beuther, H., Bourke, T. L., Zhang, Q., Hirano, N., & Shang, H. 2006, *ApJ*, 639, 292
- Lee, C.-F., Ho, P. T. P., Hirano, N., Beuther, H., Bourke, T. L., Shang, H., & Zhang, Q. 2007a, *ApJ*, 659, 499
- Lee, C.-F., Ho, P. T. P., Palau, A., Hirano, N., Bourke, T. L., Shang, H., & Zhang, Q. 2007b, *ApJ*, 670, 1188
- Lee, C.-F., Ho, P. T. P., & White, S. M. 2005, *ApJ*, 619, 948
- Lee, C.-F., Mundy, L. G., Reipurth, B., Ostriker, E. C., & Stone, J. M. 2000, *ApJ*, 542, 925
- Li, Z.-Y., Krasnopolsky, R., & Shang, H. 2011, *ApJ*, 738, 180
- Lin, D. N. C., Hayashi, M., Bell, K. R., & Ohashi, N. 1994, *ApJ*, 435, 821
- Lommen, D., Jørgensen, J. K., van Dishoeck, E. F., & Crapsi, A. 2008, *A&A*, 481, 141
- Looney, L. W., Mundy, L. G., & Welch, W. J. 2003, *ApJ*, 592, 255
- Lucas, R., & Liszt, H. 1998, *A&A*, 337, 246
- Machida, M. N., Inutsuka, S.-I., & Matsumoto, T. 2011, *PASJ*, 63, 555
- Marvel, K. B., Wilking, B. A., Claussen, M. J., & Wootten, A. 2008, *ApJ*, 685, 285
- Masunaga, H., & Inutsuka, S.-i. 2000, *ApJ*, 531, 350
- Mellon, R. R., & Li, Z.-Y. 2008, *ApJ*, 681, 1356
- Mellon, R. R., & Li, Z.-Y. 2009, *ApJ*, 698, 922



- 
- Momose, M., Ohashi, N., Kawabe, R., Nakano, T., & Hayashi, M. 1998, *ApJ*, 504, 314
- Moriarty-Schieven, G. H., Wannier, P. G., Mangum, J. G., Tamura, M., & Olmsted, V. K. 1995, *ApJ*, 455, 190
- Moriarty-Schieven, G. H., & Snell, R. L. 1989, *ApJ*, 338, 952
- Motte, F., & André, P. 2001, *A&A*, 365, 440
- Myers, P. C., Evans, N. J., II, Ohashi, N. 2000, in *Protostars and Planets IV*, ed. V., Mannings, A. P., Boss, & S. S., Russel (Tucson, AZ: Univ. of Arizona Press), 217
- Myers, P. C., & Ladd, E. F. 1993, *ApJ*, 413, L47
- Nakano, T., & Nakamura, T. 1978, *PASJ*, 30, 671
- Nakazato, T., Nakamoto, T., & Umemura, M. 2003, *ApJ*, 583, 322
- Nisini, B., et al. 1999, *A&A*, 343, 266
- Ohashi, N., Hayashi, M., Ho, P. T. P., & Momose, M. 1997a, *ApJ*, 475, 211
- Ohashi, N., Hayashi, M., Ho, P. T. P., Momose, M., & Hirano, N. 1996, *ApJ*, 466, 957
- Ohashi, N., Hayashi, M., Ho, P. T. P., Momose, M., Tamura, M., Hirano, N., & Sargent, A. I. 1997b, *ApJ*, 488, 317
- Padgett, D. L., Brandner, W., Stapelfeldt, K. R., et al. 1999, *AJ*, 117, 1490
- Penston, M. V. 1969, *MNRAS*, 144, 425
- Pérez, L. M., Carpenter, J. M., Chandler, C. J., et al. 2012, *ApJ*, 760, L17
- Piétu, V., Dutrey, A., & Guilloteau, S. 2007, *A&A*, 467, 163
- Qi, C., Ho, P. T. P., Wilner, D. J., et al. 2004, *ApJ*, 616, L11
- Qi, C., Kessler, J. E., Koerner, D. W., Sargent, A. I., & Blake, G. A. 2003, *ApJ*, 597, 986

- 
- Reipurth, B., Heathcote, S., & Vrba, F. 1992, *A&A*, 256, 225
- Saito, M., Kawabe, R., Kitamura, Y., & Sunada, K. 1996, *ApJ*, 473, 464
- Saito, M., Sunada, K., Kawabe, R., Kitamura, Y., & Hirano, N. 1999, *ApJ*, 518, 334
- Sault, R. J., & Noordam, J. E. 1995, *A&AS*, 109, 593
- Sault, R. J., Teuben, P. J., & Wright, M. C. H. 1995, in *ASP Conf. Ser. 77, Astronomical Data Analysis Software and Systems IV*, ed. R. A. Shaw, H. E. Payne, & J. J. E. Hayes (San Francisco, CA: ASP), 433
- Schuster, K. F., Harris, A. I., Anderson, N., & Russell, A. P. G. 1993, *ApJ*, 412, L67
- Scoville, N. Z., Carlstrom, J. E., Chandler, C. J., et al. 1993, *PASP*, 105, 1482
- Shang, H. 2007, *Ap&SS*, 311, 25
- Shinnaga, H., Phillips, T. G., Furuya, R. S., & Kitamura, Y. 2009, *ApJ*, 706, L226
- Shirley, Y. L., Evans, N. J., II, Rawlings, J. M. C., & Gregersen, E. M. 2000, *ApJS*, 131, 249
- Shu, F. H. 1977, *ApJ*, 214, 488
- Shu, F. H., Adams, F. C., & Lizano, S. 1987, *ARA&A*, 25, 23
- Shu, F., Najita, J., Ostriker, E., Wilkin, F., Ruden, S., & Lizano, S. 1994, *ApJ*, 429, 781
- Simon, M., Dutrey, A., & Guilloteau, S. 2000, *ApJ*, 545, 1034
- Spaans, M., Hogerheijde, M. R., Mundy, L. G., & van Dishoeck, E. F. 1995, *ApJ*, 455, L167
- Stahler, S. W., Shu, F. H., & Taam, R. E. 1980, *ApJ*, 241, 637
- Stutz, A. M., Rubin, M., Werner, M. W., Rieke, G. H., Bieging, J. H., Keene, J., Kang, M., Shirley, Y. L., Su, K. Y. L., Velusamy, T., Wilner, D. J. 2008, *ApJ*, 687, 389



- Surdej, J. 1977, *A&A*, 60, 303
- Tafalla, M., Mardones, D., Myers, P. C., Caselli, P., Bachiller, R., & Benson, P. J. 1998, *ApJ*, 504, 900
- Takakuwa, S., Saito, M., Lim, J., et al. 2012, *ApJ*, 754, 52
- Takakuwa, S., Kamazaki, T., Saito, M., & Hirano, N. 2003, *ApJ*, 584, 818
- Takakuwa, S., Kamazaki, T., Saito, M., Yamaguchi, N., & Kohno, K. 2007a, *PASJ*, 59, 1
- Takakuwa, S., Ohashi, N., Bourke, T. L., Hirano, N., Ho, P. T. P., Jørgensen, J. K., Kuan, Y. J., Wilner, D. J., Yeh, S. C. C. 2007b, *ApJ*, 662, 431
- Takakuwa, S., Ohashi, N., Ho, P. T. P., Qi, C., Wilner, D. J., Zhang, Q., Bourke, T. L., Hirano, N., Choi, M., Yang, J. 2004, *ApJ*, 616, L15
- Terebey, S., Shu, F. H., & Cassen, P. 1984, *ApJ*, 286, 529
- Tobin, J. J., Hartmann, L., Chiang, H.-F., et al. 2012a, *Nature*, 492, 83
- Tobin, J. J., Hartmann, L., Bergin, E., et al. 2012b, *ApJ*, 748, 16
- Tobin, J. J., Hartmann, L., Calvet, N., & D'Alessio, P. 2008, *ApJ*, 679, 1364
- Tobin, J. J., Hartmann, L., Chiang, H.-F., et al. 2011, *ApJ*, 740, 45
- Tobin, J. J., Looney, L. W., Mundy, L. G., Kwon, W., & Hamidouche, M. 2007, *ApJ*, 659, 1404
- Tomita, Y., Saito, T., & Ohtani, H. 1979, *PASJ*, 31, 407
- Troland, T. H., & Crutcher, R. M. 2008, *ApJ*, 680, 457
- Turner, B. E., Chan, K.-W., Green, S., & Lubowich, D. A. 1992, *ApJ*, 399, 114
- Ulrich, R. K. 1976, *ApJ*, 210, 377
- van Kempen, T. A., et al. 2009, *A&A*, 507, 1425
- van Kempen, T. A., Hogerheijde, M. R., van Dishoeck, E. F., Güsten, R., Schilke, P., & Nyman, L.-Å. 2006, *A&A*, 454, L75

Velusamy, T., & Langer, W. D. 1998, *Nature*, 392, 685

Vogel, S. N., Wright, M. C. H., Plambeck, R. L., & Welch, W. J. 1984, *ApJ*, 283, 655

Volgenau, N. H., Mundy, L. G., Looney, L. W., & Welch, W. J. 2006, *ApJ*, 651, 301

Wakelam, V., Ceccarelli, C., Castets, A., et al. 2005, *A&A*, 437, 149

Wilner, D. J., Myers, P. C., Mardones, D., & Tafalla, M. 2000, *ApJ*, 544, L69

Wilner, D. J., & Welch, W. J. 1994, *ApJ*, 427, 898

Winnewisser, G., Churchwell, E., & Walmsley, C. M. 1979, *Modern Aspects of Microwave Spectroscopy*, 313

Wright, J. T., Fakhouri, O., Marcy, G. W., et al. 2011, *PASP*, 123, 412

Zhou, S., Evans, N. J., II, Koempe, C., & Walmsley, C. M. 1993, *ApJ*, 404, 232

Zinnecker, H., McCaughrean, M. J., & Rayner, J. T. 1998, *Nature*, 394, 862

